THE ADAPTIVE COUPLING OF HEAT AND AIR FLOW MODELLING WITHIN DYNAMIC WHOLE-BUILDING SIMULATION

Ian Beausoleil-Morrison, B.A.Sc., M.A.Sc.

A thesis submitted for the
Degree of Doctor of Philosophy

Energy Systems Research Unit
Department of Mechanical Engineering
University of Strathclyde, Glasgow UK

May 2000

In the memory of my father

COPYRIGHT DECLARATION

Table of Contents

Abstract

This thesis is concerned with advancing the modelling of indoor air flow and internal surface convection within dynamic whole-building simulation. The path taken is the conflation of computational fluid dynamics (CFD) techniques with dynamic whole-building simulation, with an accurate treatment of the co-dependencies between these modelling domains.

Two flow responsive modelling techniques were devised and implemented within the ESP-r simulation program to achieve the research objectives. The *adaptive convection algorithm* enhances ESP-r's thermal simulation domain by dynamically controlling the simulation of internal surface convection. Empirical methods were extracted from the literature and a new method for characterizing mixed flow convective regimes was created to provide the algorithm with a basis of 28 convection coefficient correlations. Collectively these methods can calculate convection coefficients for most flows of practical interest. Working with this suite of correlations, the algorithm assigns appropriate equations to each internal surface and adapts the selection in response to the room's evolving flow regime.

The *adaptive conflation controller* manages all interactions between the thermal and CFD modelling domains. The controller incorporates the latest turbulence modelling advancements applicable for room air flow simulation and possesses a suite of handshaking and thermal boundary condition treatments. The job of this adaptive conflation controller is to monitor the evolving thermal and air flow conditions in the room and dynamically select an appropriate combination of modelling approaches for the prevailing conditions. The two control schemes implemented to demonstrate the controller make use of a double-pass modelling approach. Each time-step that the thermal domain handshakes with CFD, the adaptive conflation controller performs an investigative simulation to approximate the room's flow and temperature field. Using these estimates, the controller calculates dimensionless groupings to determine the nature of the flow (forced, buoyant, mixed, fully turbulent, weakly turbulent) adjacent to each internal surface. This information is used to select suitable boundary condition treatments for each surface. A second CFD simulation is then performed using the refined modelling approach to more accurately resolve the room's air flow and temperature distribution, and to predict surface convection. In order to protect the thermal domain, a two-stage screening process is used to assess (and where necessary reject) the CFD-predicted surface convection estimates.

These adaptive modelling techniques advance the modelling of indoor air flow and internal surface convection within whole-building simulation.

Acknowledgements

I would first like to acknowledge the support of my thesis supervisor, Professor Joe Clarke. He inspired, motivated, and challenged me throughout the course of my studies. He has been a mentor to me in the true sense of the word.

Many thanks to the staff and students at the Energy Systems Research Unit for creating a stimulating, welcoming, and positive atmosphere. I would especially like to thank Paul Strachan, Jon Hand, Milan Janak, Lori McElroy, Iain MacDonald, Nick Kelly, Bill Dempster, Cameron Johnstone, and Jan Hensen for many interesting conversations, hillwalks, and outings to the pub.

I wish to express the sincerest gratitude to my managers at Natural Resources Canada, Mark Riley, Frank Campbell, and Bryan Cook. This thesis would never have been written had they not believed in me and had the vision to support my studies. Special thanks to Sherif Barakat of the National Research Council of Canada for acting as my local thesis supervisor. His constant encouragement and challenging questions helped keep me pointed in the right direction. My colleagues in the Buildings Group at Natural Resources Canada have been an incredible support to me and source of encouragement. If they had not covered for me during my many absences (physical and mental) my mind would not have been sufficiently free to create. I could not ask for a finer group of colleagues. Special thanks to Rachel Beausoleil-Morrison, Jeff Blake, Jon Hand, and Duncan Phillips, who took the time to review and comment on sections of the manuscript.

I would never have thought to write this thesis had my parents not taught me the value of education and hard work, and raised me to believe I could achieve anything I set my mind to. A very special thanks to my family and friends who have understood and accepted my distracted state and infrequent communications over the past four years. And to my Scottish family, who have accepted me with open arms during my many trips to Glasgow. I will have fond memories of these visits for the rest of my life.

Finally, and most importantly, I wish to express my warmest appreciation and love for my wife, Rachel Chantal Beausoleil-Morrison. I could not have accomplished my goal without her unfaltering support, encouragement, and inspiration. During the past half year, she stubbornly refused to allow my mind's stressed and exhausted state to distort reality. She also selflessly accepted my lack of attention and time. C'est impossible pour moi de décrire en mots l'amour que j'ai pour toi, Rachel.

List of Symbols

a	Neighbouring and self-coupling coefficients of the discretized finite volume equations, or Churchill-Usagi blending coefficient	
ac/h	Volumetric flow rate measured in room air changes per hour	$\{ac/h\}$
A	Area or onstant representing wall roughness	$\{m^2\}$ or $\{\ \}$
Ar	Archimedes number	
b	Source term coefficient of the discretized finite volume equations	
c_p	Specific heat	$\{J/kgK\}$
C_1	Empirical constant in $k-\varepsilon$ model, or correlation constant	$\{\ \}$
C_2	Empirical constant in $k-\varepsilon$ model, or correlation constant	$\{\ \}$
C_3	Correlation constant	$\{\ \}$
C_μ	Empirical constant in $k-\varepsilon$ model	$\{\ \}$
D_h	Hydraulic diameter	$\{m\}$
E	Constant representing wall roughness	
F	Shear force	$\{N\}$
g	Gravitational acceleration	$\{m/s^2\}$
Gr	Grashof number	
h_c	Convection coefficient	$\{W/m^2K\}$
H	Height of a vertical surface	$\{m\}$
i, j	Grid indices in x and y directions	
k	Thermal conductivity or turbulence kinetic energy	$\{W/mK\}$ or $\{m^2/s^2\}$
l	A length scale	$\{m\}$
L	A length scale	$\{m\}$
$\dot{m}$	Mass flow rate	$\{kg/s\}$
Nu	Nusselt number	
P	Pressure	$\{Pa\}$
Pr	Prandtl number = $c_p\mu/k$	$\{\ \}$
q	Heat flow	$\{W\}$
q''	Heat flux	$\{W/m^2\}$
q'''	Heat source	$\{W/m^3\}$
R	Equation residual	

Ra	Rayleigh number	
Re	Reynolds number	
t	Time	$\{seconds\}$
T	Temperature	$\{K\ or\ {}^{o}C\}$
T_{∞}	Reference temperature	$\{K\ or\ {}^{o}C\}$
u	Velocity component in x-direction	$\{m/s\}$
v	Velocity component in y-direction	$\{m/s\}$
V	Volume	$\{m^3\}$
$\dot{V}$	Volumetric flow rate	$\{m^3/s\}$
$\bar{V}$	Magnitude of time-mean velocity	$\{m/s\}$
w	Velocity component in z-direction	$\{m/s\}$
u_j	Velocity components expressed in tensor notation	$\{m/s\}$
x, y, z	Cartesian coordinates	$\{m\}$
x_j	Cartesian coordinates expressed in tensor notation	$\{m\}$

Greek symbols

Γ	Turbulent heat diffusion	$\{Pa \cdot s\}$
ρ	Fluid density	$\{kg/m^3\}$
μ	Molecular viscosity	$\{Pa \cdot s\}$
μ_t	Eddy viscosity	$\{Pa \cdot s\}$
β	Thermal expansion coefficient of air	$\{K^{-1}\}$
$\Delta\phi$	Property difference between two points (ϕ could be temperature, pressure, etc.)	
Δy_{PN}	Distance in y-direction between P and N solution points	$\{m\}$
ΔT	Temperature difference (e.g. between surface and room air)	$\{{}^{o}C\}$
ϕ	An independent variable (temperature, pressure, turbulence energy, etc.)	
τ	Shear stress	$\{N/m^2\}$
ε	Dissipation rate of turbulence energy	$\{m^2/s^3\}$
σ_t	turbulent Prandtl number	$\{\ \}$
δ_{ij}	Kronecker delta; = 0 when $i \neq j$, = 1 when $i = j$	$\{\ \}$
σ_k	Empirical constant in $k - \varepsilon$ model	$\{\ \}$
σ_{ε}	Empirical constant in $k - \varepsilon$ model	$\{\ \}$
κ	von Kármán's constant	$\{\ \}$
Δx, Δy, Δz	Width, depth, and height of a control volume	$\{m\}$

Subscripts

$back - loss$	Conduction loss through heat transfer meter
c	Convection
$conv$	Convection
e	State at *east* face of control volume
$elec - input$	Electrical energy input to a heat transfer meter
$diffuser$	Property measured at diffuser supplying air to room
E	State at solution point of *east* neighbouring control volume
h	State at *high* face of control volume
H	State at solution point of *high* neighbouring control volume
i	A quantity evaluated within the *inner* layer of a natural convection bounary layer
l	State at *low* face of control volume
L	State at solution point of *low* neighbouring control volume, or a dimensionless quantity evaluated with length scale L
n	State at *north* face of control volume
nb	Neighbouring control volumes
N	State at solution point of *north* neighbouring control volume
o	A quantity evaluated within the *outer* layer of a natural convection bounary layer
P	State at solution point of control volume under consideration
q	A scaled quantity based on the surface convection heat flux
r	Radiation
$room$	Property of room air
$room - air$	Averaged property of the room air
s	State at *south* face of control volume
S	State at solution point of *south* neighbouring control volume
$surf$	Surface
w	State at *west* face of control volume
$wall$	Variable evaluated at a wall
W	State at solution point of *west* neighbouring control volume
$plant$	Plant interaction
$solar$	Solar gain
$cas - rad$	Radiant energy from casual sources
$cas - conv$	Convective energy from casual sources
I	State at node under consideration

$I-1, I+1$	State at neighbouring nodes
τ	A flow property based on the wall friction

Superscripts

^{o}	Value of solution variable at a previous solver iteration
*	*Guessed* value for a solution variable, or a dimensionless quantity
**	A dimensionless quantity
$'$	*Correction-term* for a solution variable, or the fluctuation of a solution variable about its time-mean value
$\overline{}$	Time-mean quantity of a solution variable
^{t}	Value of a variable at the beginning of a simulation time-step
$^{t+\Delta t}$	Value of a variable at the end of a simulation time-step

CHAPTER 1

Introduction

1.1 The Evolution of Building Simulation

Early approaches

Until the mid 1960s only simple hand-calculation methods were available for estimating energy usage in buildings. The *degree day* method was commonly used to calculate heating energy requirements while, according to Ayres and Stamper (1995), the common approach for estimating cooling energy requirements (at least in North America) was the *equivalent full load hour (EQFL)* method. The more detailed *bin* method was used for both heating and cooling analyses.

Degree days, a measure of a climate's severity, are calculated by integrating over the year the daily-averaged outdoor-air temperature relative to a fixed base (often 18 °C), $DD = \sum 1 day \cdot [\overline{T_{outdoors}} - T_{base}]$. Degree days for various locations were tabulated, published and used in conjunction with the steady-state peak heating load and a fixed heating-system efficiency to estimate the usage of heating fuel over the year. Although it was useful at the time, the degree day method neglected many significant factors, such as transient thermal storage in building materials, solar gains, internal gains, variations in outdoor-air ventilation and infiltration rates, and the non-steady operation of heating equipment. Similarly, the EQFL method estimated the cooling energy consumption by multiplying the steady-state peak cooling load by a climate severity factor. In this case, climate severity was quantified by EQFL, a factor equal to the length of time the cooling equipment would have to operate at full capacity to satisfy the annual cooling load. The efficiency of the cooling equipment was characterized by a single and constant factor.

As with the degree day approach, the bin method treats outdoor air temperature as the independent variable in the analysis. The analysis period—usually a year in that era—is sorted into "bins" according to the outdoor temperature. Each bin thus contains the number of occurrences (usually measured in hours) within its range of outdoor temperatures (typically ~3°C wide). The energy consumption of each bin is determined (independently) using simplified steady-state approaches much like those of the degree day method. The predictions from all bins are then summed, yielding an estimate of the building's heating and cooling energy consumption. Compared to the degree day approach, the bin method allows some assumptions about fixed conditions to be dropped: infiltration rates and cooling system efficiencies can vary with indoor-outdoor temperature difference, for example. However, the bin method implicitly assumes that energy flows within the building are exclusively a function of indoor-outdoor temperature difference; therefore the timing (even day versus night) of solar and internal gains, and transient indoor conditions cannot be explicitly considered. Although more resolved binning approaches have been introduced in an attempt to address this fundamental shortcoming, the unifying characteristic of all bin methods is that time has been eliminated as a variable in the analysis.

True simulation methods

The first *true* simulation methods—true in that they attempted to imitate physical conditions by treating time as the independent variable—appeared in the mid 1960s (e.g. GATC 1967). Because computing resources were limited, slow, and extremely expensive it was necessary to subdivide the problem domain. The so-called *Loads-Systems-Plant* (LSP) modelling strategy was commonly employed in these early approaches, it subdividing the simulation of the building into three sequential steps. The building's heating and cooling loads are first calculated for the entire analysis period (often a year) for an assumed set of indoor environmental conditions. These loads are then imposed as inputs to the second step of the simulation, which models the plant's air handling and energy distribution system[1] (fans, heating coils, cooling coils, air diffusers, etc.). This second simulation step (also conducted for the entire analysis period) predicts the demands placed on the plant's energy conversion systems[2] (boilers, chillers) and related equipment (cooling towers and circulation pumps). Finally, the energy conversion and related systems are simulated in the third step, receiving as input the results of the second step. Obviously, the sequential nature of the LSP approach neglects interactions between the steps. The impact of undersized heating or cooling equipment cannot be considered. Furthermore, situations in which there is strong coupling between the steps (e.g. the impact of the air handling system on infiltration; the impact of room temperatures on occupant behaviour such as the opening and closing of windows) cannot be adequately treated.

Many of the early simulation methods utilized simplified approaches for modelling building loads, such as the time-averaging approach, which smeared internal heat gains over a period of time to roughly approximate the transient thermal storage, radiation, and convection processes that were actually occurring. New techniques were introduced to address such shortcomings. The pioneering work of Stephenson and Mitalas (e.g. 1967) on the *response factor* method significantly advanced the modelling of transient heat transfer through the opaque fabric and the heat transfer between internal surfaces and the room air. They utilized the principle of superposition to decompose the complex non-linear heat transfer system into a summation of responses of the component parts. This allows, for example, solar insolation to be modelled with a simple algebraic summation, using *weighting factors* which relate the convection (of heat to the room air) to the solar radiation absorbed by internal surfaces at previous periods of time. Heat transmission through the walls is calculated by another

---

[1] Sometimes referred to as the *secondary* heating, ventilation, and air conditioning (HVAC) system.

[2] Sometimes referred to as the *central plant* or the *primary* HVAC system.

(independent) summation, this one operating on the time-series history of wall surface temperatures. In effect, the response factor method decouples the treatment of solar insolation from the modelling of heat transfer through walls.

Heat-balance approaches

Heat balance approaches were introduced in the 1970s (e.g. Kusuda 1976) to enable a more rigorous treatment of building loads. Rather than utilizing weighting factors to characterize the thermal response of the room air to solar insolation, internal gains, and heat transfer through the fabric, this methodology solves heat balances for the room air and at the surfaces of fabric components. These heat balances consider all important energy flow paths: transmission through the fabric, longwave radiation exchange between internal surfaces, solar insolation, convection from the indoor air to wall and window surfaces, etc. The heat balances are formed and solved each time step to estimate surface and room-air temperatures, and heat flows. The heat balances replace the room-air weighting factors, although response factors (or z-transfer functions, a similar but more efficient arrangement) are still employed to calculate the heat transmission through the opaque fabric. Although more computationally demanding than room-air weighting factors, the introduction of the heat balance approach allowed some significant assumptions of linearity to be dropped. For example, convection coefficients characterizing heat transfer from internal surfaces to the room air could respond to thermal states within the room, rather than being treated as constant.

Numerical discretization and simultaneous solution techniques were developed as a higher-resolution alternative to the response factor methods (Clarke 1977). Essentially, this approach extends the concept of the heat balance methodology to all relevant building and plant components. A finite-volume (or finite-difference) discretization approach to the conservation of energy is employed to represent the opaque and transparent fabric, internal air spaces, and plant components. This approach does not demand the assumption of linearity—a prerequisite when using response factors (or z-transfer functions) to calculate fabric transmission—thus allowing material properties to vary with temperature and time. As well, it provides flexibility in the choice of simulation time steps (i.e. sub-hourly).

HVAC and air flow modelling

More complex and rigorous methods for modelling HVAC systems were introduced in the 1980s. Transient models and more fundamental approaches were developed (see Lebrun, 1982, for example) as alternatives to the traditional approach which performed mass and energy balances on pre-configured templates of common HVAC systems, the components of which (fans, coils, boilers, etc.) were represented by overall efficiency values, calculated by curve fits to manufacturers' data. Additionally, in the 1980s the simulation of building loads and HVAC were integrated in order to consider the important interactions between the two (e.g. McLean 1982, Clarke 1982, Tang 1985, Park et al 1985).

Activity in the building simulation field was not limited to thermal considerations. Parallel work was underway on air flow modelling. Methods were developed for estimating wind and buoyancy-driven infiltration rates (e.g. Sherman and Grimsrud 1980), while at the other end of the resolution spectrum, computational fluid dynamics (CFD) approaches were being applied to simulate the details of air flow patterns within single rooms (Nielsen, 1974, is credited with the first application). In the 1970s *multi-zone network air flow models* were developed for simulating both infiltration and internal air flow (e.g. Jackman 1970, Sander 1974; see Feustel and Dieris, 1992, for a review). These are macroscopic models, which represent large air volumes (e.g. rooms) by single nodes, and predict flow through discrete paths (e.g. doors, cracks).

The thermal and air flow simulation approaches did not begin their convergence until the mid 1980s (e.g. Walton 1983, Maver and Clarke 1984), at which time the multi-zone network air flow models were integrated into thermal models to couple the simulation of heat and air flow, and to analyze pollutant dispersion within buildings. Until this time, the thermal simulation tools focussed strictly on energy processes. Although the thermal impact of both air infiltration and (in some cases) inter-zone air flow was considered, flow rates were either user-prescribed or estimated using simplified approaches. Air flow was not simulated, but rather merely its impact considered in the thermal simulation. As a result, configurations in which heat and air flow were strongly coupled (e.g. naturally ventilated buildings) could not be accurately simulated. Neither could configurations in which an accurate characterization of surface convection was critical (e.g. convection at windows in rooms with varying ventilation rates), because it was not possible to simulate the influence of dynamic flow regimes on the convective heat transfer.

Increased resolution and scope

In addition to these fundamental methodological developments, more rigorous, accurate, and highly resolved methods have been—and continue to be—developed for many of the significant heat transfer paths. Detailed approaches are now available for treating, to name only a few: inter-surface radiation exchange (ray-tracing approaches for view-factor calculation in conjunction with radiosity models); longwave radiation from external surfaces to the sky (with time-varying sky temperatures); time-dependent shading and insolation patterns; transient heat exchange with the ground (time-varying ground temperatures and transient heat storage of the surrounding soil); and three-dimensional heat transfer through the fabric. Additionally, building simulation continues to expand in scope beyond its original thermal focus, to integrate the simulation of related domains, such as illumination, electric power flow, occupant comfort, moisture transfer through the fabric, and gaseous pollutant migration. This continual evolution towards higher resolution and integrated simulation approaches is driven by the need to address the complex nature of real-world design and analysis problems. Rapidly expanding computing power has been a significant factor in the evolution, eliminating the prime motivating factor for many of the simplified methods.

User perspectives

Usage of simulation by the design professions is growing. In large part this is attributable to the convincing evidence that the effective application of simulation can lead to more energy efficient, comfortable, and healthier buildings. Another driving factor is that building regulations are increasingly relying on simulation for demonstrating compliance (e.g. NRC 1997, CEC 1999). Moreover, simulation tools form a key component of many government and utility energy efficiency programmes (e.g. NRCan 1999). As a result of this growing demand, building designers and analysts will continue to call for models that more closely resemble reality, necessitating continual refinement in the treatment of the relevant physical processes.

Notwithstanding the growth in simulation usage, many significant barriers—in addition to the need for more refined models—remain. For example, many users (and potential users) perceive that the learning curve for simulation is too steep; that user interfaces are too cumbersome; and that data gathering and input time is too onerous. There are also liability concerns over design decisions derived from simulation-based analyses, and questions regarding the credibility of results. Initiatives are underway to address these barriers. These range from creating user interfaces that are responsive to the iterative and evolving nature of the building design process (Hand 1998); to enabling the use of simulation at the conceptual design stage (Papamichael 1999); to allowing simulation programs to share data models with other tools such as CAD drawing packages (Bazjanac and Crawley 1997; Clarke et al 1995c). The delivery of training and the production of learning materials (e.g. Hand et al 1998) is also receiving increasing attention. Additionally, many validation exercises have been conducted (e.g. Judkoff and Neymark 1995; Lomas et al 1994; Jensen 1993) and test procedures developed (e.g. ASHRAE 1998) to assess, improve, and demonstrate the integrity of simulation tools. Without doubt, removing barriers to the use of simulation by the design professions will continue to be a focus in the building simulation field for years to come.

Continuing the evolution

Although the accomplishments of the past three and a half decades have been significant, further evolution is required in some key modelling areas to meet the demands of users. One such area—the focus of the current work—is advancing the modelling of indoor air flow within the context of whole-building simulation, while concurrently accurately treating the impact of this flow on heat transfer at internal building surfaces. The path taken is the conflation of high-resolution indoor air flow modelling with dynamic whole-building simulation, with an accurate treatment of the co-dependencies between the modelling domains. This work encompasses two highly related components. The first concerns the integration of CFD techniques to improve the modelling of indoor air flow, while the second relates to modelling the impact of indoor air flow on convective heat transfer at internal building surfaces. Issues pertinent to each of these components are raised in the subsequent sections to place the work in context. Following this, the objectives of the research are outlined.

1.2 The Integration of CFD

CFD has been widely and successfully applied in the prediction of room air motion for a quarter century. Whittle (1986), Nielsen (1989), and Jones and Whittle (1992) provide a thorough review of the applications. Due to high computational requirements analysis is usually restricted to single rooms or spaces within buildings. Prediction accuracy is—as with all modelling techniques—highly sensitive to the boundary conditions supplied (assumed) by the user (e.g. Awbi 1998; Emmerich 1997; Xu and Chen 1998). Essentially, the flow inside the CFD solution domain (i.e. a room) is driven by the boundary conditions. The importance of boundary conditions is underlined by Versteeg and Malalasekera (1995) who describe a CFD solution as nothing more than the extrapolation of boundary conditions into the domain interior.

The application of boundary conditions with whole-building thermal simulation is relatively straightforward. The model boundary is (typically) placed at the exterior of the building fabric. Boundary conditions can be established in the form of exterior conditions—dry-bulb temperature, wind velocity, humidity, etc.—drawn from an appropriate weather-data file. However in modelling room air flow with CFD, the model boundary is located *within* the building. The user must supply boundary conditions in the form of internal wall conditions (surface temperatures or heat flow) and air flows entering or leaving the room. The fundamental dilemma is clear: a room does not exist in isolation. Wall temperatures and air flows through openings are dynamic and dependent on external weather conditions, states prevailing throughout the rest of the building, and the operation of plant equipment, these in turn depending on conditions within the room. CFD researchers have begun to address this issue by integrating dynamic fabric models and inter-surface radiation models into CFD codes (e.g. Holmes et al 1990, Chen et al 1995, Moser et al 1995, Schild 1997). This allows room air flow to be calculated by prescribing boundary conditions external to the building or in adjoining spaces, rather than within the room.

Negrão (1995) extended this concept by integrating a CFD code into the ESP-r building simulation program (ESRU 1999). The two modelling domains operate in tandem, "handshaking" on a time-step basis. The synergy of this integrated modelling approach is evident. The thermal and network air flow simulation domains can supply CFD with realistic and time-varying boundary conditions. CFD has the potential to predict the details of flow and temperature fields within particular zones, thus enabling flow visualisation, studies on pollutant dispersion, thermal comfort assessments, and enhanced modelling of convection heat transfer at internal building surfaces.

Despite this great potential there remain some significant issues impeding the applicability of the conflated modelling approach. Firstly, conventional CFD simulation techniques were developed for highly turbulent flows. This contrasts with the weakly turbulent, relaminarized, or even stagnant flow regimes that typically exist in rooms (particularly in regions remote from air-supply systems). Secondly, with the integrated modelling approach, the thermal simulation and CFD domains interact at solid boundaries, yet it is precisely these locations—the so-called *near-wall* regions—that CFD has the greatest difficulty resolving.

1.3 The Treatment of Internal Surface Convection

The common approach for modelling internal surface convection is to employ the so-called *well-stirred* assumption (refer to Figure 1.1). This treats the room air as uniform and characterizes surface convection by a convection coefficient (h_c) and by the temperature difference between the room air (T_{air}) and the solid surface ($T_{surface}$, also assumed to be of uniform temperature):

$$q''_{conv} = h_c \cdot (T_{air} - T_{surface}) \tag{1.1}$$

where q''_{conv} is the convective heat flux from the air to the surface. In this manner the surface convection term enters the energy balances of both the room air volume and the internal surface, influencing predictions of T_{air} and $T_{surface}$.

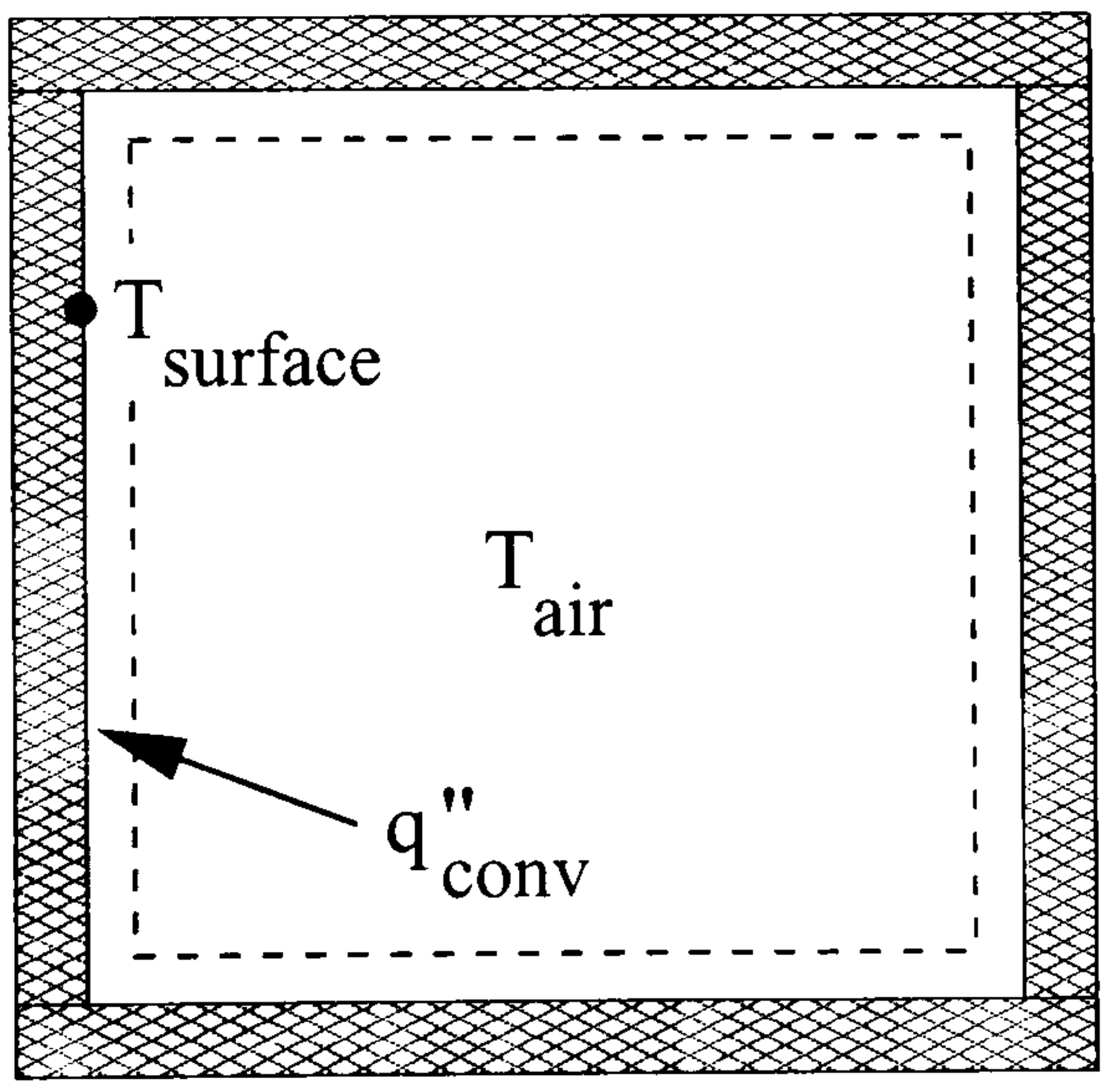

Figure 1.1: Well-stirred convection model

The convection heat transfer varies from surface to surface in the building, as well as with time, in response to local air flow patterns. The local flow, in turn, depends upon: flow regimes existing throughout the building; operational states of plant equipment; external weather conditions; surface orientations; and local air and surface temperatures. The type of flow in the vicinity of the surface significantly influences heat transfer. Impinging flows, wall jets, free jets, and buoyancy-driven flows are all commonly encountered in buildings and all result in substantially different convection regimes.

Moreover, the nature of the flow (fully turbulent, laminar, transitional, or weakly turbulent) has a profound influence.

Accurately capturing the impact of these factors requires the high-resolution simulation of air flow and tight binding between the thermal and air flow calculation domains. The calculation of convection coefficients for use in equation 1.1 must respond to local flow conditions in a dynamic fashion. In some cases the restrictions imposed by the well-stirred approach will preclude an accurate treatment of the physics. In these cases alternate approaches must be found.

Since the thermal and air flow modelling domains interact at solid boundaries—as discussed in the previous section—the treatment of surface convection is critical to the success of the conflated approach. In other words, co-dependency of the two modelling domains is manifested in this treatment. Any errors in the modelling of surface convection will be propagated (perhaps amplified) from one domain to the other.

1.4 Research Objectives and Thesis Outline

The objectives of the research are the following:

- advancing the modelling of indoor air flow within the context of whole-building simulation;
- accurately treating the impact of indoor air flow on heat transfer at internal building surfaces.

These objectives can only be realized through a convergence of thermal and air flow modelling techniques. Accordingly, the research will be based on an integrated modelling approach whereby CFD techniques are incorporated into whole-building simulation (thermal and network air flow). The thermal and network air flow domains will supply realistic boundary conditions to CFD, enabling high-resolution air flow predictions for specific spaces within the building; while CFD air flow predictions will enhance the thermal domain's modelling of convection heat transfer at internal fabric surfaces. This integrated modelling approach has been proposed by many researchers (Chen and Xu 1998; Nielsen and Tryggvason 1998; Fischer et al 1998) and its feasibility shown by Negrão (1995).

The platform for implementing and demonstrating this research will be the ESP-r system with the integrated CFD capabilities developed by Negrão. The issues discussed in Section 1.2 will be addressed by populating the CFD model with a suite of turbulence and near-wall modelling approaches. As each approach will have limited applicability (e.g. buoyancy-driven flow over vertical surfaces) an *adaptive conflation controller* will be developed to enable the simulator to (dynamically) select an appropriate approach based on an appraisal of the flow regime. In this manner the modelling will adapt with the flow regime.

Various methods will be incorporated for estimating surface convection from the CFD-predicted flow and temperature fields. Additionally, a suite of empirical methods will be implemented for calculating convection coefficients for use with the well-stirred approach and for supplying boundary conditions to the CFD domain. An *adaptive convection algorithm* will, much like the adaptive conflation controller, control the calculation of surface convection in a dynamic fashion. It will select from the alternate approaches, responding to changes in the flow regime. The adaptive convection algorithm and the adaptive conflation controller will collectively ensure an accurate treatment of the co-dependencies between the thermal and CFD modelling domains, thus addressing the issues raised in Section 1.3.

A review of ESP-r's simulation methodology, including a treatment of the current integrated CFD capabilities, is given in Chapter 2. Chapter 3 describes CFD's modelling methodology and explores issues regarding its applicability for room air flow and heat transfer analysis. Emphasis is placed on methods for modelling the turbulent nature of room air flows.

The modelling of internal surface convection is the topic of Chapter 4. The significance of accurately modelling this heat transfer path is demonstrated and the suite of convection coefficient correlations selected to support the adaptive convection algorithm are described. Chapter 5 describes the new adaptive convection algorithm and new adaptive conflation controller. This focuses on techniques for improving the modelling of indoor air flow and the interactions between the air flow and thermal modelling domains. Application and validation of the new modelling capabilities are demonstrated in Chapter 6. Finally, in Chapter 7 conclusions are drawn and recommendations made for future work.

ESP-r's Simulation Methodology

2.1 Introduction

The ESP-r building simulation system (ESRU 1999) has been in a constant state of evolution and renewal since its first prototype was developed over two decades ago (Clarke 1977). More resolved and advanced modelling approaches have been incorporated and the scope has broadened to embrace the simulation of non-energy domains (see ESRU, 1999, and Hensen, 1991, for an historical perspective). ESP-r is applied in a host of building design, analysis, teaching, and research capacities (some examples are provided by Hand 1998), and is actively developed and supported.

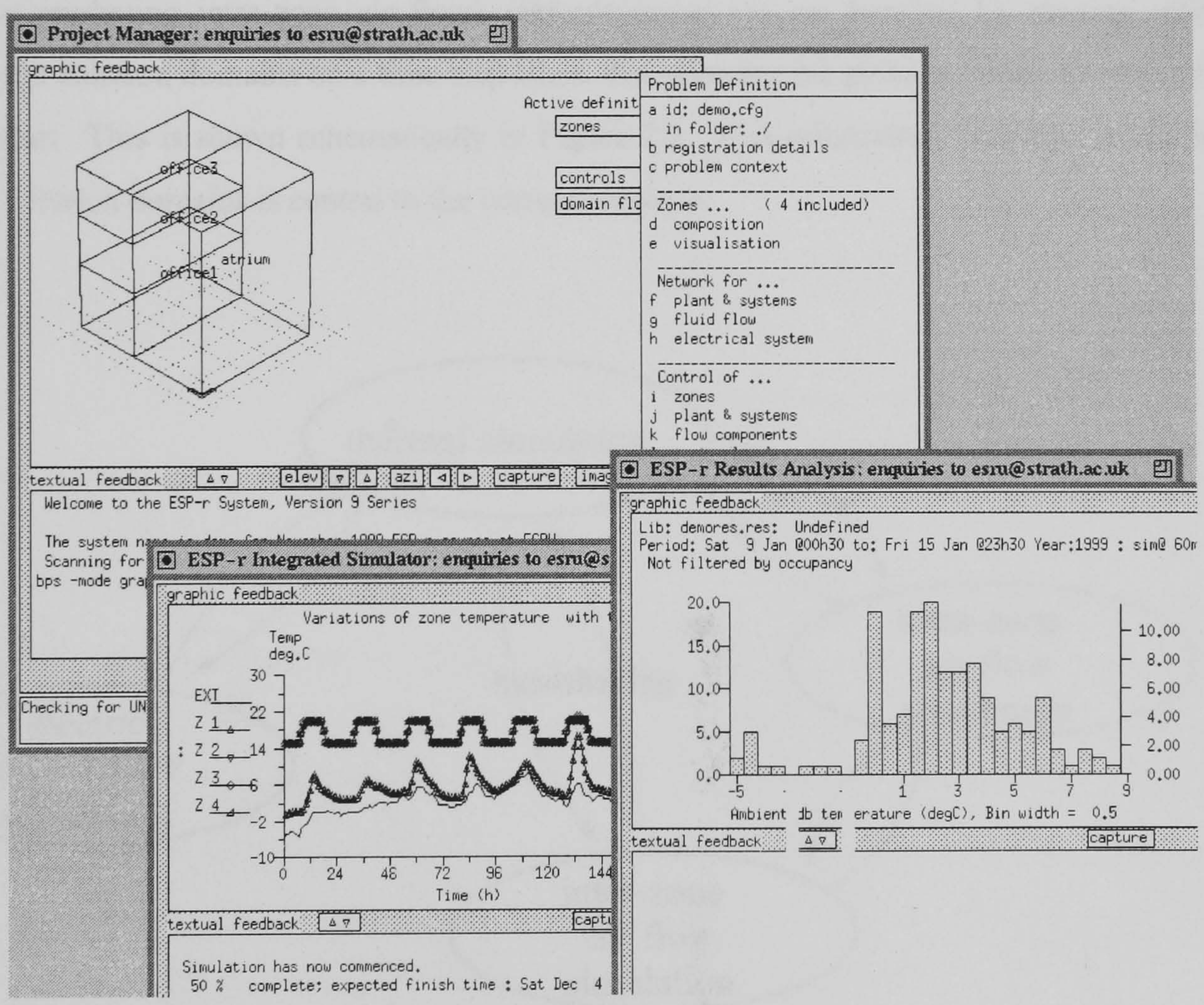

```
Welcome to the ESP-r System, Version 9 Series

The system n
Scanning for
bps -mode gra
Checking for UN
```

```
Simulation has now commenced.
 50 %   complete; expected finish time : Sat Dec  4
```

```
Lib: demores.res:  Undefined
Period: Sat  9 Jan @00h30 to: Fri 15 Jan @23h30 Year:1999 : sim@ 60m
 Not filtered by occupancy
```

Figure 2.1: Montage of typical ESP-r session

While most building analysis tools exclusively simulate thermal processes, ESP-r, in contrast, strives to model all relevant physical processes in an integrated and rigorous fashion (Clarke 1999). To this end, it considers heat transfer, inter-zone air flow, intra-zone air flow, water flow (in hydronic plant systems), electric power flow, moisture transfer, and illumination: and it couples the modelling of these domains. The underlying theory and its implementation is thoroughly documented (Clarke 1985; Hensen 1991; Aasem 1993; Negrão 1995; Nakhi 1995; MacQueen 1997; Hand 1998; Kelly 1998).

ESP-r's *Project Manager* controls all aspects of model creation, simulation, and results analysis, and provides a graphical and interactive interface between the user and the underlying data model. It controls: the maintenance of databases; the execution of pre-simulation calculations (e.g. to predict solar insolation and shading, to determine radiation view factors); the performance of the time-step simulation of heat, air, moisture, and electric power flow; and the visualization of results. Figure 2.1 illustrates a typical ESP-r session, the *Project Manager* controlling the simulator and the results analyzer.

ESP-r employs a partitioned solution approach, applying customized solvers to each model domain (thermal, electric power flow, inter-zone air flow, intra-zone air flow, etc.). This enables an optimized treatment of each of the disparate equation sets. In this manner, one solver processes the thermal domain, another treats network air flow (to resolve inter-zone flow), while yet another handles CFD (for predicting intra-zone air flow). Interdependencies are handled by passing information between the solution domains on a time-step basis, this allowing the global solution to evolve in a coupled manner. This is shown schematically in Figure 2.2. This information passing (or handshaking) between solution domains is central to the current research.

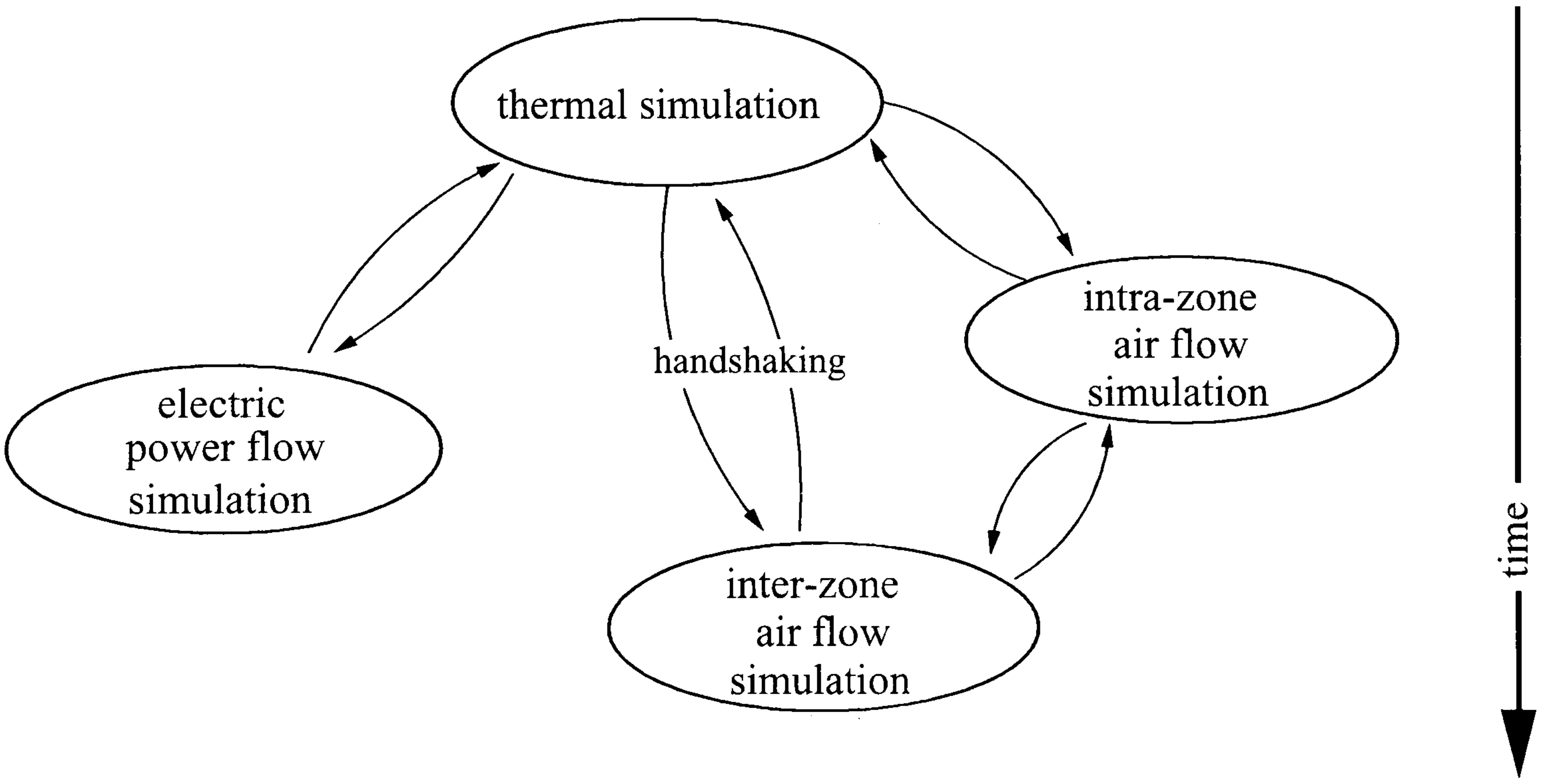

Figure 2.2: Handshaking between partitioned solvers

This chapter sets out to describe the aspects of ESP-r which are germane to the current research. Consequently, emphasis is placed on the modelling of internal surface convection (key to integrating

CFD into whole-building simulation, as explained in Chapter 1) and the handshaking between the CFD and thermal domains. Necessary elaboration is provided to place these elements in context. However, no attempt is made to provide a comprehensive review of ESP-r's modelling approaches. Rather, the interested reader is referred to Clarke (1985), who provides a detailed treatise of the topic.

Section 2.2 describes ESP-r's thermal simulation methodology. As an understanding of the methods used to mathematically describe and solve the thermal domain is necessary to place the treatment of internal convection in context, significant detail is provided in this section. Section 2.3 briefly describes ESP-r's multi-zone network air flow model, including its integration with the thermal domain. Treatment is succinct, as the coupling between inter- and intra-zone air flow is not a focus of the current research. Section 2.4 describes how CFD handshakes with the thermal and network air flow domains. Finally, closing remarks are provided in Section 2.5.

2.2 Thermal Model

This section reviews ESP-r's thermal simulation methodology. The control-volume heat-balance approach at the heart of the method is first described. The formation of a heat balance is then demonstrated by focusing on the simplest case, a homogeneous material layer within the building's fabric. Following this, the modelling of internal surface convection is elucidated by forming heat balances for internal surfaces and the room air. Finally, the procedure used to solve the set of heat balances is described.

2.2.1 Finite-difference control-volume heat-balance approach

ESP-r is based on the numerical discretization and simultaneous solution class of heat-balance methods (see page 3). Specifically, ESP-r simulates the thermal state of the building by applying a finite-difference formulation based on a control-volume heat-balance to represent all relevant energy flows. This encompasses three principle steps:

1) The building is discretized by representing air volumes (such as rooms), opaque and transparent fabric components (walls, windows, roofs, floors), solid-fluid interfaces (such as the internal and external surfaces of walls and windows), and plant components (such as boilers and heat exchangers) with finite-difference *nodes*. Numerous nodes are placed through each fabric component to represent these multi-layered constructions. This is illustrated in Figure 2.3, although only a few nodes are shown for the sake of clarity.
2) A heat balance considering the relevant energy flow paths (some are shown in Figure 2.3) is written for each node. These balances are cast in algebraic and discrete form, and thus approximate the partial differential equations which govern the heat transfer. As each heat balance expresses the thermal interaction between a node and its neighbours, the resulting equation set links all inter-node heat flows over time and space.

3) A simultaneous solution is performed on the equation set to predict—for a given point in time—the thermal state of each node and the heat flows between nodes. Steps 2 and 3 are repeated to reform and resolve the equation set for each subsequent time-step of the simulation.

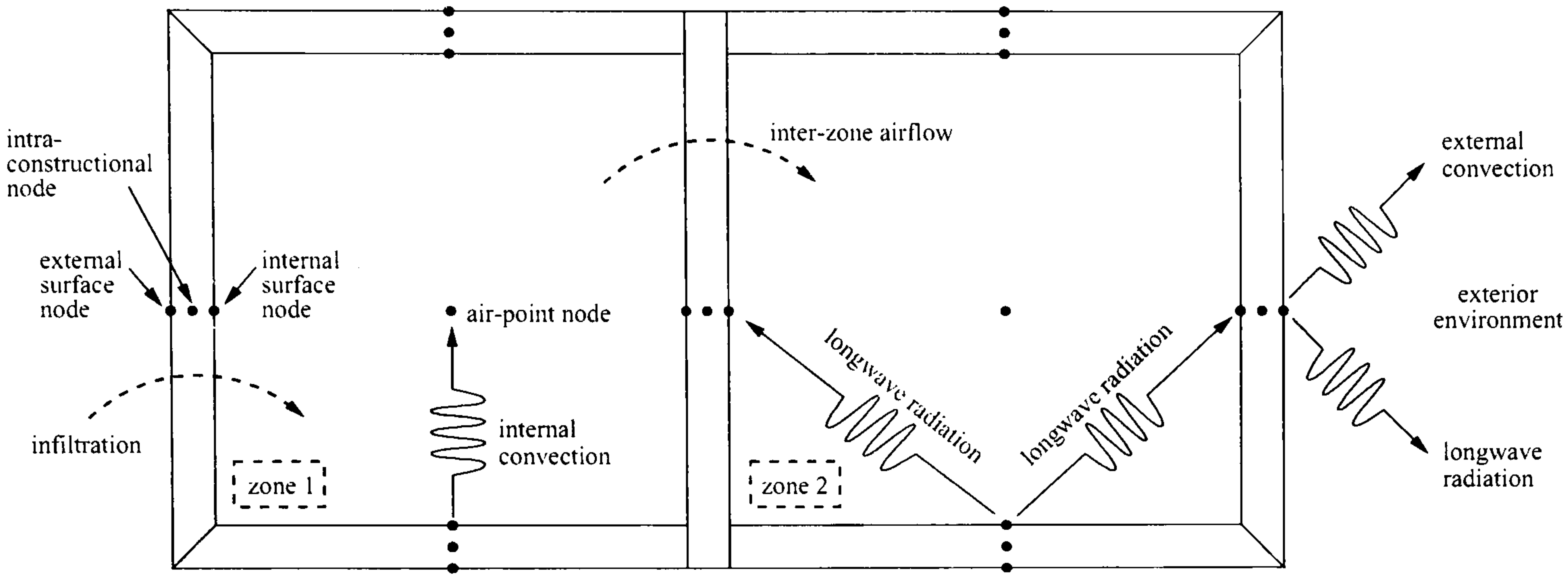

Figure 2.3: Finite-difference discretization and inter-nodal heat flows

The following subsection demonstrates how the heat balances are formed (step 2 above) by focusing on the simplest case, a node within a homogeneous material layer of the building's fabric.

2.2.2 Heat balance for intra-constructional nodes (opaque constructions)

Heat exchange within opaque fabric components is highly complex, usually involving numerous modes of heat transfer: solid conduction, gaseous conduction, convection within porous materials, and radiation (between fibrous insulation strands and between bounding surfaces separated by porous insulation). The problem is further complicated by moisture transfer, contact resistances between materials, and multi-dimensional heat flow around structural members and corners.

Although detailed treatment of this complex heat transfer system is possible on a number of levels (Nakhi 1995)[3], the default (and common) approach is to treat heat transfer through the opaque fabric as a one-dimensional conduction-only problem with constant thermophysical properties. This level of abstraction is the standard within the building simulation field. It is appropriate given that building materials are characterized by the effective thermal conductivity, this accounting for non-conduction modes of heat transfer.

By default, each homogeneous layer is represented by three nodes (greater grid density is an option): one at each layer boundary and one within the layer. Figure 2.4 shows this nodal distribution

---

[3] Thermophysical properties can be made to vary dynamically with temperature to (approximately) account for the effects of radiation and other heat transfer modes. Moisture transfer through the fabric can be explicitly simulated and coupled to the thermal domain. It is also possible to finely discretize fabric components to calculate two- and three-dimensional conduction effects.

for a typical wall section.

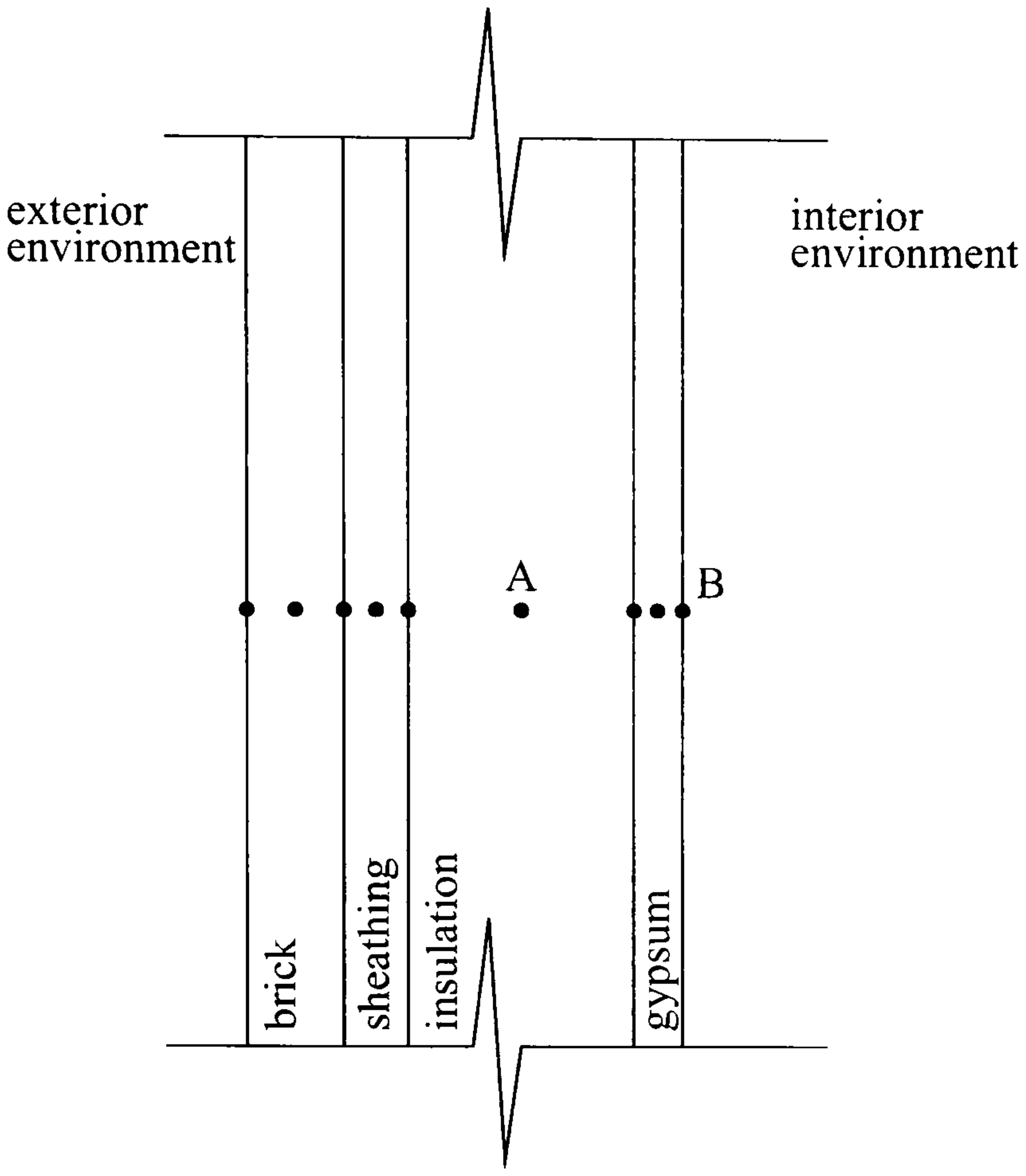

Figure 2.4: Nodal discretization for a typical opaque fabric component

Figure 2.5 focuses on an intra-constructional node located within a homogeneous material layer (node *A* from Figure 2.4). *I* represents the node under consideration while *I+1* and *I-1* represent the immediate neighbours in the x-direction (the direction of heat flow). The control volume (greyed in the figure) enclosing node *I* is Δx wide and extends Δz in the vertical direction and Δy in the direction perpendicular to the page. The user controls the extent of Δy and Δz depending upon the degree of modelling resolution desired.

The heat balance for node *I*'s control volume (CV) can be described with three terms,

$$\left\{\begin{matrix} storage\ of \\ heat\ in\ CV \end{matrix}\right\} = \left\{\begin{matrix} net\ conduction \\ into\ CV \end{matrix}\right\} + \left\{\begin{matrix} source\ of\ heat \\ within\ CV \end{matrix}\right\} \tag{2.1}$$

This relation simply states that the material will store or release energy in proportion to the amount of heat transferred in by conduction and in proportion to the amount of heat generation. The rate of change of the control volume's temperature characterizes the storage term. The source term represents interaction with a plant component (perhaps an embedded heating element, as used with in-floor heating). Given this, the balance of equation 2.1 is expressed in mathematical terms by,

$$\rho c_p \frac{\partial T}{\partial t} = -\frac{\partial q_x''}{\partial x} + q_{plant}''' \tag{2.2}$$

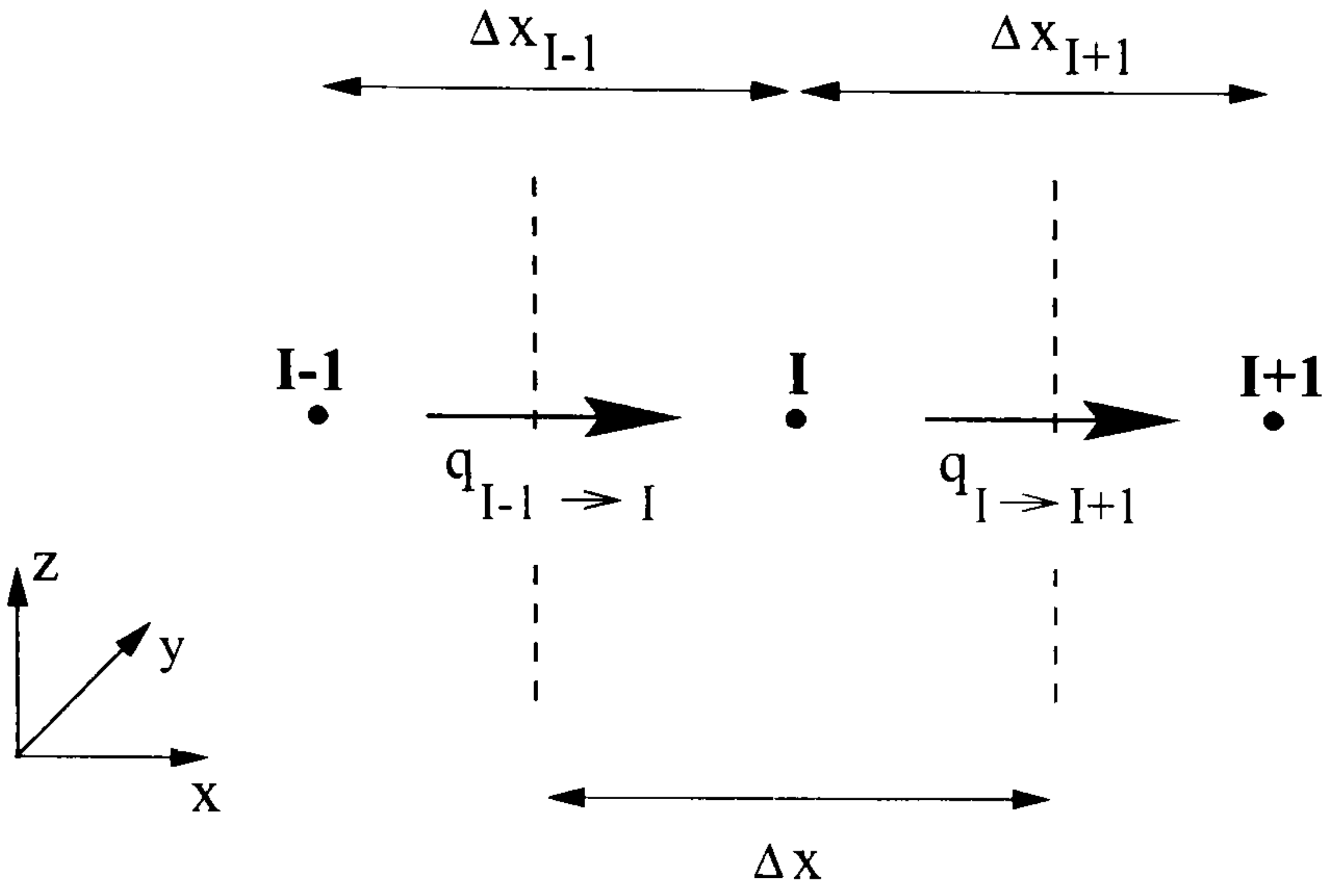

Figure 2.5: Heat balance on node within homogeneous layer of multi-layer construction

where c_p is the specific heat $\{J/kgK\}$ and ρ the density $\{kg/m^3\}$ of the material; T is temperature $\{^oC \text{ or } K\}$; t is time $\{s\}$; q_x'' is the conductive heat flux in the x-direction $\{W/m^2\}$; and q_{plant}''' is the heat injection from the embedded plant component $\{W/m^3\}$.

Equation 2.2 can be approximated by integrating over the control volume,

$$\int_{\Delta V} \rho c_p \frac{\partial T}{\partial t} dV = -\int_{\Delta V} \frac{\partial q_x''}{\partial x} dV + \int_{\Delta V} q_{plant}''' dV \tag{2.3}$$

and by representing the first derivative of temperature in time term with a backwards difference scheme over the finite time-step Δt,

$$(\rho c_p \Delta x \Delta y \Delta z)_I \frac{T_I^{t+\Delta t} - T_I^t}{\Delta t} = q_{I-1 \to I} - q_{I \to I+1} + q_{plant} \tag{2.4}$$

T_I^t is the temperature of node I at the beginning of the time-step. This is a known quantity, a result of the simulation of the previous time-step. $T_I^{t+\Delta t}$ is the temperature of node I at the end of the time-step, a quantity yet to be solved. Time t is known as the *present* time-row and time $t + \Delta t$ is known as the *future* time-row.

$q_{I-1 \to I}$ and $q_{I \to I+1}$ are the conductive heat flows across the faces of the control volume $\{W\}$, as shown in Figure 2.5. These terms can can be approximated in discrete form using the nodal temperatures. The explicit form of the approximations results when present time-row temperatures are used,

$$q_{I-1 \to I} \approx \frac{k_{I-1} \Delta y \Delta z}{\Delta x_{I-1}} (T_{I-1}^t - T_I^t) \tag{2.5}$$

$$q_{I \to I+1} \approx \frac{k_{I+1} \Delta y \Delta z}{\Delta x_{I+1}} (T_I^t - T_{I+1}^t) \tag{2.6}$$

where k_{I-1} is the thermal conductivity $\{W/mK\}$ of the material between nodes I and *I-1*, and k_{I+1} is the thermal conductivity of the material between nodes I and *I+1*.

Substituting equations 2.5 and 2.6 into equation 2.4 and expressing the plant injection at the present time-row gives rise to the fully explicit form of the discretized approximation of the heat balance,

$$\frac{(\rho c_p \Delta x \Delta y \Delta z)_I}{\Delta t}(T_I^{t+\Delta t} - T_I^t) = \frac{k_{I-1}\Delta y \Delta z}{\Delta x_{I-1}}(T_{I-1}^t - T_I^t) - \frac{k_{I+1}\Delta y \Delta z}{\Delta x_{I+1}}(T_I^t - T_{I+1}^t) + q_{plant}^t \tag{2.7}$$

If the conductive heat flows and the plant term are approximated using future—rather than present—values, the fully implicit form of the heat balance results,

$$\frac{(\rho c_p \Delta x \Delta y \Delta z)_I}{\Delta t}(T_I^{t+\Delta t} - T_I^t) = \frac{k_{I-1}\Delta y \Delta z}{\Delta x_{I-1}}(T_{I-1}^{t+\Delta t} - T_I^{t+\Delta t}) - \frac{k_{I+1}\Delta y \Delta z}{\Delta x_{I+1}}(T_I^{t+\Delta t} - T_{I+1}^{t+\Delta t}) + q_{plant}^{t+\Delta t} \tag{2.8}$$

ESP-r approximates the heat balance with an equally weighted average of the explicit and implicit relations. This is known as the Crank-Nicolson difference formulation, and is preferred over the fully explicit and fully implicit schemes for its numerical stability (the user can optionally select any weighting of the two, including fully explicit and fully implicit). Thus, adding equations 2.7 and 2.8, dividing through by volume ($\Delta x \Delta y \Delta z$), and grouping the future time-row terms on the left and the present time-row terms on the right gives,

$$\begin{aligned} &\left[\frac{2 \cdot (\rho c_p)_I}{\Delta t} + \frac{k_{I-1}}{\Delta x \Delta x_{I-1}} + \frac{k_{I+1}}{\Delta x \Delta x_{I+1}}\right] T_I^{t+\Delta t} - \left[\frac{k_{I-1}}{\Delta x \Delta x_{I-1}}\right] T_{I-1}^{t+\Delta t} - \left[\frac{k_{I+1}}{\Delta x \Delta x_{I+1}}\right] T_{I+1}^{t+\Delta t} - \frac{q_{plant}^{t+\Delta t}}{\Delta x \Delta y \Delta z} \\ &= \left[\frac{2 \cdot (\rho c_p)_I}{\Delta t} - \frac{k_{I-1}}{\Delta x \Delta x_{I-1}} - \frac{k_{I+1}}{\Delta x \Delta x_{I+1}}\right] T_I^t + \left[\frac{k_{I-1}}{\Delta x \Delta x_{I-1}}\right] T_{I-1}^t + \left[\frac{k_{I+1}}{\Delta x \Delta x_{I+1}}\right] T_{I+1}^t + \frac{q_{plant}^t}{\Delta x \Delta y \Delta z} \end{aligned} \tag{2.9}$$

This is the basic equation ESP-r employs to characterize the heat balance for nodes located within homogeneous material layers of opaque multi-layered constructions. It considers heat storage, conduction to adjacent nodes, and plant interaction. All unknown solution variables (nodal temperatures and plant injections) are collected on the left, and known quantities are on the right.

2.2.3 Heat balance for internal surface nodes

Now that the control-volume heat-balance approach has been demonstrated for the simplest case, the focus is turned to nodes located at internal surfaces. It is here that internal surface convection operates.

Figure 2.6 focuses on a node (*I*) located on the internal surface of a construction (node *B* from Figure 2.4). As before, the left face of the control volume (shown in grey) is located between nodes *I* and *I-1*. The right face, however, is located at the interface of the solid construction and the room air. The neighbouring node to the right (*I+1*) represents the room's air-point. The heat balance for node *I*'s control volume has a similar structure to that for the intra-constructional node, but includes two additional modes of heat transfer,

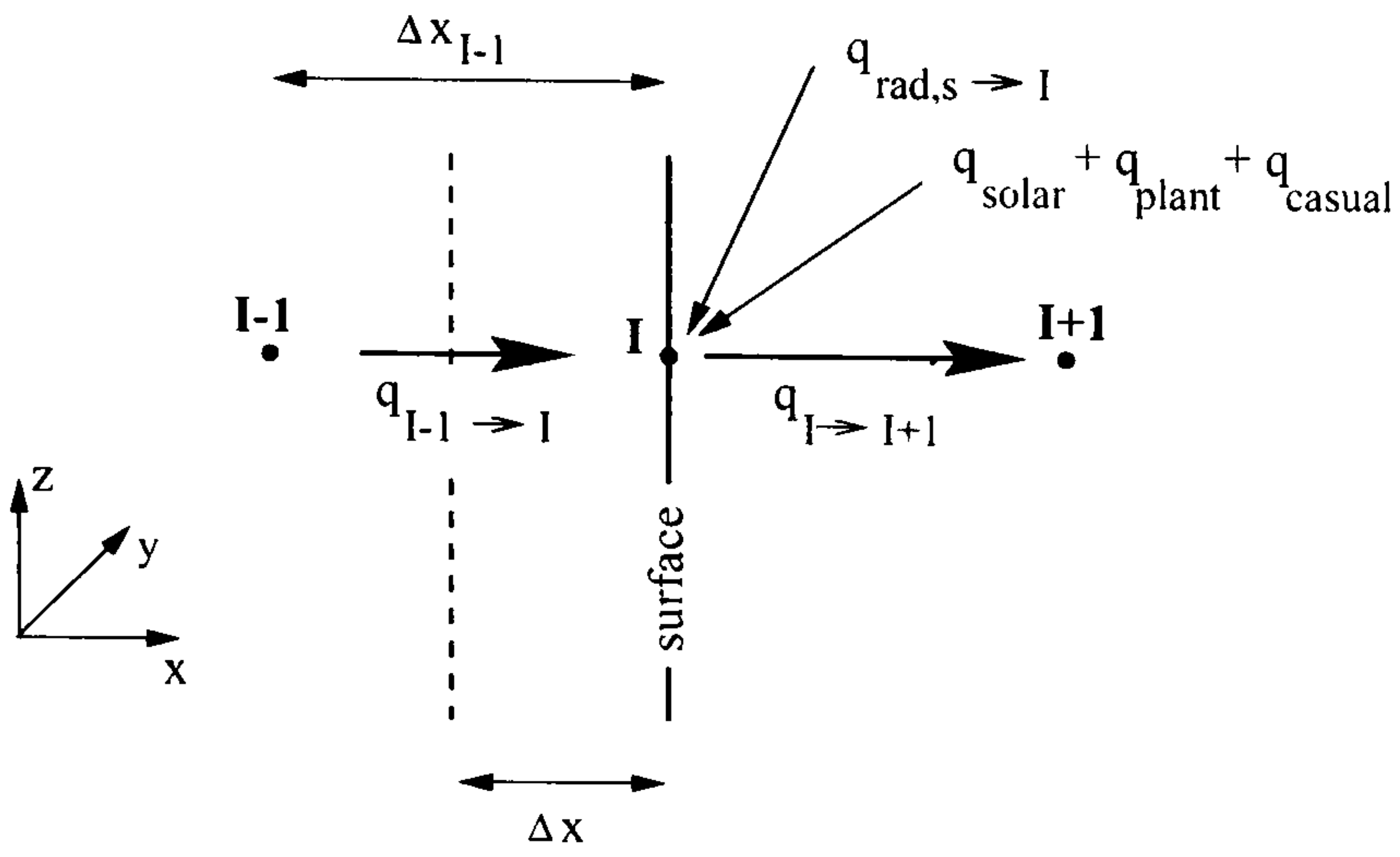

Figure 2.6: Heat balance on node at internal-surface

$$\left\{\begin{matrix} storage\ of \\ heat\ in\ CV \end{matrix}\right\} = \left\{\begin{matrix} net\ conduction \\ into\ CV \end{matrix}\right\} + \left\{\begin{matrix} source\ of\ heat \\ within\ CV \end{matrix}\right\} + \left\{\begin{matrix} net\ longwave \\ radiation \\ into\ CV \end{matrix}\right\} + \left\{\begin{matrix} net\ convection \\ into\ CV \end{matrix}\right\} \quad (2.10)$$

Since conduction into the control volume occurs only at the boundary with the next-to-surface node (*I-1*), the discretized explicit form of the conduction term is,

$$\left\{\begin{matrix} net\ conduction \\ into\ CV \end{matrix}\right\} = \frac{k_{I-1}\Delta y \Delta z}{\Delta x_{I-1}}(T_{I-1}^t - T_I^t) \quad (2.11)$$

In addition to plant injection, the source term includes solar gains and longwave radiation from sources of heat within the room. The explicit form is given by,

$$\left\{\begin{matrix} source\ of\ heat \\ within\ CV \end{matrix}\right\} = q_{solar,I}^t + q_{cas-rad,I}^t + q_{plant,I}^t \quad (2.12)$$

$q_{solar,I}^t$ is the solar radiation absorbed at node I at the present time. $q_{cas-rad,I}^t$ represents the radiant energy absorbed from casual sources (such as occupants, lights, office equipment). $q_{plant,I}^t$ represents a radiant plant input to node I, perhaps from a radiant heater located within the room.

The longwave radiation term represents the net heat exchange with surrounding surfaces that are in longwave contact (i.e. other internal surfaces of the room). The discretized explicit form is given by,

$$\left\{\begin{matrix} net\ longwave \\ radiation \\ into\ CV \end{matrix}\right\} = \sum_{s=1}^{N} h_{r,s \rightarrow I}^t \Delta y \Delta z (T_s^t - T_I^t) \quad (2.13)$$

N is the number of surrounding surfaces in longwave contact. $h_{r,s \rightarrow I}^t$ is a linearized radiation heat transfer coefficient $\{W/m^2K\}$. These coefficients are recalculated each time-step on a surface-by-surface basis. A grey-body exchange approach that considers diffuse surface reflections and employs geometric view factors is used to calculate the radiation coefficients. These geometric view factors are either determined from geometric relations or with ray-tracing procedures.

The convection term represents heat exchange between the room air and the solid surface, and is modelled using the well-stirred assumption (see Section 1.3, page 7). With this, the room air is treated as uniform. Consequently, the temperature at node *I+1* represents conditions throughout the room. The convection term is given in discretized explicit form by,

$$\begin{Bmatrix} net\ convection \\ into\ CV \end{Bmatrix} = h_{c,I}^{t}\Delta y\Delta z(T_{I+1}^{t} - T_{I}^{t}) \tag{2.14}$$

where $h_{c,I}^{t}$ is the convection heat transfer coefficient $\{W/m^2K\}$ between the surface at node *I* and the room air-point, evaluated at the present time-row.

The convection coefficients are recalculated each time-step on a surface-by-surface basis. This contrasts with the treatment of some other simulation programs which employ time-invariant convection coefficients (either user-prescribed or "hard-wired" in the program's source code). By default, the Alamdari and Hammond (1983) correlations for buoyancy-driven flow are used. These equations (see Table 2.1) express the convection coefficient as a function of the surface's characteristic dimension and the surface-air temperature difference. Separate correlations are used for: vertical surfaces; stably-stratified horizontal surfaces (e.g. warm air above a cool floor); and buoyant flow from horizontal surfaces (e.g. cool air above a warm floor). Optionally, another set of correlations for buoyancy-driven flow can be employed. These equations (also given in Table 2.1) are extracted from an experimental study conducted in a room-sized test cell (Khalifa and Marshall 1990).

It is interesting to note that these two methods produce substantially different convection coefficients. Take, for example, a 2.4 m high wall with a 3°C surface-air temperature difference. The Alamdari and Hammond correlation gives an h_c of 1.9 W/m^2K, whereas the Khalifa and Marshall equation leads to a value of 3.0 W/m^2K. With in-floor heating it is common for the floor surface to be up to 6°C warmer than the room air. In this case, the two calculation methods give h_c values of 3.0 and 3.5 W/m^2K (again the Khalifa and Marshall equation gives the larger result). Therefore, when the user selects the optional h_c-calculation method, ESP-r predicts substantially more (58% and 17% in these cases, respectively) heat transfer by convection between the wall and the room air. The actual impact of h_c differences on the calculation of nodal temperatures and inter-nodal heat flows depends, of course, on the relative magnitude of the convection term in equation 2.10. The significance of this is explored in detail in Chapter 4.

The user also has the option of employing time-invariant values, rather than recalculating convection coefficients each time-step. These can either be input by the user, or selected from the three options shown in Table 2.1. The *low* and *high* time-invariant values in the table are extracted from a report which surveyed approaches for establishing convection coefficients (Halcrow 1987); the *low* and *high* values span the range of these data. The CIBSE values are recommended for use in steady-state calculations (CIBSE 1988).

Therefore, although ESP-r recalculates convection coefficients as the simulation evolves, it cannot adapt the calculation approach in response to changes in air flow regimes: the same h_c-calculation method is used throughout the simulation. As well, the same approach must be used throughout the building. Although ESP-r offers an optional method for calculating h_c, some common flow regimes cannot be characterized (e.g. forced flow induced by an air-based mechanical system). Measures to address these limitations are put forward in Chapters 4 and 5.

calculation method	**vertical surfaces**	**horizontal surfaces**	
		buoyant	**stably stratified**
Alamdari and Hammond	$\left\{\left[1.5\cdot\left(\frac{\Delta T}{H}\right)^{1/4}\right]^6+\left[1.23\Delta T^{1/3}\right]^6\right\}^{1/6}$	$\left\{\left[1.4\cdot\left(\frac{\Delta T}{D_h}\right)^{1/4}\right]^6+\left[1.63\Delta T^{1/3}\right]^6\right\}^{1/6}$	$0.6\cdot\left(\frac{\Delta T}{D_h^2}\right)^{1/5}$
Khalifa & Marshall	$2.30\cdot\Delta T^{0.24}$	$2.27\cdot\Delta T^{0.24}$	$3.10\cdot\Delta T^{0.17}$
time-invariant *low*	1.0	1.0	0.1
time-invariant *high*	6.0	6.0	1.2
CIBSE	3.0	4.3	1.5

- ΔT is the absolute value of the surface-air temperature difference $\{^oC\}$.
- H is the height of vertical surfaces $\{m\}$.
- D_h is the hydraulic diameter of horizontal surfaces: $D_h = \frac{4A}{P}$, where A is the area $\{m^2\}$ and P the perimeter $\{m\}$.
- All convection coefficients in $\{W/m^2K\}$.

Table 2.1: h_c **calculation methods at commencement of research**

Substituting equations 2.11 through 2.14 into 2.10 and representing the storage term with a backwards difference scheme, leads to the explicit form of the heat balance. The implicit form of the heat balance results when convection and radiation coefficients, and the conduction, convection, radiation, and source terms are evaluated with future values. Concatenating these, dividing through by volume, and grouping future time-row terms on the left and present time-row terms on the right results in the generalized form of the internal-surface heat balance,

$$
\begin{aligned}
&\left[\frac{2\cdot(\rho c_p)_I}{\Delta t}+\frac{k_{I-1}}{\Delta x\Delta x_{I-1}}+\frac{h_{c,I}^{t+\Delta t}}{\Delta x}+\frac{\sum\limits_{s=1}^{N}h_{r,s\rightarrow I}^{t+\Delta t}}{\Delta x}\right]T_I^{t+\Delta t}-\left[\frac{k_{I-1}}{\Delta x\Delta x_{I-1}}\right]T_{I-1}^{t+\Delta t} \qquad (2.15)\\
&-\left[\frac{h_{c,I}^{t+\Delta t}}{\Delta x}\right]T_{I+1}^{t+\Delta t}-\frac{\sum\limits_{s=1}^{N}h_{r,s\rightarrow I}^{t+\Delta t}T_s^{t+\Delta t}}{\Delta x}-\frac{q_{solar,I}^{t+\Delta t}}{\Delta x\Delta y\Delta z}-\frac{q_{cas-rad,I}^{t+\Delta t}}{\Delta x\Delta y\Delta z}-\frac{q_{plant,I}^{t+\Delta t}}{\Delta x\Delta y\Delta z}\\
&=\left[\frac{2\cdot(\rho c_p)_I}{\Delta t}-\frac{k_{I-1}}{\Delta x\Delta x_{I-1}}-\frac{h_{c,I}^{t}}{\Delta x}-\frac{\sum\limits_{s=1}^{N}h_{r,s\rightarrow I}^{t}}{\Delta x}\right]T_I^{t}+\left[\frac{k_{I-1}}{\Delta x\Delta x_{I-1}}\right]T_{I-1}^{t}\\
&+\left[\frac{h_{c,I}^{t}}{\Delta x}\right]T_{I+1}^{t}+\frac{\sum\limits_{s=1}^{N}h_{r,s\rightarrow I}^{t}T_s^{t}}{\Delta x}+\frac{q_{solar,I}^{t}}{\Delta x\Delta y\Delta z}+\frac{q_{cas-rad,I}^{t}}{\Delta x\Delta y\Delta z}+\frac{q_{plant,I}^{t}}{\Delta x\Delta y\Delta z}
\end{aligned}
$$

This is the basic equation ESP-r employs to characterize the heat balance for internal-surface nodes. This simulation equation considers heat storage, conduction within the innermost layer of the fabric, convection with the room air, longwave radiation exchange with surrounding surfaces, and the absorption of solar radiation, radiant casual gains, and radiant plant injections. Although the coefficients are more complex, this equation has exactly the same form as that for intra-constructional nodes (equation 2.9).

2.2.4 Heat balance for air-point nodes

The mechanism for heat transfer between the zone air and internal surfaces is convection (as shown in the previous section). Consequently, convection coefficients also appear in the heat balance for the zone air.

Figure 2.7 focuses on a node representing the air-point of a zone. The solid constructions enclosing the zone form the boundaries of the control volume (greyed in the figure). In this case, node *I* represents the air-point and the nodes labelled *S* represent the surface nodes of the bounding constructions. Node *J* represents the air-point of another zone while Node *o* represents the outdoor air. Consistent with the well-stirred assumption (see Section 1.3, page 7) the room air is treated as uniform. Consequently, node *I* represents conditions throughout the control volume.

The heat balance for the air-point node must consider: bulk air flow from adjacent zones and the outdoors; surface convection at the bounding fabric components; and convective sources of heat,

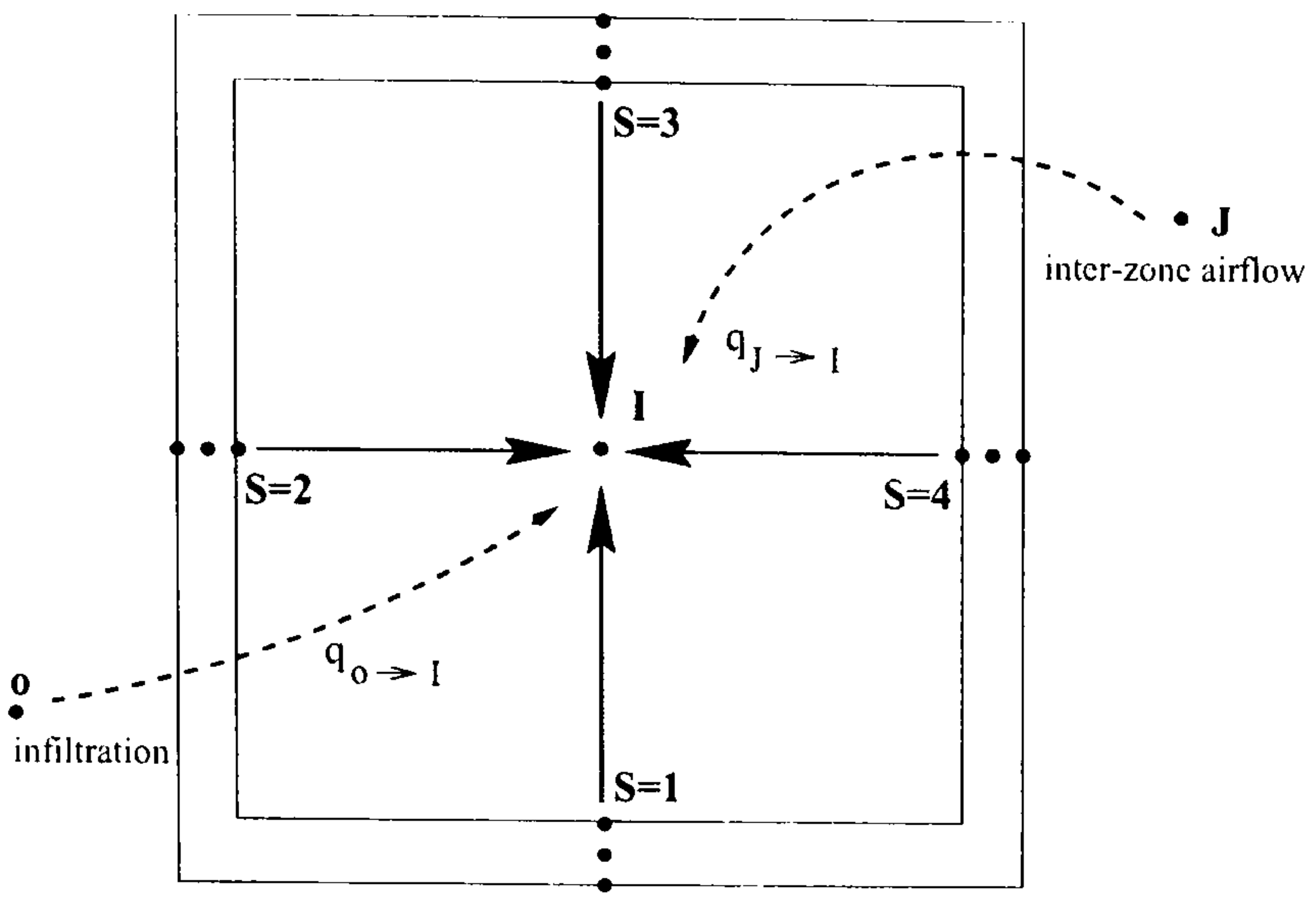

Figure 2.7: Heat balance on air-point node

$$\left\{\begin{matrix} \textit{storage of} \\ \textit{heat in CV} \end{matrix}\right\} = \left\{\begin{matrix} \textit{net convection} \\ \textit{into CV} \end{matrix}\right\} + \left\{\begin{matrix} \textit{advection} \\ \textit{into CV by} \\ \textit{inter-zone} \\ \textit{air flow} \end{matrix}\right\} + \left\{\begin{matrix} \textit{advection} \\ \textit{into CV by} \\ \textit{infiltration} \end{matrix}\right\} + \left\{\begin{matrix} \textit{source of heat} \\ \textit{within CV} \end{matrix}\right\} \tag{2.16}$$

The convection term represents the total heat transfer from all bounding surfaces (walls, roof, floor, windows) to the room air, and is given in discretized explicit form by,

$$\left\{\begin{matrix} \textit{net convection} \\ \textit{into CV} \end{matrix}\right\} = \sum_{S=1}^{N} h_{c,S}^{t} A_S (T_S^t - T_I^t) \tag{2.17}$$

where N is the number of bounding surfaces. A_S is the area $\{m^2\}$, and $h_{c,S}^{t}$ the present time-row convective heat transfer coefficient, for surface S. The convection coefficients are evaluated in the same manner as for the internal surface nodes.

The advection terms represent the thermal energy carried by air flowing into the control volume from other zones or from the outdoors. These terms are given in discretized explicit form by,

$$\left\{\begin{matrix} \textit{advection} \\ \textit{into CV by} \\ \textit{inter-zone} \\ \textit{air flow} \end{matrix}\right\} = \sum_{J=1}^{M} \dot{m}_{J \to I}^{t} c_p (T_J^t - T_I^t) \tag{2.18}$$

$$\left\{\begin{matrix} \textit{advection} \\ \textit{into CV by} \\ \textit{infiltration} \end{matrix}\right\} = \dot{m}_{o \to I}^{t} c_p (T_o^t - T_I^t) \tag{2.19}$$

M is the number of zones supplying air to the control volume. $\dot{m}_{J \to I}^{t}$ is the air flow from zone J to zone I $\{kg/s\}$ at the present time-row and $\dot{m}_{o \to I}^{t}$ is the infiltration rate $\{kg/s\}$ from the outdoors for the present time-row. T_J^t and T_o^t are the present time-row temperatures of the air-point in zone J and the outdoor air, respectively.

There are various techniques for establishing $\dot{m}^t_{J \to I}$ and $\dot{m}^t_{o \to I}$. At the simplest extreme (appropriate for many analyses) the user can prescribe time-invariant or scheduled values. Greater refinement can be achieved by imposing a control scheme to make air flow rates vary as a function of a sensed condition (the zone air-point temperature or wind speed, for example). The most general approach is to employ a network air flow model to calculate the infiltration and inter-zone air flows in response to prevailing weather conditions and thermal states within the building. This will be described in Section 2.3.

The source term can be given in discretized explicit form by,

$$\begin{Bmatrix} source\ of\ heat \\ within\ CV \end{Bmatrix} = q^t_{cas-conv,I} + q^t_{plant,I} \tag{2.20}$$

$q^t_{cas-conv,I}$ is the heat transferred convectively from casual sources (such as occupants, lights, office equipment) at the present time. $q^t_{plant,I}$ represents a convective plant input to node I at the present time, perhaps from a convective heater located within the room or from an air-based mechanical system delivering a supply of conditioned air to the room.

When the explicit and implicit forms of the heat balance (equation 2.16) are added, the equation divided by the volume (the room's volume in this case, VOL_{room}), and the future time-row terms gathered on the left and the present time-row terms on the right, the following relation results,

$$\begin{aligned}
&\left[\frac{2\cdot(\rho c_p)_I}{\Delta t} + \frac{\sum_{s=1}^{N} h^{t+\Delta t}_{c,s} A_s}{VOL_{room}} + \frac{\sum_{J=1}^{M} \dot{m}^{t+\Delta t}_{J \to I} c_p}{VOL_{room}} + \frac{\dot{m}^{t+\Delta t}_{o \to I} c_p}{VOL_{room}}\right] T_I^{t+\Delta t} - \left[\frac{\sum_{s=1}^{N} h^{t+\Delta t}_{c,s} A_s T_s^{t+\Delta t}}{VOL_{room}}\right] \\
&- \left[\frac{\sum_{J=1}^{M} \dot{m}^{t+\Delta t}_{J \to I} c_p T_J^{t+\Delta t}}{VOL_{room}}\right] - \left[\frac{\dot{m}^{t+\Delta t}_{o \to I} c_p T_o^{t+\Delta t}}{VOL_{room}}\right] - \frac{q^{t+\Delta t}_{cas-conv,I}}{VOL_{room}} - \frac{q^{t+\Delta t}_{plant,I}}{VOL_{room}} \\
&= \left[\frac{2\cdot(\rho c_p)_I}{\Delta t} - \frac{\sum_{s=1}^{N} h^{t}_{c,s} A_s}{VOL_{room}} - \frac{\sum_{J=1}^{M} \dot{m}^{t}_{J \to I} c_p}{VOL_{room}} - \frac{\dot{m}^{t}_{o \to I} c_p}{VOL_{room}}\right] T_I^{t} + \left[\frac{\sum_{s=1}^{N} h^{t}_{c,s} A_s T_s^{t}}{VOL_{room}}\right] \\
&+ \left[\frac{\sum_{J=1}^{M} \dot{m}^{t}_{J \to I} c_p T_J^{t}}{VOL_{room}}\right] + \left[\frac{\dot{m}^{t}_{o \to I} c_p T_o^{t}}{VOL_{room}}\right] + \frac{q^{t}_{cas-conv,I}}{VOL_{room}} + \frac{q^{t}_{plant,I}}{VOL_{room}}
\end{aligned} \tag{2.21}$$

This is the basic simulation equation ESP-r employs to characterize the heat balance for room air-point nodes. It considers heat storage by the room air, convection to the bounding constructions, inter-zone and infiltration air flows, convective casual gains, and convective plant injections. The coefficients differ but the equation has exactly the same form as those for the intra-constructional nodes (equation 2.9) and internal-surface nodes (equation 2.15).

2.2.5 Thermal solution procedure

The methods for forming the control-volume heat-balances have been elaborated. This section now describes the procedure for solving the equations. This will demonstrate how pervasive convection coefficients are in the system of heat balance equations which collectively predict nodal state points and inter-nodal energy flows.

Similarity of heat balance equations

The three previous subsections demonstrated how heat balances are formed for intra-constructional nodes, internal-surface nodes, and air-point nodes. The structural similarity of the resulting equations (2.9, 2.15, and 2.21) was observed, as were the differences in the self-coupling[4], cross-coupling[5], and source-term coefficients. Forming heat balances for the other nodal placements in the building (external fabric surfaces, window surfaces, plant components, etc.) results in the same equation structure in each case, although the coefficients vary from equation to equation. Each equation has terms representing the future temperature of nodes in thermal contact and corresponding present time-row terms (these representing the thermal history of the system).

Considering this, a general heat balance can be written that applies for all nodal placements,

$$\alpha_I T_I^{t+\Delta t} + \sum_{J=1}^{N} \alpha_J T_J^{t+\Delta t} + \beta_{I,I} q_{plant,I}^{t+\Delta t} + \sum_{s=\begin{cases} solar \\ cas-rad \\ cas-conv \end{cases}} \gamma_{I,s} q_{s,I}^{t+\Delta t} + \sum_{a=\begin{cases} out-air \\ env-rad \\ ground \end{cases}} \omega_{I,a} T_a^{t+\Delta t} \tag{2.22}$$

$$= \chi_I T_I^t + \sum_{J=1}^{N} \chi_J T_J^t + \psi_{I,I} q_{plant,I}^t + \sum_{s=\begin{cases} solar \\ cas-rad \\ cas-conv \end{cases}} \xi_{I,s} q_{s,I}^t + \sum_{a=\begin{cases} out-air \\ env-rad \\ ground \end{cases}} \zeta_{I,a} T_a^t$$

α and χ are the self-coupling and cross-coupling coefficients. These may contain thermophysical properties, convection coefficients, radiation coefficients, and inter-zone air flows depending upon the location of the node under consideration. β and ψ are plant coefficients. The nature of the plant

---

[4] Coefficients that modify the present and future temperatures of the node under consideration, such as $[2 \cdot (\rho c_p)_I/\Delta t + k_{I-1}/\Delta x \Delta x_{I-1} + k_{I+1}/\Delta x \Delta x_{I+1}]$ in equation 2.9.

[5] Coefficients that modify the present and future temperatures of nodes in thermal contact, such as $[k_{I-1}/\Delta x \Delta x_{I-1}]$ in equation 2.9.

injection depends upon the nodal placement: it may be convective or radiative, or it may be a direct injection to a node. γ and ξ are the coefficients for solar and casual gains.

The last terms on the right and left sides of the equation represent the coupling between the building and the external environment. The outdoor air temperature is connected to the external-surface nodes through convection, and to zone air-point nodes through infiltration. Below-grade fabric components exchange heat with the ground while external surfaces exchange longwave radiation with the surrounding environment. $T_{env-rad}$ is the equivalent radiant temperature of the surrounding environment and is used to approximate the net radiant exchange from the external surface. It is a weighted sum of the temperatures of the sky, ground surface, and surrounding obstructions (e.g. neighbouring buildings). Consequently, external convection coefficients, radiation coefficients, and ground-coupling coefficients are used to calculate ω and ζ.

Linearization

Equation 2.22 is evaluated for each finite difference node in the model. Consequently, a large matrix of equations is formed in which the (unknown) future time-row nodal temperatures, plant injections, source terms, and external environment excitations are gathered on the left, with the corresponding (known) present time-row quantities on the right. The system of equations is non-linear as the coefficients of the future time-row cannot be evaluated until the future time-row temperatures are computed. This quandary is overcome by evaluating coefficients one time-step in arrears: future time-row coefficients are calculated using present temperatures, while present time-row coefficients are calculated with immediate past results. In this manner, $h_{r,s\rightarrow I}^{t+\Delta t}$ and $h_{c,I}^{t+\Delta t}$ are calculated with T_s^t and T_I^t, while $h_{r,s\rightarrow I}^{t}$ and $h_{c,I}^{t}$ are calculated with $T_s^{t-\Delta t}$ and $T_I^{t-\Delta t}$. This linearization technique has minimal consequences for small (one hour or less) time-steps. Indeed, it should be noted that many simulation programs hold the convection and radiation coefficients constant over the entire analysis period.

Linearization also allows the future time-row ambient excitation terms (last grouping on left side) to be moved to the right since the ω coefficients are calculated with known temperatures and the external environment data are drawn from a user-specified weather data file.

Each time-step ESP-r processes the casual gain and solar gain terms prior to forming the nodal heat balances. Pre-processing casual gains introduces no approximation, as the magnitude of the convective and radiant gains and their schedule is a user input. In general, pre-processing the absorbed solar gains introduces no approximation either, as available solar radiation is a function of sun position and sky conditions, but not of the building's thermal state[6]. Essentially, this moves $q_{solar,I}^{t+\Delta t}$, $q_{cas-rad,I}^{t+\Delta t}$, and $q_{cas-conv,I}^{t+\Delta t}$ to the right side, thus treating these terms as known boundary excitations on the system of equations.

---

[6] The only exception is when the user has made the operation of window blinds a function of indoor thermal conditions. In this case, one time-step in arrears values are used to control the blind operation.

Closure

With these manipulations, the set of heat balance relations is reduced to a linear system of equations of the form,

$$\mathbf{A}\theta^{t+\Delta t} = \mathbf{B}\theta^{t} + \mathbf{C} = \mathbf{Z} \tag{2.23}$$

θ is a vector of nodal temperatures and plant injections of dimension $2n$, where n is the number of finite-difference nodes in the model: each node has a temperature and a plant injection. **A** and **B** are sparse matrices of dimension $n \times 2n$ holding nodal temperature self- and cross-coupling coefficients and plant injection coefficients. **A** contains the future time-row coefficients (α and β from equation 2.22) while **B** holds present time-row values (χ and ψ). **C** is a vector of dimension n holding the known boundary excitation terms (the sum of the $q_s^{t+\Delta t}$, q_s^{t}, $T_a^{t+\Delta t}$, and T_a^{t} terms). As θ^{t} is known for the time-step being solved, the right side can be collapsed into **Z**, a known vector of dimension n.

The mathematical system represented by equation 2.23 contains twice as many unknowns as equations, and consequently cannot be solved in this form. The problem is *closed* through the application (by the user) of a control scheme which governs the relationship between the building's thermal state and the operation of its plant. For example, if the building is allowed to free float (no heating or cooling), the plant interaction terms disappear, thus reducing the system to n unknowns (the nodal temperatures) in n equations. If the zone is conditioned with a convective heater which is controlled by a thermostat sensing the air-point temperature, then all plant terms but one (injection to the air-point node) disappear. Further, the temperature of the air-point node is fixed at the set-point value. Again, this constrains the problem to n unknowns (1 plant injection and $n - 1$ nodal temperatures) in n equations.

Partitioning

As the problem has been reduced to a linear set of n equations in n unknowns, the focus becomes matrix solution. For this, ESP-r employs a simultaneous direct solution approach based on matrix partitioning and Gaussian elimination. This is best illustrated by example.

Figure 2.8 illustrates a simple four-zone model of a house. The foyer, dining, and kitchen zones are heated by an in-floor system controlled by a thermostat sensing the foyer's air temperature. The attached garage is unconditioned, its temperature free floating in response to thermal conditions in the foyer and outdoors. The common walls connecting the zones are shown in grey. All other fabric components face the external environment.

If a matrix in the form of equation 2.23 were formed for the whole house, it would include cross-coupling coefficients linking the thermal states of the zones. The result would be a large sparse matrix, necessitating large memory requirements and an intensive computational method. Instead, ESP-r takes the pragmatic approach of partitioning the building domain into zone matrices, and processing these independently each time-step. Zone-coupling information is exchanged between time-steps, thus linking the zone matrices and enabling a global solution of the building to evolve. This treats neighouring zones as known quantities for the current time-step, effectively moving the zone cross-coupling terms to the right side of equation 2.23. Zone partitioning has minimal consequences on accuracy, particularly when small (one hour or less) time-steps are used.

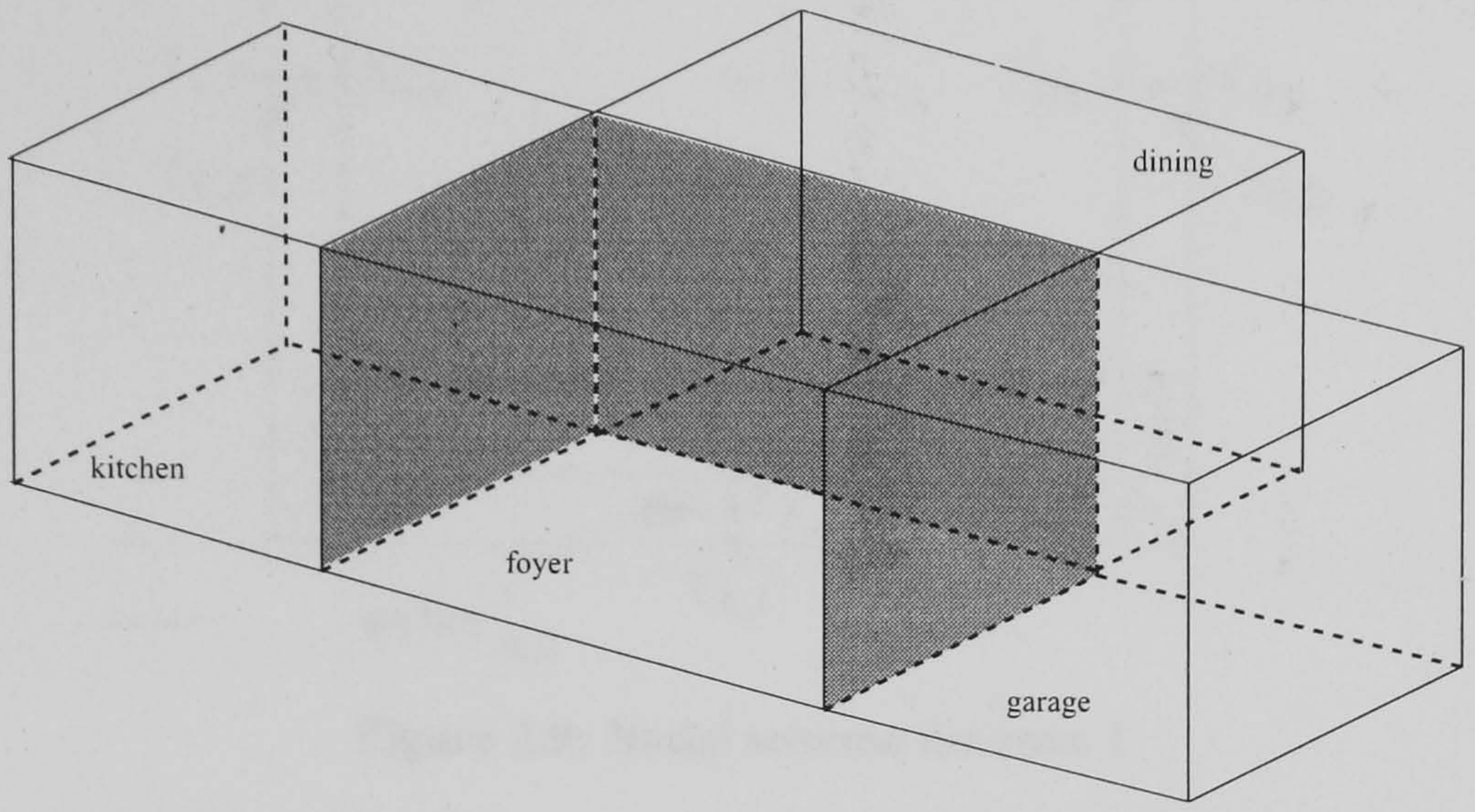

Figure 2.8: Four zone representation of a house

Matrix of zone heat balance equations

The technique for processing the zone matrices is demonstrated by focusing on the foyer of Figure 2.8. A very simple model of the foyer is used to elucidate the matrix processing technique. The foyer zone is a windowless rectangular box enclosed by six fabric components, each of which is constructed of a single material layer. Figure 2.9 illustrates the default nodal scheme (four of the fabric components are shown). There is a node representing the zone's air-point (identified by T_a in the figure). Each of the six fabric components is represented by three nodes, one at the internal surface (e.g. C, s), one at the external surface (e.g. $C, 1$), and one within the construction (e.g. $C, 2$). The foyer is heated with a hydronic in-floor system which is controlled to maintain a constant room-air temperature. Accordingly, the hydronic system is controlled to inject heat at node $A, 2$ to maintain T_a at the set-point.

Application of equation 2.22 for each of the 19 nodes and subsequent arrangement in the form of equation 2.23, gives rise to the system of 19 equations with 20 unknowns (19 nodal temperatures and one plant injection) shown in Figure 2.10. The equations for external surface nodes are located in rows 1, 4, 7, 10, 13, and 16 while those for the intra-constructional nodes are located in rows 2, 5, 8, 11, 14, and 17. The heat balances for the internal-surface nodes are located in rows 3, 6, 9, 12, 15, and 18. Finally, row 19 contains the heat balance for the air-point node. Note that the $t + \Delta t$ superscript has been dropped from the vector of independent variables for the sake of clarity, it being understood that these are future time-row values.

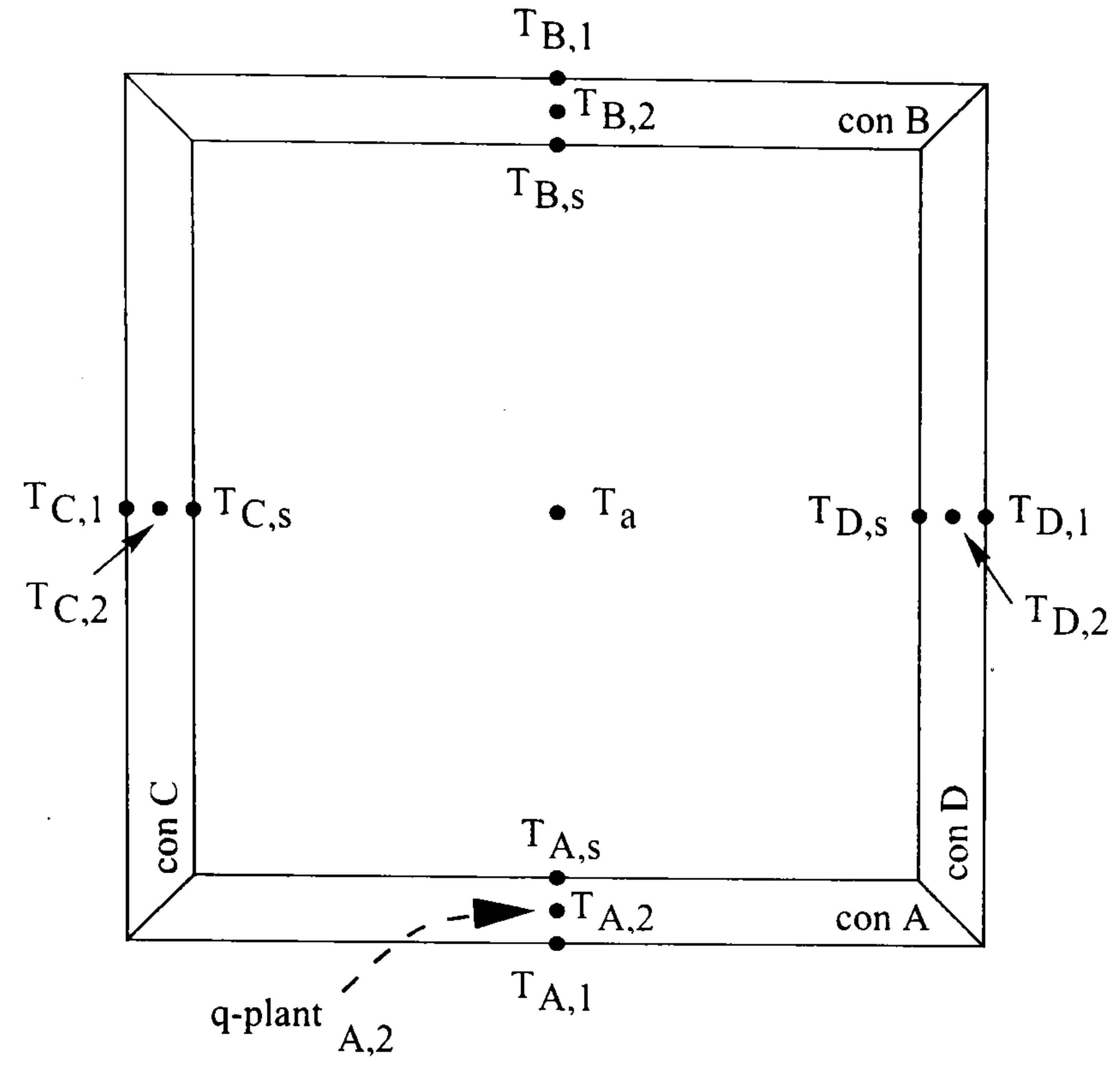

Figure 2.9: Nodal scheme for zone 1

$$
\left[\begin{array}{cccccccccccccccccccc}
a_{1.1} & a_{1.2} \\
a_{2.1} & a_{2.2} & a_{2.3} & & & & & & & & & & & & & & & & & a_{2.20} \\
& a_{3.2} & \boxed{a_{3.3}} & & & a_{3.6} & & & a_{3.9} & & & a_{3.12} & & & a_{3.15} & & & a_{3.18} & \boxed{a_{3.19}} \\
& & & a_{4.4} & a_{4.5} \\
& & & a_{5.4} & a_{5.5} & a_{5.6} \\
& & a_{6.3} & & a_{6.5} & \boxed{a_{6.6}} & & & a_{6.9} & & & a_{6.12} & & & a_{6.15} & & & a_{6.18} & \boxed{a_{6.19}} \\
& & & & & & a_{7.7} & a_{7.8} \\
& & & & & & a_{8.7} & a_{8.8} & a_{8.9} \\
& & a_{9.3} & & & a_{9.6} & & a_{9.8} & \boxed{a_{9.9}} & & & a_{9.12} & & & a_{9.15} & & & a_{9.18} & \boxed{a_{9.19}} \\
& & & & & & & & & a_{10.10} & a_{10.11} \\
& & & & & & & & & a_{11.10} & a_{11.11} & a_{11.12} \\
& & a_{12.3} & & & a_{12.6} & & & a_{12.6} & & a_{12.11} & \boxed{a_{12.12}} & & & a_{12.15} & & & a_{12.18} & \boxed{a_{12.19}} \\
& & & & & & & & & & & & a_{13.13} & a_{13.14} \\
& & & & & & & & & & & & a_{14.13} & a_{14.14} & a_{14.15} \\
& & a_{15.3} & & & a_{15.6} & & & a_{15.9} & & & a_{15.12} & & a_{15.14} & \boxed{a_{15.15}} & & & a_{15.18} & \boxed{a_{15.19}} \\
& & & & & & & & & & & & & & & a_{16.16} & a_{16.17} \\
& & & & & & & & & & & & & & & a_{17.16} & a_{17.17} & a_{17.18} \\
& & a_{18.3} & & & a_{18.6} & & & a_{18.9} & & & a_{18.12} & & & a_{18.15} & & a_{18.17} & \boxed{a_{18.18}} & \boxed{a_{18.19}} \\
& & \boxed{a_{19.3}} & & & \boxed{a_{19.6}} & & & \boxed{a_{19.9}} & & & \boxed{a_{19.12}} & & & \boxed{a_{19.15}} & & & \boxed{a_{19.18}} & \boxed{a_{19.19}}
\end{array}\right]
\times
\begin{bmatrix} T_{A.1} \\ T_{A.2} \\ T_{A.s} \\ T_{B.1} \\ T_{B.2} \\ T_{B.s} \\ T_{C.1} \\ T_{C.2} \\ T_{C.s} \\ T_{D.1} \\ T_{D.2} \\ T_{D.s} \\ T_{E.1} \\ T_{E.2} \\ T_{E.s} \\ T_{F.1} \\ T_{F.2} \\ T_{F.s} \\ T_a \\ q_{plant} \end{bmatrix}
=
\begin{bmatrix} z_1 \\ z_2 \\ \boxed{z_3} \\ z_4 \\ z_5 \\ \boxed{z_6} \\ z_7 \\ z_8 \\ \boxed{z_9} \\ z_{10} \\ z_{11} \\ \boxed{z_{12}} \\ z_{13} \\ z_{14} \\ \boxed{z_{15}} \\ z_{16} \\ z_{17} \\ \boxed{z_{18}} \\ \boxed{z_{19}} \end{bmatrix}
$$

Figure 2.10: Zone matrix of heat balance equations

Significantly, convection coefficients appear in 26 of the 105 coefficients. Each coefficient enclosed in a box in Figure 2.10 includes a convection coefficient. The internal-surface nodes's self-coupling coefficients ($a_{3,3}$, $a_{6,6}$, $a_{9,9}$, $a_{12,12}$, $a_{15,15}$, $a_{18,18}$), known boundary excitations (z_3, z_6, z_9, z_{12},

z_{15}, and z_{18}), and cross-coupling coefficients to the air-point ($a_{3,19}$, $a_{6,19}$, $a_{9,19}$, $a_{12,19}$, $a_{15,19}$, and $a_{18,19}$) all include h_c values. h_c also appears in every coefficient of the air-point balance ($a_{19,3}$, $a_{19,6}$, $a_{19,9}$, $a_{19,12}$, $a_{19,15}$, $a_{19,18}$, $a_{19,19}$, and z_{19}). In general, models will have more intra-constructional nodes (because constructions usually have multiple material layers). Therefore, the fraction of coefficients including h_c will usually be less than this case, although still significant. As well, the air-point balance will usually include terms that do not involve h_c, such as inter-zone air flow and infiltration.

Given this pervasiveness, it is clear that erroneous h_c values would substantially distort the zone matrix. This would cause inaccuracies in nodal temperatures, plant injections, and inter-nodal energy flows. This is significant considering how h_c values can vary substantially between calculation methods (see page 18). The sensitivity of simulation results to h_c variations is explored in detail in Chapter 4.

Appendix A describes how the zone matrix is solved to predict the nodal temperatures and plant injections. Knowledge of the zone matrix solution procedure is helpful, but not critical, in understanding the handshaking between CFD and the thermal domain.

2.3 Inter-zone Air Flow

This section briefly describes ESP-r's multi-zone network air flow model, including its integration with the thermal domain. This is necessary for understanding the integration of CFD with whole-building simulation. However, treatment is succinct, as the coupling between inter- and intra-zone air flow is not a focus of the current research.

2.3.1 Multi-zone network air flow model

The concept of multi-zone network air flow models was introduced in Chapter 1. As explained, these macroscopic models represent large air volumes (e.g. rooms) with uniform conditions, and predict flow through discrete paths (e.g. doors, cracks). Although the method presumes one-dimensional steady-state flow, boundary conditions (wind, temperatures, fan operation, window openings) can vary in time. Stack effects caused by indoor-outdoor and inter-zone temperature differences are also considered. Complex buildings can be analyzed efficiently, and the method allows the simulation of both infiltration and internal air flow.

The multi-zone network air flow model implemented in ESP-r is based on the work of Cockcroft (1979), with extensions and refinements by Hensen (1991). Four principle steps are involved:

1) The building is discretized by representing air volumes (usually zones) by *nodes* (see 1-4 in Figure 2.11). Nodes are also used to represent conditions external to the building (see a, b, and c). It is also possible place air flow nodes within plant systems[7].

---

[7] Water networks can also be established to represent hydronic plant systems.

2) *Components* are defined to represent leakage paths (through the fabric), and pressure drops associated with doors, windows, supply grills, ducts, fans, etc.

3) The nodes are linked together through components to form *connections* (shown with double-headed arrows in the figure), this establishing a flow network.

4) A mass balance is expressed for each node in the building. The resulting system of equations is solved to yield the nodal pressures and the flows through the connections.

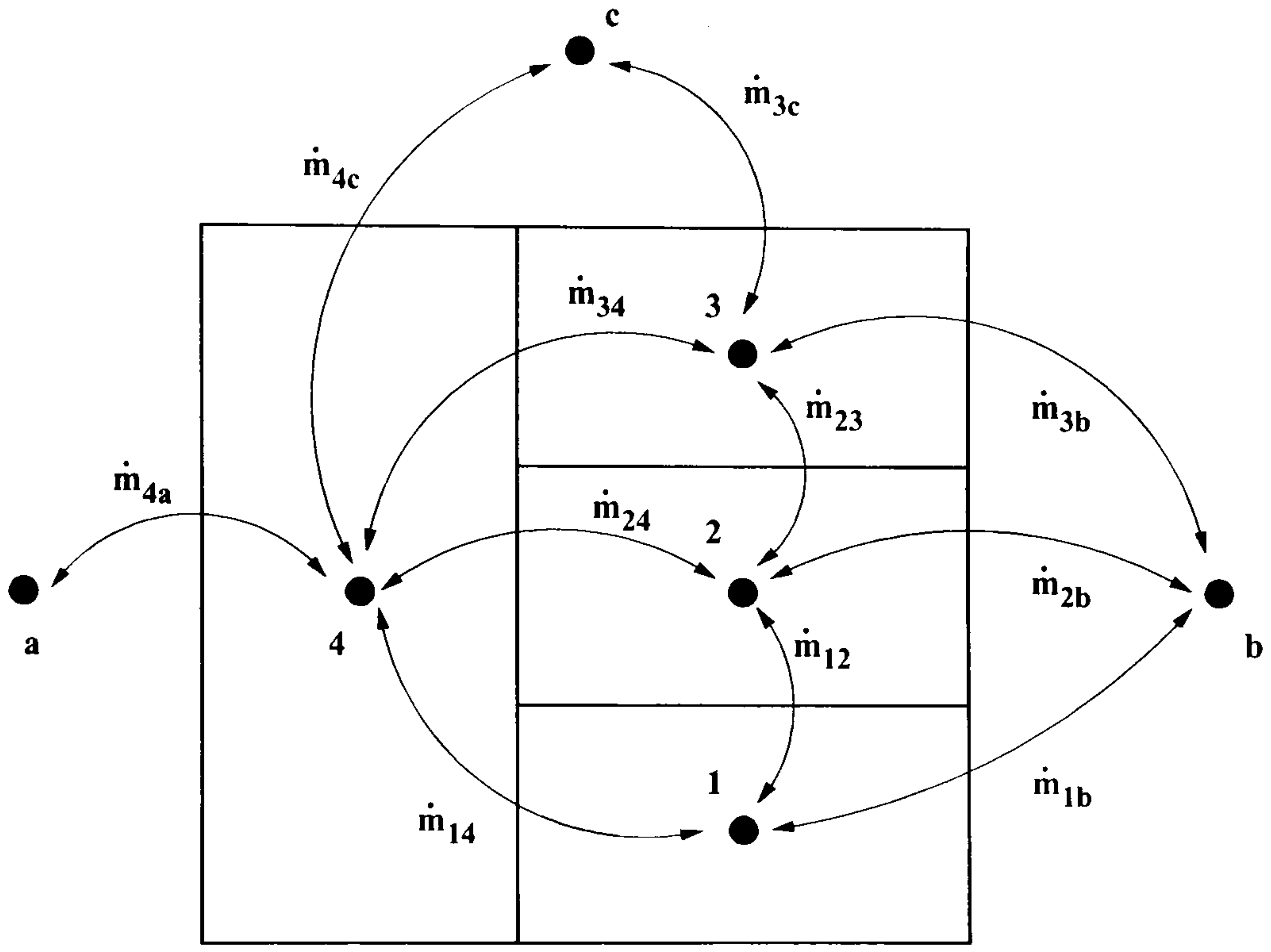

Figure 2.11: Air flow network: nodes and connections

The components (step 2) relate the air flow rate through a connection to the pressure difference across the connection,

$$\dot{m}_{ij} = f(P_i, P_j) = f(\Delta P_{ij}) \tag{2.24}$$

where $\dot{m}_{ij}$ is the flow rate $\{kg/s\}$ from node i to node j, P_i is the pressure {Pa} at node i, and ΔP_{ij} is the pressure difference {Pa} between nodes i and j. As an example, an intentional opening made in the building fabric to supply a furnace with make-up air could be represented by,

$$\dot{m}_{ij} = C_d A \sqrt{2\rho \Delta P_{ij}} \tag{2.25}$$

where C_d is the discharge factor (user-prescribed), A the opening area (user-prescribed), and ρ the air density. ESP-r contains many similar component models to represent cracks, open windows, open doors, etc.

The mass balances (step 4) written for each node relate the flow rates through the connections associated with that node. As mass is conserved and a steady-state solution is sought each time-step, the sum of the mass flows to a node must equal zero,

$$\sum_{j=1}^{n} \dot{m}_{ij} = 0 \tag{2.26}$$

where n is the number of nodes connected to node i. Substituting the flow component relations (equation 2.24) into equation 2.26 gives the following form for the nodal mass balance,

$$\sum_{j=1}^{n} f(\Delta P_{ij}) = 0 \tag{2.27}$$

Evaluating equation 2.27 for each node gives rise to a non-linear set of equations. ESP-r solves the equations using a guess-and-correct iterative procedure. An arbitrary pressure is assigned to each node within the building (the pressure of external nodes is determined by the prevailing wind and building geometry). These guessed pressures are used to estimate the flow along each connection using the component relations (equation 2.24). The flow rates will be erroneous since the pressures are guessed, so the mass balance (equation 2.27) will not be satisfied. The nodal pressures are then iteratively corrected, and the flow rates recalculated until the residuals of the mass-balance equations reach an acceptable convergence criterion. The iterative approach for correcting the pressure estimates is based on a Newton-Raphson technique, described in detail by Hensen (1991).

2.3.2 Integration of network air flow and thermal models

The building's thermal state affects air flow in two ways. Firstly, stack pressures caused by indoor-outdoor and inter-zone temperature differences cause buoyancy forces which can significantly affect infiltration and internal air flow. Secondly, windows may open and close and fans may operate in response to temperatures within the building. Similarly, the building's thermal state is affected by infiltration and inter-zone air flows. Consequently, a realistic treatment of this interdependency demands a coupling of the thermal and air flow modelling domains.

The previous subsection described the network air flow model's solution procedure. This contrasts substantially with the procedure for solving the thermal domain (see Section 2.2.5). This demonstrates ESP-r's partitioned solution approach: customized solvers are applied to each model domain to enable an optimized treatment of each of the disparate equation sets.

In order to couple the simulation of heat and air flow, ESP-r overlays its thermal and network air flow models. The user specifies the linkages between the zone air-point nodes in the thermal domain and the network air flow nodes. The two models are coupled by passing information between the solution domains each time-step (this handshaking was shown schematically in Figure 2.2, page 11).

The thermal results from the previous time-step are used to establish the temperatures of the network air flow nodes for the current time-step. This effects the stack pressures, which are significant in buoyancy-driven flow. External boundary conditions (e.g. external temperatures and wind velocities) are established for the current time-step, and the network air flow equations solved. The results of the network air flow simulation then map directly to the infiltration and inter-zone air flow advection terms in the heat balances for air-point nodes for the current time-step. In other words, the network air flow model establishes $\dot{m}_{J \to I}$ and $\dot{m}_{o \to I}$ in equations 2.18 and 2.19 (see page 21). Consequently, the air flow results affect the zone matrices and thus the thermal solution.

These steps are repeated for each time-step of the simulation, thus allowing the heat and air flow solution to evolve in a coupled manner.

2.4 Coupling of CFD with Thermal and Inter-zone Air Flow

Chapter 1 introduced ESP-r's integrated CFD capabilities. This conflation, accomplished by Negrão (1995), is consistent with ESP-r's partitioned solution approach. The CFD model is integrated with the thermal and network air flow models within a single executable but uses its own customized solver, it exchanging information with the thermal and network air flow domains on a time-step basis. A thermal and (optionally) a network air flow representation of the whole building and plant is established, while a CFD model is created for a single room (shown schematically in Figure 2.12).

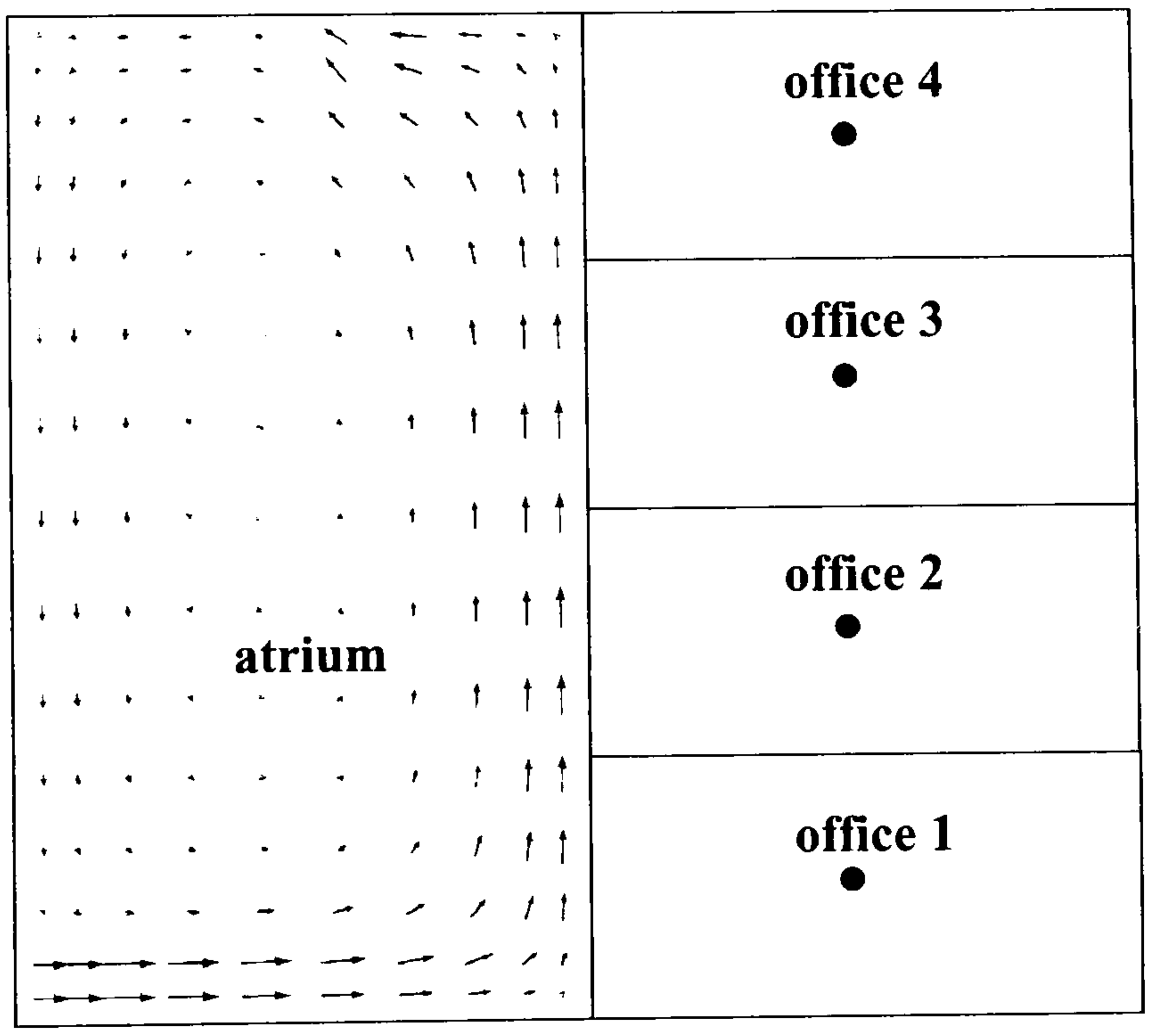

Figure 2.12: Integration of CFD with thermal and network air flow domains

At each time-step the boundary conditions for the CFD model are established by the thermal or network air flow domains. Once converged, CFD passes its results back to the thermal or network air flow domains, which use the data to calculate the surface temperatures, energy flows, and air flows throughout the building.

The integration of CFD was motivated by the following factors:

- The thermal and network air flow simulation domains can supply CFD with realistic and time-varying boundary conditions, thus improving CFD's ability to calculate room air flow and heat transfer (see the discussion of CFD boundary conditions in Section 1.2).
- The thermal and network air flow domains can drop the well-stirred assumption by using CFD to predict the details of flow and temperature fields within zones.
- CFD can predict internal surface convection in response to local flow patterns.

ESP-r's CFD model shares much in common with other CFD codes that have been used for modelling room air flow (for example, see Lemaire et al 1993 and Liddament 1991). It uses the SIMPLEC pressure-correction solution approach, is finite-volume based, and employs a three-dimensional, Cartesian, staggered grid. The turbulent diffusion of heat and momentum is estimated with the widely applied standard $k-\varepsilon$ model, while log-law wall functions are used to account for viscous effects in the near-wall regions. ESP-r's CFD model has undergone analytical, empirical and inter-program validation (Negrão 1995; Loomans 1995). These numerical approaches are described, and numerous issues regarding their applicability for room air flow and heat transfer modelling are discussed, in Chapter 3.

At the commencement of the current research, three mechanisms existed for the CFD model to handshake with the thermal and network air flow domains. These are outlined below. The interested reader is referred to Negrão (1995) and Clarke et al (1995a, 1995b) for further details.

Method 1

With this the thermal and CFD domains handshake, although there is no interaction between CFD and the network air flow model (in fact, network air flow cannot be active).

The thermal domain establishes boundary conditions for CFD using the surface temperatures calculated the previous time-step. Once the CFD model converges to a solution, air-to-surface heat transfer is determined from the CFD-predicted flow and temperature fields using the log-law wall functions (the wall function method is described in detail in Chapter 3). Surface-averaged convection coefficients for each surface of the zone are then calculated and passed back to the thermal domain.

Essentially, CFD is used as an alternative to the methods listed in Table 2.1 (see page 19) to calculate h_c values for a single room (although the well-stirred assumption is still in effect). Consequently, this method is critically dependent upon the wall functions to accurately predict the air-to-surface heat transfer. However, the log-law wall functions are deficient at this task, for reasons that are explained in Chapter 3. Apart from the calculation of h_c, the remainder of the thermal simulation proceeds as usual. The CFD-calculated h_c values are used in equations 2.14 and 2.17 (see pages 18 and

21) to establish the energy balances for internal surfaces and zone air-points. And, the zone matrix is solved using the techniques (unaltered) outlined in Section 2.2.5.

Method 2

This also involves handshaking on the thermal level. Again, a network air flow model cannot be active. Whereas in the previous scheme h_c values were calculated by CFD prior to zone matrix formation, here CFD interacts directly with the thermal matrix solver in order to drop (to a degree) the well-stirred assumption. This is accomplished by using CFD to solve the zone air-point temperature and internal surface convection.

The heat balances for internal surface nodes and the zone air-point node are rewritten by evaluating the surface convection terms using CFD results. The convection terms are not expressed with surface and air-point nodal temperatures and convection coefficients, but rather the CFD-predicted heat transfer is directly used in the nodal balances. In this way, equations 2.14 and 2.17 (see pages 18 and 21) are replaced by,

$$\left\{\begin{array}{c} \textit{net convection} \\ \textit{into surface} \\ \textit{node CV} \end{array}\right\} = q_{air \to surface}^{CFD\text{-}wall\ functions} \tag{2.28}$$

$$\left\{\begin{array}{c} \textit{net convection} \\ \textit{into air-point} \\ \textit{node CV} \end{array}\right\} = \sum_{S=1}^{N} q_{S \to air}^{CFD\text{-}wall\ functions} \tag{2.29}$$

Again, the wall function method used by CFD to calculate the heat transfer is treated in detail in Chapter 3. Substituting equation 2.28 into the internal surface heat balance (equation 2.10, page 17) and equation 2.29 into the air-point node heat balance (equation 2.16, page 21) leads to the general heat balance (equation 2.22, page 23) as before. However in this case, there are no convection coefficients, and the surface convection terms ($q_{air \to surface}^{CFD\text{-}wall\ functions}$ and $\sum q_{S \to air}^{CFD\text{-}wall\ functions}$) appear on the right side, these treated as known boundary excitations in the thermal solution domain.

This affects the form of the zone matrix of equations. The internal surface nodes no longer have cross-coupling coefficients to the air-point node, because surface convection appears in the right side coefficients. Relating this to the example of Section 2.2.5, the coefficients $a_{3,19}$, $a_{6,19}$, $a_{9,19}$, $a_{12,19}$, $a_{15,19}$, and $a_{18,19}$ disappear from Figure 2.10 (see page 27). In their place, $q_{air \to surface}^{CFD\text{-}wall\ functions}$ appears in z_3, z_6, z_9, z_{12}, z_{15}, and z_{18}. Similarly, $a_{19,3}$, $a_{19,6}$, $a_{19,9}$, $a_{19,12}$, $a_{19,15}$, and $a_{19,18}$ are eliminated, replaced by $\sum q_{S \to air}^{CFD\text{-}wall\ functions}$ in z_{19}. This revised form of the zone matrix is shown in Figure 2.13. The empty boxes indicate the coefficients that have been eliminated by the CFD domain.

$$\left[\begin{array}{cccccccccccccccccccc}
a_{1,1} & a_{1,2} & & & & & & & & & & & & & & & & & & \\
a_{2,1} & a_{2,2} & a_{2,3} & & & & & & & & & & & & & & & & & a_{2,20} \\
 & a_{3,2} & a_{3,3} & & & a_{3,6} & & & a_{3,9} & & & a_{3,12} & & & a_{3,15} & & & a_{3,18} & \square & \\
 & & & a_{4,4} & a_{4,5} & & & & & & & & & & & & & & & \\
 & & & a_{5,4} & a_{5,5} & a_{5,6} & & & & & & & & & & & & & & \\
 & & a_{6,3} & & a_{6,5} & a_{6,6} & & & a_{6,9} & & & a_{6,12} & & & a_{6,15} & & & a_{6,18} & \square & \\
 & & & & & & a_{7,7} & a_{7,8} & & & & & & & & & & & & \\
 & & & & & & a_{8,7} & a_{8,8} & a_{8,9} & & & & & & & & & & & \\
 & & a_{9,3} & & & a_{9,6} & & a_{9,8} & a_{9,9} & & & a_{9,12} & & & a_{9,15} & & & a_{9,18} & \square & \\
 & & & & & & & & & a_{10,10} & a_{10,11} & & & & & & & & & \\
 & & & & & & & & & a_{11,10} & a_{11,11} & a_{11,12} & & & & & & & & \\
 & & a_{12,3} & & & a_{12,6} & & & a_{12,6} & & a_{12,11} & a_{12,12} & & & a_{12,15} & & & a_{12,18} & \square & \\
 & & & & & & & & & & & & a_{13,13} & a_{13,14} & & & & & & \\
 & & & & & & & & & & & & a_{14,13} & a_{14,14} & a_{14,15} & & & & & \\
 & & a_{15,3} & & & a_{15,6} & & & a_{15,9} & & & a_{15,12} & & a_{15,14} & a_{15,15} & & & a_{15,18} & \square & \\
 & & & & & & & & & & & & & & & a_{16,16} & a_{16,17} & & & \\
 & & & & & & & & & & & & & & & a_{17,16} & a_{17,17} & a_{17,18} & & \\
 & & a_{18,3} & & & a_{18,6} & & & a_{18,9} & & & a_{18,12} & & & a_{18,15} & & a_{18,17} & a_{18,18} & \square & \\
 & & \square & & & \square & & & \square & & & \square & & & \square & & & \square & a_{19,19} &
\end{array}\right] \times \left[\begin{array}{c}
T_{A.1} \\ T_{A.2} \\ T_{A.s} \\ T_{B.1} \\ T_{B.2} \\ T_{B.s} \\ T_{C.1} \\ T_{C.2} \\ T_{C.s} \\ T_{D.1} \\ T_{D.2} \\ T_{D.s} \\ T_{E.1} \\ T_{E.2} \\ T_{E.s} \\ T_{F.1} \\ T_{F.2} \\ T_{F.s} \\ T_a \\ q_{plant}
\end{array}\right] = \left[\begin{array}{c}
z_1 \\ z_2 \\ z_3 \\ z_4 \\ z_5 \\ z_6 \\ z_7 \\ z_8 \\ z_9 \\ z_{10} \\ z_{11} \\ z_{12} \\ z_{13} \\ z_{14} \\ z_{15} \\ z_{16} \\ z_{17} \\ z_{18} \\ z_{19}
\end{array}\right]$$

Figure 2.13: Revised zone matrix of heat balance equations

It was shown earlier how pervasive convection coefficients are in the zone matrix when the well-stirred assumption is employed. Because of this, it was explained, erroneous h_c values would distort the system of equations and lead to inaccurate nodal temperature, plant injection, and inter-nodal energy flow predictions. This method of coupling CFD with the thermal domain eliminates convection coefficients from the zone matrix. However, it does not solve this problem. The $q_{air\rightarrow surface}^{CFD-wall\ functions}$ and $\sum q_{S\rightarrow air}^{CFD-wall\ functions}$ right-side surface convection terms have the same affect on the system of equations. If CFD inaccurately predicts the surface convection, errors will propagate throughout.

An alternate procedure is required to solve this revised zone matrix. Appendix B describes the solution procedure, including the interaction between CFD and the thermal matrix solver. Knowledge of this solution procedure is helpful, but not critical, in understanding the material that follows.

Although substantially different in approach, the two thermal conflation methods produce very similar results when time-steps are sufficiently small.

Method 3

With the third handshaking method the air flow network and CFD interact, although there is no interaction between CFD and the thermal domain.

A single air flow network node is replaced by a CFD domain to drop the assumption of well-mixed conditions for a zone (for the purposes of air flow modelling; however, the well-stirred assumption is still in effect in terms of the thermal model). New connections are added to the air flow network to link the CFD domain to the network (e.g. node "lounge" is connected to node "A" in the CFD domain shown in Figure 2.14), while connections to the removed node are eliminated.

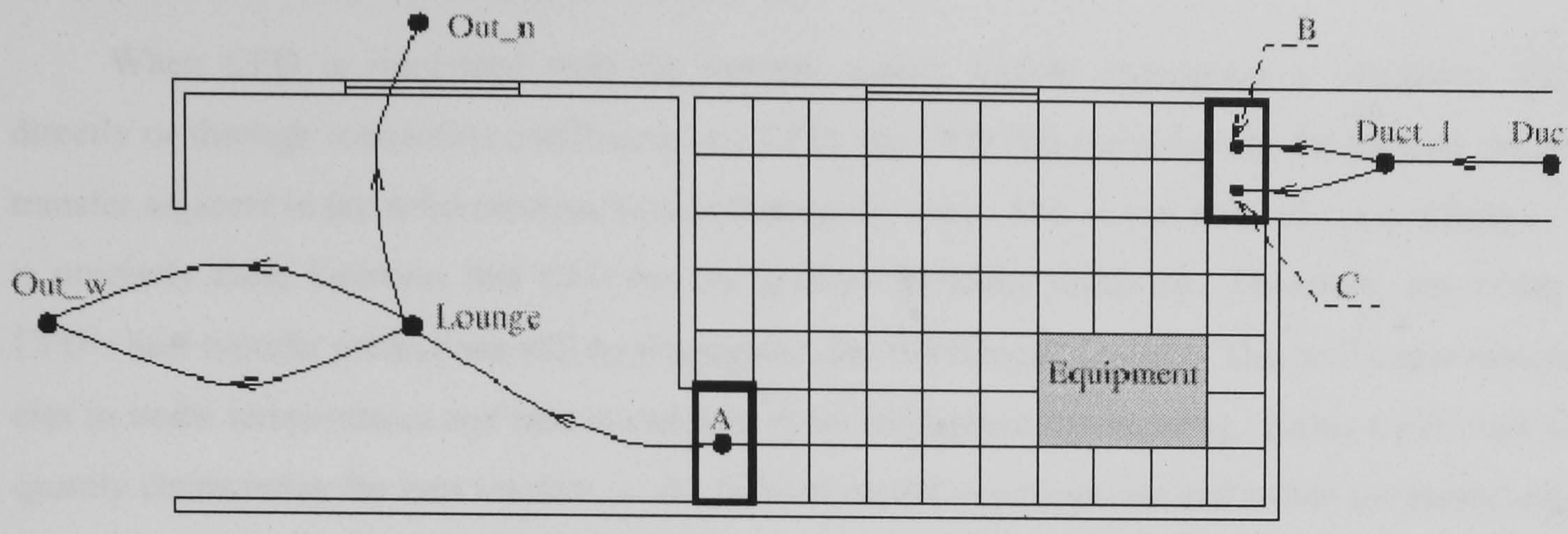

Figure 2.14: Conflation between CFD and network air flow (from Negrão 1995)

The network air flow domains establish boundary conditions for CFD (temperatures and flow conditions at diffusers, extracts, and other openings). Once CFD converges to a solution, the CFD-predicted air flows into and out of the zone are passed to the network air flow solver, where they are treated as sources or sinks of mass. The network is then solved in its usual manner to determine the flow through the remaining connections in the network. Following this, the thermal system is simulated for the current time-step using the approach (unaltered) described in Section 2.2.

2.5 Closing Remarks

This chapter has provided an overview of ESP-r's simulation methodology. Its approaches for modelling the thermal domain, inter-zone air flow, and (using CFD) intra-zone air flow and heat transfer were described. The techniques used to handle the interdependencies between these modelling domains were reviewed. Emphasis was placed, in particular, on the coupling between the thermal domain and CFD. Stress was also given to ESP-r's modelling of internal surface convection within the context of its thermal simulation approach.

Chapter 1 described how convection heat transfer varies from surface to surface (and with time) in response to local air flow patterns. It argued that the modelling of internal surface convection should respond to local flow conditions in a dynamic fashion. This chapter has described how ESP-r employs the well-stirred assumption with surface-specific convection coefficients to model internal surface convection. It does recalculate convection coefficients each time-step, yet it does not have the ability to adapt the calculation approach to changes in the air flow regime. Additionally, important flow regimes cannot currently be characterized since both the default and optional h_c algorithms treat only buoyancy-driven flow.

ESP-r's default and optional h_c algorithms result in substantially different convection coefficients. This is significant given how pervasive convection coefficients are in the matrix of heat balance equations that characterize the zone's thermal state. Although this chapter has demonstrated the central role that internal convection plays in the thermal system, the sensitivity of simulation results to convection coefficients has not yet been quantified.

When CFD is integrated with the thermal model, surface convection is calculated (either directly or through convection coefficients) by CFD, the CFD domain resolving the air flow and heat transfer adjacent to the solid constructions enclosing the zone. Yet, as was pointed out in Chapter 1, it is precisely these locations that CFD has the greatest difficulty resolving. Therefore, any errors in CFD's heat transfer predictions will be propagated into the thermal domain. This will cause inaccuracies in nodal temperatures and inter-nodal heat flows throughout the building. Either CFD must adequately characterize the heat transfer, or the thermal model must appraise and (when necessary) reject the results received from the CFD domain.

CHAPTER 3

Applicability of CFD for Modelling Room Air Flow and Heat Transfer

3.1 Introduction

Computation Fluid Dynamics (CFD) means the numerical modelling of physical processes occurring within a fluid. This includes not only fluid motion, but also heat transfer, mass transfer, and chemical reactions (e.g. combustion).

CFD was not developed specifically for modelling buildings, but rather as a general purpose simulation technology. Its use in a wide range of engineering and scientific fields is growing rapidly, as evidenced by the number of publications appearing in journals and at conferences, and by the increasing sophistication of commercial CFD software packages. Applications include:

- aircraft aerodynamics;
- ship hydrodynamics;
- meteorology;
- biomedical engineering;
- the study of pollutant effluents;
- the design of micro-electronic cooling systems;
- the design of gas turbines and other combustion equipment.

Chapter 1 alluded to some issues regarding the applicability of CFD for room air flow and heat transfer modelling. Chapter 2 showed how the handshaking between ESP-r's thermal domain and CFD was critically dependent upon CFD's ability to resolve the surface convection heat transfer. An understanding of CFD's theoretical basis is necessary in order to explore these issues, and to understand the solutions put forward in subsequent chapters. Consequently, this chapter sets out to describe CFD's essential extractions and to appraise its applicability for modelling room air flow and heat transfer.

Section 3.2 describes CFD's conceptual basis and introduces its numerical approaches. The previous applications of CFD for predicting room air flow and heat transfer are reviewed in Section 3.3. The nature of room air flow is discussed in Section 3.4, and the various approaches for modelling turbulent motion treated in Section 3.5. These are key to understanding the applicability of CFD within the context of the conflated simulation approach. The most popular turbulence model—the standard $k-\varepsilon$ model—is described in detail in Section 3.6, while its applicability is assessed in Section 3.7. An overview of alternatives to the standard $k-\varepsilon$ model is provided in Section 3.8. Finally, closing remarks are provided in Section 3.9.

3.2 The Conceptual Basis of CFD

In essence, CFD involves the solution of a set of non-linear partial differential equations using numerical techniques. The partial differential equations express the fundamental physical laws that govern fluid flow and related phenomena—the conservation of mass, momentum, and energy. The equations are discretized and linearized, and the computational domain enclosed with boundary conditions. This yields a set of coupled algebraic relations which are solved iteratively to predict (at discrete points) the distribution of pressure, temperature, and velocity (and perhaps other physical quantities).

Material presented in subsequent sections and chapters presumes an understanding of CFD's conceptual basis and general familiarity with its numerical approaches. Consequently, the pertinent aspects are treated in the following subsections: the equations of motion; discretization and linearization; boundary conditions; and solution procedures. Treatment is succinct and focuses on the numerical approaches currently used by ESP-r's CFD model and those most relevant to the current work. The reader should refer to a basic CFD text (e.g. Patankar 1980; Versteeg and Malalasekera 1995) for a more comprehensive and detailed treatise of these topics. Awbi (1991), Whittle (1986), and Jones and Whittle (1992) provide additional information related to the specific problem of room air flow and heat transfer modelling.

3.2.1 Equations of motion

Both mechanical and buoyant forces can be significant drivers of room air motion. Mechanical forces are generally caused by fans or by wind entering through openings, while buoyant forces can result from heat sources within the room (radiators, occupants, office equipment, etc.) or from surface-air temperature differences. Room air flow can be considered incompressible as velocities tend to be low, in the order of metres or centimetres per second (air is considered incompressible at Mach numbers less than 0.3, about 100 m/s). Air, like many common fluids such as water, is newtonian (newtonian fluids display a linear relationship between shear and strain rate). Given this problem description, the following set of differential equations, which express the fundamental physical laws of the conservation of momentum and the conservation of mass (continuity), can be written to describe room air flow. These are presented in the common Navier-Stokes formulation (see Schlichting 1968) and in three-dimensional Cartesian coordinates.

conservation of momentum in x-direction

$$\frac{\partial}{\partial t}(\rho u)+\frac{\partial}{\partial x}(\rho uu)+\frac{\partial}{\partial y}(\rho vu)+\frac{\partial}{\partial z}(\rho wu)=-\frac{\partial P}{\partial x}+\frac{\partial}{\partial x_j}\left[\mu\left(\frac{\partial u}{\partial x_j}+\frac{\partial u_j}{\partial x}\right)\right] \tag{3.1}$$

conservation of momentum in y-direction

$$\frac{\partial}{\partial t}(\rho v)+\frac{\partial}{\partial x}(\rho uv)+\frac{\partial}{\partial y}(\rho vv)+\frac{\partial}{\partial z}(\rho wv)=-\frac{\partial P}{\partial y}+\frac{\partial}{\partial x_j}\left[\mu\left(\frac{\partial v}{\partial x_j}+\frac{\partial u_j}{\partial y}\right)\right] \tag{3.2}$$

conservation of momentum in z-direction

$$\frac{\partial}{\partial t}(\rho w)+\frac{\partial}{\partial x}(\rho uw)+\frac{\partial}{\partial y}(\rho vw)+\frac{\partial}{\partial z}(\rho ww) \tag{3.3}$$

$$=-\frac{\partial P}{\partial z}+\frac{\partial}{\partial x_j}\left[\mu\left(\frac{\partial w}{\partial x_j}+\frac{\partial u_j}{\partial z}\right)\right]-\rho g\beta(T_\infty-T)$$

continuity

$$\frac{\partial}{\partial x}(\rho u)+\frac{\partial}{\partial y}(\rho v)+\frac{\partial}{\partial z}(\rho w)=0 \tag{3.4}$$

The z-axis of the Cartesian coordinate system is aligned in the vertical direction (illustrated in Figure 3.1). u, v, and w are the velocity components in the x, y, and z directions, respectively $\{m/s\}$. ρ is the density $\{kg/m^3\}$, μ the viscosity $\{Pa\cdot s\}$, and β the thermal expansion coefficient of air $\{K^{-1}\}$. t is time $\{s\}$, P is pressure $\{Pa\}$, and T is temperature $\{^oC\}$.

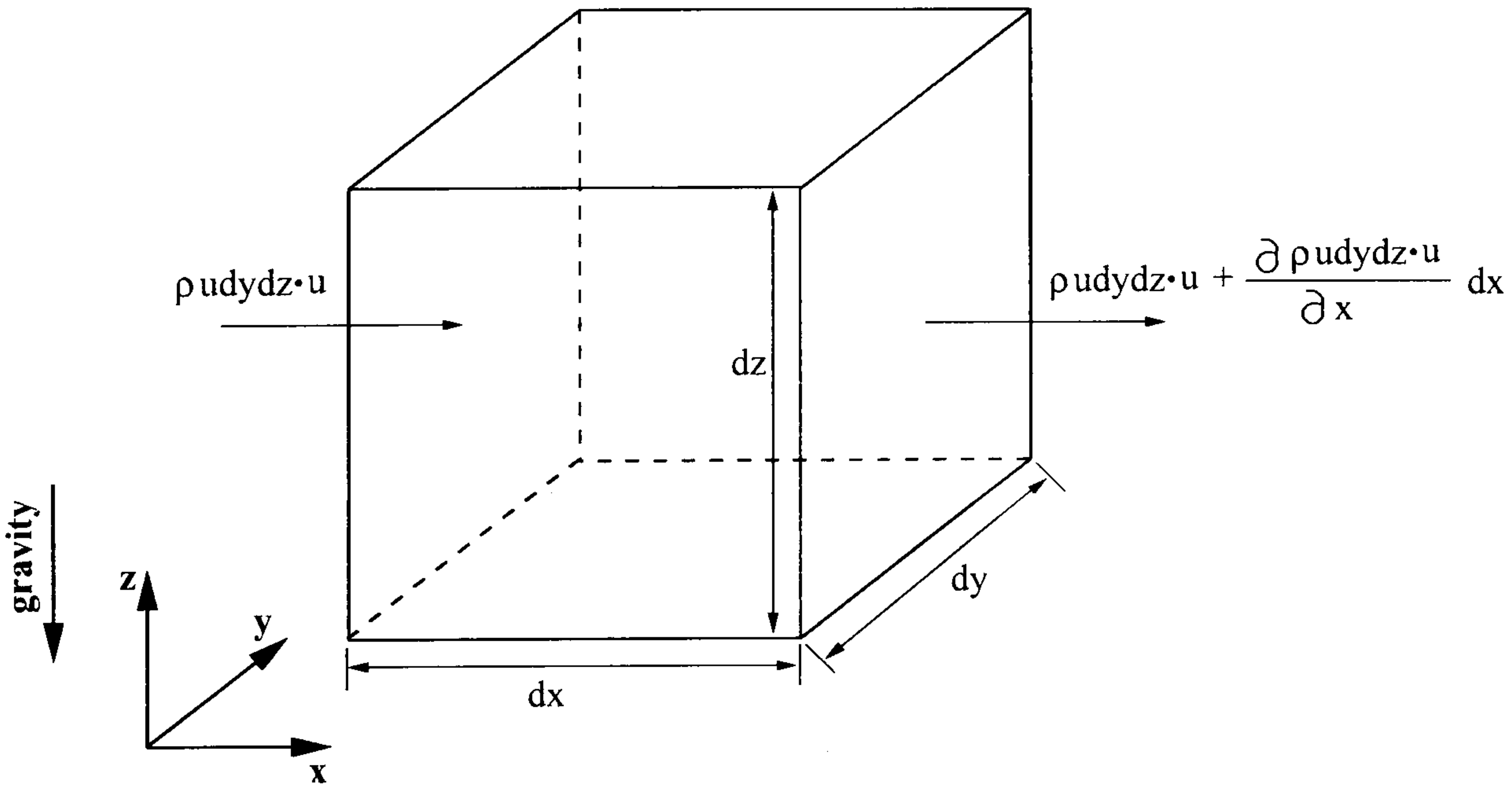

Figure 3.1: Control volume and coordinate system

The dependent variable in each momentum equation is a velocity component. For example, u is the dependent variable in the x-momentum equation. Consequently, each momentum equation can be thought of as a balance of the forces that affect a single velocity component. The meaning of the individual terms is demonstrated by considering an arbitrary control volume of the fluid (see Figure 3.1) while examining the x-momentum equation (3.1). The first term $[\partial(\rho u)/\partial t]$ represents the rate of change of x-direction momentum with respect to time[8]. This transient term can be thought of as the rate of accumulation of momentum within the control volume.

The second term $[\partial(\rho uu)/\partial x]$ represents the net outflow of x-direction momentum from the control volume for flow crossing the faces perpendicular to the x-axis, and is derived as follows. The inflow of x-direction momentum at the left face of the control volume (see Figure 3.1) is equal to the mass flow rate through the face ($\rho u A_x = \rho u dydz$) multiplied by the x-direction velocity:

$$momentum_{left} = \rho udydz \cdot u$$

When the control volume is sufficiently small, the outflow of x-direction momentum at the right face can be approximated by the first two terms of a Taylor series expansion:

$$momentum_{right} \approx momentum_{left} + [\partial(momentum_{left})/\partial x]dx$$

$$= \rho udydz \cdot u + [\partial(\rho udydz \cdot u)/\partial x]dx$$

The net outflow of momentum is the difference between the outflow at the right face and at the inflow at the left face. When divided by the control volume's volume ($dxdydz$) this leads to the second term in equation 3.1.

The third term $[\partial(\rho vu)/\partial y]$ is similar in construct, it also representing the net transfer of x-direction momentum out of the control volume; however, in this case it is for flow crossing the faces perpendicular to the y-axis. Similarly, the fourth term $[\partial(\rho wu)/\partial z]$ represents the net outlfow of x-direction momentum for flow crossing the faces perpendicular to the z-axis. These three *net outflow of x-direction momentum* terms represent the transport of momentum caused by *bulk* fluid motion crossing the faces of the control volume, a phenomenon known as *advection* (often called *convection*).

Moving to the right side of the equation, the $[-\partial P/\partial x]$ term represents the net pressure force acting in the positive x-direction. The last term, shown in compact tensor notation[9], represents the net viscous force acting in the positive x-direction. Although known as a force, this term really represents the transport of momentum caused by *random molecular* motion across the faces of the control volume, a phenomenon known as *diffusion*.

The momentum equations in the other two directions (3.2 and 3.3) are of identical construct, but with the addition of one term to the z-momentum equation. This $[-\rho g\beta(T_\infty - T)]$ represents the

---

[8] As the equation is normalized by volume, the terms are given in units of force per volume.

[9] $\frac{\partial}{\partial x_j}\left[\mu\left(\frac{\partial u}{\partial x_j}+\frac{\partial u_j}{\partial x}\right)\right]$ expands to $\frac{\partial}{\partial x}\left[\mu\left(\frac{\partial u}{\partial x}+\frac{\partial u}{\partial x}\right)\right]+\frac{\partial}{\partial y}\left[\mu\left(\frac{\partial u}{\partial y}+\frac{\partial v}{\partial x}\right)\right]+\frac{\partial}{\partial z}\left[\mu\left(\frac{\partial u}{\partial z}+\frac{\partial w}{\partial x}\right)\right]$

gravitational force—caused by density gradients in the fluid—acting in the positive z-direction and is expressed here using the Boussinesq approximation (Incropera and DeWitt 1985).

The continuity equation (3.4) simply states that the net accumulation of mass in the control volume must be equal to zero (i.e. mass is conserved). $[\partial(\rho u)/\partial x]$ is the net mass flow[10] leaving the control volume for flow crossing the faces perpendicular to the x-axis. The other terms represent the flows in the other two Cartesian directions.

Equations 3.1 to 3.4 characterize the fluid flow, but not the heat transfer. Although temperature appears in equation 3.3, it is an independent variable. An additional equation, representing another fundamental physical law—the conservation of energy—is introduced to characterize the heat transfer and to predict the temperature distribution.

conservation of energy

$$\frac{\partial}{\partial t}(\rho c_p T) + \frac{\partial}{\partial x}(\rho c_p u T) + \frac{\partial}{\partial y}(\rho c_p v T) + \frac{\partial}{\partial z}(\rho c_p w T) = \frac{\partial}{\partial x_j}\left(k\frac{\partial T}{\partial x_j}\right) + q''' \qquad (3.5)$$

where c_p is the specific heat $\{J/kgK\}$, and k the conductivity $\{W/mK\}$ of air.

The dependent variable in this case is temperature. Consequently, the conservation of energy equation can be thought of as a balance of the energy flows that affect the temperature. Considering again the control volume in Figure 3.1, the first term $[\partial(\rho c_p T)/\partial t]$ represents the rate of change of energy with respect to time[11]: how quickly energy is stored within the control volume. The second term $[\partial(\rho c_p u T)/\partial x]$ is the net convection of energy leaving the control volume: a result of bulk flow crossing the faces perpendicular to the x-axis. Likewise, the third and fourth terms $[\partial(\rho c_p v T)/\partial y$ and $\partial(\rho c_p w T)/\partial z]$ represent the net convection of energy leaving the control volume as a result of bulk flow crossing the faces perpendicular to the y and z axes.

Tensor notation[12] is used to express the first term on the right side of the equation $[\partial(k(\partial T/\partial x_j))/\partial x_j]$. This represents the net diffusion of energy into the control volume, that is the net transport of energy caused by random molecular motion. The last term (q''') is the generation of heat within the control volume, perhaps due to a chemical reaction or due to a heat source located within the room. As can be seen, the energy equation has a structural similarity with the momentum equations. Each contains transient, convection, diffusion, and source terms.

Equations 3.1 to 3.5 fully characterize the transient fluid motion and heat transfer throughout the air volume of a room. The problem is said to be closed, there being five unknowns (temperature, pressure, and three velocity components) in the five equations. It is important to note that the field

---

[10] This equation is also normalized by volume, so the terms are given in units of mass flow per volume.

[11] This equation is been normalized by volume, so the terms are given in units of energy per volume.

[12] $\frac{\partial}{\partial x_j}\left(k\frac{\partial T}{\partial x_j}\right)$ expands to $\frac{\partial}{\partial x}\left(k\frac{\partial T}{\partial x}\right)+\frac{\partial}{\partial y}\left(k\frac{\partial T}{\partial y}\right)+\frac{\partial}{\partial z}\left(k\frac{\partial T}{\partial z}\right)$

variables (pressure, velocity, temperature) in these equations represent *instantaneous* quantities. Because most flows of practical interest experience chaotic high-frequency velocity fluctuations—a state known as *turbulence*—it is usually impossible to solve for the instantaneous values. Instead, turbulence modelling techniques are used to simplify the solution process, a topic that will be treated in detail in Sections 3.5 and 3.6. However, the objectives of this section are best achieved with the instantaneous form of the equations of motion.

3.2.2 Discretization and linearization

The partial differential equations (3.1 to 3.5) given in the previous subsection fully describe room air flow and heat transfer. However, the equations are highly non-linear and strongly coupled: each momentum equation contains all three velocity components; temperature appears in the *z*-momentum equation; and the energy equation contains the velocity components. Consequently, they can be solved analytically for only the simplest of problems.

Numerical discretization techniques are introduced to render the problem to a solveable level. In essence, this involves approximating the governing differential equations by a system of algebraic relations. With the *finite volume* method (other approaches are possible), this is achieved by subdividing the room into finite volumes using a gridding system. Rather than solving over the continuum, temperatures, pressures, and velocities are predicted only at discrete points, these located at the centres of the finite volumes. This is illustrated in Figure 3.2 for a Cartesian coordinate system (other coordinate systems are possible). Note that usually the velocity components are solved at different points than the scalar quantities (temperature and pressure). This "staggered" grid approach overcomes difficulties that arise in linking the pressure and velocity solutions and will be discussed in a later section.

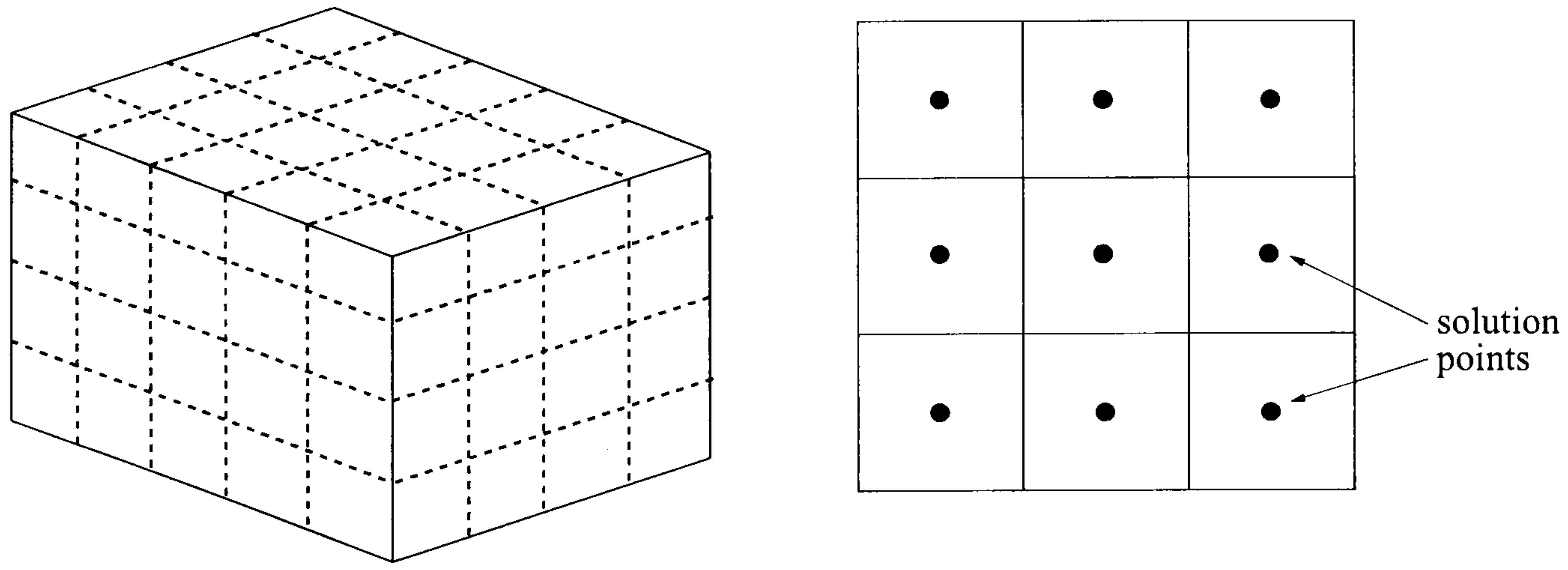

Figure 3.2: Finite-volume discretization, three- and two-dimensional views

The individual terms of the conservation equations (transient, convection, diffusion, and source) are approximated by algebraic relations in terms of quantities at these discrete points. This is demonstrated by examining the energy equation's (3.5) y-direction diffusion term $[\partial(k(\partial T/\partial y))/\partial y]$. Figure 3.3 illustrates an arbitrary finite volume and its neighbours (in two dimensions). The solution points, located at the centres of the finite volumes, are indicated in upper-case letters: P is the point representing the finite volume under consideration, N the point located above P in the figure, E is the point to the right. Lower-case letters are used to denote conditions at the faces of the finite volume (variables are not solved at these points, but they are necessary in this derivation). The diffusion term, representing the net influx of energy through the faces perpendicular to the y-direction, is first integrated over the finite volume,

$$\int_{\Delta V} \frac{\partial}{\partial y}\left(k\frac{\partial T}{\partial y}\right) dV = \int_x \int_y \int_z \frac{\partial}{\partial y}\left(k\frac{\partial T}{\partial y}\right) dz dy dx = [dxdz]\cdot\left[\left(k\frac{\partial T}{\partial y}\right)_n - \left(k\frac{\partial T}{\partial y}\right)_s\right] \tag{3.6}$$

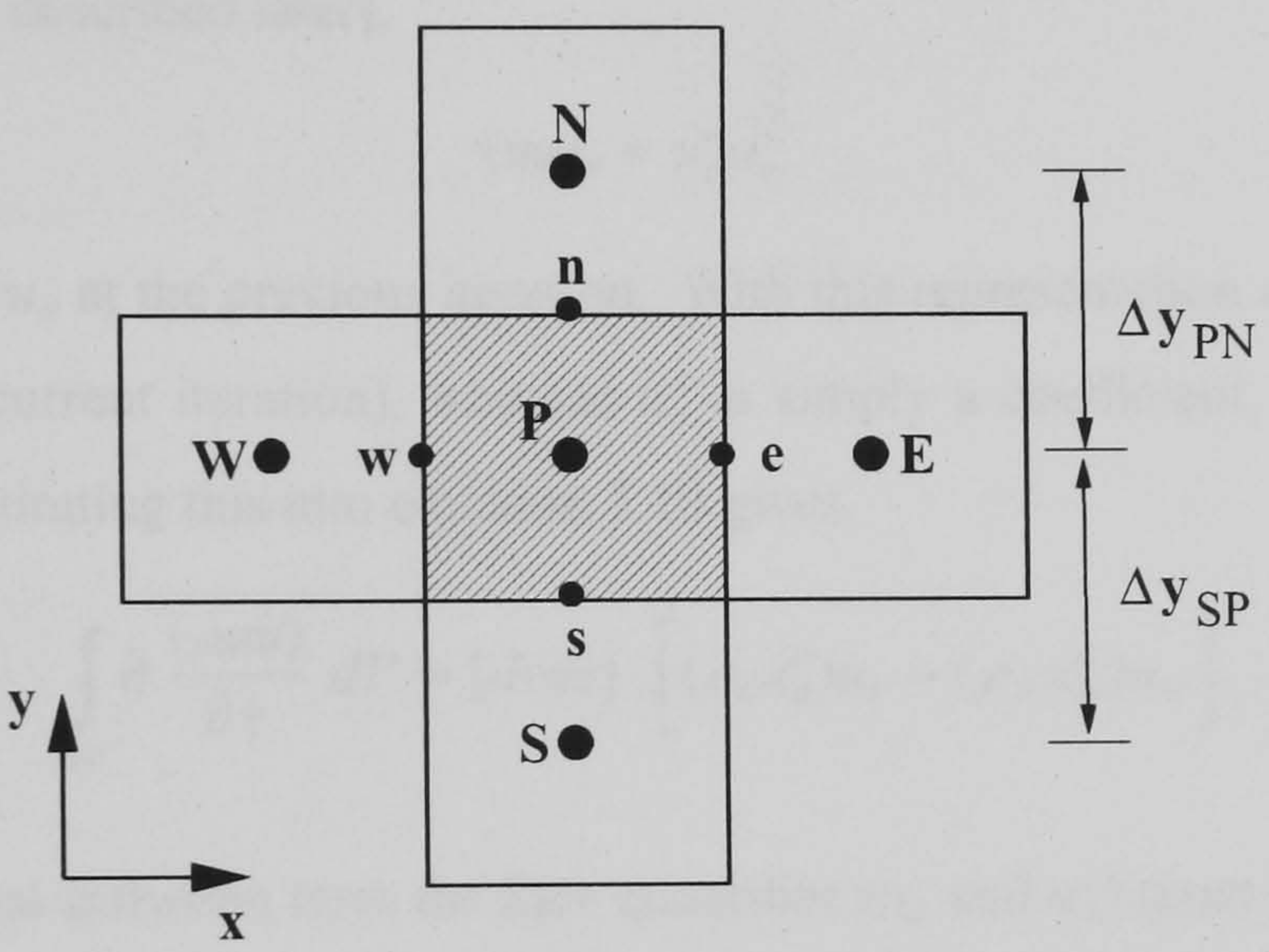

Figure 3.3: A finite volume and its neighbours

A piecewise-linear variation of T in y is assumed in order to evaluate the temperature profiles at the s and n faces. This assumes that T varies linearly between adjacent points (other profile assumptions are possible),

$$\left(k\frac{\partial T}{\partial y}\right)_n \approx \frac{k_n}{\Delta y_{PN}}\cdot(T_N - T_P) \tag{3.7}$$

$$\left(k\frac{\partial T}{\partial y}\right)_s \approx \frac{k_s}{\Delta y_{SP}}\cdot(T_P - T_S) \tag{3.8}$$

Substituting equations 3.7 and 3.8 into 3.6 approximates the integral of the heat diffusion term using temperatures at the discrete points,

$$\int_{\Delta V} \frac{\partial}{\partial y}\left(k\frac{\partial T}{\partial y}\right) dV \approx [dxdz]\cdot\left[\left\{\frac{k_n}{\Delta y_{PN}}\cdot(T_N - T_P)\right\} - \left\{\frac{k_s}{\Delta y_{SP}}\cdot(T_P - T_S)\right\}\right] \tag{3.9}$$

$$= a_N T_N + a_S T_S - a_P T_P$$

where $a_N = k_n dxdz/\Delta y_{PN}$, $a_S = k_s dxdz/\Delta y_{SP}$, and $a_P = a_N + a_S$. The second derivative term has been approximated by a simple algebraic summation, one whose coefficients can be easily calculated.

A similar approach is used to linearize the terms which contain two solution variables. This is demonstrated by considering a convection term $[\partial(\rho uu)/\partial x]$ from the x-momentum equation (3.1). This term represents the net outflow of x-direction momentum for flow crossing the faces perpendicular to the x-axis, and contains the u-velocity component raised to the second order. The term is first integrated over the finite volume,

$$\int_{\Delta V} \partial \frac{(\rho uu)}{\partial x}\, dV = \int_x \int_y \int_z \partial \frac{(\rho uu)}{\partial x}\, dzdydx = [dydz] \cdot \left[(\rho uu)_e - (\rho uu)_w\right] \tag{3.10}$$

The second order is then reduced to a product of u at two subsequent solver iterations (the iterative solution approach is described later),

$$(uu)_e \approx u_e^o u_e \tag{3.11}$$

where u_e^o is the value of u_e at the previous iteration. With this representation u_e is the dependent variable (unknown for the current iteration), whereas u_e^o is simply a coefficient, having been solved the previous iteration. Substituting this into equation 3.10 gives,

$$\int_{\Delta V} \partial \frac{(\rho uu)}{\partial x}\, dV \approx [dydz] \cdot \left[(\rho_e u_e^o)u_e - (\rho_w u_w^o)u_w\right] \tag{3.12}$$

As with the thermal diffusion term the face quantities (u_e and u_e^o) must be expressed in terms of values at the discrete points that are solved (P, E, N, and so on). u_e^o is normally assumed to vary in a piecewise linear manner, being calculated as a geometrically weighted average of u_E^o and u_P^o. u_e could be evaluated in a similar manner (this is called central differencing), but this is rarely done in practice as unrealistic solutions can result for all but the lowest velocity flows. Rather, a more complex differencing scheme (many are available, such as upwind, exponential, hybrid, and power-law) is usually employed. Regardless of the choice of differencing scheme, equation 3.12 reduces to the same form as equation 3.9.

$$\int_{\Delta V} \partial \frac{(\rho uu)}{\partial x}\, dV \approx a_E u_E + a_W u_W - a_P u_P \tag{3.13}$$

Using these discretization and linearization techniques, each term of the governing equations can be approximated by a simple algebraic summation operating on the solution variables at the discrete points. This leads to the following general relation, which is formed for each solution point, for each governing equation,

$$a_P\phi_P = a_E\phi_E + a_W\phi_W + a_N\phi_N + a_S\phi_S + a_H\phi_H + a_L\phi_L + b \tag{3.14}$$

$$= \sum a_{nb}\phi_{nb} + b$$

where ϕ is the relevant dependent variable. P is the point under consideration, and E, W, N, S, H, and L are the neighbouring points. b results from source terms and from terms which do not include the dependent variable (e.g. the $[-\partial P/\partial x]$ term in the x-momentum equation).

Therefore, discretization and linearization reduce the complex non-linear governing differential equations into a set of simple algebraic relations.

3.2.3 Boundary conditions

The governing equations (3.1 to 3.5) characterize the transient fluid motion and heat transfer throughout the air volume of the room's computational domain. When boundary conditions are applied to define the domain boundary (e.g. wall surfaces, diffusers), these fully describe the distribution of air flow and heat transfer within the room. Essentially, the boundary conditions impose the influence of the domain's boundary upon the equations of motion.

The computational domain is normally defined to encompass a single room's air volume. This is illustrated schematically in Figure 3.4. The domain boundary is placed at the internal surfaces of the fabric components (walls, windows, etc.), thus excluding the solid masses from the computational domain. As a result, the boundary conditions must accurately account for the effect of the fabric components upon the room air, otherwise predictions of air flow and heat transfer throughout the room will suffer. Similarly, the domain boundary is placed at the outlet of the supply air diffuser, and at the inlet to the extract. Consequently, air flow upstream of the diffuser and downstream of the extract is excluded from the computational domain. The boundary conditions, therefore, must account for the impact that flow within the ductwork has upon the room air.

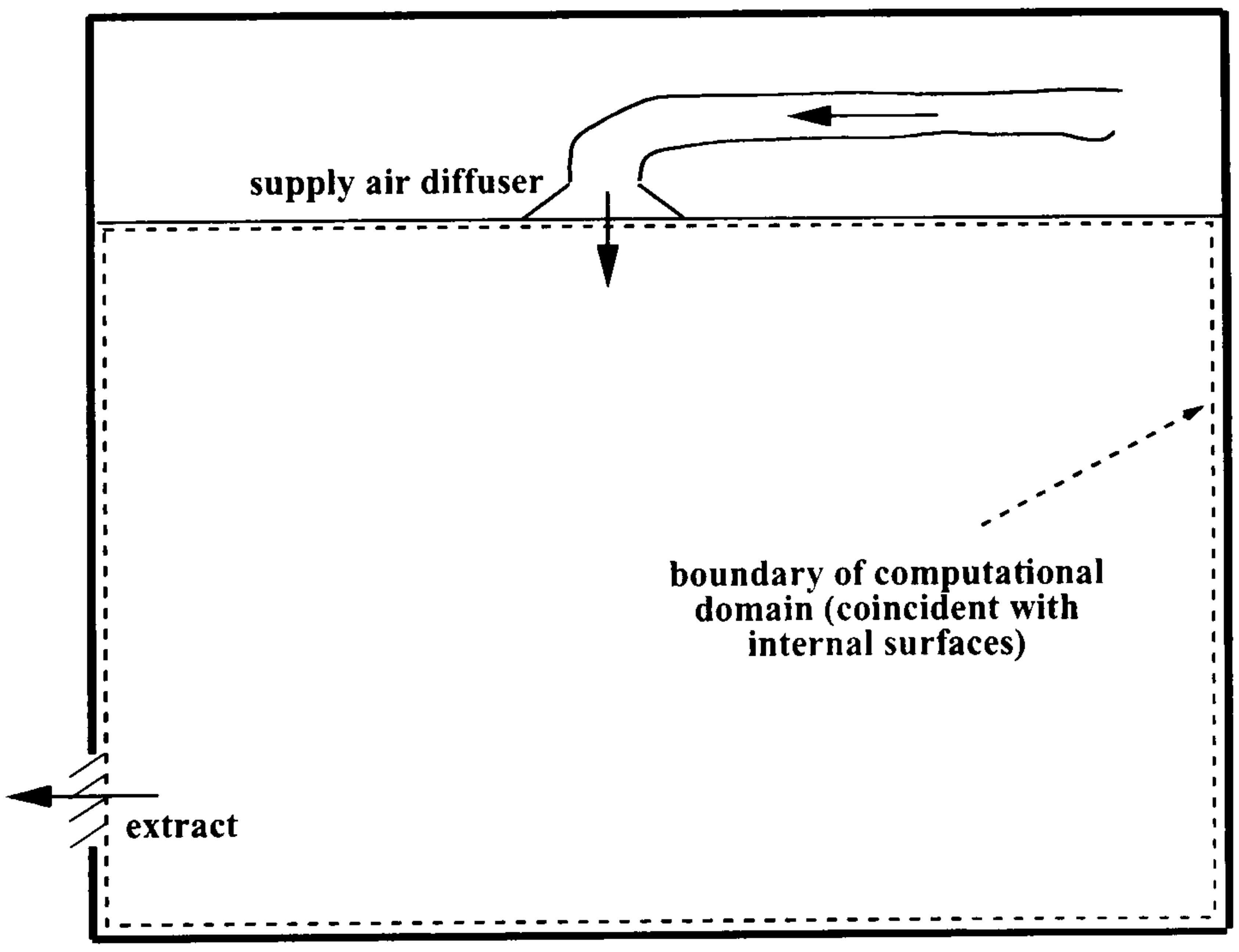

Figure 3.4: Computational domain

The location of the computational domain described above is typical, but other treatments are possible. For example, a section of ductwork upstream of the diffuser could be included if characterizing flow within the duct were felt to be significant in predicting the room air flow. Another approach is to excluded a region of room air surrounding the diffuser (the so-called box method); rather than modelling the jet emanating from the diffuser, the influence of the supply air is imposed by applying boundary conditions at planes within the room. Another possibility is to include the fabric components within the computational domain, this leading to a conjugate heat transfer problem.

Some common boundary condition treatments for solid surfaces, diffusers, and extracts are presented in this subsection. The methods used to absorb the boundary conditions into the algebraic form of the governing equations are also presented. The computational grid shown in Figure 3.5 is used in this presentation. This grid is "staggered", the velocity components being represented at different discrete points than the scalar quantities. An *(i,j)* indexing system is used to identify the discrete points, where *i* represents the grid number in the *x*-direction and *j* represents the grid number in the *y*-direction. It is common practice to number the first solution grids as 2, 1 being reserved for "fictitious" cells located outside the solution domain. A consequence of the staggered grid is that for a given *i* and *j*, *T(i,j)*, *u(i,j)*, and *v(i,j)* are located at different points in space.

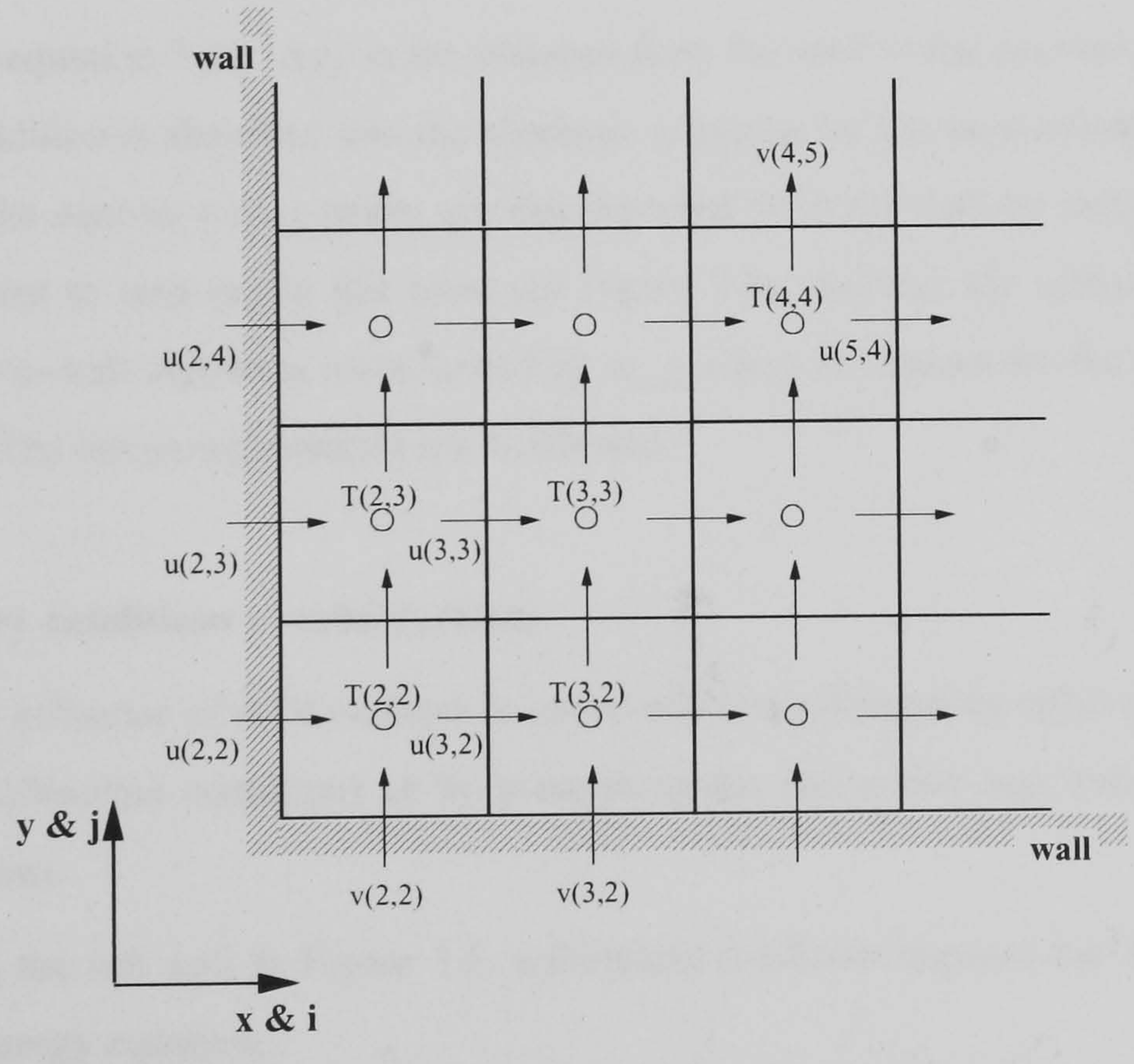

Figure 3.5: Two-dimensional staggered grid

Air flow boundary conditions at solid surfaces

The no-slip condition is applied for the velocity components at solid surfaces,

$$u = v = w = 0 \tag{3.15}$$

This is easily represented in the algebraic form of the momentum equations for the velocity components normal to the solid surfaces, as demonstrated by considering the left wall in Figure 3.5. Recall that the x-momentum equation is approximated by forming an algebraic relation (in the form of equation 3.14) for each u solution point. The no-slip condition is applied simply by forcing $u(2,j)$ to zero over the range of j covering the solid surface. As such, there is no need to solve the algebraic relations for the u-points along the left wall. The equations for the next-to-wall u-points (i=3) and all other u-points are unaffected by the application of this boundary condition.

For the velocity components parallel to the surfaces, the no-slip condition manifests itself in the diffusion term representing wall shear. Considering the x-momentum equation along the lower wall, the wall shear is given by,

$$F_{wall} = A_{wall} \cdot \tau_{wall} = A_{wall} \cdot \mu\left(\frac{\partial u}{\partial y}\right)_{wall} \tag{3.16}$$

This is approximated by assuming a piecewise-linear variation of u in y,

$$A_{wall} \cdot \mu\left(\frac{\partial u}{\partial y}\right)_{wall} \approx A_{wall} \cdot \mu\left(\frac{u(i,2) - u|_{wall}}{\Delta y_P}\right) \tag{3.17}$$

$$= \frac{A_{wall} \cdot \mu \cdot u(i,2)}{\Delta y_P}$$

since $u|_{wall} = 0$ by equation 3.15. Δy_P is the distance from the wall to the next-to-wall u-points $\{m\}$. This boundary condition is absorbed into the algebraic relations for the next-to-wall u-points (j=2) in two steps. First, the next-to-wall u-points are disconnected from the wall by setting the appropriate neighbour coefficient to zero (a_S in this case; see Figure 3.3). Second, the self-coupling coefficient (a_P) for each next-to-wall u-point is incremented by $A_{wall}\mu/\Delta y_P$ to account for the retarding influence of the wall shear. The remaining u-points are unaffected.

Thermal boundary conditions at solid surfaces

The thermal influence of solid surfaces is commonly characterized by either prescribing the surface temperature (Dirichlet condition) or by prescribing the convective heat transfer at the surface (Neumann condition).

Considering the left wall in Figure 3.5, a Dirichlet condition imposes the following boundary condition on the energy equation,

$$q_{wall} = -kA_{wall}\left.\frac{\partial T}{\partial x}\right|_{wall} \tag{3.18}$$

where q_{wall} is the heat transfer from the wall to the air. By assuming a piecewise-linear variation of T in x, this can be represented by,

$$-kA_{wall}\left.\frac{\partial T}{\partial x}\right|_{wall} \approx -kA_{wall}\frac{T(2,j)-T_{wall}}{\Delta x_P} \tag{3.19}$$

where Δx_P is the distance from the wall to the next-to-wall T-points and T_{wall} is the (known) wall surface temperature. This boundary condition is absorbed into the algebraic relations for the next-to-wall grid points (i=2) in three steps. First, the points are disconnected from the wall by setting the neighbour coefficient to zero (a_W in this case). The self-coupling coefficients (a_P) are incremented by $kA_{wall}/\Delta x_P$, and finally the source terms (b) are incremented by $kA_{wall}T_{wall}/\Delta x_P$. Again, the relations for all other grid points are unaffected.

The application of a Neumann condition is trivial, q_{wall} being known. Considering the left wall once more, the Neumann condition is absorbed by disconnecting the next-to-wall T-points from the wall by setting the a_W coefficients to zero. The b coefficients for the next-to-wall points are then incremented by q_{wall}. Once again, the relations for all other grid points are unaffected.

Air flow boundary conditions at diffusers and extracts

Supply-air diffusers are normally treated with prescribed-velocity boundary conditions. These are imposed by setting the velocity components for the solution points at the diffuser to prescribed values. For a diffuser located in the lower wall in Figure 3.5 this takes the form,

$$v|_{wall} = v_{diffuser} \tag{3.20}$$

where $v_{diffuser}$ is the prescribed value. This is imposed simply be setting v(i,2) to $v_{diffuser}$. In other words, there is no need to solve the algebraic relations of the y-momentum equations for the v-points located at the diffuser. The algebraic relations for the remaining v-points are unaffected.

Air extracts are often modelled with the zero-gradient boundary condition, this assuming that conditions are not changing in the flow direction (i.e. a fully developed flow). This takes the form of,

$$\left.\frac{\partial v}{\partial y}\right|_{wall} = 0 \tag{3.21}$$

for an extract on the lower wall in Figure 3.5. This is absorbed into the y-momentum algebraic relations by making v at the diffuser equal to the upstream value,

$$v(i,2) = v(i,3) \tag{3.22}$$

Once again, the algebraic relations for the remaining v-points are unaffected.

Many other boundary conditions are possible. However, all are imposed using the techniques demonstrated here. First, the boundary condition is expressed in terms of quantities at the discrete solution points. Second, the boundary condition is absorbed by modifying the coefficients of the algebraic relations for the wall or next-to-wall solution points.

Prior to applying boundary conditions an algebraic relation in the form of equation 3.14 existed for each solution point, for each governing equation. The application of boundary conditions does not alter this situation, but rather only modifies some of the coefficients of the algebraic relations. The resulting set of equations fully characterize the room air flow and heat transfer and include the effect of the domain's boundary upon the room air.

The above development was performed with the instantaneous form of the equations of motion. This implies a very fine discretization grid which results in the next-to-wall grid points being located within the laminar region of the solid-surface boundary layers. Consequently, the boundary conditions considered here are rather simple in form. More complex relations result when turbulence modelling techniques are employed (in particular for equations 3.17 and 3.19), as will be shown in Section 3.6. However, the principles presented here for absorbing the boundary conditions into the equations of motion still apply.

3.2.4 Solution procedure

Sequential solution approach

Even though the governing equations (3.1 to 3.5) contain five unknowns (u, v, w, T, and P) in five equations, further manipulation is required before they can be solved. There is an equation for solving each velocity component (x-momentum for u, etc.) and for solving temperature (the energy equation). However, there is no equation for solving pressure. Pressure appears in every momentum equation, but not in the remaining equation, continuity. An approach is required to deal with this pressure-velocity linkage and the lack of an equation for solving pressure.

The SIMPLE (*S*emi-*I*mplicit *M*ethod for *P*ressure-*L*inked *E*quations) family of pressure-correction solution strategies was devised to overcome these problems. Essentially, these are guess-and-correct iterative procedures for calculating the pressure field. The pressure-velocity linkage is dealt with by guessing a pressure field (called P^*) which is then used to solve the momentum equations. This yields estimates of the velocity field (u^*, v^*, and w^*). As the guessed pressure field will inevitably contain inaccuracies, a pressure-correction term (P') is introduced. It is the difference between the correct pressure whose solution is sought (P) and the guessed pressure, and is evaluated at each solution point,

$$P' = P - P^* \tag{3.23}$$

Since the velocity field is calculated using guessed pressures, velocity-correction terms also arise, e.g.

$$u' = u - u^* \tag{3.24}$$

Next, the x-momentum equation expressed in guessed quantities (P^*, u^*, etc.) is subtracted from the x-momentum equation expressed in correct quantities (P, u, etc.). When assumptions are applied to eliminate insignificant terms a relation between the velocity and pressure corrections results,

$$u' = \frac{A_e}{a_P - \sum a_{nb}} \cdot (P'_w - P'_e) \tag{3.25}$$

The a coefficients are those generated for the x-momentum equation. Similar relations exist for v' and w'. Note that the SIMPLEC formulation is shown here. Other assumptions lead to different SIMPLE formulations.

Substituting the velocity-pressure correction relations (3.25 and those for v' and w') into the continuity equation (3.4) eliminates the velocity variables, resulting in a balance between neighbouring P' points. The discretized algebraic relations for this P' balance have the same general form found for the other governing equations (3.14),

$$a_P P'_P = \sum a_{nb} P'_{nb} + b' \tag{3.26}$$

The P' coefficients are derived from the momentum-equations' coefficients, thus tightly linking velocity and pressure.

Replacing the velocity form of the continuity equation (3.4) with equation 3.26 thus provides pressure with its own equation. The velocity-pressure linkage necessitates a sequential solution process: A pressure field is guessed and the momentum equations solved. P' is calculated using equation 3.26, and the velocity and pressure estimates updated using equations 3.23 and 3.24. The energy equation is then solved to complete the iteration loop. The entire process is repeated—using the previous iteration's corrected pressures and velocities as the current iteration's guesses—until the system of equations is driven to convergence. This is illustrated in Figure 3.6.

Equation solver

The velocity-pressure procedure described above generates five sets of (identically structured) linear algebraic equations each iteration. An efficient equation solver is required, as it will be called upon thousands of times for even the simplest of problems. Although direct solvers are a possibility, iteration solution approaches are normally employed due to their efficiency at dealing with large sparse matrices. Of these, the tri-diagonal matrix algorithm (TDMA) is most often employed, although others, such as the conjugate gradient method, are increasingly used.

TDMA employs a line-by-line calculation procedure, which has two basic steps: forward elimination and backwards substitution. Take, for example, a west-east line of solution points for given y and z locations. The neighbours in the y and z directions are treated as known (values are taken from the previous iteration) since these points are outside the sphere of the line solver. Starting at the westmost point and traversing east, a process of substitution is used to disconnect each point from its west neighbour. The modified equation set at the end of this forward elimination step, therefore, connects each point to only a single unknown point, the neighbour to the east. The solution for the eastmost

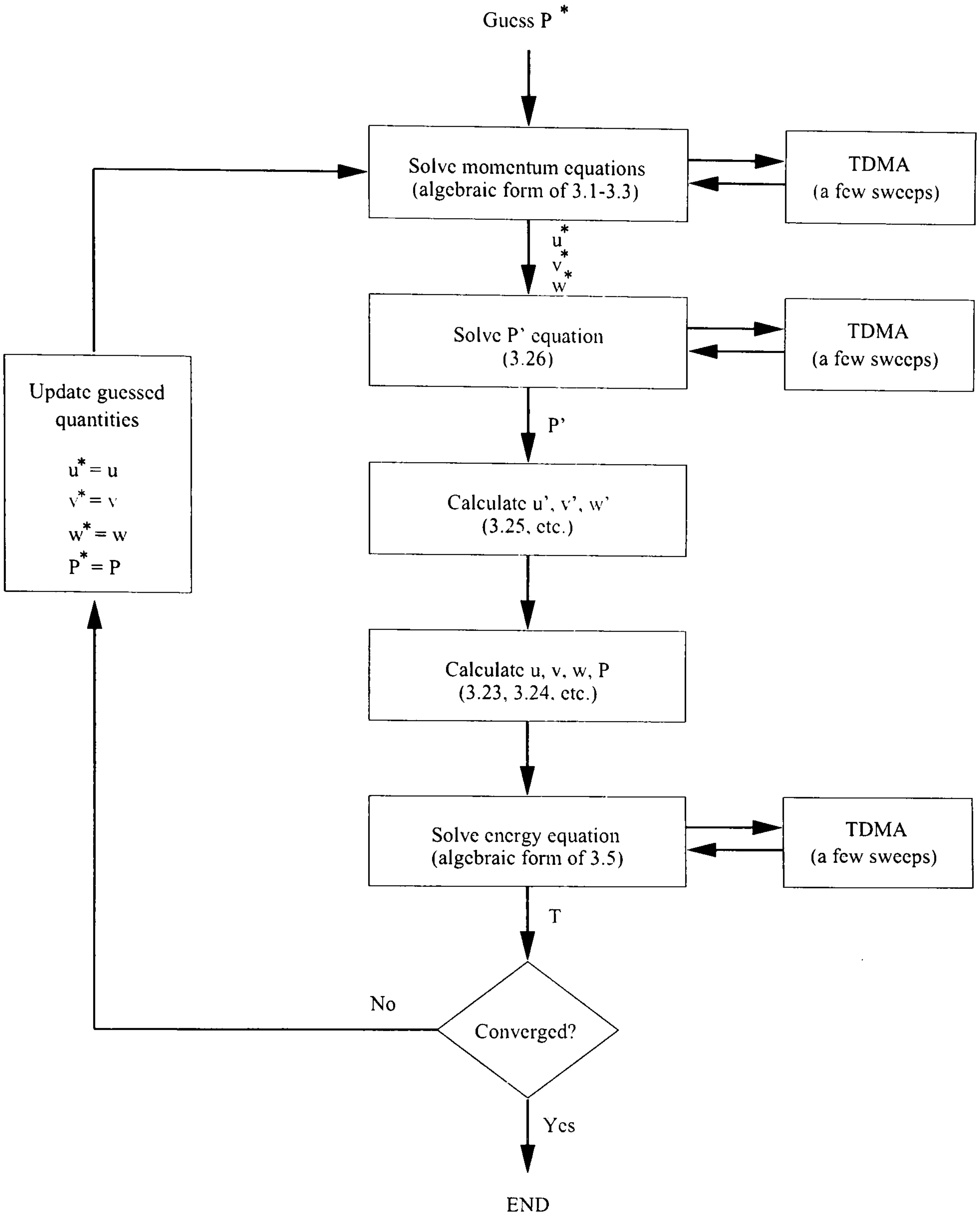

Figure 3.6: Sequential and iterative solution process

point is easily attained (since it is only connected to the known boundary), and the traversing direction reversed. The backwards substitution step proceeds from east to west, a solution being attained for each point by simply substituting the newly calculated east point value into the modified equation set.

A sweeping procedure is employed as only a single line can be processed at a time. The calculation domain is swept plane-by-plane, then line-by-line within each plane, until the entire domain has been traversed. Alternate sweep directions are usually employed to improve convergence. For example, south-to-north plane sweeping with low-to-high line sweeping followed by west-to-east plane sweeps with low-to-high line sweeps.

The TDMA iterative solution procedure is employed within the pressure-velocity iterative loop. As the coefficients generated each pressure-velocity iteration are themselves converging, it is futile to drive the TDMA solver to convergence each invocation. Consequently, the TDMA procedure is normally employed for a only a few sweeps at a time. This is illustrated in Figure 3.6

Convergence

The iterative solution procedure continues until a converged state is achieved, that is, until further iteration produces no significant change in the solution variables. Various criteria are used to judge whether a solution has converged. A critical variable could be tracked (e.g., a surface heat flux or velocity at a particular location in the room) and the solution halted when the relative change between two successive iterations is sufficiently small.

A more common approach is to calculate the equation residual for each grid point, this gauging how well the discretized equation is satisfied by the current values of the solution variables,

$$R = \left|\sum a_{nb}\phi_{nb} + b - a_P\phi_P\right| \tag{3.27}$$

R will be zero if the discretized equation is perfectly satisfied at that grid point. When the maximum point value or the sum over the domain ($\sum R$) is less than some critical value, the solution can be considered converged.

Although coverage has been succinct, the pertinent aspects of CFD's conceptual basis and its numerical approaches have been described in this section. Many other approaches are possible, but the techniques reviewed here are generally used for room air flow and heat transfer simulation, and are those employed within ESP-r's CFD model.

3.3 Applications of CFD for Room Air Flow and Heat Transfer Prediction

CFD has been used to simulate air flow in and around buildings for a quarter century, and there has been a progression of activity in the past decade. For example, two IEA annexes (Annex 20, Lemaire et al 1993; Annex 26, Heiselberg et al 1998), two ASHRAE research projects (Baker et al 1992; Chen and Srebric 1999), and an entire issue of the journal *Building and Environment* (1989) have addressed the topic. This level of interest is explained by the potential benefits the technology offers building designers and analysts: CFD can be used to analyze wind forces and wind flow patterns, interior and exterior dispersion of pollutants, air infiltration, thermal boundary layer development over fabric surfaces, and thermal comfort.

Nielsen (1974) is credited with the first application, the two-dimensional modelling of a room with flow driven by a supply air diffuser. Predictions of the jet's decay were found to agree well with experimental measurements. Modelling was soon extended to three dimensions (e.g. Gosman et al 1980) and more complex building geometries (e.g. Broyd et al 1983). Positive results increased the confidence in CFD's ability to predict complex flows within buildings. The scope was then broadened to consider the effects and prediction of heat transfer (e.g. Chen and van der Kooi 1988), this introducing the complexities of buoyancy forces and highlighting the significance of accurately treating thermal boundary conditions.

By the 1990s CFD was being successfully applied within the building design process (e.g. Jones and Waters 1990). It has been used to predict thermal comfort and to compare the performance of alternate air distribution systems (e.g. Awbi et al 1992; Knappmiller and Kirkpatrick 1995). It has also proven to be a useful tool for analyzing the impact of diffuser and extract placement within rooms (e.g. Murakami et al 1989).

Recently there has been focus on specialized applications, such as the modelling of displacement (e.g. Nakamura et al 1996) and task ventilation (e.g. Loomans 1998), and the analysis of large spaces such as atria (e.g. Schild 1997; Heiselberg et al 1998). Even detailed factors which influence flow and pollutant dispersion—from furnishings (Nielsen et al 1998; Stankov et al 1999) to occupants (Murakami et al 1998), to moving buoyancy-inducing sun patches (Arnold et al 1998)—have been simulated.

There have been so many successful applications of CFD for room modelling that no attempt is made to enumerate them here—a good overview is provided by Whittle (1986), Nielsen (1989), Jones and Whittle (1992), and Emmerich (1997). One very interesting trend is revealed in this literature: the vast majority of the successful applications have been for predicting room *air flow*. Attempts to predict room *heat transfer*—in particular convective heat transfer at internal surfaces—have met with much less success. The crux of this dichotomy concerns the nature of building air flows and the modelling of turbulent motion, the subjects of the following two sections.

3.4 The Turbulent Nature of Room Air Flow

Chapter 1 raised some issues regarding CFD's suitability for predicting room air flow and heat transfer, and indicated how these could impede applicability of the conflated thermal and air flow modelling approach. In particular, the importance of accurately treating the near-wall regions was highlighted. These issues, related to the nature of room air flow, are expanded upon here.

As explained earlier, some form of model is normally employed to characterize turbulent velocity fluctuations. Numerous approaches exist, but the *standard* $k-\varepsilon$ *turbulence model* has enjoyed the greatest usage by far in the numerical simulation of room air flow and heat transfer. Its preponderance can be seen by reviewing the literature (e.g. Whittle 1986; Nielsen 1989; Jones and Whittle 1992; Chen and Jiang 1992; Lemaire et al 1993; Chen 1995). However, strictly speaking this model is only valid for fully-developed turbulence (notwithstanding near-wall regions for which adjustments are made to account for viscous effects). Consequently, the application of the standard $k-\varepsilon$ model implies a very important assumption: that the flow is fully turbulent or at least behaves like a fully turbulent flow.

But, in general, room air flows are not fully turbulent. Baker et al (1994a) characterize room air motion as typically turbulent, although only weakly so. Baker et al (1994b) state that most room air flows are at least locally turbulent, but flows away from HVAC supply systems and obstructions with edges tend to be subtly turbulent. According to Chen and Jiang (1992), room air flows may be laminar unsteady, locally artificially induced turbulent, transitional, or fully turbulent. Although air flow at diffuser outlets tends to be turbulent, measurements indicate that the flow in the main body of ventilated rooms may be transitional (Jones and Whittle 1992). A mix of flow regimes will be found adjacent to most heated or cooled surfaces, such as radiators and windows.

This raises questions regarding the applicability of the standard $k-\varepsilon$ model for predicting room air motion and heat transfer. How the model reacts to flows that are not fully turbulent is really at the root of these questions. Baker et al (1994b) indicate that the standard $k-\varepsilon$ model will overpredict the transfer of heat and momentum in regions where the flow is "subtly" turbulent. According to Chen and Jiang (1992), few results on the subject are available but it is doubtful that a $k-\varepsilon$ model can successfully characterize a partially turbulent flow.

Therefore, can the standard $k-\varepsilon$ model lead to accurate predictions of room air flow and heat transfer? Is the approach limited to the few building configurations which are truly fully turbulent? How does the standard $k-\varepsilon$ model react to a flow that is not fully turbulent? If it poorly characterizes the transport of heat and momentum in regions that are not fully turbulent, does it matter? How does this impact the modelling of the near-wall regions, which are critical to the integrated modelling approach? Is the standard $k-\varepsilon$ model the appropriate choice for this application?

Further information on turbulence modelling approaches, and on the $k-\varepsilon$ model in particular, is necessary to explore these issues. These are the topics of the next two sections.

3.5 Turbulence Modelling

Most flows of practical interest experience some degree of random turbulent fluctuations. These fluctuations are caused by instabilities between inertial and viscous forces. As the turbulent fluctuations enhance the transport of momentum, heat, and pollutants, they must be considered in the formulation and solution of the equations of motion. Although the problem has been investigated for well over a century, there is still no general approach to the solution of turbulent flows. According to Tennekes and Lumley (1972), it is next to impossible to make accurate quantitative predictions without relying heavily on empirical data.

Techniques of various levels of complexity and computational intensity have been developed to characterize this chaotic motion. Some approaches (known as *direct numerical simulation* and *large-eddy-simulation*) attempt to model the details of the turbulent fluctuations with few or no assumptions, necessitating very fine grids and time steps. Applications to room air flow modelling have already been made (Nielsen 1998; Emmerich and McGrattan 1998) but computational costs remain extremely high and further refinement is necessary.

In contrast to these high-resolution techniques, *turbulence transport models* are able to apply coarser grids and larger time steps by treating the random fluctuations with statistical methods. The equations of motion are filtered with respect to time, so that rather than modelling the details of the turbulent motion, these methods account for the influence of turbulence on the time-mean motion. The time filtering generates new terms in the equations, these approximating the impact of the high-frequency fluctuations on the time-mean motion.

However, the introduction of the turbulence terms creates a new problem: the equations of motion no longer constitute a closed system since they contain more unknowns than equations. Empirical information is, therefore, introduced to evaluate the turbulence terms to bring closure to the system of equations. A plethora of models have been developed to evaluate the turbulence terms. Rodi (1980) provides a detailed review of the various methods, which include Reynolds-stress models, algebraic-stress models, and zero-, one-, and two-equations eddy-viscosity models. Of these, one approach (the standard $k-\varepsilon$ model) has enjoyed the greatest usage by far, not only in the domain of buildings, but in most fields of study (aerodynamics, hydraulics, combustion, etc). For reasons of accuracy, efficiency, and stability, the standard $k-\varepsilon$ model has stood the test of time. The $k-\varepsilon$ model is described in the following section.

3.6 The $k-\varepsilon$ Turbulence Model

3.6.1 Reynolds' averaging

The time-filtering process mentioned in the previous section is known as *Reynolds' averaging*, named for the person who proposed the approach over a century ago. This is accomplished by replacing each instantaneous variable in the equations of motion with the sum of a time-mean quantity and a fluctuating quantity (eg. $T = \bar{T} + T'$)[13]. The time-mean quantity is the average value over a time period (on the order of a few seconds) that is long relative to the frequency of the turbulent fluctuations. Substituting these expressions into equations 3.1 to 3.5 results in the *Reynolds-averaged* form of the equations of motion.

---

[13] The use of the ′ symbol should not be confused with the usage in Section 3.2.4 related to the SIMPLE solution procedure.

conservation of momentum in x-direction

$$\frac{\partial}{\partial t}(\rho\bar{u}) + \frac{\partial}{\partial x}(\rho\bar{u}\bar{u}) + \frac{\partial}{\partial y}(\rho\bar{v}\bar{u}) + \frac{\partial}{\partial z}(\rho\bar{w}\bar{u}) = -\frac{\partial\bar{P}}{\partial x} + \frac{\partial}{\partial x_j}\left[\mu\left(\frac{\partial\bar{u}}{\partial x_j} + \frac{\partial\bar{u}_j}{\partial x}\right) - \boldsymbol{\rho}\overline{\mathbf{u}'\mathbf{u}'_j}\right] \tag{3.28}$$

conservation of momentum in y-direction

$$\frac{\partial}{\partial t}(\rho\bar{v}) + \frac{\partial}{\partial x}(\rho\bar{u}\bar{v}) + \frac{\partial}{\partial y}(\rho\bar{v}\bar{v}) + \frac{\partial}{\partial z}(\rho\bar{w}\bar{v}) = -\frac{\partial\bar{P}}{\partial y} + \frac{\partial}{\partial x_j}\left[\mu\left(\frac{\partial\bar{v}}{\partial x_j} + \frac{\partial\bar{u}_j}{\partial y}\right) - \boldsymbol{\rho}\overline{\mathbf{v}'\mathbf{u}'_j}\right] \tag{3.29}$$

conservation of momentum in z-direction

$$\frac{\partial}{\partial t}(\rho\bar{w}) + \frac{\partial}{\partial x}(\rho\bar{u}\bar{w}) + \frac{\partial}{\partial y}(\rho\bar{v}\bar{w}) + \frac{\partial}{\partial z}(\rho\bar{w}\bar{w}) \tag{3.30}$$

$$= -\frac{\partial\bar{P}}{\partial z} + \frac{\partial}{\partial x_j}\left[\mu\left(\frac{\partial\bar{w}}{\partial x_j} + \frac{\partial\bar{u}_j}{\partial z}\right) - \boldsymbol{\rho}\overline{\mathbf{w}'\mathbf{u}'_j}\right] - \rho\beta(\bar{T}_\infty - \bar{T})g$$

continuity

$$\frac{\partial}{\partial x}(\rho\bar{u}) + \frac{\partial}{\partial y}(\rho\bar{v}) + \frac{\partial}{\partial z}(\rho\bar{w}) = 0 \tag{3.31}$$

conservation of energy

$$\frac{\partial}{\partial t}(\rho c_p\bar{T}) + \frac{\partial}{\partial x}(\rho c_p\bar{u}\bar{T}) + \frac{\partial}{\partial y}(\rho c_p\bar{v}\bar{T}) + \frac{\partial}{\partial z}(\rho c_p\bar{w}\bar{T}) = \frac{\partial}{\partial x_j}\left(k\frac{\partial\bar{T}}{\partial x_j} - \boldsymbol{\rho}\mathbf{c_p}\overline{\mathbf{T}'\mathbf{u}'_j}\right) + q''' \tag{3.32}$$

These equations relate time-mean (e.g. $\bar{T}$) rather than instantaneous (e.g. T) quantities, but their form has not been altered by the Reynolds-averaging process. New terms (shown in bold), however, have been introduced into the momentum and energy equations to represent the *influence* of the turbulent motion on the time-mean quantities. The new terms appearing in the momentum equations ($-\rho\overline{u'_i u'_j}$) contain the high-frequency fluctuating velocity components and are known as *Reynolds stresses*. The new terms appearing in the energy equation ($-\rho c_p\overline{T'u'_j}$) contain the fluctuating components of temperature and velocity, and are known as *turbulent heat fluxes*.

As their appearance is somewhat similar to those for molecular diffusion (viscosity and conduction), the Reynolds stresses and turbulent heat flux terms are commonly known as *turbulent diffusion*. To illustrate the analogy consider the diffusion term in the x-momentum equation,

$$\frac{\partial}{\partial x_j}\left[\mu\left(\frac{\partial\bar{u}}{\partial x_j} + \frac{\partial\bar{u}_j}{\partial x}\right) - \rho\overline{u'u'_j}\right] \tag{3.33}$$

The term $[\mu(\partial\bar{u}/\partial x_j + \partial\bar{u}_j/\partial x)]$ involves gradients of the time-mean velocities and the molecular viscosity, and represents the diffusion of momentum through random molecular motion. The term

$[-\rho \overline{u'u'_j}]$ involves the fluctuating velocities, and represents the diffusion of momentum through bulk turbulent motion.

3.6.2 Eddy viscosity concept

Boussinesq proposed the *eddy-viscosity concept* a century ago, based on the analogy between molecular and turbulent diffusion. Like the viscous stresses in laminar flow, the turbulent stresses are assumed to be proportional to the mean-velocity gradients,

$$-\overline{u'_i u'_j} = \frac{\mu_t}{\rho}\left(\frac{\partial \bar{u}_i}{\partial x_j} + \frac{\partial \bar{u}_j}{\partial x_i}\right) - \frac{2}{3} k\delta_{ij} \tag{3.34}$$

where μ_t is defined to be the *eddy viscosity*, k is the turbulence kinetic energy (defined in the next section), and δ_{ij} is the Kronecker delta[14]. Essentially this assumes that the turbulent motions behave like an apparent viscosity on the time-mean flow. The molecular viscosity (μ) is a property of the *fluid*. In contrast μ_t is a property of the *flow*: it can differ significantly from one flow to another and can vary throughout a flow domain. Similarly, the turbulent heat fluxes are assumed to be proportional to the mean-temperature gradients,

$$-\rho c_p \overline{T'u'_j} = c_p \Gamma \frac{\partial \bar{T}}{\partial x_i} \tag{3.35}$$

Γ is the turbulent diffusivity of heat. Like the eddy viscosity, it is a property of the flow rather than of the fluid. The turbulent Prandtl number, σ_t is introduced to relate the turbulent diffusivity of heat and the eddy viscosity,

$$\sigma_t = \frac{\mu_t}{\Gamma} \tag{3.36}$$

Experiments have shown that Γ and μ_t can vary substantially over a flow or between flows, whereas σ_t does not (Rodi 1980). Accordingly, σ_t can be assumed constant.

The eddy viscosity concept eliminates the fluctuating quantities from the Reynolds-averaged equations of motion, turbulent diffusion now being completely characterized by gradients in the mean quantities and by the eddy viscosity. By substituting equations 3.34 to 3.36 into equations 3.28 to 3.32 (the $\frac{2}{3} k\delta_{ij}$ terms are absorbed into the pressure-gradients, as discussed by Rodi 1980), the governing equations become,

---

[14] $\delta_{ij} = 1$ for $i = j$ and $\delta_{ij} = 0$ for $i \neq j$.

conservation of momentum in x-direction

$$\frac{\partial}{\partial t}(\rho\bar{u}) + \frac{\partial}{\partial x}(\rho\bar{u}\bar{u}) + \frac{\partial}{\partial y}(\rho\bar{v}\bar{u}) + \frac{\partial}{\partial z}(\rho\bar{w}\bar{u}) = -\frac{\partial\bar{P}}{\partial x} + \frac{\partial}{\partial x_j}\left[(\mu+\mu_t)\left(\frac{\partial\bar{u}}{\partial x_j} + \frac{\partial\bar{u}_j}{\partial x}\right)\right] \tag{3.37}$$

conservation of momentum in y-direction

$$\frac{\partial}{\partial t}(\rho\bar{v}) + \frac{\partial}{\partial x}(\rho\bar{u}\bar{v}) + \frac{\partial}{\partial y}(\rho\bar{v}\bar{v}) + \frac{\partial}{\partial z}(\rho\bar{w}\bar{v}) = -\frac{\partial\bar{P}}{\partial y} + \frac{\partial}{\partial x_j}\left[(\mu+\mu_t)\left(\frac{\partial\bar{v}}{\partial x_j} + \frac{\partial\bar{u}_j}{\partial y}\right)\right] \tag{3.38}$$

conservation of momentum in z-direction

$$\frac{\partial}{\partial t}(\rho\bar{w}) + \frac{\partial}{\partial x}(\rho\bar{u}\bar{w}) + \frac{\partial}{\partial y}(\rho\bar{v}\bar{w}) + \frac{\partial}{\partial z}(\rho\bar{w}\bar{w}) \tag{3.39}$$

$$= -\frac{\partial\bar{P}}{\partial z} + \frac{\partial}{\partial x_j}\left[(\mu+\mu_t)\left(\frac{\partial\bar{w}}{\partial x_j} + \frac{\partial\bar{u}_j}{\partial z}\right)\right] - \rho\beta(\bar{T}_\infty - \bar{T})g$$

continuity

$$\frac{\partial}{\partial x}(\rho\bar{u}) + \frac{\partial}{\partial y}(\rho\bar{v}) + \frac{\partial}{\partial z}(\rho\bar{w}) = 0 \tag{3.40}$$

conservation of energy

$$\frac{\partial}{\partial t}(\rho c_p\bar{T}) + \frac{\partial}{\partial x}(\rho c_p\bar{u}\bar{T}) + \frac{\partial}{\partial y}(\rho c_p\bar{v}\bar{T}) + \frac{\partial}{\partial z}(\rho c_p\bar{w}\bar{T}) = \frac{\partial}{\partial x_j}\left[\left(k + \frac{c_p\mu_t}{\sigma_t}\right)\frac{\partial\bar{T}}{\partial x_j}\right] + q''' \tag{3.41}$$

This gives the Reynolds-averaged equations a form which is nearly identical to the instantaneous equations. The only differences are the momentum and heat diffusion coefficients, which are constant in the instantaneous equations, but vary from point-to-point in the Reynolds-averaged equations. Therefore, once discretized and linearized using the techniques described earlier, the Reynolds-averaged conservation equations reduce to the general algebraic form (equation 3.14), and thus can be solved using the approaches described earlier.

3.6.3 Calculating the μ_t distribution

The distribution of the eddy viscosity throughout the flow domain must be established in order to calculate the momentum and heat diffusion coefficients for equations 3.37 to 3.39 and 3.41. This is the job of the turbulence model. By calculating the μ_t distribution, the turbulence model implicitly establishes the relative strengths of turbulent and molecular diffusion. This can be seen by examining the diffusion terms in the momentum and energy equations, e.g.

$$\frac{\partial}{\partial x_j}\left[(\mu + \mu_t)\left(\frac{\partial \bar{u}}{\partial x_j} + \frac{\partial \bar{u}_j}{\partial x}\right)\right] \tag{3.42}$$

and

$$\frac{\partial}{\partial x_j}\left[\left(k + \frac{c_p \mu_t}{\sigma_t}\right)\frac{\partial \bar{T}}{\partial x_j}\right] \tag{3.43}$$

If $\mu_t/\mu \gg 1$ the turbulent diffusion terms will dominate the molecular terms (μ in equation 3.42; k in 3.43). Whereas, if $\mu_t/\mu \approx 0$, molecular effects will prevail. Consequently, the ratio μ_t/μ can be thought of as an indicator of "how turbulent" a flow is locally.

Launder and Spalding (1974) proposed a modified version of the $k - \varepsilon$ model. This version has been the most widely applied, and is commonly referred to as the *standard* $k - \varepsilon$ model. The eddy viscosity at each grid point is related to local values of the *turbulence kinetic energy* (k) and the *dissipation rate of turbulence energy* (ε):

$$\mu_t = \frac{C_\mu \rho k^2}{\varepsilon} \tag{3.44}$$

where C_μ is an empirical constant. The turbulent kinetic energy is defined by the fluctuating velocities, $k = \frac{1}{2}(\overline{u'^2} + \overline{v'^2} + \overline{w'^2})$.

The local distributions of k and ε require the solution of two additional transport equations, which are derived from the Navier-Stokes equations. The k transport equation is given by,

$$\frac{\partial}{\partial t}(\rho k) + \frac{\partial}{\partial x_j}(\rho u_j k) = \frac{\partial}{\partial x_j}\left(\frac{\mu_t}{\sigma_k}\frac{\partial k}{\partial x_j}\right) + \mu_t\left(\frac{\partial u_i}{\partial x_j} + \frac{\partial u_j}{\partial x_i}\right)\frac{\partial u_i}{\partial x_j} - \rho\varepsilon - g\beta\frac{\mu_t}{\sigma_t}\frac{\partial T}{\partial z} \tag{3.45}$$

where σ_k is an empirical constant. The ε transport equation is given by,

$$\frac{\partial}{\partial t}(\rho\varepsilon) + \frac{\partial}{\partial x_j}(\rho u_j \varepsilon) = \tag{3.46}$$

$$\frac{\partial}{\partial x_j}\left(\frac{\mu_t}{\sigma_\varepsilon}\frac{\partial \varepsilon}{\partial x_j}\right) + C_1\frac{\varepsilon}{k}\mu_t\left(\frac{\partial u_i}{\partial x_j} + \frac{\partial u_j}{\partial x_i}\right)\frac{\partial u_i}{\partial x_j} - C_2\rho\frac{\varepsilon^2}{k} - C_1\frac{\varepsilon}{k}g\beta\frac{\mu_t}{\sigma_t}\frac{\partial T}{\partial z}$$

where σ_ε, C_1, and C_2 are empirical constants. The last terms in equations 3.45 and 3.46, representing the production of turbulence energy by buoyancy, are not given by Launder and Spalding (1974), but rather by Rodi (1980).

Empiricism is introduced into the model through the five constants: C_μ, σ_k, σ_ε, C_1, and C_2. Launder and Spalding (1974) recommended values for these constants based on experience with free turbulent jets and mixing layers: flow regimes substantially different in nature than those found in rooms.

Despite their more complex appearance, equations 3.45 and 3.46 have the same general structure as the momentum and energy equations. There are transient, convection, diffusion, and source terms. When the discretization, linearization, and boundary condition techniques described in Section 3.2 are applied, these can reduced to the familiar algebraic form of equation 3.14. Therefore, the k and ε equations can be solved in the same manner as the other governing equations.

The solution process illustrated in Figure 3.6 remains unchanged, except with the addition of the k and ε equations. These are solved just before or after the energy equation in the sequential process. Following each iteration the local values of μ_t are calculated with equation 3.44 using the k and ε solutions. μ_t is then used to update the diffusion coefficients in the momentum and energy equations for the next iteration.

3.6.4 Near-wall regions

The standard form of the $k - \varepsilon$ model presented above is only valid in the fully turbulent regions of a flow. Consequently, a different treatment is required near solid walls, where viscous diffusion dominates turbulent diffusion.

The common approach is to use the *the wall function method.* With this, no attempt is made to compute the flow within the laminar and semi-laminar regions of the boundary layer where molecular diffusion is significant. Rather, the next-to-wall grid points are placed in the fully-turbulent region, where laminar diffusion is overwhelmed by turbulent effects. The field variables for these next-to-wall grid points are solved using the procedures described previously, but the simple boundary conditions for wall shear and surface convection (3.17 and 3.19) are replaced with *wall functions* (rearranged from Launder and Spalding 1974),

$$\tau_{wall} = \frac{C_\mu^{1/4} k_P^{1/2} \rho u_P}{\dfrac{1}{\kappa} \ln\left(\dfrac{E \rho \Delta x_P C_\mu^{1/4} k_P^{1/2}}{\mu} \right)} \tag{3.47}$$

and

$$q''_{wall} = \frac{C_\mu^{1/4} k_P^{1/2} \rho c_p (T_P - T_{wall})}{\sigma_t \left[\dfrac{1}{\kappa} \ln\left(\dfrac{E \rho \Delta x_P C_\mu^{1/4} k_P^{1/2}}{\mu} \right) + \dfrac{\pi/4}{\sin(\pi/4)} \cdot \left(\dfrac{A}{k} \right)^{1/2} \left(\dfrac{Pr}{\sigma_t} - 1 \right) \left(\dfrac{\sigma_t}{Pr} \right)^{1/4} \right]} \tag{3.48}$$

As illustrated in Figure 3.7, the subscript P indicates values at the next-to-wall grid points, and Δx_P is the distance from the wall to the next-to-wall grid point. A and E are constants representing wall roughness while κ is von Kármán's constant. Since the turbulence kinetic energy of the next-to-wall points appears in the wall functions, the boundary condition coefficients must be updated each solution iteration as the k solution field evolves.

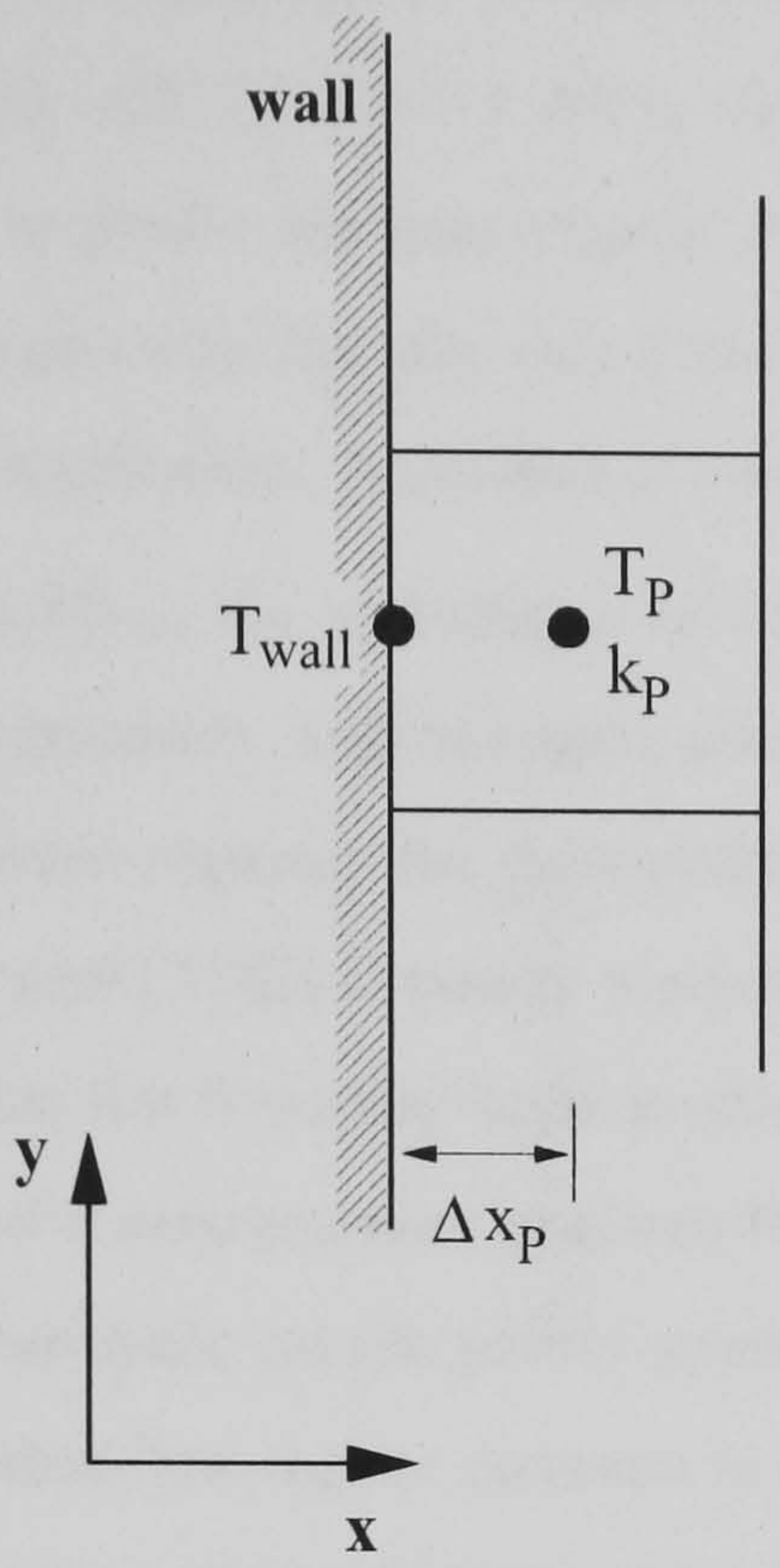

Figure 3.7: Wall functions

In essence, the wall-function method assumes the form of velocity and temperature profiles within the boundary layer. If behaviour within the boundary layer deviates from the assumed profiles, errors will be introduced. Of the many constructs of wall functions that had been developed and applied, Launder and Spalding (1974) recommended these semi-empirical formulations based on their experience with fully turbulent flows. It is important to note that the *logarithmic velocity profile* (see White 1979, for example) for forced flow is the foundation of Launder and Spalding's wall functions. For this reason, Launder and Spalding's wall functions are often referred to as the "log-law" wall functions.

3.7 Applicability of the Standard $k-\varepsilon$ Model

3.7.1 Resolving surface convection with the log-law wall functions

The significance of accurately resolving the near-wall regions was highlighted in Chapter 1. Success of the conflated thermal and air flow modelling approach is critically dependent upon the treatment of the physics at solid surfaces, the locations at which the thermal and CFD domains interact. Any errors in the modelling of convection heat transfer at these surfaces will be propagated (perhaps amplified): if the thermal domain supplies inaccurate boundary conditions for CFD, CFD will calculate an incorrect temperature and flow field for the zone; the erroneous results passed from CFD back to the thermal domain will lead to errors in surface temperatures and energy flows throughout the building, causing errors in the boundary conditions supplied to CFD for the next time step. Clearly, an accurate treatment of surface convection in both the thermal and CFD domains is critical.

This leads to the question, Does the standard $k-\varepsilon$ model with log-law wall functions accurately treat surface convection? The thermal wall function (3.48) is used to both impose the influence of a wall's temperature on the room, and to predict the heat transfer from the room air to the wall surface. The wall functions can accurately predict heat transfer only if their form and their empirical constants are appropriate for the flow under consideration. A number of workers have examined this issue.

Recall that the logarithmic profile is the foundation of Launder and Spalding's log-law wall functions. The logarithmic profile reasonably approximates over the full thickness of the boundary layer (laminar, semi-laminar, and outer regions) for *fully-developed, zero-pressure-gradient* flows. However, as demonstrated by Hammond (1982) it poorly represents the temperature profile in *plane wall jets*. Chen et al (1990) state that the boundary-layer profile for forced air flow in a room will likely lie somewhere between that of a zero-pressure-gradient flow and a plane wall jet. Similarly, Yuan et al (1994) show that the logarithmic profile poorly approximates velocities in the boundary layer for buoyancy-driven flows, another flow regime common in rooms. This is significant given that with the wall-function method, the next-to-wall grid points are placed in the outer region. If the wall functions poorly approximate the profile between the wall and the first grid point, then errors in the wall shear and surface convection (see u_P and T_P in equations 3.47 and 3.48) will result.

Chen et al (1990) compare experimental data from two natural-convection flows against numerical predictions from the standard $k-\varepsilon$ model with log-law wall functions. Relative to the experimental data and another modelling approach, the wall functions overpredicted the surface convection. The authors conclude that the log-law wall-functions can result in significant errors in the prediction of surface convection for natural-convection and mixed-convection flows, and that results are sensitive to the location of the next-to-wall grid points.

Chen and Jiang (1992) report a case in which the log-law wall functions resulted in a substantial underprediction of surface convection. The case involved an office with displacement ventilation. The CFD-predicted surface-convection coefficients ranged from 1 to 3 W/m^2K, while the experimental data ranged from 2 to 8 W/m^2K.

Yuan et al (1994) demonstrate the sensitivity of surface-convection predictions to the location of the next-to-wall grid points. When the spacing between the wall and the first grid points was changed from 1mm to 30mm, the surface-convection prediction was reduced by a factor of four times. Poor agreement was found against experimental data from two natural convection flows. Consequently, they conclude that the log-law wall functions are not appropriate for natural-convection flows.

In comparing the ability of alternate approaches to predict a variety of flow types, Chen (1995) found the wall functions to give less than encouraging results, and also noted their grid sensitivity. Niu and van der Kooi (1992) compare numerical predictions to experimental results for buoyancy-driven flow in a room-sized enclosure. They found that the wall functions overpredicted the surface convection when the next-to-wall grid points were located too close to the wall, and underpredicted when they were too far. Awbi (1998) showed how surface convection predictions can vary five-fold depending on the location of the next-to-wall grid points.

These observations clearly indicate the deficiencies of the standard $k-\varepsilon$ model with log-law wall functions in treating surface convection in room air flows.

3.7.2 Predicting the eddy viscosity in low flow regions

Strictly speaking the $k-\varepsilon$ model is only valid for fully turbulent flow, whereas weakly turbulent, relaminarized, or even stagnant flow can exist in rooms (particularly in regions remote from air-supply systems). Consequently, an important assumption is implicit when the standard $k-\varepsilon$ model is applied to a room: that the flow behaves as though it were fully turbulent. This section examines the implications of that assumption. Specifically, it assesses how the $k-\varepsilon$ model reacts to a room air flow which is not fully turbulent and assesses the sensitivities of air flow and heat transfer predictions to uncertainties in turbulence characterization.

A well-known benchmark was selected as the object of this study, the IEA Annex 20 two-dimensional test case. Geometry, boundary conditions, and measured data for this configuration are given by Nielsen (1990). The flow, which enters the room at the upper left corner and exits at the lower right (see Figure 3.8), can be treated as two-dimensional and has been successfully simulated by a number of CFD programs.

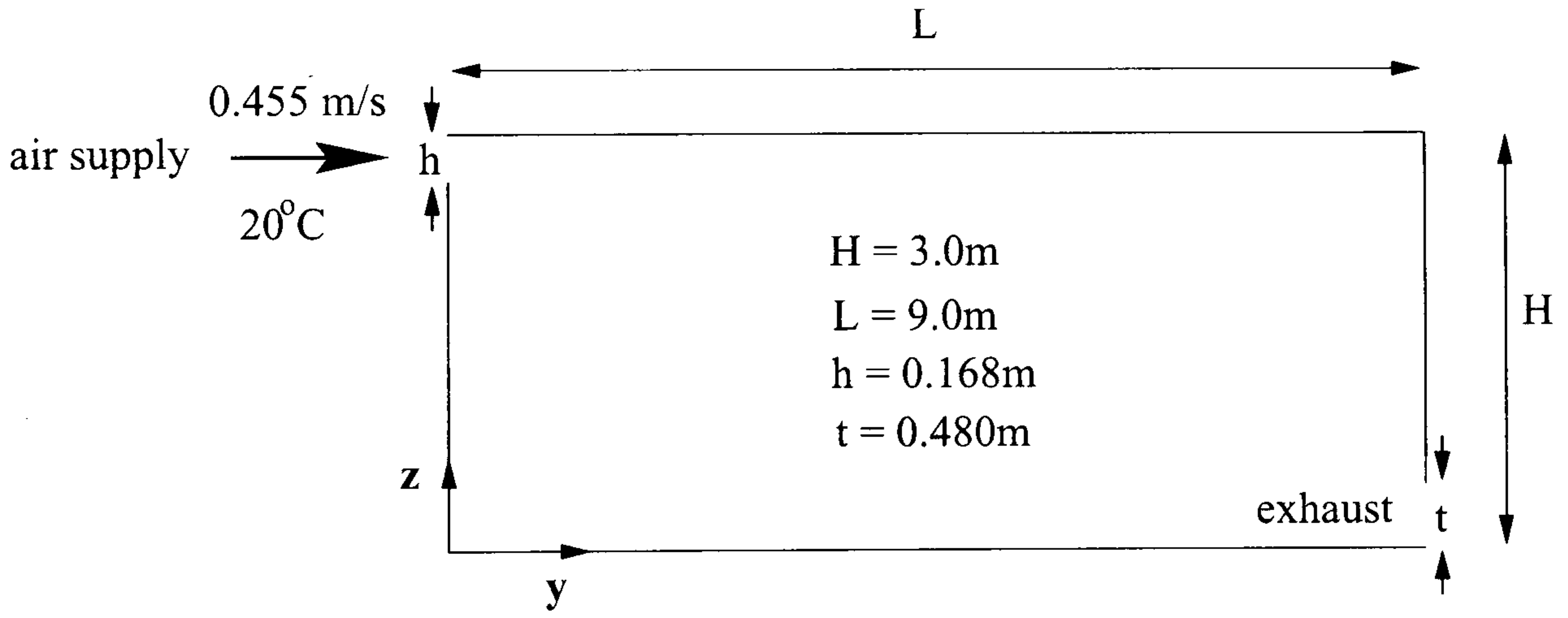

Figure 3.8: IEA Annex 20 two-dimensional test room

The flow pattern predicted by ESP-r is illustrated in Figure 3.9. The numerical predictions of the horizontal mean velocity and the turbulent fluctuations compared favourably with Nielsen's measured data, although agreement is less good near the floor and ceiling. The flow recirculations in the upper-right and lower-left corners were not predicted. These results are consistent with those of the CFD programs examined in Annex 20 (Lemaire et al 1993).

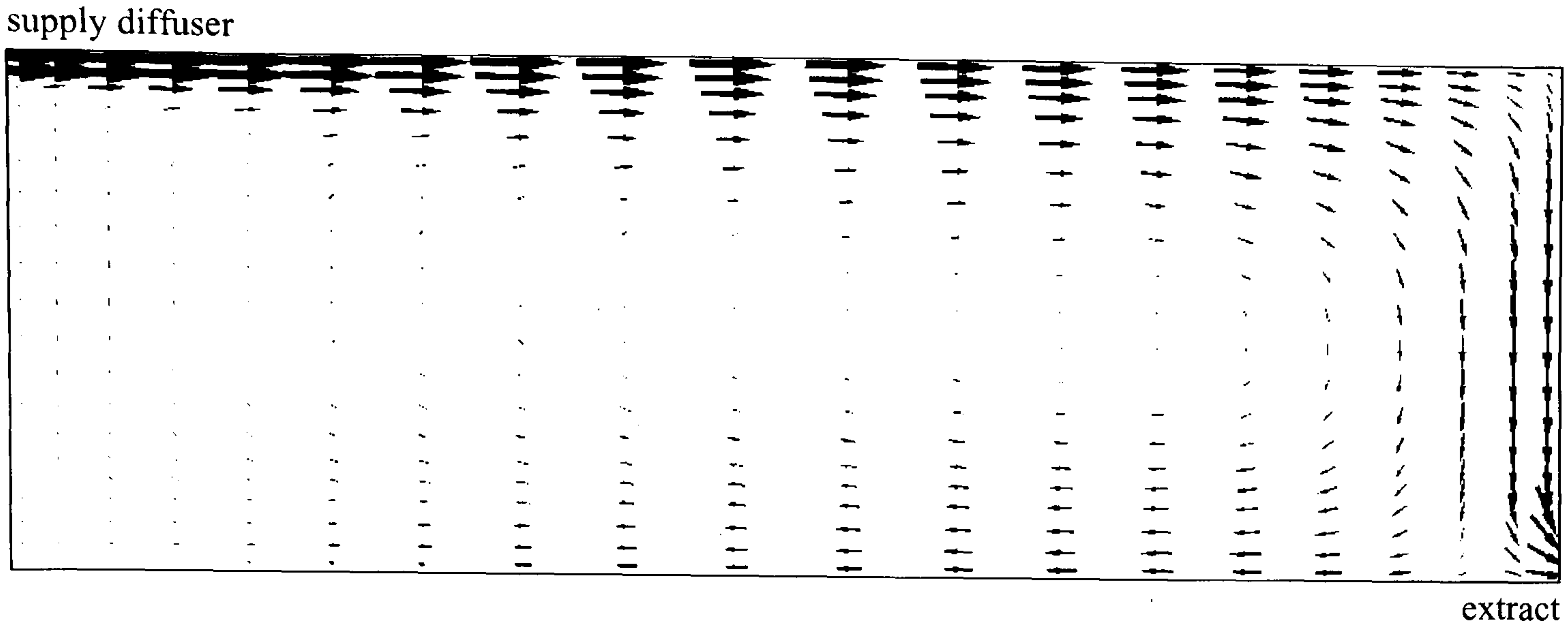

Figure 3.9: Air flow predictions for Annex 20 test room using $k-\varepsilon$ model

Eddy viscosity predictions

Examining Figure 3.9, it can be seen that there is a strong flow along the ceiling and down the right wall. The rest of the room experiences a recirculating flow, induced by the incoming air stream. This recirculation is strongest in the right and middle portions of the room, but is quite weak in the left of the room, particularly within a 1m distance of the wall (from the floor level to within a few centimetres of the air inlet). Mean velocities in this low-flow region are less than one tenth of those at the air inlet.

The $k-\varepsilon$ model has well characterized the turbulent fluctuations, but this does not necessarily mean that it has well characterized the turbulent diffusion of energy and momentum. An examination of the predicted eddy viscosity field is quite revealing. Recall that the μ_t/μ ratio indicates the relative strength of turbulent to molecular diffusion. Along the flow path of the incoming air μ_t/μ ranges from 25 to 300. These values characterize a fully turbulent flow, or at least a flow which is transitional from weakly to fully turbulent (see Baker et al 1994b). This is in agreement with expectations.

The numerical results do not agree with expectations near the left wall, however, where turbulent diffusion is expected to be weaker. The flow is very low, verging on stagnant. The turbulent kinetic energy should be lower than in the main flow stream, and the predictions are, by an order of magnitude. Despite this, the $k-\varepsilon$ model predicted μ_t/μ ratios are as high as those in the main flow stream, ranging from 50 to 300. This is a result of very low calculated turbulent-energy dissipation rates (refer to equation 3.44), which unfortunately cannot be compared with measurements.

The $k-\varepsilon$ model has predicted μ_t values near the left wall which are consistent with fully turbulent flow. There is some uncertainty in the nature of the flow near the left wall. It could be weakly turbulent and may possibly have relaminarized, but certainly, it is not fully turbulent. Therefore, it can be concluded that the $k-\varepsilon$ model has overpredicted the eddy viscosity near the left wall. This conclusion is corroborated by Baker et al (1994b) who stated that the $k-\varepsilon$ model will produce an "excessive dose of eddy viscosity for the subtly-turbulent flows existing throughout indoor rooms away from HVAC supply systems and obstructions with edges".

Implications of μ_t overprediction on air flow calculations

A series of numerical experiments were then performed to determine the implications of over-predicting μ_t near the left wall. The boundary conditions of the isothermal room were altered so that both heat transfer and air flow could be assessed. The energy equation was added to the solution domain and the temperature of the air flowing into the room set to 25°C, the floor and ceiling to 18°C, the right wall to 10°C, and the left wall to 0°C.

With the standard $k-\varepsilon$ model the μ_t distribution is calculated with equation 3.44 each iteration, following the solution of the k and ε equations, but before the energy and momentum-equation coefficients are calculated for the next iteration. A simulation with the new boundary conditions was performed with this standard treatment. In the next two simulations, equation 3.44 was modified to derate μ_t near the left wall ($0m < y < 1m$ and $0m < z < 2.5m$). In one simulation μ_t was halved, reducing turbulent diffusion next to the left wall by 50%. In the second simulation μ_t was set to zero, eliminating turbulent diffusion in this region. Equation 3.44 was unaltered throughout the rest of the room.

It is not implied that these modifications to the $k-\varepsilon$ model more accurately reflect the reality, but they will give a bound on the errors caused by the excessive dose of eddy viscosity by the left wall. Comparing the results of these three simulations will indicate how sensitive air flow and heat transfer predictions are to μ_t in this region.

The mean-velocity predictions were compared by superimposing flow-vectors and by plotting results at two vertical planes ($y = 3m$ and $y = 6m$) and at two horizontal planes ($z = 0.08m$ and $z = 2.9m$). The mean-velocity predictions of the three simulations were nearly identical. In addition, the turbulent fluctuations were compared at the four planes, and found to be nearly identical, except at the grid points next to the left wall. Therefore, it can be concluded that the air flow predictions are highly insensitive to μ_t adjacent to the left wall.

This insensitivity can be explained by examining the diffusion terms in the momentum equations (see equation 3.42, page 59). Velocities adjacent to the left wall are very low, as are velocity gradients. Consequently, momentum diffusion is not significant (here) and high relative errors in its estimation can be tolerated. This is a fortuitous feature of the $k-\varepsilon$ model.

Implications of μ_t overprediction on thermal calculations

Very different results are observed in the thermal predictions, however. The simulations with the modified $k-\varepsilon$ model resulted in significantly lower temperature gradients along the left wall. Surface convection at the left wall was highly sensitive to μ_t in the surrounding air, as illustrated in

Figure 3.10. Halving μ_t reduced heat transfer to the left wall by 17%, while eliminating turbulent diffusion reduced the surface convection by 31%. But significantly, the heat transfer differences at the right wall, floor, and ceiling are trivial. It is worth noting that the predicted surface convection rates given in Figure 3.10 are quite low, this a result of the log-law wall function's inability to accurately resolve the heat transfer[15].

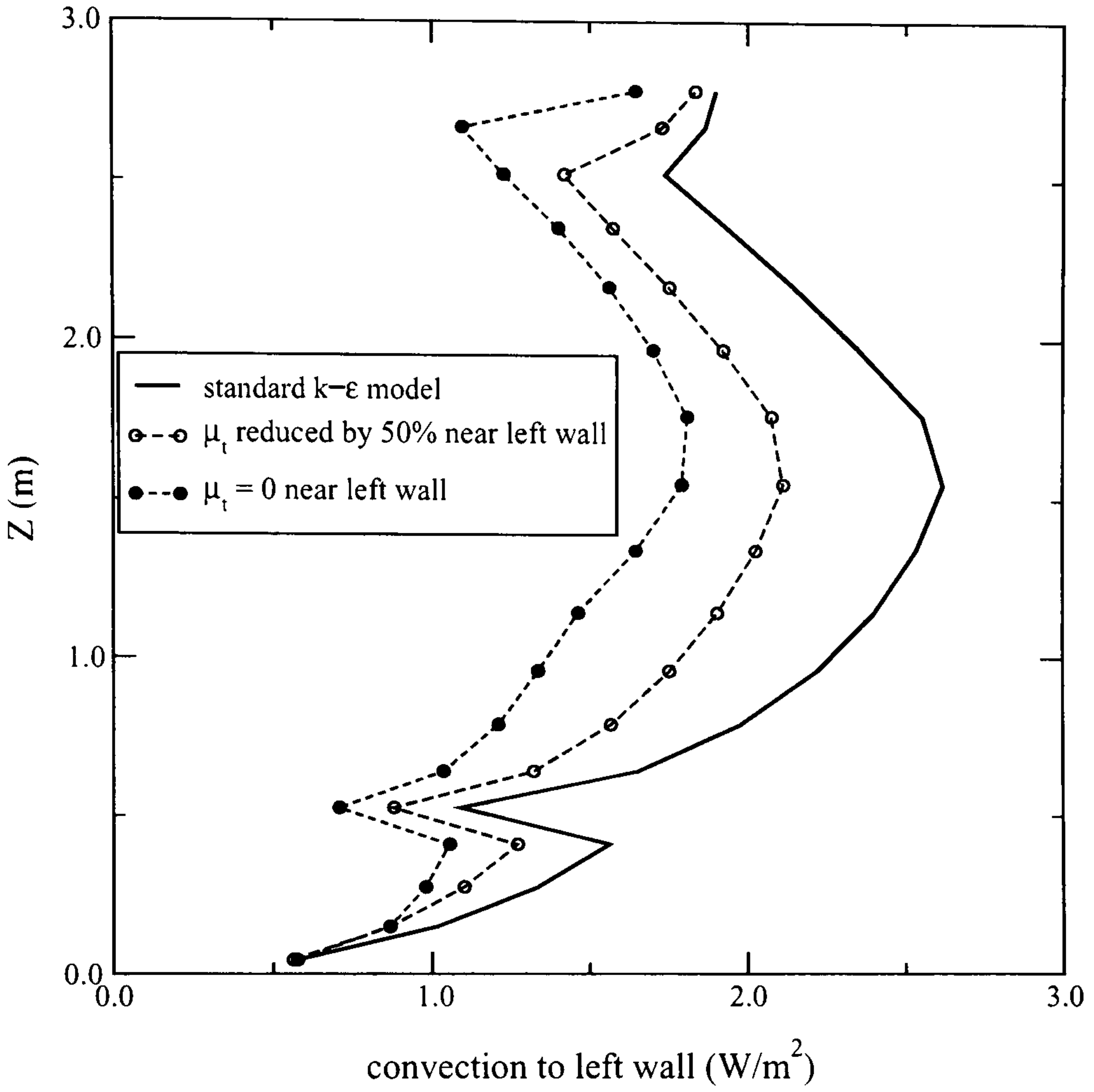

Figure 3.10: Impact of μ_t on surface convection at left wall

The sensitivity of the heat transfer at the left wall can be explained by examining the diffusion terms in the energy equation (see equation 3.43, page 59). When large temperature gradients exist in the vicinity of poor turbulence characterization, significant errors in the estimation of thermal diffusion result. Further, as there is little flow adjacent to the left wall thermal convection is relatively weak, so diffusion plays a significant role in the energy equation (see the convection and diffusion terms in equation 3.41). The standard $k-\varepsilon$ model produces Peclet numbers (the dimensionless ratio of the strength of convection to diffusion) in the order of $10^0 - 10^1$ near the left wall, whereas when μ_t is set to zero, the Peclet numbers are in the order of 10^2. With Peclet numbers this low, an accurate calculation of turbulent thermal diffusion (hence μ_t) is very important.

---

[15] The local minimums in surface convection at the 0.5m and 2.5m heights are a result of the turbulence kinetic energy predictions. It is expected that these minimums would not appear if a finer mesh were employed.

These results clearly indicate that the $k-\varepsilon$ model cannot accurately predict the eddy viscosity distribution in regions which are subtly turbulent. Although this has a negligible impact on flow calculations, it significantly influences thermal predictions. However, the errors are localized to the surfaces adjacent to the low flow region. This reality of the $k-\varepsilon$ model must be considered in the handshaking mechanisms employed in the the integrated modelling approach.

3.8 Alternate Turbulence Modelling Approaches

Despite the shortcomings noted above, the standard form of the $k-\varepsilon$ model in conjunction with the log-law wall functions has been applied more than any other turbulence modelling approach for predicting room air flow and heat transfer. This section discusses some alternatives that have been assessed. As well, recently developed and emerging approaches specifically for room air flow and heat transfer modelling are reviewed.

3.8.1 Low-Reynolds number modelling with $k-\varepsilon$

Launder and Spalding (1974) describe the *low-Reynolds-number modelling method* as an alternate approach for treating the near-wall regions with the $k-\varepsilon$ model. In contrast to the wall-function method, grid points are placed within the boundary layer, including the laminar region. This requires adjustments to the k and ε equations. As well, two of the empirical "constants" (C_μ and C_2) are made to vary with the local turbulence Reynolds number. Since solution points are located within the laminar region of the boundary layer, the wall shear and thermal boundary conditions can be treated with the simple relations in equations 3.16 to 3.19, rather than the complex wall functions. So, unlike the wall-function method, the low-Reynolds-number approach does not assume the velocity and temperature profiles across the boundary layer. The cost of dropping this assumption is substantially higher computational requirements due to the additional grid points in the boundary layer.

Lam and Bremhorst (1981) put forward another low-Reynolds-number $k-\varepsilon$ formulation. Rather than introduce new destruction terms to the k and ε equations, they add new functions to make three of the constants (C_1, C_2, and C_μ) vary with the local turbulence Reynolds number. New empirical constants—whose values were established by tuning simulations to experimental data for a fully-developed pipe flow—are also introduced. Other low-Reynolds formulations are also available.

Low-Reynolds number models have been applied for room air flow modelling (Chen et al 1990, Chen 1995; Nielsen 1998; Awbi 1998). Some improvements relative to the log-law wall wall functions were found, but this at the expense of substantially higher computational requirements and stability.

3.8.2 Alternate $k-\varepsilon$ models

Chen (1995) compared the performance of the standard, Lam-Bremhorst low-Reynolds number, and three alternate $k-\varepsilon$ models at predicting a series of room air flows. One of the alternate formulations was a *two-layer* model, which, like the low-Reynolds number models, places grid points within the laminar and semi-laminar regions of the boundary layer. However, unlike the low-Reynolds models described above, the ε equation is not solved within the near-wall region, but rather is replaced by an algebraic equation. This leads to fewer grid points and one fewer differential equation to solve in the boundary layer.

The second alternative was a *two-scale* model, which divides the energy spectrum into two parts: the production region and the transfer region. Transport equations are written for k and ε for each of these regions, which results in a more computationally intense solution. The third alternative, a *renormalization-group* model, is identical to the standard $k-\varepsilon$ model, except that the five empirical constants assume different values. Also, an additional source term is included in the ε equation.

Generally speaking, Chen found that the alternative $k-\varepsilon$ formulations performed well in some cases, while poor in others. The renormalization-group model was as stable as the standard $k-\varepsilon$ model and produced slightly better results; however like the standard model, surface convection predictions are sensitive to the placement of the next-to-wall grid points. The two-layer model was more computationally intense than the standard model, and proved to be less stable. The two-scale model generally performed worse than the standard $k-\varepsilon$ model.

Chikamoto et al (1992) and Nielsen (1998) discuss a modified $k-\varepsilon$ model that utilizes damping functions to reduce the eddy viscosity in areas with low velocity and relaminarization. This technique may address the problem of overpredicting heat transfer in the subtly turbulent regions, as discussed in Section 3.7.2.

3.8.3 Higher resolution options to $k-\varepsilon$

As previously mentioned, large eddy simulation methods have been applied to buildings (Nielsen 1998; Emmerich and McGrattan 1998), but only for isothermal air flows. Performance has been adequate, but not substantially better than the standard $k-\varepsilon$ model. Further refinement will be necessary before this method's extremely high computational requirements can be justified.

Reynolds-stress models, which require the solution of nine additional transport equations, have also been applied to room air flow and heat transfer modelling (Chen 1996). Only slight accuracy improvements relative to the standard $k-\varepsilon$ model were found, and this at the expense of substantially higher computational requirements and stability.

3.8.4 Alternate near-wall approaches for $k-\varepsilon$

Takemasa et al (1992) found that the $k-\varepsilon$ model with alternate wall functions that consider the thickness of the viscous sub-layer provided accurate and grid-independent surface convection predictions. However, as data from only a single configuration were available, it is not known whether these observations can be extended to the general case.

Yuan et al (1993) developed new wall functions appropriate for natural convection flows, as an alternate to Launder and Spalding's log-law wall functions. A dimensional analysis was performed to establish the functional form, while the constants appearing in the wall functions were determined by correlating to existing experimental data. Applicability is limited to buoyancy-driven flow over vertical surfaces. Yuan et al (1994) found good agreement with experimental data for two natural convection flows: accurate and grid-independent surface convection predictions were acquired. Arnold et al (1998) and Heiselberg et al (1998), however, did find greater grid sensitivity with the Yuan wall functions.

Research is underway to develop other methods to accurately resolve the wall heat transfer. Barp and Moser (1998) are currently developing a near-wall treatment for buoyancy-driven flow over horizontal surfaces. Their work may lead to a replacement for the log-law wall functions for this flow regime, and thus would complement the Yuan wall functions.

Xu et al (1998) have developed a two-layer modelling approach for buoyancy-driven flows. The standard $k-\varepsilon$ model is used in the regions remote from walls, whereas the near-wall regions are treated with a one-equation near-wall model. As only 7-10 grid points are required within the near-wall region, this results in substantially less computer requirements than a low-Reynolds model. Xu (1998) presented another two-layer model, this treating the general case of forced, natural, or mixed convection within rooms.

Neitzke (1998) developed new wall functions for use with the standard $k-\varepsilon$ model. He found these to give accurate and grid-independent results for a buoyancy-driven flow within a closed-cavity; however, flow regimes more typical of rooms were not assessed.

3.8.5 Zero-equation turbulence models

Zero-equation turbulence models utilize the eddy-viscosity concept but are relatively simple in form. Rather than solving the k and ε equations to calculate μ_t using equation 3.44, zero-equation models use a fixed value for the the eddy viscosity or relate it to the mean-velocity distribution. This substantially reduces computational requirements compared with $k-\varepsilon$ and more complex approaches.

Nielsen (1998) shows that simply setting μ_t to some fixed multiple of the molecular viscosity can lead to useful results in some cases. He also discusses the advantages of using a fixed μ_t zero-equation model to stabilize solutions prior to invoking the $k-\varepsilon$ model.

Chen and Xu (1998) present a zero-equation model specifically developed for modelling room air flow and heat transfer. They relate the local eddy viscosity to the local mean velocity ($\bar{V}$) and a length scale,

$$\mu_t = 0.03874 \rho \bar{V} l \tag{3.49}$$

The length scale (l) varies from solution point to solution point and equals the distance to the nearest solid surface (Xu 1998). The constant 0.03874 has a semi-empirical basis, but is treated as universal for room air flows.

Chen and Xu (1998) show simulation results for four room air flows—displacement ventilation, and natural, forced, and mixed convection. Good agreement between the zero-equation model predictions and the experimental data was found. In fact, in some cases the zero-equation model outperformed the $k - \varepsilon$ model. Srebric et al (1999) provide further validation of the approach by comparing the zero-equation model's predictions to experimental data for three additional room air flow cases: natural convection with infiltration, forced convection, and mixed convection with displacement ventilation. They found good agreement between the computed and measured air velocity and temperature profiles.

Although Chen and Xu (1998) provide heat transfer boundary conditions for the zero-equation model, neither they nor Srebric et al (1999) compare surface convection predictions against experimental results or the $k - \varepsilon$ wall functions.

3.9 Closing Remarks

Chapter 1 raised some issues regarding CFD's suitability for predicting room air flow and heat transfer, and indicated how these could impede applicability of the conflated thermal and air flow modelling approach. This chapter has provided the technical basis for understanding these issues.

Most applications of CFD for room air flow and heat transfer simulation have employed the standard $k - \varepsilon$ turbulence model with log-law wall functions. This approach was formulated for fully developed turbulent flows, which contrasts with the flow regimes commonly found in rooms. Although there have been many successful *air flow* predictions, the technology has proven deficient at predicting *convective heat transfer* at solid surfaces. Poor surface convection predictions are the result of the inability of the log-law wall functions to resolve the near-wall regions in room air flows. And, due to the overprediction of the eddy viscosity in low flow regions. Given this, it is clear that approaches currently used in ESP-r for handshaking between the thermal and CFD domains (as described in Chapter 2) must be improved.

Numerous alternatives to the standard $k - \varepsilon$ turbulence model with log-law wall functions were outlined. Although low Reynolds number $k - \varepsilon$ modelling approaches have shown some promise, they are not well suited to the conflated simulation approach because of stability problems and high computational requirements. At this time, none of the other alternatives have proven to be suitable universal replacements for the standard $k-\varepsilon$ model. The possible exception is the Chen and Xu (1998) zero-equation model, although its ability to predict heat transfer has yet to be assessed.

New near-wall treatments for the $k-\varepsilon$ model suitable for room air flow prediction are now available, and more are under development. In contrast to the universal nature of the log-law wall functions—which were meant to be applicable for a broad range of flow regimes and surface orientations—some of these methods are only appropriate for specific cases (e.g. buoyancy-driven flow over vertical surfaces). Consequently, these techniques can only be exploited in the conflated modelling approach if the simulator is given the ability to (dynamically) select an appropriate method based on an appraisal of the flow regime.

CHAPTER 4

Modelling Internal Surface Convection

4.1 Introduction

One objective of this research is to improve the modelling of internal surface convection. Chapter 1 described why surface convection varies spatially and temporally, while Chapter 2 outlined how the well-stirred assumption is used to model this heat transfer path. An example illustrated how pervasive convection coefficients are in the resulting system of equations that characterize the zone's thermal state. This led to the hypothesis that erroneous convection coefficients would distort the system of equations and lead to inaccuracies in nodal temperature, plant injection, and inter-nodal energy flow predictions. While Chapter 2 gave some indication of the potential for error by comparing the convection coefficients calculated by ESP-r's default and optional algorithms, this chapter substantiates the hypothesis. This underlines the importance of calculating convection coefficients using an algorithm appropriate for the flow regime under consideration.

The second objective of this research is to advance the modelling of indoor air flow through the integration of CFD into dynamic whole-building simulation. The previous chapters have explained why this conflated modelling approach is critically dependent upon the treatment of internal surface convection: this is the pivot point for handshaking between the thermal and CFD modelling domains. There are three basic options for resolving this pivot point:

- have CFD calculate the air-to-surface heat transfer based on the CFD-predicted flow and temperature fields;
- have the thermal domain calculate the heat transfer using convection coefficients in conjunction with uniform zone air temperatures;
- have the CFD and thermal domains cooperatively calculate the heat transfer.

Chapter 3 demonstrated CFD's deficiencies at predicting convective heat transfer at surfaces. Although some methods to address this deficiency are put forward in Chapter 5, the first option listed above is not sufficiently robust and general to rely upon exclusively, at least at this point in CFD's evolution. The third option will be described in Chapter 5. Like the second option, it requires the thermal domain to predict convection coefficients.

Therefore, realizing both research objectives requires populating the thermal modelling domain with a suite of algorithms for calculating convection coefficients for various flow regimes. This need is addressed in the current chapter. Section 4.2 presents a scheme for classifying the flow regimes commonly found within buildings. It then summarizes a literature survey of h_c algorithms for resolving these flow regimes. The four methods selected from the literature are described in Section 4.3. These are reviewed in detail and their implementation into ESP-r is described. In Section 4.4, a new method is put forward for calculating convection coefficients for mixed flow (where both buoyant and mechanical forces are present), a convective regime not adequately treated in the literature.

Drawing upon the newly incorporated algorithms, Section 4.5 demonstrates the significance of convection coefficients to thermal simulation predictions. It surveys the literature for previous sensitivity studies and presents some new results. Chapter 1 argued that in some cases ignoring stratification within the room air would preclude an accurate treatment of internal surface convection. Section 4.6 substantiates this by examining a case with significant stratification. This places some bounds on the applicability of modelling with the well-stirred assumption, and sets the stage for methods proposed in Chapter 5 for using the conflated approach to consider stratification. Finally, issues are summarized in Section 4.7.

4.2 The Principle Convective Regimes

It would be an impossible task to develop and implement models for predicting convection coefficients for all possible flow regimes encountered within buildings. Even the presence and location of furniture, and the movement and metabolic functioning of occupants alters indoor air flow patterns, and thus convective heat transfer at internal surfaces. Given this, the pragmatic way forward is to broadly classify the air flows encountered within buildings and to establish methods for resolving their influence on internal convection.

The following subsections present a scheme for classifying the flow regimes commonly found within buildings, and summarize a literature survey of h_c algorithms for resolving these flow regimes.

4.2.1 A classification scheme

The forces that drive indoor air flow can be described as either mechanical or buoyant. Mechanical forces are generally caused by fans or by wind entering through openings. Fans can be located within the room and circulate air from a heating or cooling device. Or, they can be located in an air-handling unit that supplies and extracts air to the room for ventilating, heating, or cooling purposes. Buoyant forces can result from heat sources located within the room (radiators, occupants, office equipment, etc.) or from surface-to-air temperature differences. The surface-to-air temperature differences can be caused by heat transfer through the building fabric (e.g. the cold surface of a window), solar insolation, or fabric-embedded conditioning devices (e.g. in-floor heating, chilled ceiling panels). In some cases, both mechanical and buoyant forces can be significant drivers of room air motion.

Further subdivision is possible. For example, in the case of buoyancy-driven flow resulting from the presence of a wood stove, whether the stove is located in the middle of the room, or next to an external window, will have an affect of the room's air flow pattern. In the latter case, the warm plumes rising from the stove will be cooled by heat transfer through the window, causing a competition in the buoyant effects. Similarly, in the case of mechanically driven flows, the location of the supply air diffuser and the extract will influence which walls experience wall jet flow and which experience impinging flow. Clearly some factors have a greater influence than others. Whether the room is mechanically ventilated or not has a more profound influence on the convective regime than does the location of diffusers and extracts.

A pragmatic approach was established for calculating convection coefficients for this research—both for the purposes of thermal simulation, and for resolving the pivot point between the thermal and CFD modelling domains. This classifies the indoor air flow into one of five categories according to the type and cause of the driving force. This scheme is presented in Table 4.1. A scheme based upon fundamental considerations could have been devised, however this pragmatic approach best fits the building simulation process.

Convective regimes A and B describe situations where the flow is caused principally by buoyant forces. In the former case, the buoyancy is caused by surface-to-air temperature differences resulting from heat transfer through the fabric, a sun patch, or a embedded conditioning device. The latter describes a substantially different buoyancy induced flow regime, this caused by the presence of a heating device located within the room. Flows which are principally mechanically driven have been broken into two categories: regime C considers HVAC systems that deliver and extract air to the room, while regime D is for sealed rooms with circulating fans. Finally, convective regime E covers the case of mixed flow where both mechanical and buoyant forces are present and significant.

Given this classification scheme, the task becomes one of selecting methods for calculating convection coefficients for each of these five regimes.

4.2.2 Calculating convection coefficients: summary of a literature survey

The literature was extensively surveyed for methods appropriate for calculating convection coefficients for the five flow regimes. No attempt is made here to provide a comprehensive listing of the available algorithms. Rather, the reader is referred to the following sources which collectively provide a listing of the available methods: Dascalaki et al (1994), Spitler (1996), Halcrow (1987), Khalifa and Marshall (1990), and Hatton and Awbi (1995).

Many methods exist, but none is universal. Some are general in nature while the applicability of others is restricted to specific building geometries and HVAC systems. Most are simple in form, often regressions of empirical data which give h_c as a function of room-air and surface temperatures.

convective regime	driving force	cause of driving force
A	Buoyant	Surface-to-air temperature difference, caused by one of the following: • heat transfer through the external envelope; • solar insolation to walls or floor (i.e. sun patch); • in-floor heating; • chilled ceiling panels; • heated walls (e.g. hydronic wall panels).
B	Buoyant	Heating device (e.g. radiator, stove) located within room.
C	Mechanical	Air handling system (central or zonal) delivering supply of heated or cooled air to room through ceiling, floor, or wall-mounted diffusers. Exhaust air mechanically extracted or exfiltrated.
D	Mechanical	Heating or cooling device with circulating fan. No intentional supply or extract of air from room.
E	Mixed flow (mechanical and buoyant)	Mechanical forces caused by air handling system (central or zonal) delivering supply of heated or cooled air to room through ceiling, floor, or wall-mounted diffusers. Buoyant forces caused by surface-to-air temperature differences (as described above).

Table 4.1: Classifying the principle convective regimes

Many of the methods were rejected for the current research because their applicability is too restricted, or they are of limited appeal in building modelling. For example, the method of Chandra and Kerestecioglu (1984) is only applicable for rooms naturally ventilated by open windows. Further, it applies only to the wall opposite the open windows. Another example is the method of Min et al (1956), one of the first for calculating h_c for internal building surfaces. It is applicable for buoyancy-driven flow, but only for floor-heated and ceiling-heated rooms.

Some other methods are of questionable accuracy or applicability in the buildings context. For example, the method of Bohn et al (1984) was rejected because it was developed from experiments conducted within a water-filled enclosure. Given that the transition to turbulence is Prandtl-number dependent, it is difficult to assess how appropriate these correlations are for use in simulating convection within buildings. The method of Altmayer et al (1983) was rejected for different reasons. Firstly, their method is based on a regression of numerical (CFD), rather than empirical, data. Secondly, the CFD-predicted surface convection results were generated for laminar flow, a flow regime rarely encountered in real buildings (as discussed in Chapter 3).

Based upon this review, four methods were selected to address the the buoyant (A and B) and mechanical (C and D) flow regimes listed in Table 4.1. Each of these is described in detail in the following section. Their derivation, applicability, and implementation into ESP-r are treated. No appropriate method could be found for the mixed flow regime (E). Consequently, a new approach is put forward in Section 4.4.

4.3 Convection Coefficient Algorithms Selected from the Literature

4.3.1 The Alamdari and Hammond method

The Alamdari and Hammond (1983) method was introduced in Chapter 2. Their correlations (the equations are given in Table 2.1 on page 19) are applicable for purely buoyant flow, and only where buoyancy is caused by a temperature difference between a surface and the surrounding room air. They are not (as discussed by Alamdari and Hammond) appropriate for cases where buoyancy is generated by a heating device, such as a radiator. Consequently, the applicability of this method is restricted to Table 4.1's convective regime A (all causes of the driving force).

The Alamdari-Hammond method was one of the first to be developed specifically for building applications. Their correlations are cast in a convenient dimensional and continuous form. Separate correlations are given for: vertical surfaces; stably-stratified horizontal surfaces (e.g. warm air above a cool floor); and buoyant flow from horizontal surfaces (e.g. cool air above a warm floor). The correlations span laminar, transitional, and turbulent flow regimes, and cover the full range of temperatures and dimensions relevant to building applications.

Rather than conducting new experiments, they drew upon data reported in the literature to develop their correlations. These data were derived from experiments conducted with *isolated* or *free* surfaces. This is significant as some authors (e.g. Awbi and Hatton 1999) claim that isolated surface data may not be applicable for characterizing internal convection; this because room air motion more closely approximates flow within an *enclosure*. Results reported in the literature (e.g. Khalifa and Marshall 1990; Awbi and Hatton 1999) indicate that the Alamdari-Hammond equations tend to predict lower h_c than data collected within enclosures (some of these comparisons have been erroneously made, for reasons that will be explained later). However, there is contrasting empirical evidence to suggest that the Alamdari-Hammond correlations accurately predict convection within enclosures (Arnold et al 1998). As the Alamdari-Hammond equations have been utilized in a number of simulation programs (ESP-r and others, such as APACHE and TAS), there is also significant experience to speak to their validity.

4.3.2 The Khalifa method

Experimental approach

Khalifa (1989) conducted experiments in a room-sized test cell to produce correlations specific to internal convection within buildings. The test cell's configuration was varied and experiments repeated to assess a number of common convection regimes. Different heating systems (e.g. radiator, in-floor heating, convective heating) were analyzed, as was the placement of the heating device (e.g. underneath a window or facing a window). The room was windowless in some cases, whereas a single-glazed window was present in others.

The walls, ceiling, window, and heating devices were instrumented with thermocouples and thermistors. Convective heat transfer at internal surfaces was not measured directly, but rather derived from temperature measurements. This was accomplished by treated the building surfaces as heat-flux meters. Once steady-state conditions were reached, the convective heat transfer was derived by evaluating heat balances at the internal surfaces (see Figure 4.1),

$$q_{conv} = q_{rad} + q_{back-loss} \tag{4.1}$$

Where q_{conv} $\{W\}$ is the convective heat transfer from the room air to the surface and q_{rad} $\{W\}$ is the net radiant exchange with the room's other internal surfaces and objects located within the room. $q_{back-loss}$ $\{W\}$ is the conductive heat transfer (assumed to be one-dimensional) through the wall.

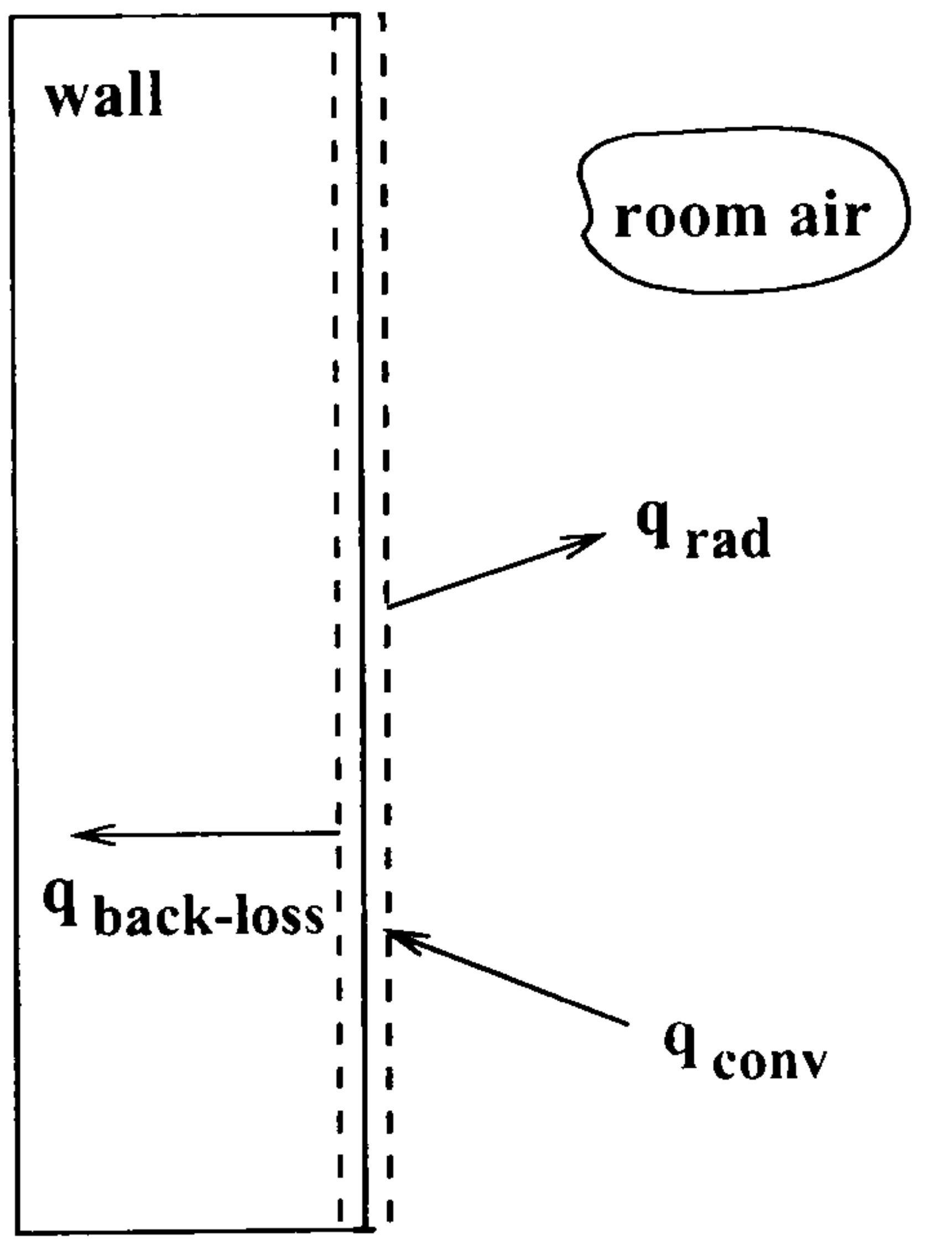

Figure 4.1 Heat balance at internal surface of wall

The convection coefficient was then calculated from q_{conv} using the averaged room air ($T_{room-air}$) and surface (T_{surf}) temperatures,

$$h_c = \frac{q_{conv}}{A_{surf}(T_{room-air} - T_{surf})} \tag{4.2}$$

Where A_{surf} is the surface area $\{m^2\}$.

Since one-dimensional conduction was assumed and steady-state conditions prevailed, $q_{back-loss}$ was easily calculated from the measured temperature difference across the wall section, the wall's conductivity having been characterized with a guarded-box test. $T_{room-air}$ and T_{surf} were measured, so the remaining step in calculating h_c was to quantify q_{rad}.

q_{rad} could have been determined using measured surface temperatures and emissivities and calculated view factors. However, because he felt its magnitude was sufficiently small, Khalifa chose to neglect q_{rad} in equation 4.1. Care was taken to minimize radiation exchange by covering surfaces with aluminum foil (which has a low emissivity in the longwave spectrum). Further, Khalifa assessed that neglecting q_{rad} would introduce only small errors in h_c (14% in the worst case). However, this error analysis was performed using a mean-radiant-temperature approach. With this, the "equivalent" temperature for a surface's radiant exchange is calculated using an area-weighted average of the surface temperatures within the room. This tends to underestimate the radiant exchange because small surfaces (such as a hot radiator) have little impact on the equivalent temperature, even though they significantly affect q_{rad} due to their placement and high temperature. q_{rad} would be most significant in cases with the greatest temperature differences, such as the hot radiator facing the cold window. Furthermore, it is uncertain whether the radiator and window surfaces were foil covered. If not, the high emissivities of these surfaces would result in even greater q_{rad}.

For these reasons, it is felt that neglecting q_{rad} had a more significant impact on the derived h_c values than Khalifa estimated. Consequently, it is believed that Khalifa's results tend to overestimate h_c. Although there are insufficient data available to determine the degree of overestimation, the errors would be greatest in the cases with large temperature differences between surfaces (such as the hot radiator facing the cold window). Notwithstanding, Khalifa's work represents a significant contribution, as he provides h_c data for room configurations not analyzed by others.

h_c correlations

Khalifa correlated the derived h_c to surface-air temperature differences ($\Delta T = |T_{room-air} - T_{surf}|$). Some local h_c values are reported, but since the variation over the surfaces was not large, the correlations are given in surface-averaged form. Variations in the room air temperature were observed from measurement point to measurement point, but averaged values were used in developing the correlations. Therefore, the resulting correlations are in a form that can be used with the well-stirred model. It is important to note that the Khalifa correlations do not include a length scale. This because all experiments were conducted in a single chamber of fixed dimensions. Consequently, these equations should not be applied for geometries that deviate significantly from the experimental conditions.

A total of 36 correlations were generated, but by combining similar results the data were collapsed into a series of 10 equations. These 10 equations are recommended for use in building simulation programs and are summarized in Khalifa and Marshall (1990). Of these, 8 correlations were selected for inclusion in ESP-r. These are recorded in Table 4.2. The table's *equation* column corresponds to the equation numbers assigned by Khalifa and Marshall.

As can be seen, Table 4.2 lists correlations for walls, windows, and ceilings. No correlations are given for floors, because Khalifa did not derive h_c values for the floor. The *applicability* column describes the configurations covered by each equation. Rooms heater by radiators, warm walls, warm floors, and circulating fan heaters can be characterized. Two radiator placements are considered: underneath a window or located elsewhere. In addition, the selection of the h_c equation for walls is sensitive to the placement of the heating device. For instance, when the room is heated by a circulating fan heater, equation 8 is used to calculate h_c for the wall with impinging flow, whereas equation 3 is used for all other walls.

As mentioned, eight of the 10 recommended correlations were implemented into ESP-r. The two correlations that were excluded were those for "large" vertical and horizontal surfaces (equations 11 and 12 in Khalifa and Marshall, 1990). Unlike the other correlations, these were not generated with data collected at the room's internal surfaces, but rather from measurements taken on the exterior surfaces of the test cell. As such, they characterize the heat transfer from the experimental chamber to the surrounding laboratory. For this reason, and for the fact that the data span a very narrow temperature range, these two equations were deemed inappropriate for the current application.

In terms of the air flow classification scheme presented in Table 4.1, the eight Khalifa correlations implemented into ESP-r address convective regimes A (all sources of the driving force but chilled ceiling panels), B, and D.

Comparison with other methods

Some comparisons of the h_c values predicted by the Alamdari-Hammond correlations and two of the Khalifa equations were made in Chapter 2. Comparisons like this are problematic, however, in that the two methods consider different flow regimes. The Alamdari-Hammond method characterizes cases where convection is driven by surface-air temperature differences, whereas many of Khalifa's equations characterize convection caused by heating devices or a fan. Four equations do resolve flows generated by heated surfaces, but these cannot predict h_c for the heated surfaces themselves. For example, for a 2.5m high wall which is 2°C cooler than the room air, Alamdari-Hammond predicts a convection coefficient of 1.7 W/m^2K. For the same temperatures, the Khalifa method predicts: $h_c = 2.7W/m^2K$ if the room is conditioned by a radiator located under a window; if the room is conditioned with a radiator located elsewhere, it predicts $h_c = 2.5W/m^2K$ for the wall next to the radiator and $h_c = 2.4W/m^2K$ for the other walls; and if the room is conditioned with a circulating fan heater, $h_c = 3.5W/m^2K$ for the wall opposite the fan.

equation	surface	applicability	h_c correlation
5	walls	• Rooms heated by radiator. • Radiator not located under window. • Only for surfaces adjacent to radiator.	$1.98 \cdot \Delta T^{0.32}$
6	walls	• Rooms heated by radiator. • Radiator located under window.	$2.30 \cdot \Delta T^{0.24}$
		• Rooms with heated walls. • Not applicable for heated wall.	
8	walls	• Rooms heated by circulating fan heater. • Only for surfaces opposite fan.	$2.92 \cdot \Delta T^{0.25}$
3	walls	• Rooms heated by circulating fan heater • For surfaces not opposite fan.	$2.07 \cdot \Delta T^{0.23}$
		• Rooms with heated floors.	
		• Rooms heated by radiator. • Radiator not located under window. • For surfaces not next to radiator.	
9	windows	• Rooms heated by radiator. • Radiator located under window.	$8.07 \cdot \Delta T^{0.11}$
10	windows	• Rooms heated by radiator. • Radiator not located under window.	$7.61 \cdot \Delta T^{0.06}$
7	ceilings	• Rooms heated by radiator. • Radiator located under window.	$3.10 \cdot \Delta T^{0.17}$
		• Rooms with heated walls.	
4	ceilings	• Rooms heated by circulating fan heater.	$2.72 \cdot \Delta T^{0.13}$
		• Rooms with heated floors.	
		• Rooms heated by radiator. • Radiator not located under window.	

Table 4.2: Khalifa (1989) h_c correlations implemented into ESP-r

It is interesting to compare the h_c values predicted by Khalifa's equations for walls and windows. For a room heated with a radiator located under the window, a wall which is 3°C cooler than the room air has a convection coefficient of 3.0 W/m^2K. A window located within the wall at the same temperature (in practice it would usually be lower) has an h_c of 9.1 W/m^2K. For an 8°C ΔT, the wall has $h_c = 3.8 W/m^2K$ (27% higher than the lower ΔT) and the window has $h_c = 10.1 W/m^2K$

(only 11% higher than before). Therefore, the window has significantly higher h_c, but is less sensitive to ΔT. This may be because the convective regime is dominated by the warm plume rising from the radiator, and is relatively unaffected by the downwards buoyancy forces created next to the cold window. It is also very likely that neglecting q_{rad} in deriving the correlations has inflated the window h_c values more than the wall values (as discussed above).

Implementation

As mentioned in Chapter 2, ESP-r uses a single h_c calculation method throughout the building: the same equation is used to calculate h_c for every wall, for example. A redesign of this approach was necessary in order to implement the suite of Khalifa methods because, as described above, different equations are used for walls in the same room depending on their location relative to the heating device. As well, convection regimes may vary from room to room, necessitating different treatments throughout the building. Therefore, a scheme was devised in which each internal surface was attributed with a flag (named ICOR) to associate it with an h_c equation. Chapter 5 will show how a surface's ICOR flag can vary dynamically to respond to changing flow regimes. Figure 4.3 shows a code fragment illustrating how the ICOR flag was used to implement the suite of Khalifa equations and to reimplement the Alamdari-Hammond correlations.

```
[fragment of SUBROUTINE HTBUOY]
      IF(ICOR.EQ.1)THEN
C-------Alamdari and Hammond.
        HC=((1.50*((DT/HEIGHT)**0.25))**6.0
     &     +(1.23*((DT)**(1.0/3.0)))**6.0)**(1.0/6.0)

      ELSEIF(ICOR.EQ.5)then
C------ Khalifa & Marshall correlation for walls for the following
C-------room configurations (Table 2, eq.6 of K&M paper):
C-------1) radiator located under window;
C-------2) room heated by heated vertical wall, but NOT applicable for
C-------   the heated surface.
        HC=2.30*(DT**0.24)

      ELSEIF(ICOR.EQ.7)THEN
C-------Khalifa & Marshall correlation for the following
C-------room configuration (Table 2, eq.5 of K&M paper):
C-------1) radiator in room, but radiator NOT located under a window,
C-------   surface under consideration located next to radiator.
        HC = 1.98*(DT**0.32)
 . . .
```

Figure 4.3: Code fragment illustrating ICOR and implementation of Khalifa correlations

4.3.3 The Awbi and Hatton method

Experimental approach

Awbi and Hatton (1999) performed a series of experiments to characterize natural convection from heated room surfaces. Convection was experimentally determined in two enclosures of differing size in order to assess scale affects. One chamber was of typical room dimensions, while the other was a 1m cube. Like Khalifa's experiments, a single wall surface was cooled. The room was conditioned by electrically heated plates affixed to the surfaces. A single surface (wall, floor, or ceiling) was heated in each experiment.

Like Khalifa, they derived the convective heat transfer from temperature measurements. However, there were some significant differences in the approach. The surface heat balance also considered the electrical energy input to the heater plates ($q_{elec-input}$),

$$q_{conv} = q_{rad} + q_{back-loss} - q_{elec-input} \tag{4.3}$$

Unlike Khalifa's experiments q_{rad} was not minimized by covering the surfaces with a low emissivity material, but nor was it neglected from the surface heat balance. It was calculated using a radiosity approach that considered view factors between surfaces.

Convection coefficients were calculated from q_{conv} in the same manner as Khalifa (equation 4.2, page 77). However, unlike Khalifa who used average room conditions for the reference temperature ($T_{room-air}$ in equation 4.2), Awbi and Hatton used the temperature at a distance of 100 mm from the heated surface. This could disqualify the use of the Awbi-Hatton equations in conjunction with the well-stirred method. However, as they observed that the air temperature varied little outside the 100 mm layer next to the surface, the temperature at 100mm can act as a reasonable proxy for the room's air-point temperature.

h_c correlations

Two separate walls were examined in the large chamber: one facing the cold surface and one adjacent to the cold surface. A single wall of the small cube was also assessed. Interestingly, they found that the surface-averaged h_c (local h_c variations were not found to be that significant) for all three walls could be represented with a single equation when the hydraulic diameter was used as the length scale. This equation and a similar one for the floor are presented in Table 4.4.

Only a portion of the wall or floor surface was heated in some of the experiments. This simulated a solar patch, for example, where solar insolation strikes only part of a wall or floor. Awbi and Hatton found that these data could also be represented with the general equation if h_c was evaluated with the hydraulic diameter of the entire surface. In other words, the scale effect of the convection is a function of the enclosure size, and not of the size of the heated area.

Awbi and Hatton also produced a correlation for heated ceilings, but this was not implemented into ESP-r for two reasons. Firstly, this configuration is rarely found in practice. Secondly, there was significant stratification in the chamber during these experiments, making the measurement of a reference temperature difficult. Rather than taking the temperature at 100mm from the ceiling (as was done for the wall and floor cases), they used the room's midpoint to establish the reference

surface	h_c correlation
heated walls	$\frac{1.823 \cdot \Delta T^{0.293}}{D_h^{0.121}}$
heated floors	$\frac{2.175 \cdot \Delta T^{0.308}}{D_h^{0.076}}$
• D_h is the hydraulic diameter of the surface: $D = \frac{4A}{P}$, where A is the area and P the perimeter.	

Table 4.4: Awbi and Hatton (1999) h_c correlations implemented into ESP-r

temperature. Therefore, application of this correlation within the context of a well-mixed convection model would introduce significant errors.

The Awbi-Hatton equations are useful for characterizing Table 4.1's convective regime A (all but the chilled ceilings). However, it is important to note these equations apply only to the heated surface. For example, the floor of a room conditioned with an in-floor heating system can be characterized with the Awbi-Hatton method, but the walls cannot (these are cooled surfaces). As such, the Awbi-Hatton method is complimentary to Khalifa's. Building on the example above, Khalifa's equation 3 can characterize the walls, and his equation 4 can characterize the ceiling. The Khalifa method lacks a correlation for the floor but this is the one surface (in this case) that can be resolved with the Awbi-Hatton method. Therefore, together these methods can collectively establish the convection coefficients for the entire enclosure.

Comparison with other methods

It is tempting to compare the h_c values predicted by the Awbi-Hatton method against those calculated with the Khalifa correlations; however, such a comparison would be erroneous and misleading. Khalifa's equations 3, 4, 6, and 7 do characterize the same convective regime as Awbi-Hatton: flow in an enclosure generated by a single heated surface. But, the Awbi-Hatton equation applies only to the heated surface, whereas the Khalifa correlations can calculate h_c for all surfaces except the heated one. Therefore, no direct comparison of the two methods is possible.

Comparison with the Alamdari-Hammond method is possible, however. Figures 4.2 and 4.3 compare the two methods for floors and walls for surface-air temperature differences of 1°C to 6°C. Two floor and two wall geometries are considered: square floors with 3m and 8m widths; and 3m and 8m wide, 2.4m high walls.

Figure 4.2 illustrates the Awbi-Hatton equation's inverse relation between h_c and wall width. This is a result of boundary layer interaction, which has a greater influence in smaller enclosures. However, the influence of width is seen to be minor: there is only a 4% variance from 3m to 8m over

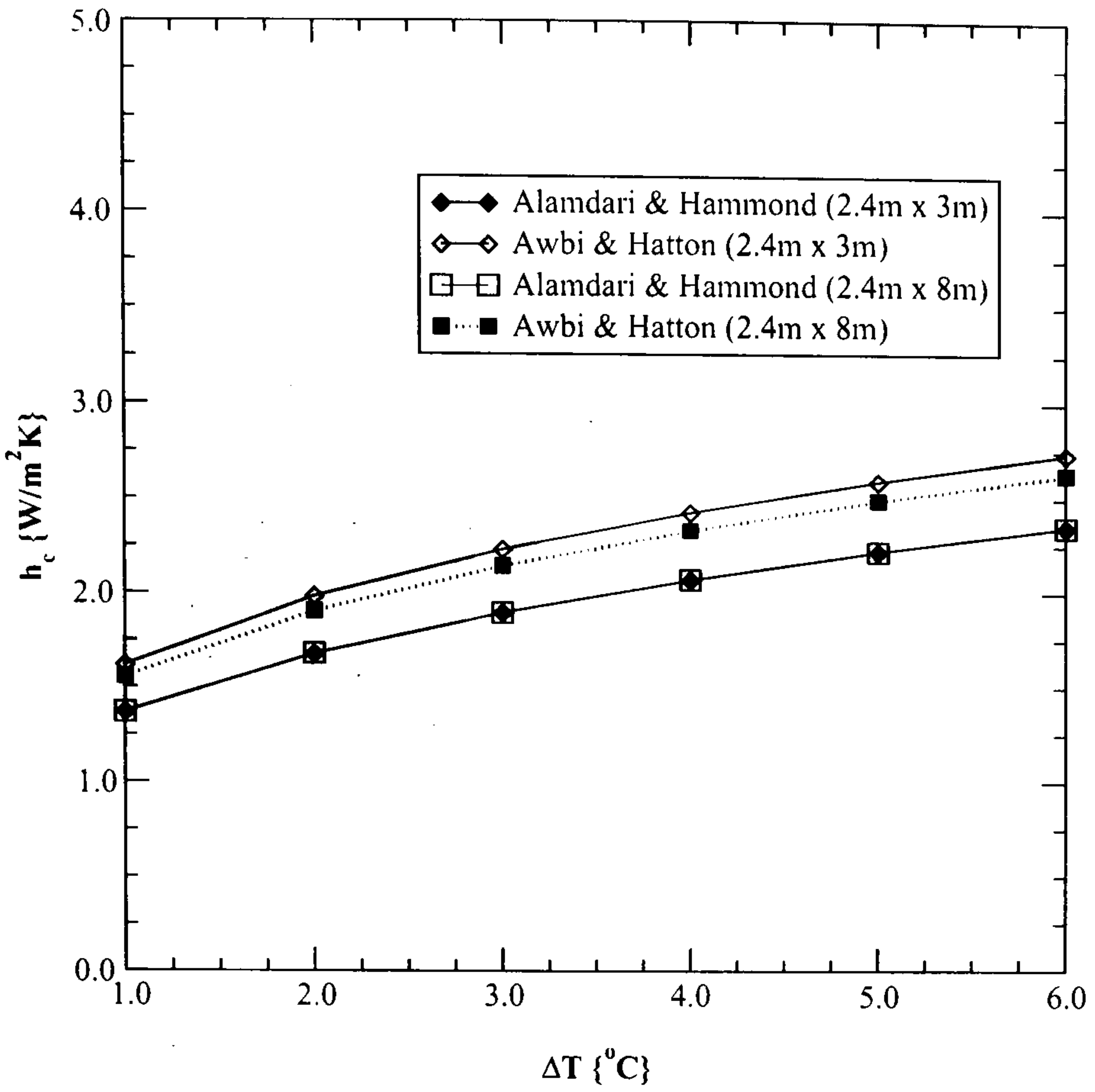

Figure 4.2 Convection coefficients for heated walls

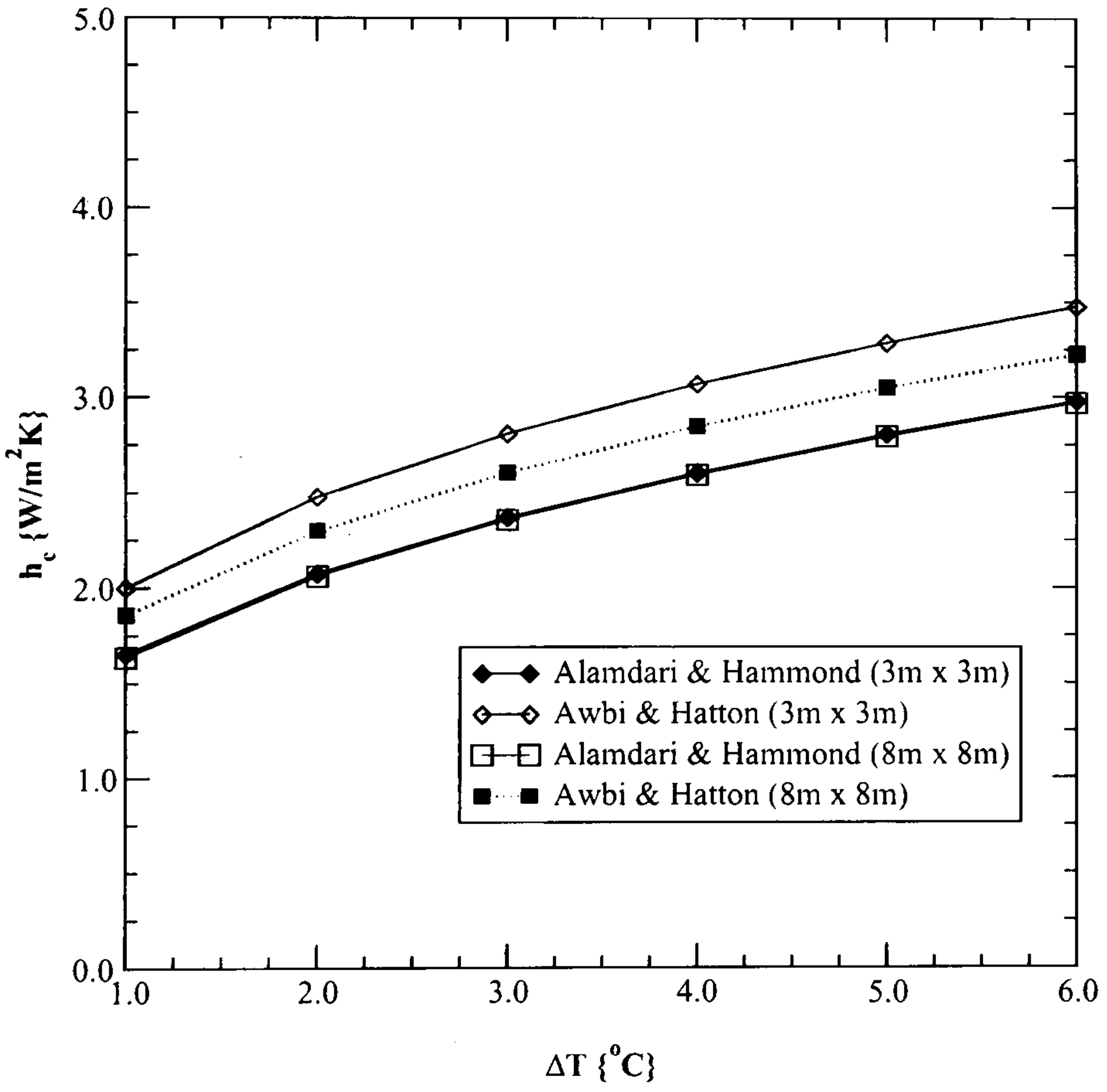

Figure 4.3 Convection coefficients for heated floors

the range of temperatures examined. Since the Alamdari-Hammond method was developed with isolated surface data, it does not respond to the wall width. Compared to the Alamdari-Hammond method, the Awbi-Hatton equation results in higher h_c. Differences are significant, but not dramatic:

they range from 12% to 18% in this case.

Although the hydraulic diameter appears in Alamdari and Hammond's correlation for buoyant flow over horizontal surfaces, Figure 4.3 shows that the equation is quite insensitive to geometry: nearly identical h_c values are calculated for the small and large floor. This is because the hydraulic diameter appears only in the laminar portion of Alamdari-Hammond's blending formula (see Table 2.1 on page 19), whereas turbulent effects dominate even at modest temperature differences. Therefore, in effect the Alamdari-Hammond equation is insensitive to geometry over the range of dimensions and temperatures found within buildings. In contrast, the Awbi-Hatton equation responds significantly to geometry. It produces h_c values about 8% higher for the small floor compared to the large floor. Again, this reflects the effect of the enclosure: cool boundary layers descending down the walls interact with the warm plumes rising from the floor. As with the walls, the Awbi-Hatton method produces greater h_c than Alamdari-Hammond. The differences between the two methods is again significant, but not dramatic: in the order of 15% to 20% for the small floor and 10-15% for the larger floor.

The two Awbi-Hatton equations were implemented into ESP-r in a similar fashion as the Khalifa method.

4.3.4 The Fisher method

Experimental approach

Fisher (1995) performed a series of experiments to characterize the convection heat transfer at the internal surfaces of rooms. He examined forced convection regimes for typical air flow rates and for a typical room geometry. Two types of jets, both important in room air flow analysis, were assessed: radial ceiling jets (air-supply diffusers located in centre of ceiling) and free horizontal jets (air supply located in wall).

The room was isothermal (all internal surfaces were maintained at the same temperature) in most of the experiments. However, a single wall was chilled in one group of ceiling-diffuser experiments to examine the combined influence of buoyancy and forced effects. The experiments only examined room cooling, the incoming air stream always being colder than the air within the room and the room surfaces.

The room's interior surfaces were covered by 53 panels, each an independent electrical resistance heater. The heat input to each panel was controlled to maintain the desired surface temperature, and each panel's surface temperature measured with a pair of thermocouples. The surface convection was derived from these measurements by evaluating surface energy balances for each panel using the same approach as Awbi-Hatton (see equation 4.3, page 82).

$q_{back-loss}$ was minimized by enclosing the experimental room within a larger enclosure maintained at a similar temperature, resulting in a negligible temperature difference across the walls of the experimental chamber. Knowing the view factors between, and temperatures of, all 53 panels, q_{rad}

was calculated for each surface. All 53 panels were of similar temperature in the isothermal experiments, so q_{rad} was minimized (this contrasts with Awbi-Hatton's approach). Therefore q_{conv} and $q_{elec-input}$ were the only significant variables in the heat balances. This minimized the uncertainty in deriving the convection coefficients.

The experiments spanned a range of air flows and inlet temperatures. For each experiment, once steady conditions within the room were achieved, measurements were taken for at least one hour. q_{conv} was calculated for each panel using time-averaged data and the individual panel results assembled to give the convective heat transfer from the ceiling, floor, and walls (the results for all four walls were grouped).

Convection coefficients were calculated from q_{conv} by normalizing the heat transfer by the temperature difference between the surface (T_{surf}) and the air supplied to the room through the ventilation system ($T_{diffuser}$),

$$h_c = \frac{q_{conv}}{A_{surf}(T_{surf} - T_{diffuser})} \tag{4.4}$$

$T_{diffuser}$ was found to be the most appropriate choice for normalizing the convection coefficients as this minimized the uncertainly of the correlations. This contrasts with the approaches of Khalifa and Awbi-Hatton, who used the room air temperature as the reference (see equation 4.2, page 77).

h_c correlations

Correlations for h_c were developed for three classes of flow: ceiling jets in isothermal rooms; ceiling jets in non-isothermal rooms; and free horizontal jets in isothermal rooms. For the first class, Fisher found the surface convection to be independent of the inlet velocity of the ceiling jet, but rather to depend upon the jet's volumetric flow rate. He also found the buoyancy forces of the cold jet to be negligible relative to the viscous Coanda effect adhering the jet to the ceiling and walls. The form of the correlations, expressed in dimensionless parameters, reflect these observations,

$$Nu = C_1 + C_2 \cdot \mathrm{Re}_e^{C_3} \tag{4.5}$$

The Nusselt number and *enclosure* Reynolds number are given by,

$$Nu = \frac{h_c V_{room}^{1/3}}{k} \tag{4.6}$$

$$\mathrm{Re}_e = \frac{\rho \dot{V}_{diffuser}}{\mu V_{room}^{1/3}} \tag{4.7}$$

Where V_{room} is the room volume $\{m^3\}$, k is the thermal conductivity of air $\{W/mK\}$, $\dot{V}_{diffuser}$ is the volumetric flow rate of the air entering the room at the diffuser $\{m^3/s\}$, and μ is the molecular viscosity of air $\{Pa \cdot s\}$. C_1 and C_2 are empirical constants.

With the free horizontal jets the buoyancy forces of the cold jet also had a negligible impact on convection from the walls and floor. Therefore, equation 4.5 was also used to correlate these data. Convection from the ceiling, though, was affected by buoyancy. Consequently, an alternate equation was used to correlate the ceiling data,

$$Nu = C_1 + C_2 \cdot \frac{\mathrm{Re}_e^{C_3}}{Ar_e} \tag{4.8}$$

The enclosure Archimedes number is given by,

$$Ar_e = \frac{g\beta V_{room}^{5/3} \Delta T}{\dot{V}_{diffuser}^2} \tag{4.9}$$

Where β is the thermal expansion coefficient of air and ΔT is the temperature difference between the air supplied to the room ($T_{diffuser}$) and the extracted air (effectively the room air temperature if well-mixed conditions prevail).

As ESP-r operates with convection coefficients and temperatures, Fisher's non-dimensionalized correlations were recast in dimensional form. Air properties were evaluated at typical temperatures, and the room's volume was removed as a variable (all Fisher's experiments were conducted with a single room geometry, so inclusion of V_{room} in equations 4.6, 4.7, and 4.9 is difficult to justify anyway). The resulting correlations, as they were implemented into ESP-r, are given in Table 4.5. Two sets of equations for the ceiling jets are given in the table. The first were derived from Fisher's non-dimensional correlations while the second are from Fisher and Pedersen (1997), who correlated the same data using a different functional form. Both sets of correlations were implemented into ESP-r because the differences are substantial at some flow rates of interest (the two are compared in Appendix C). The ceiling jet correlations span a very wide range of air flows, $3 \leq ac/h \leq 100$ (the data of Spitler et al 1991, acquired in the same experimental facility, were used for the higher flow rates), while the horizontal jet correlations are applicable for $3 \leq ac/h \leq 12$.

Fisher's third set of correlations, those for ceiling jets in non-isothermal rooms, were not implemented into ESP-r. In these experiments a single wall was maintained at a cold temperature while the remaining surfaces were heated. The data illustrated that buoyancy forces, both of the cold jet and due to density gradients adjacent to the cold wall, influenced surface convection. However, these experiments only examined cases for which $T_{coldwall} < T_{diffuser} < T_{hotwalls}$, a regime unlikely to be encountered in real (or modelled) buildings. Consequently, although the observations are of interest, the results are of limited applicability in building simulation.

Implementation

Application of the Alamdari-Hammond, Khalifa, and Awbi-Hatton correlations within ESP-r was straightforward. These methods express h_c as a function of T_{surf}, $T_{room-air}$, and room geometry.

configuration	**surface**	**h_c correlation**
Ceiling jets in isothermal rooms	walls	$-0.199+0.190\cdot(ac/h)^{0.8}$
		$0.19\cdot(ac/h)^{0.8}$
	floor	$0.159+0.116\cdot(ac/h)^{0.8}$
		$0.13\cdot(ac/h)^{0.8}$
	ceiling	$-0.166+0.484\cdot(ac/h)^{0.8}$
		$0.49\cdot(ac/h)^{0.8}$
Free horizontal jets in isothermal rooms	walls	$-0.110+0.132\cdot(ac/h)^{0.8}$
	floor	$0.704+0.168\cdot(ac/h)^{0.8}$
	ceiling	$0.064+0.00444\cdot\frac{(ac/h)^{2.8}}{\Delta T}$

- ac/h is ventilation rate measured in room air changes per hour.
- ΔT is the temperature difference between the air supply and the extract.

Table 4.5: Fisher (1995) and Fisher and Pedersen (1997)
h_c correlations as implemented into ESP-r

The geometry is supplied by the user while both temperatures are a product of ESP-r's time-step thermal simulation. Calculating h_c with Fisher's correlations is more complex. These require additional data: the flow rate of air mechanically supplied to the room (ac/h) and (for the free horizontal jets) the air temperatures at the diffuser ($T_{diffuser}$) and the extract ($T_{room-air}$ is a reasonable proxy for well-mixed rooms). Furthermore, the h_c calculated with Fisher's correlations cannot be used directly in the internal surface and air-point heat balance equations because ESP-r uses $T_{room-air}$ as the reference temperature for convection, whereas Fisher's method uses $T_{diffuser}$ (contrast the convection term in equation 2.14, page 18 with equation 4.4, page 86).

The latter issue was addressed by scaling the h_c predicted by Fisher's correlations so that the heat transfer was preserved in the internal surface and zone air-point heat balances. Equating the convection term in the internal surface heat balance (equation 2.14) with q_{conv} in equation 4.4 leads to,

$$h_{c,ESP-r}=h_{c,Fisher}\cdot\frac{(T_{surf}-T_{diffuser})}{(T_{surf}-T_{room-air})} \qquad (4.10)$$

Where $h_{c,ESP-r}$ is the convection coefficient required for the internal surface and zone air-point heat balances and $h_{c,Fisher}$ is the convection coefficient predicted by the correlations in Table 4.5. Alternatively, the surface convection term could have been moved to the right side of the internal surface (equation 2.15, page 20) and zone air-point (equation 2.21, page 22) heat balance equations, with q_{conv}

being calculated each time-step using equation 4.4. This alternate approach was investigated but discarded because it effectively retarded the simulation of surface convection by one time-step without offering any advantage over the scaling approach.

The remaining step in implementing the Fisher correlations was then to establish ac/h and $T_{diffuser}$ on a time-step basis. These variables reflect the operational state of the HVAC system and are a result of the dynamic interaction between it and the building. ac/h and $T_{diffuser}$ can be solved by ESP-r, but only if the user constructs an explicit model of the secondary HVAC system (creating zones to represent ducts, adding component models to represent coils, fans, dampers, and establishing control laws governing the component interactions). Although possible, this modelling resolution is undesirable for many types of analyses.

Consequently, a more general approach was developed whereby the HVAC system was modelled in an idealized fashion. With this, the control behaviour of the system is modelled in order to predict the air flow regime induced in the zone, an approach consistent with ESP-r's idealized control capabilities. Models for the two most common forced-air HVAC systems are covered: variable-volume (VAV) and constant-volume variable-temperature (CVVT) systems. The algorithm, which is described in detail in Appendix D, considers user-specified ranges for ac/h and $T_{diffuser}$ and the conditioning of outdoor ventilation air, and returns the ac/h and $T_{diffuser}$ required to condition the zone.

Having calculated ac/h and $T_{diffuser}$, the convection coefficients for use in the internal surface and air-point heat balances are calculated using equation 4.10 and the correlations in Table 4.5.

Applicability

The room was cooled by the mechanically supplied air in all of Fisher's experiments: forced-air heating systems were not examined. An obvious question is whether the correlations are equally applicable to heated rooms. For the ceiling jet, Fisher found the buoyancy forces of the cold jet to be negligible relative to the viscous Coanda effect adhering the jet to the ceiling and walls. The functional form of the ceiling jet correlations, which do not include terms representing the buoyancy of the incoming jet, reflect this observation. When the system is heating, supplying air at a warmer temperature than the room air and surfaces, the buoyancy forces will in fact assist the jet to adhere to the ceiling.

Consequently, there should be no significant difference in the flow regime between heating and cooling, at least for this room geometry and for these air flow rates. Therefore, it is believed that Fisher's correlations are equally applicable to room heating when there are negligible surface-air temperature differences. The impact of extrapolating the method beyond the temperature ranges examined by Fisher ($10^oC \le T_{diffuser} \le 20^oC$ for horizontal jets; $10^oC \le T_{diffuser} \le 25^oC$ for ceiling jets) was examined with a series of exploratory simulations. This revealed stable and predictable behaviour. Therefore, the method described in this section is used equally for characterizing forced convection with heating and cooling systems[16].

Buoyant forces caused by temperature differences between internal surfaces and the room air were very small in Fisher's experiments. Sixteen combinations of ventilation rate and temperature were assessed in the isothermal ceiling-jet case. In all cases, the internal surfaces were controlled to 30°C. The corresponding mean room-air temperatures (not reported) were estimated by performing a heat balance on the room: the average surface-air temperature difference over the 16 experiments was 2.4°C; the greatest difference was 3.8°C. Therefore, the correlations listed in Table 4.5 are strictly applicable when the flow regime is dominated by a mechanically driven jet, buoyancy caused by surface-air temperature differences being negligible (convective regime C in Table 4.1). They are not generally applicable to mixed flow (convective regime E), wherein buoyant forces adjacent to some surfaces are important (e.g. a window exposed to the outside) and may assist or oppose the mechanical forces.

4.4 A New Method for Establishing Convection Coefficients for Mixed Flow

The previous section described the four algorithms selected for characterizing convection coefficients for the buoyancy and mechanical regimes listed in Table 4.1 (i.e. regimes A through D). However, no suitable method was found in the literature for resolving mixed flow (regime E) in which both mechanical and buoyancy forces are important. This section demonstrates how common this flow regime is within buildings and then presents a new h_c calculation approach.

The need

In mechanically ventilated rooms both buoyant and mechanical forces will, in general, be present, and both can be significant. Additionally, it is difficult (usually impossible) to predetermine whether a configuration will be dominated by buoyant forces or mechanical forces. This is best illustrated by example (the data cited in this example were generated with an ESP-r simulation).

A well-insulated office with large glazing area is heated by a constant-volume forced-air system delivering 6 ac/h through ceiling-mounted diffusers. On a relatively cold day (-20°C) a supply air temperature of about 30°C is adequate to heat the office, the heating load being offset by solar gains and gains from lights, occupants, and office equipment. The internal surface of a wall exposed to the outdoors is about 4°C colder than the averaged room air temperature. The warm jet emanating from the diffuser spreads across the ceiling towards the walls (see Figure 4.4). The jet adheres to the ceiling rather than dropping due to viscous and buoyant forces. The jet cools as it flows down the external wall. Velocity is relatively low by this point due to the jet's spread. As the surface of the wall is

---

[16] For free horizontal jets, ΔT in the ceiling correlation is set to unity when there is heating. The presence of ΔT in this equation accounts for the dropping of the jet from the ceiling when the jet is colder than the room air. Since in the case of heating this effect would be reversed and there is insufficient information to determine the positive impact ΔT would have on h_c, this conservative approach was taken to negate the impact of the jet's buoyancy.

colder than the surrounding room air, air adjacent to the wall contracts (becomes more dense) and sinks due to gravity: buoyancy assists the mechanically driven jet, both effects forcing flow down the wall.

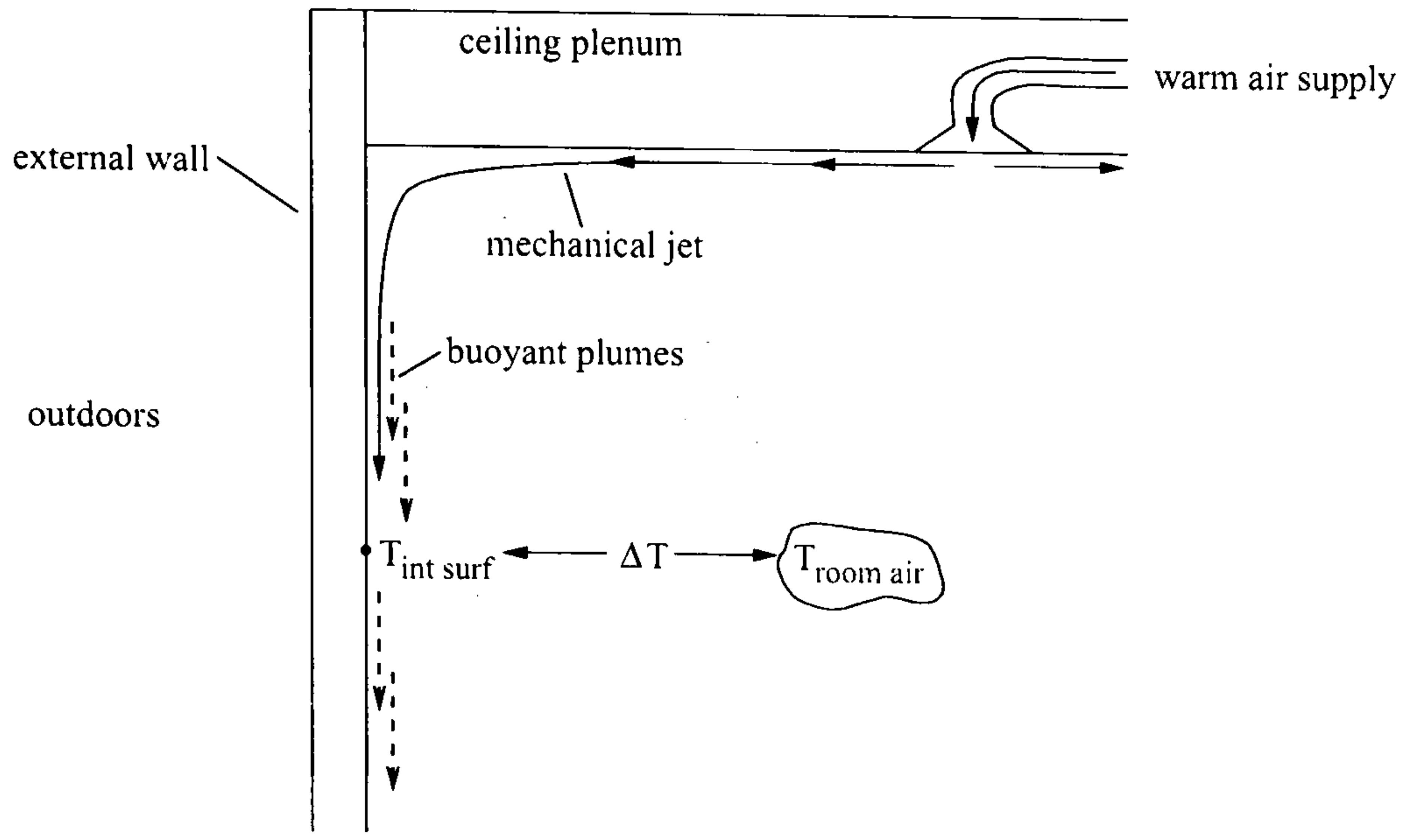

Figure 4.4: Assisting mechanical and buoyant forces

Both mechanical and buoyant forces drive the air down the wall, but is the flow predominantly buoyant or mechanically driven? This question can be answered (qualitatively) by comparing the surface convection predictions resulting from the use of two of the previously described h_c algorithms. The Alamdari-Hammond method predicts the strength of convection caused by the buoyancy forces while ignoring the impact of the jet. In contrast, the Fisher method predicts the strength of the convection regime established by the jet while ignoring the influence of the buoyancy forces. For these conditions, the Alamdari-Hammond correlation results in approximately 8 W/m^2 of convection from the room air to the external wall. The Fisher ceiling jet correlation predicts about 7 W/m^2. As the predictions are of the same order, it is concluded that both buoyant and mechanical forces are significant in this case. Since the forces are assisting, the surface convection should be higher than either method alone predicts. In this case, flow is mixed and the forces are assisting.

But during the morning start-up period when the mechanical system has to recover from a night setback, the temperature of the supply air is much warmer (about 40°C) while the wall-air temperature difference is lower (approximately 3°C). In this situation, the Alamdari-Hammond correlation leads to 6 W/m^2 whereas 15 W/m^2 of convection results when the Fisher equation is used. In this situation the mechanical forces are dominant.

And on a sunny and relatively warm (-3°C) day the heating system supplies air just above the room air temperature and the wall is only about 2°C cooler than the room air. In this situation, use of the Alamdari-Hammond algorithm results in 3.5 W/m^2 of convection, whereas there is only about 1 W/m^2 of convection when the Fisher equation is used. Therefore, in this situation buoyant forces are dominant.

The examination of other mechanically ventilated buildings in different climates would, of course, lead to different observations. Although, in general, it would be seen that buoyant forces are dominant for some thermal and operational states, while for others mechanical forces are dominant, while yet for others both are important. In some cases the mechanical and buoyant forces will assist (act in the same direction) while in others they will oppose (act in opposite directions) or act transversely (act in perpendicular directions). Neither the Alamdari-Hammond nor the Fisher approach alone can fully characterize the convective regime in these mixed flow cases. Consequently, an algorithm is required that can consider the combined influences of buoyant and mechanical forces on surface convection.

The algorithm

The new mixed flow algorithm builds upon the strengths of the Alamdari-Hammond and Fisher methods. It models the mixed flow regime by "blending" the impacts of the buoyant and mechanical forces using the Churchill and Usagi (1972) approach. Churchill and Usagi presented a general expression for correlating heat transfer processes in which asymptotic solutions (X and Z) are known for small and large values of the independent variable,

$$Y = (X^a + Z^a)^{1/a} \tag{4.11}$$

where a is the Churchill-Usagi blending coefficient, an empirical constant selected to best represent the data. This blending approach is shown schematically in Figure 4.5.

Churchill and Usagi proposed the use of their method for representing any data (experimental or theoretical) for which the limiting behaviour is known. It has been used extensively and successfully in correlating heat transfer problems which are governed by two or more driving forces (many examples are provided by Churchill and Usagi themselves; further examples are given by Raithby and Hollands, 1985). Indeed, the Churchill-Usagi expression was used by Alamdari and Hammond (and Awbi and Hatton to correlate local h_c values) to blend laminar and turbulent effects.

Although the Alamdari-Hammond and Fisher correlations employ different independent variables, the two can be considered as assymptotic solutions for the general mixed flow case. Essentially, the two methods characterize the limiting behaviour of mixed flow. When forced effects are overwhelmed by buoyancy, surface convection can be adequately characterized with the Alamdari-Hammond correlations. Whereas the Fisher correlations are sufficient to calculate surface convection when forced effects dominate. When both forces are significant and assisting (or acting transversely) the mechanical and buoyant effects will combine to enhance the heat transfer. This situation will arise, for example, when the wall surfaces are at a lower temperature than the room air. This typically occurs at external walls and windows during the heating season. Given this, the convection coefficients for assisting mixed flow can be established with a Churchill-Usagi blending expression,

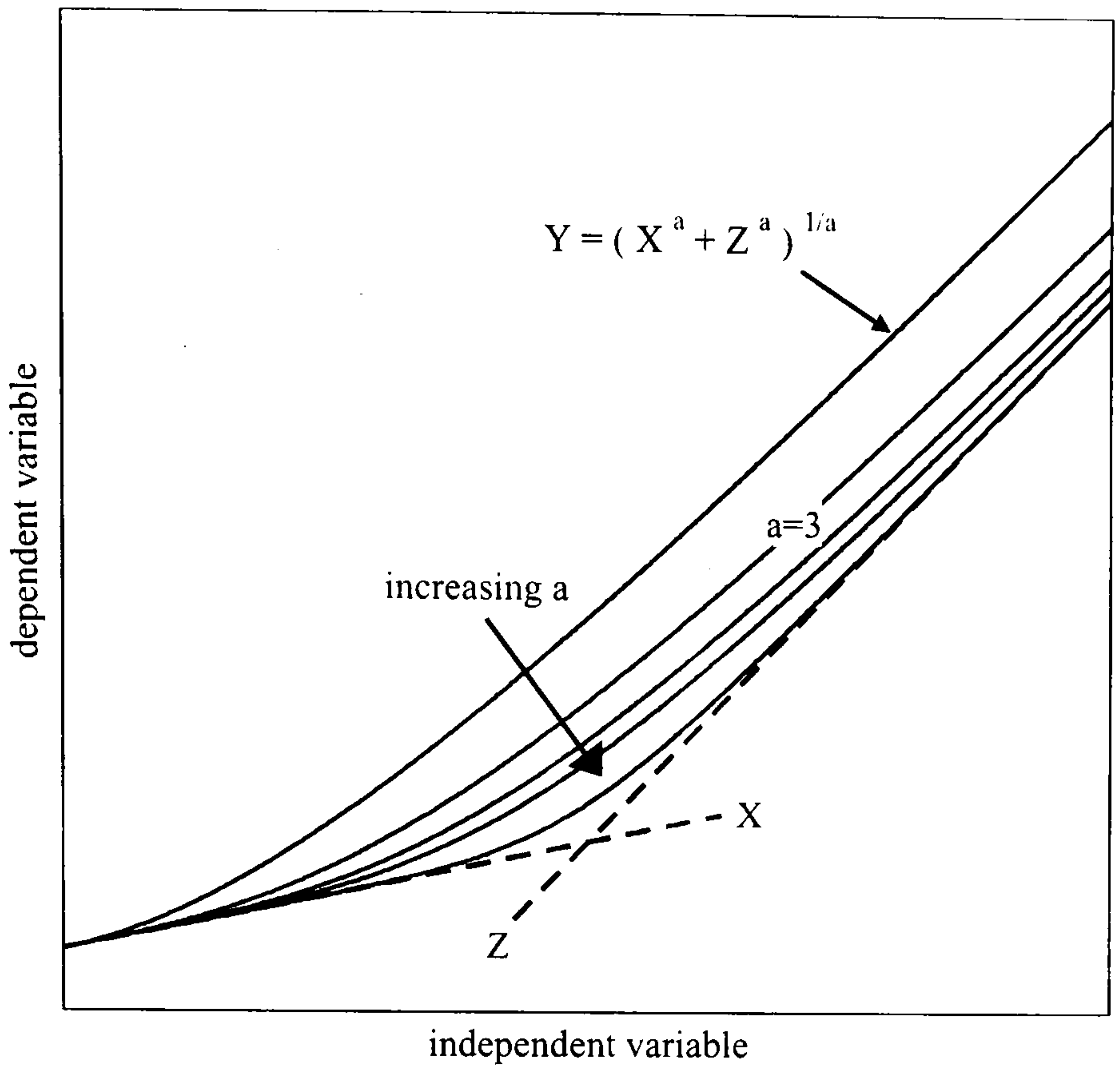

Figure 4.5: Churchill-Usagi blending approach

$$h_{c,mixed,assisting} = \left[(h_{c,forced})^a + (h_{c,buoyant})^a\right]^{1/a} \tag{4.12}$$

Where $h_{c,forced}$ and $h_{c,buoyant}$ are the convection coefficients resulting from the mechanical and buoyant forces, respectively.

The blending coefficient (a) is set to three in this model, a value recommended by Incropera and Dewitt (1985) for internal and external mixed convection flows. As shown schematically in Figure 4.5 when both forces are important, a blending coefficient of three significantly augments heat transfer beyond the assymptotic solutions. Larger blending coefficients (greater than 10) give tighter agreement with the assymptotic solutions (and therefore less heat transfer). However, a series of exploratory simulations confirmed that modest changes from the selected value of three have a minimal impact on calculations.

Equation 4.12 reflects the fact that when the forces are assisting or acting transversely, the mechanical and buoyant effects will combine to enhance the heat transfer. The converse is true when the forces oppose. This situation will arise, for example, when the wall surfaces are at a higher temperature than the room air. This typically occurs at external walls and windows during the cooling season and at internal walls receiving significant solar gain. To address this eventuality, a blending formula that subtracts the mechanical and buoyant effects is used when the forces oppose,

$$h_{c,mixed,opposing} = \left|(h_{c,forced})^a - (h_{c,buoyant})^a\right|^{1/a} \tag{4.13}$$

A subtractive-blending formula similar to this is discussed by Churchill (1983). The absolute value of the difference between the convection coefficients is taken here because in certain cases (the discussion at the beginning of this section provided two examples) the buoyant effects may dominate. It is intuitive that opposing forces will reduce the heat transfer; however, convection coefficients approaching zero would be physically unrealistic. Even in stagnant conditions the gaseous conduction between the wall surface and the room air point would justify a finite convection coefficient. Therefore, limits are placed on the applicability of equation 4.13. The blending formula is not allowed to derate the convection coefficient by more than 20% of the greater of the forced or buoyant value. The choice of the value 20% is somewhat arbitrary, although exploratory simulations confirmed that results are relatively insensitive to values in the range of 10% to 40%. Unfortunately, at this time there are no empirical data to validate this heuristic approach.

The final form of the mixed flow correlations is presented in Table 4.6. These reproduce identically the Alamdari-Hammond result when forced effects are unimportant and reproduce identically the Fisher result when buoyant effects are insignificant. When both effects are important and are assisting, it results in a greater h_c than either method alone. And when both effects are significant and oppose, it produces a smaller h_c.

The additive blending equation (equation 4.12) is applied for all floors and ceilings, because on these surfaces buoyant forces always act in a transverse direction to the jet resulting from radial ceiling diffusers. For walls, the simulator performs a test each time-step to determine whether the wall-air temperature difference results in a buoyant force that assists or opposes the mechanically driven jet, and subsequently selects the corresponding equation. As with the Fisher correlations, the algorithm described in Appendix D is used to support the implementation of the mixed flow model by simulating the convective regime induced by HVAC air handling systems.

Example application

A simulation of the office described at the beginning of this section was performed with the new mixed flow model. The calculations were conducted for the month of March using Ottawa weather data. Figure 4.6 plots the convective heat transfer from the room air to an outside facing wall. It compares the predictions of the mixed flow model with those of the Alamdari-Hammond and Fisher methods. The heat transfer is plotted against the surface-air temperature difference (ΔT) to best illustrate the impact of the mixed flow model (alternatively, the surface-diffuser temperature difference could have been selected as the independent variable).

The Alamdari-Hammond model correlates well to ΔT, as expected (see the equations in Table 2.1 on page 19). However, the Fisher correlation does not, as it responds to $T_{diffuser}$, a function of the room's heating load. As factors other than surface-air temperature differences (e.g. infiltration, internal gains) contribute to the room's heating load, there is only a loose correlation between the two. At

surface		h_c correlation
walls	assisting forces	$\left(\left\{\left[1.5\cdot\left(\frac{\Delta T}{H}\right)^{1/4}\right]^6+\left[1.23\Delta T^{1/3}\right]^6\right\}^{(3\cdot 1/6)}+\left\{\left[\frac{T_{surf}-T_{diffuser}}{\Delta T}\right]\cdot\left[-0.199+0.190\cdot(ac/h)^{0.8}\right]\right\}^3\right)^{1/3}$
	opposing forces	$max\ of\left\{\begin{array}{l}\left\lvert\left\{\left[1.5\cdot\left(\frac{\Delta T}{H}\right)^{1/4}\right]^6+\left[1.23\Delta T^{1/3}\right]^6\right\}^{(3\cdot 1/6)}-\left\{\left[\frac{T_{surf}-T_{diffuser}}{\Delta T}\right]\cdot\left[-0.199+0.190\cdot(ac/h)^{0.8}\right]\right\}^3\right\rvert^{1/3}\\ 80\%\cdot\left\{\left[1.5\cdot\left(\frac{\Delta T}{H}\right)^{1/4}\right]^6+\left[1.23\Delta T^{1/3}\right]^6\right\}^{1/6}\\ 80\%\cdot\left\{\left[\frac{T_{surf}-T_{diffuser}}{\Delta T}\right]\cdot\left[-0.199+0.190\cdot(ac/h)^{0.8}\right]\right\}\end{array}\right.$
floor	buoyant	$\left(\left\{\left[1.4\cdot\left(\frac{\Delta T}{D_h}\right)^{1/4}\right]^6+\left[1.63\Delta T^{1/3}\right]^6\right\}^{(3\cdot 1/6)}+\left\{\left[\frac{T_{surf}-T_{diffuser}}{\Delta T}\right]\cdot\left[0.159+0.116\cdot(ac/h)^{0.8}\right]\right\}^3\right)^{1/3}$
	stably stratified	$\left(\left\{0.6\cdot\left(\frac{\Delta T}{D_h^2}\right)^{1/5}\right\}^3+\left\{\left[\frac{T_{surf}-T_{diffuser}}{\Delta T}\right]\cdot\left[0.159+0.116\cdot(ac/h)^{0.8}\right]\right\}^3\right)^{1/3}$
ceiling	buoyant	$\left(\left\{\left[1.4\cdot\left(\frac{\Delta T}{D_h}\right)^{1/4}\right]^6+\left[1.63\Delta T^{1/3}\right]^6\right\}^{(3\cdot 1/6)}+\left\{\left[\frac{T_{surf}-T_{diffuser}}{\Delta T}\right]\cdot\left[-0.166+0.484\cdot(ac/h)^{0.8}\right]\right\}^3\right)^{1/3}$
	stably stratified	$\left(\left\{0.6\cdot\left(\frac{\Delta T}{D_h^2}\right)^{1/5}\right\}^3+\left\{\left[\frac{T_{surf}-T_{diffuser}}{\Delta T}\right]\cdot\left[-0.166+0.484\cdot(ac/h)^{0.8}\right]\right\}^3\right)^{1/3}$
• ac/h is ventilation rate measured in room air changes per hour. • ΔT is the absolute value of the surface-air temperature difference $\{^oC\}$. • H is the height of vertical surfaces $\{m\}$. • D_h is the hydraulic diameter of horizontal surfaces: $D_h = \frac{4A}{P}$, where A is the area $\{m^2\}$ and P the perimeter $\{m\}$.		

Table 4.6: Mixed flow correlations implemented into ESP-r

higher surface-air temperature differences, Alamdari-Hammond tends to dominate, but at lower temperature differences, where buoyant forces are small, the mixed flow result approaches the Fisher value (see region A in Figure 4.6). For a large number of data points the mixed flow model predicts greater heat transfer than both the Fisher model and the Alamdari-Hammond model, indicating that buoyant and forced effects are often both important (see B in Figure 4.6). It is important to note that at low surface-air temperature differences, the Alamdari-Hammond estimates approach zero heat transfer, whereas the mixed flow model produces much higher results.

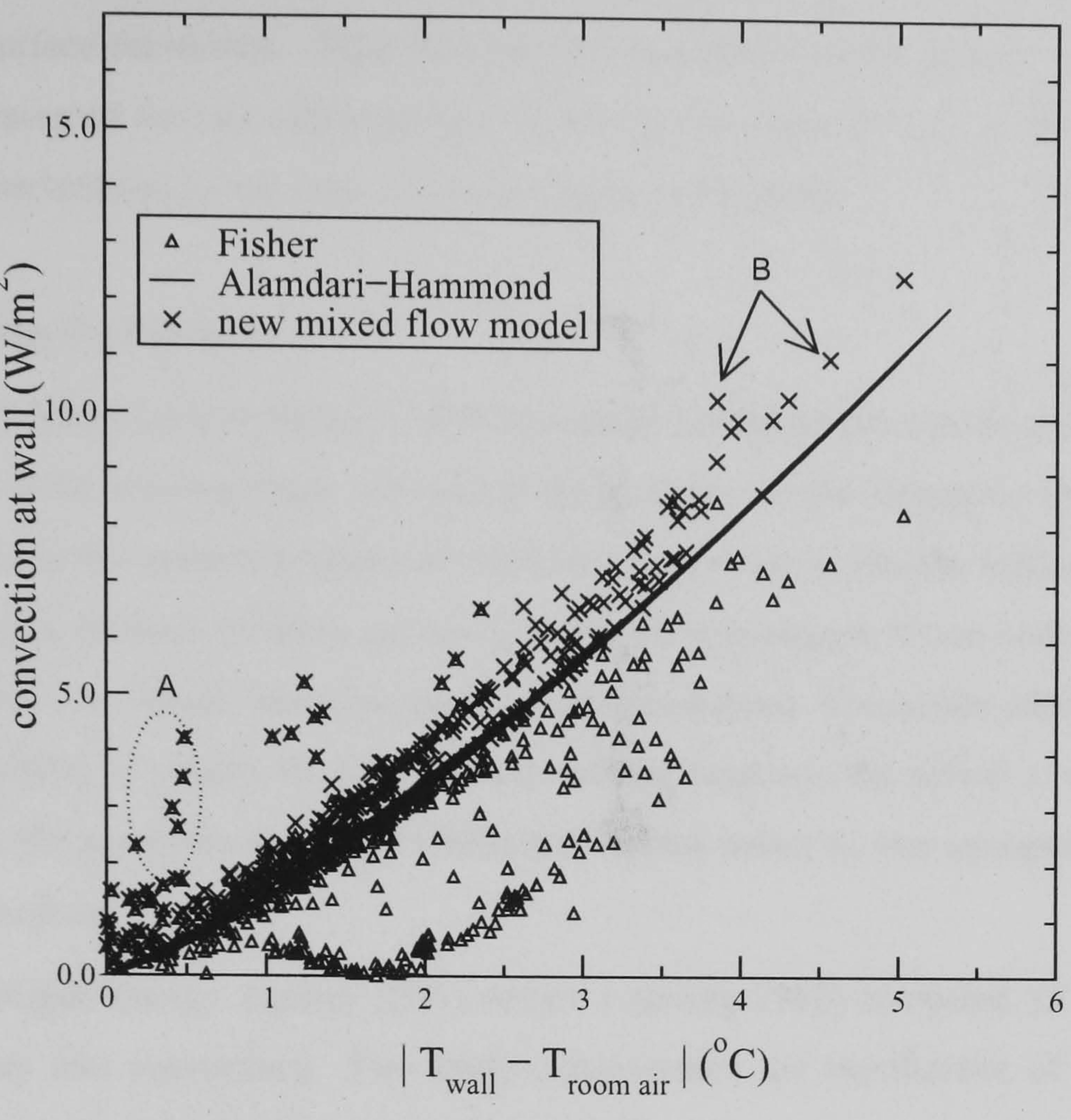

Figure 4.6 Comparison of mixed flow, buoyancy, and forced flow models

Applicability

The mixed flow model is applicable for mechanically ventilated rooms which are heated or cooled with air supplied through ceiling diffusers. Because one of its building blocks is the Alamdari-Hammond method, it is restricted to cases where buoyancy is caused by a temperature difference between a surface and the surrounding room air. It would be trivial to extend the mixed flow model to overcome these restrictions since, in principle, any of the previously outlined forced and buoyant methods could be blended. So, for example, Khalifa's equations 6, 7, and 9 could be blended with one of Fisher's correlations to produce a method for resolving mechanically ventilated rooms with reheating devices located underneath windows.

4.5 Sensitivity of Thermal Simulation to Convection Coefficients

Chapter 2 demonstrated how pervasive convection coefficients are in the zone matrix of equations and it hypothesized that erroneous h_c values would distort the system of equations and lead to prediction errors. A suite of methods for calculating h_c for different flow regimes has been put forward in this chapter. The differences in the h_c values predicted by these methods has been seen to be significant. The significance of these differences is demonstrated in this section by exploring the impact of convection coefficients on thermal simulation results.

A number of researchers have explored how sensitive building simulation results are to the treatment of internal surface convection. Their findings are summarized in this section. To augment this, new results are presented for two configurations. The first is a small test cell, while the second is a (hypothetical) office building constructed to typical Canadian standards.

4.5.1 Evidence from the literature

During a validation exercise Waters (1980) compared simulation predictions against experimental measurements from two buildings. He found the accuracy of the simulation predictions to be strongly influenced by the modelling approach used for heat transfer at internal surfaces. He assessed numerous approaches for each building, including a combined treatment of convection and radiation, various time-invariant h_c values, and a buoyancy-driven correlation. The reason cited for the simulation program's inability to predict the instantaneous heating load over the period of a day (in one of the buildings) was the use of time-invariant coefficients, which meant h_c was unresponsive to changes in internal air movement.

The International Energy Agency (IEA) Annex 1 (Irving 1982) compared 23 simulation programs for accuracy and consistency. This study demonstrated the significance of convective heat transfer predictions on both peak and annual building loads.

Bauman et al (1983) examined the sensitivity of a simulation program to internal convection treatment. They modelled the south-facing zone of a building located in a cold climate. The physical surfaces within the zone were sub-divided in the model (three model surfaces per physical surface) in order to examine local effects. In one simulation time-invariant h_c values (from ASHRAE Fundamentals) were used. In the second simulation h_c was calculated using standard correlations for buoyancy-driven laminar flow. A more complex procedure was used for the third simulation: the thermal program's predictions of surface temperatures were input as boundary conditions into a CFD code; the CFD program resolved the flow pattern within the room and predicted the h_c for each surface; the h_c values were then input to the thermal simulation program and the simulations repeated until convergence was achieved (very similar to ESP-r's integrated modelling approach outlined on page 32, but performed manually). The heating load predictions over a day were compared, and the differences were seen to be significant. The heating load predicted by the integrated modelling approach was about 50% lower than that predicted with the simpler methods. Of particular interest was the observation that for one surface in the model (the opaque wall beneath the window) the integrated model and the well-stirred approaches predicted heat flow in *opposite* directions, a result of the well-stirred model failing to recognize the local influence of the cold downdraft of air by the window.

Alamdari et al (1984) performed an analysis to quantify the sensitivity of heating load predictions to convection coefficients (at both internal and external surfaces). They modelled a hypothetical house with a simulation program, repeating the calculations with two different h_c algorithms. The first used correlations for buoyancy-driven flow while the second employed a more complex procedure based on forced flow. The predicted heating load over a winter day varied by 17% between the two convection algorithms.

The objective of the recently completed IEA BESTEST project (Judkoff and Neymark 1995) was to develop a method for systematically testing, and diagnosing the sources of disagreement between, building simulation programs. Simulations of simple (hypothetical) test buildings were performed with a number of simulation programs and the results compared. Three modelling areas were identified as the primary causes of disagreement between programs, among them the modelling of surface convection and radiation. Specifically on the topic of internal surfaces, the final BESTEST report stated the following:

> *The importance of the internal surface heat transfer coefficients is often underestimated because of the steady state argument that they are only a very small portion of the overall resistance through the exterior wall. However, under transient conditions these coefficients also play an important role in*
>
> - *linking the capacitance of the building to the thermostat control node*
> - *determining how responsive the thermostat is to radiation and convection*
> - *determining how heat from mechanical or solar sources is distributed, and how quickly the thermostat is affected*
> - *affecting surface temperature, especially on solar receiving surfaces.*

Spitler et al (1991) found the choice of h_c to have a significant impact of the predicted benefits of night purging (the use of high ventilation rates at night to pre-cool a building). A room with a thermally massive fabric was simulated with weather data from a hot climate. During the night, whenever the outdoor temperature was sufficiently cool, a high ventilation rate (100 ac/h) was imposed. This strategy was used to pre-cool the building to as low as 13°C to offset the heat gains during the day. Two simulations were performed: the first with h_c values typical of natural convection; in the second an h_c correlation appropriate for these high-ventilation rates was used. The effectiveness of night purging was predicted to be much greater in the second simulation: 35% less cooling was required in January and 13% less in August in the simulation with the appropriate algorithm.

Lomas (1996) compared the predictions of three simulation programs and found that differences in internal convection algorithms were a significant factor in inter-program variability. A number of h_c schemes were assessed in two of the programs: annual heating energy demand was seen to vary by up to 27%.

Clarke (1991) investigated the sensitivity of two simulation programs to a range of alternate internal convection algorithms. The choice of convection algorithm was found to have a significant impact (up to 37%) on both programs' predictions of the annual heating energy consumption of a typical British house. He concluded that alternative h_c algorithms may lead to significantly different design decisions. These results show that when fabric losses dominate the energy balance and when h_c contributes significantly to the fabric's resistance to heat transfer, thermal simulation results will be highly sensitive to h_c.

This literature review indicates that building simulation predictions can be highly sensitive to the modelling of internal surface convection. Although the degree of sensitivity is case-specific, variances of 20 to 40% in energy demand and consumption were noted by some of these authors. More importantly, the predicted benefits from design measures were, in some cases, found to be sensitive to the approach used to model internal surface convection. As a result, the choice of convection algorithm (made by program developer or user) could influence the design decisions drawn from a simulation-based analysis.

4.5.2 First case study: the IEA empirical validation test room

Description of test room

The IEA empirical validation project was undertaken by a joint group from the Energy Conservation in Buildings and Community Systems Programme Annex 21 Subtask C and the Solar Heating and Cooling Programme Task 12 Subtask B. The project consisted of comparing predictions of simulation programs against measured data. Twenty-five results sets from 17 different simulation programs were compared. The project is thoroughly documented in a three-volume report (Lomas et al 1994a, 1994b, 1994c).

Three simple test rooms located in Cranfield (England) were the subject of the comparison (see Figure 4.7). The rooms were built in pairs and separated by heavily insulated party walls. The rooms had attics, they were well insulated, had low infiltration, and had no direct thermal contact with the ground. One room had a double-glazed window, one a single-glazed window, and one was unglazed.

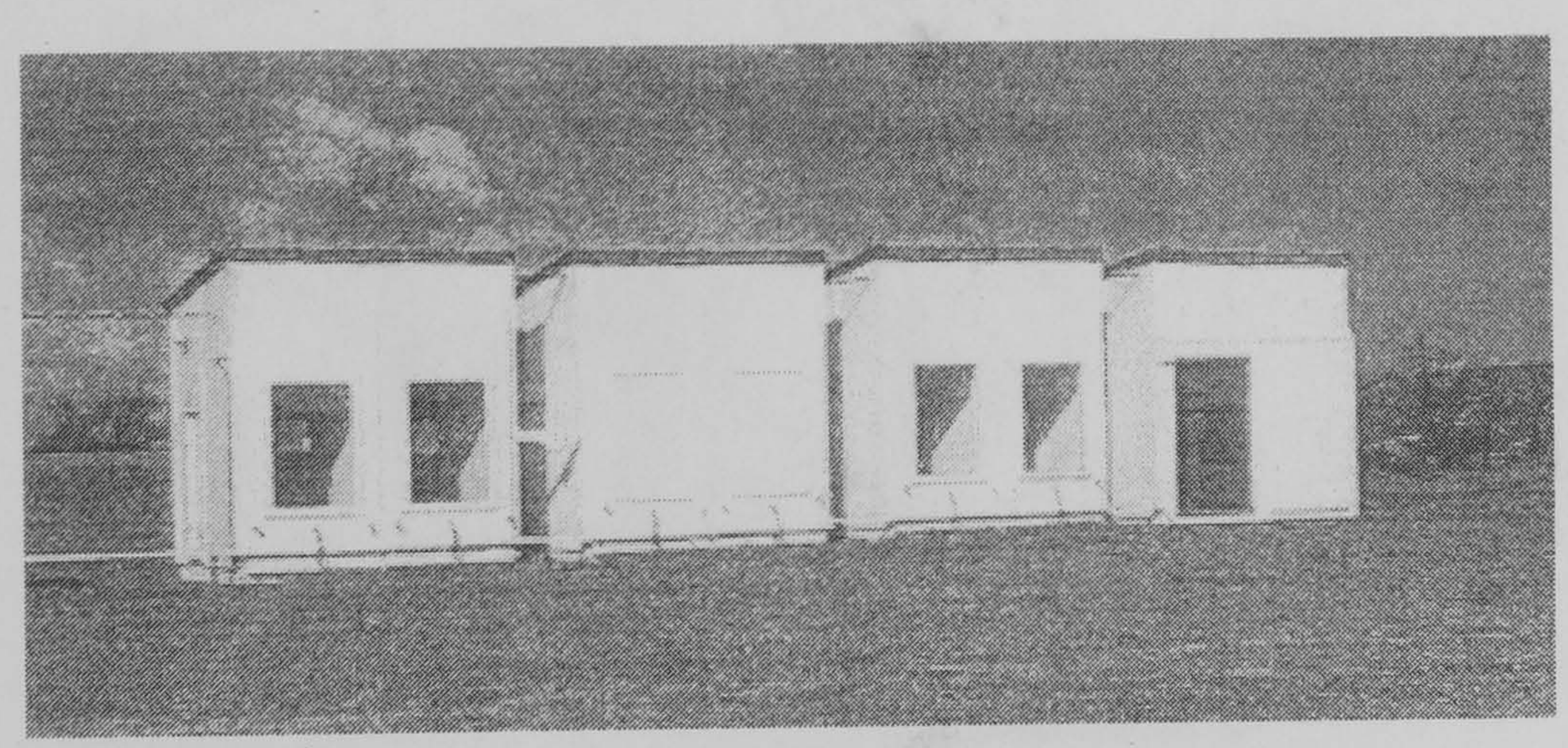

Figure 4.7: Cranfield test rooms (from Lomas et al 1994a)

Each room contained a single oil-filled electrically-heated radiator. These were floor-mounted and located close to the windows. The rooms were monitored over two seven-day periods. During one period (in October), the rooms were heated to a constant temperature of 30°C during the day and were unheated (free floating) at night. The rooms were free-floating during the second seven-day period (in May).

The simulation programs were assessed for their ability to predict the energy consumption (during the heated period) and the temperature extremes. The comparisons of the simulated and monitored performance produced some interesting observations:

- Most programs underpredicted the measured energy consumption.
- Energy-consumption predictions varied considerably between programs (52% variance in the case of the double-glazed room).
- Most programs underpredicted the lowest and highest temperatures in the test rooms.

The IEA report discusses a number of issues that likely contributed to these less-than encouraging results. The modelling of internal convection and the influence of temperature stratification are indicated as two of the primary causes for the discrepancies between programs and between simulated and measured results.

ESP-r model of test room

An ESP-r model of the double-glazed room was created (see Figure 4.8). The model includes the monitored test room, its attached neighbour, their attics, and an obstruction representing the solar shading by the adjacent but unattached test room.

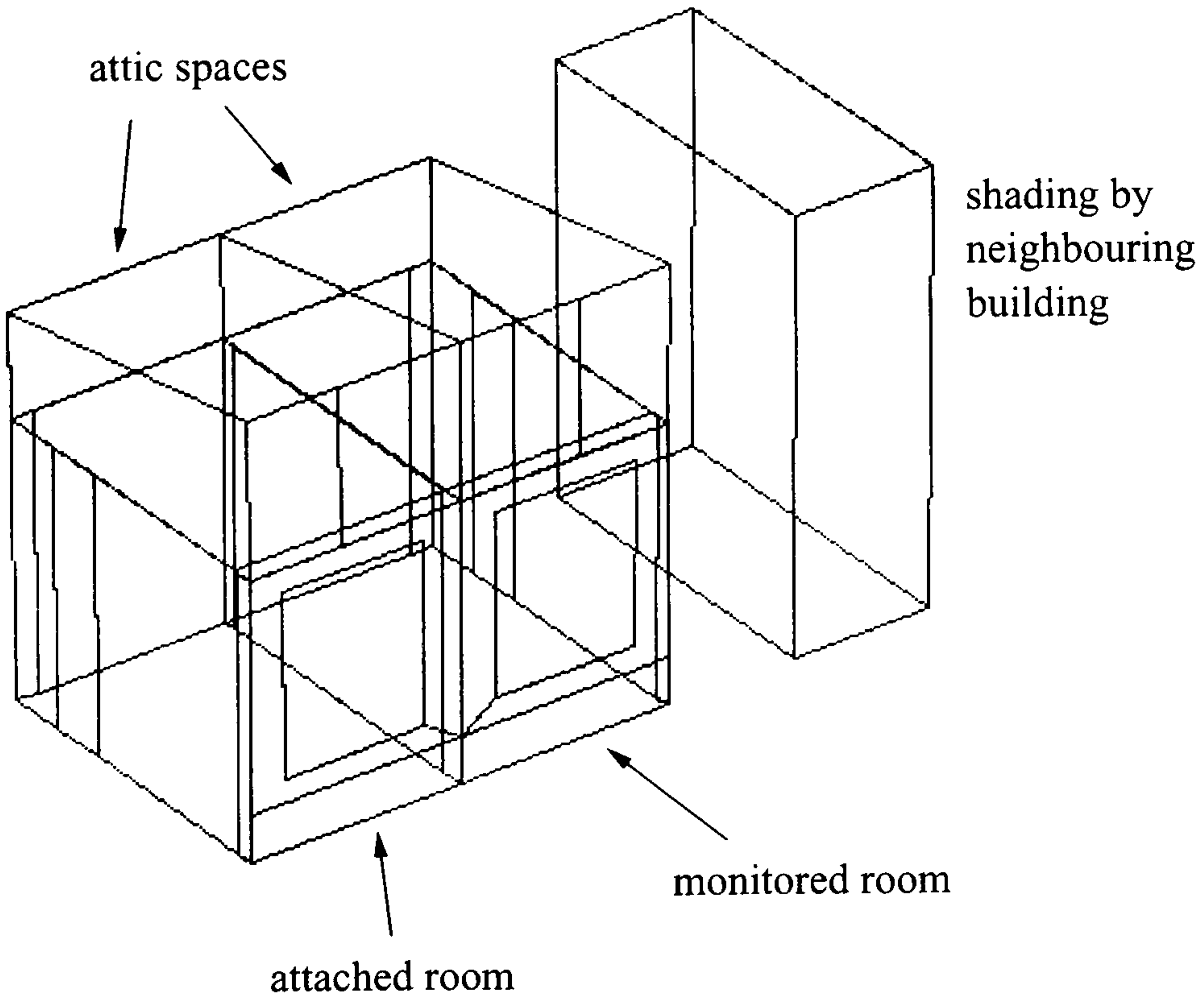

Figure 4.8: ESP-r model of double-glazed test room

The following assumptions were made in creating the model:

- Although there was a heavily insulated party wall separating the monitored test room and its attached neighbour, the neighbouring room was explicitly simulated as there would be slight differences in the thermal conditions of the two rooms due to the timing of solar gains on exterior surfaces and differences in solar shading.
- ESP-r's optional sun-tracking algorithm was used to account for the solar shading caused by the adjacent room to the east (see Figure 4.7).
- The geometric view factors required for simulating internal longwave radiation exchange were calculated using ESP-r's optional ray-tracing procedure.
- As the test rooms were tightly sealed to eliminate air infiltration, zero infiltration was assumed.
- A time-step of 15 minutes was used in the simulation.
- The Perez anisotropic sky model (ESP-r's default) was used to estimate the amount of diffuse solar radiation striking the building surfaces.
- The distribution of solar beam radiation to the room's internal surfaces was determined using ESP-r's optional insolation algorithm.
- The fabric thermal property data provided in the IEA report were used unmodified. The IEA report discusses how these data were derived to account for three-dimensional conduction near corners and how they may underestimate edge effects and thermal bridges.
- ESP-r requires the sky temperature to calculate the net longwave exchange between external surfaces and the surrounding environment (see equation 2.22 on page 23). The sky temperature is not available in weather files, but rather is a derived quantity calculated as a function of the humidity. No humidity data were provided in the IEA study for the October heated period, so typical values for England were assumed.
- Convection coefficients for internal surfaces were calculated using ESP-r's default treatment (the Alamdari-Hammond correlations).
- Convection coefficients for external surfaces were calculated using ESP-r's default correlation involving wind speed and direction.

Simulations covering both the heated and free-floating periods were performed with this base model. These results agreed closely with the ESP-r results recorded in the IEA report, which were generated for a different model and with an earlier version of ESP-r, thus giving confidence in this model. The energy consumption of the base model for the heated period was predicted to be 67.4 MJ, 24.5% less than the measured value of 89.3 MJ (the uncertainty bands of the measurement were reported to be from 78.1 MJ to 92.7 MJ).

Sensitivity to modelling assumptions and algorithms

The above discussion demonstrates how the building simulationist is forced to make numerous assumptions to abstract the complexities of reality to a model of manageable resolution—this is the art of building simulation. Deciding how to sub-divide the building into thermal zones, selecting which geometric features to include and exclude, and choosing whether to model shading by external objects are common decisions faced by the simulationist. Decisions regarding modelling resolution must be made: should an integrated air-flow model be employed to calculate infiltration and inter-zone air flows or will prescribed values suffice? Should the sun be tracked to determine which internal surfaces absorb solar radiation or is it adequate to use a simpler approach?

The simulationist must deal with uncertainly in many of the input data (e.g. material properties, HVAC equipment efficiencies, weather data) and select representative values. Additionally, some simulation programs offer alternate algorithms from which the simulationist must choose. For example, various algorithms exist for predicting the distribution of diffuse solar radiation on non-horizontal surfaces, for predicting ground heat transfer, and for estimating sky temperatures.

Each one of these myriad decisions will influence simulation results. Some decisions affect the model of the test room, some affect the program algorithms, and some affect simulation parameters. The significance of each decision will depend upon the configuration and upon the goal of the simulation exercise. To assess the sensitivity of internal convection modelling relative to other decisions in this case, a series of 11 additional simulations were performed. In each case a single modelling decision was altered and the IEA test room resimulated for the October heated period. Table 4.7 describes the variance in the modelling approach of each simulation. The first column contains labels which identify each run, while the second and third columns describe the modelling treatment in the base case and the modified case. The modelling variances spanned a realistic range of possible options. For example, as the thermal properties of the fabric were measured there is relatively little uncertainty associated with these inputs; in contrast, there is greater uncertainty in the convection coefficients as these were not measured.

The base simulation was performed with the Alamdari-Hammond correlations. Their use in this case is clearly unjustified as the convective regime in the room is dominated by the radiator located under the window. A plume of warm air will rise from the heater, augmenting surface convection to the window and wall surfaces next to the radiator. Alamdari and Hammond (1983) specifically state that their correlations are not appropriate for this type of convection regime. Notwithstanding, the Alamdari-Hammond correlations were used for the following reasons:

- As this is ESP-r's default approach they are almost invariably used unless specific information is available to characterize the convective regime.
- Little information on the convection regime within the test rooms was provided to the participants in the IEA validation exercise (in contrast to the detailed data provided for the opaque envelope).
- In this absence of information, use of the Alamdari-Hammond correlations could be justified as they are generally accepted and applied widely within the building simulation community.

To assess the sensitivity of this model to internal convection coefficients the *internal surface convection* case listed in Table 4.7 was simulated using Khalifa's correlations for radiators located under windows (equations 6, 7, and 9 in Table 4.2, page 80). Since Khalifa did not generate correlations for floors, the Alamdari-Hammond relations were used for the floor. Strictly speaking, these Khalifa correlations are only applicable when there is a heat output from the radiator, as they were generated for this convective regime. Consequently, a control capability was added to ESP-r's convection algorithm: the Khalifa correlations were used when the simulation predicted a heat output from the radiator while the Alamdari-Hammond correlations were used when the heater was off.

The results of these simulations are presented in Figure 4.9. These results clearly demonstrate that the IEA test room is much more sensitive to the modelling of internal convection than to any of the other modelling decisions and algorithms examined. Changing the h_c algorithm for internal surfaces increased the heating requirement by 7.9%. This sensitivity is significant, considering that many of the programs involved in the IEA validation exercise model surface convection with fixed convection coefficients (either fixed by the user or "hard coded"). Perhaps surprisingly, the impact of a rather significant change in the fabric characteristics had a much smaller impact (3.3%). Similarly, a significant increase in the room's air leakage was seen to have—in relative terms—little impact (2.7%). The impact of the sky modelling approach is of significance because many simulation programs employ a simplified isotropic treatment, but again this factor is much less significant (4.7%) than decisions regarding internal convection (for this test cell). The influence of a number of the modelling decisions (insolation, the connection to the neighbour, solar shading, view factor calculation, and the simulation time-step) was found to be trivial.

4.5.3 Second case study: a mechanically ventilated office

Description of building

A two-zone (150 m^2 floor area per zone) ESP-r model representing one storey of a shallow floor-plate office building was created (see Figure 4.10). The building, located in Ottawa, has a north-south alignment and is moderately glazed (35% of external wall area), all windows facing east or west. The fabric assemblies, insulation levels, and internal gains are typical of Canadian construction (NRC 1997).

Each zone is conditioned with a constant-volume forced-air mechanical system whose supply-air temperature varies from 13°C to 43°C in response to loads. During occupied hours (5h00 to 20h00 weekdays) the system delivers 60 L/s of outdoor air to each zone. The building is heated to 22°C, with an 18°C setback during unoccupied hours. The cooling setpoint is 24°C but the building is allowed to free float during unoccupied periods in the summer. At 6 ac/h, the HVAC system is adequately sized to meet the peak heating load but cannot satisfy the peak cooling load.

Run	Modelling Variance	
	Treatment in base model	Treatment in this run
internal surface convection	h_c calculated with Alamdari-Hammond correlations.	h_c calculated with Khalifa "radiator under window" correlations when radiator on; with Alamdari-Hammond correlations when radiator off.
simulation time step	Δt = 15 minutes	Δt = 5 minutes
connection to neighbouring cell	The attached room was explicitly simulated.	The attached room was removed and the party wall treated as adiabatic.
solar shading	Shading was explicitly simulated.	Shading was ignored.
view factors for internal long-wave radiation	Explicitly calculated using ray-tracing.	Estimated using an area-weighted approach.
insolation	Accurately calculated using ESP-r's insolation tracking algorithm.	A simplified insolation scheme was applied: all solar gains struck the floor.
infiltration	No infiltration.	0.1 ac/h.
external surface convection	ESP-r's default treatment.	The external convection coefficients were augmented by 50%.
sky model	Perez anisotropic sky model.	Isotropic sky model.
fabric losses	Modelled with data given in IEA report.	Conductivity of wall insulation increased by 10%.
humidity	Typical values for England.	Relative humidity reduced by 20%.

Table 4.7: Sensitivity runs on IEA test room

Impact of h_c algorithm on load predictions

Three annual simulations—identical except for the treatment of internal convection—were performed. The Alamdari-Hammond correlations were used in the first simulation, Fisher's ceiling-jet correlations applied in the second, while the new mixed flow model was utilized in the third. As the Fisher and mixed flow methods are only applicable when the HVAC system is operating, a control capability was added to ESP-r's convection algorithm to revert to the Alamdari-Hammond method when the system is off to more closely approximate the convective regime. It should be noted that the Alamdari-Hammond correlations are not applicable in this case. They are used here to demonstrate

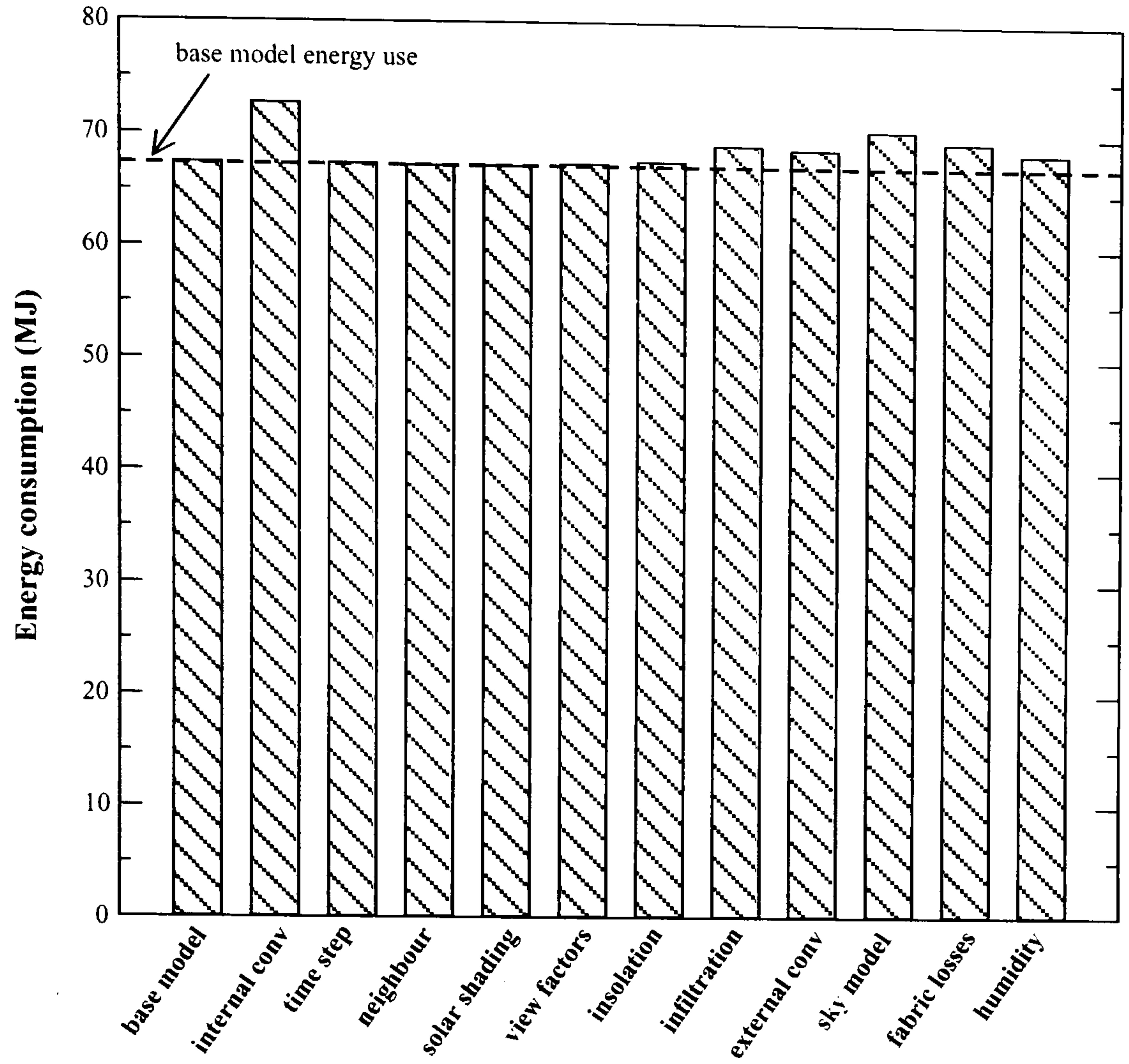

Figure 4.9: Sensitivity analysis of IEA test room

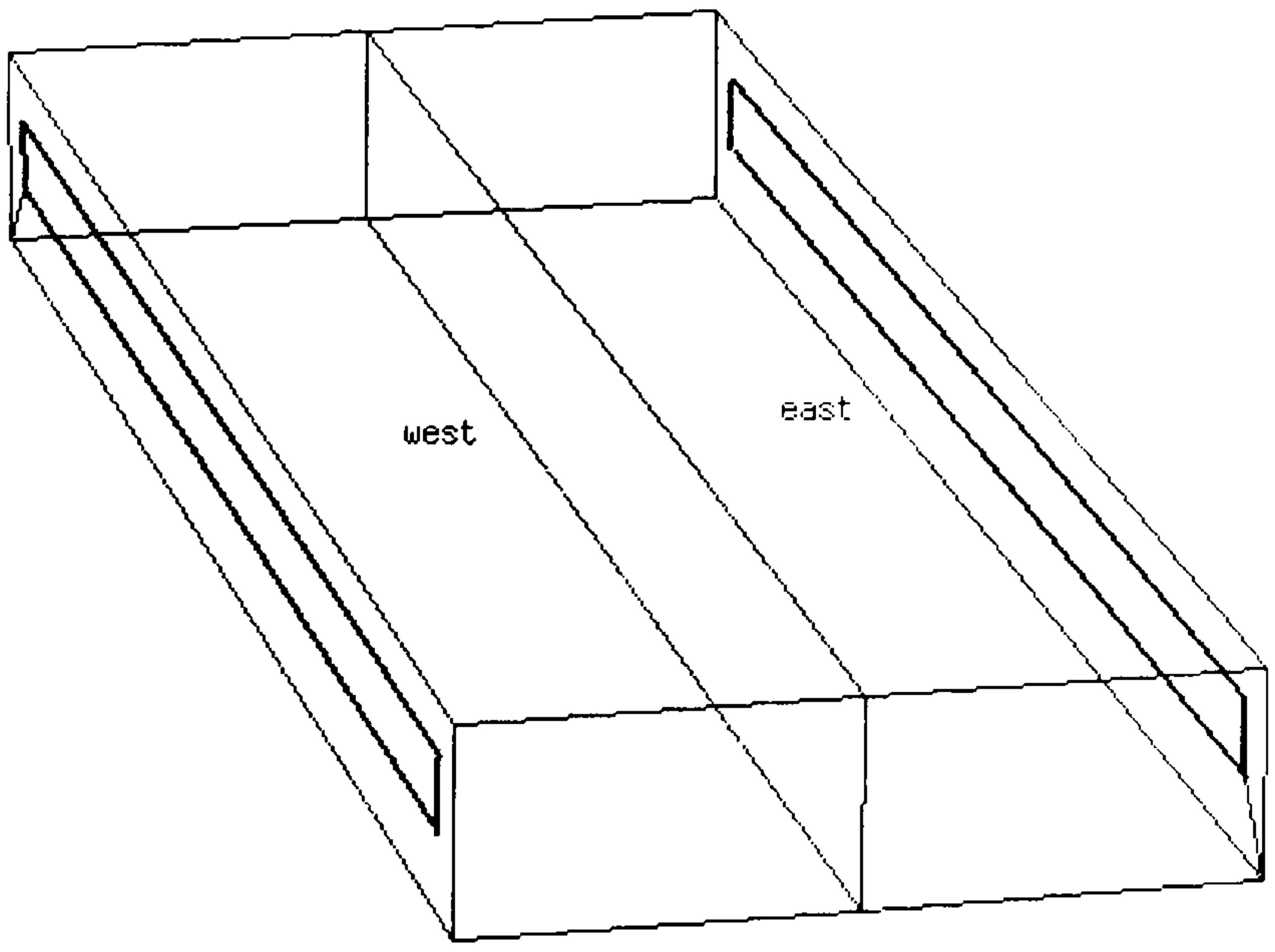

Figure 4.10: ESP-r model of office

the errors that can result when internal surface convection coefficients are not selected in response to the prevailing conditions.

The annual loads (normalized by floor area) placed on the HVAC system's heating and cooling coils are given in Figure 4.11. The mixed flow model predicts significantly higher heating loads than

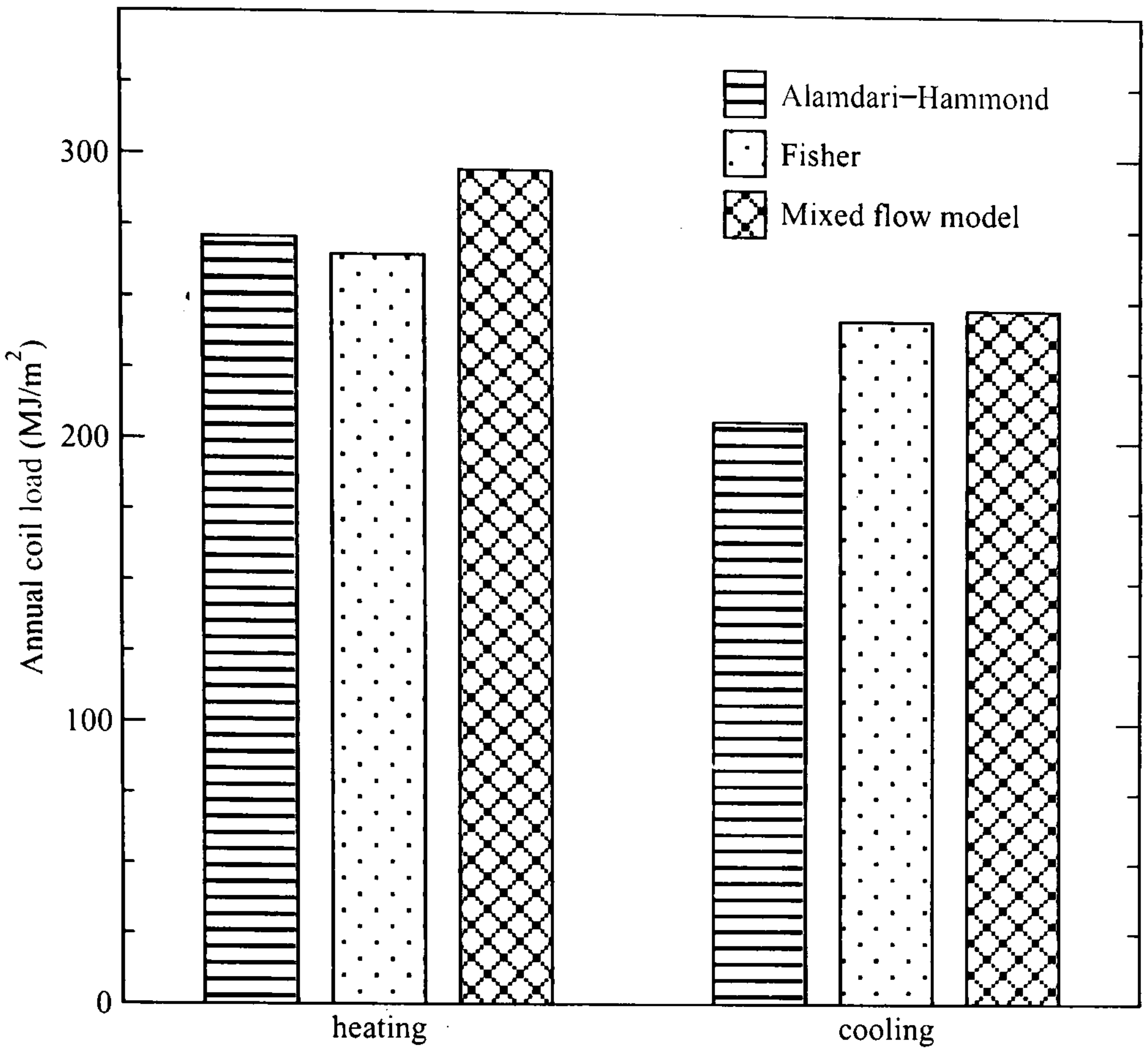

Figure 4.11: Annual coil loads predicted with the three convection methods

either Alamdari-Hammond (9% higher) or Fisher (11% higher). It also predicts substantially higher cooling loads than Alamdari-Hammond (19% higher) but only slightly more (less than 2%) than Fisher. These differences are, of course, climate and building sensitive.

Impact on h_c algorithm on thermal comfort predictions

Clearly, the choice of h_c algorithm has a significant impact on the prediction of annual heating and cooling loads (and thus energy consumption). Another (perhaps more) significant implication of algorithm choice can be seen by examining Figure 4.12, which plots the air temperature in the west zone on July 5, a day with very high cooling loads.

The system was not sized to meet the peak cooling loads. This is a valid design decision in a climate with a short cooling season: significant capital cost savings can be realized by sizing equipment to maintain the setpoint temperature through the majority of the cooling season, but allowing temperatures to rise on the most severe days. In such a case a designer might use simulation to assess whether thermal comfort will be unduly compromised by the undersizing.

In this case, the ESP-r results indicate that although the setpoint temperature is maintained most of the time, there are a few problematic days. On July 5, for example, the system is unable to maintain the setpoint temperature, particularly in the afternoon when solar gains reach their peak. The

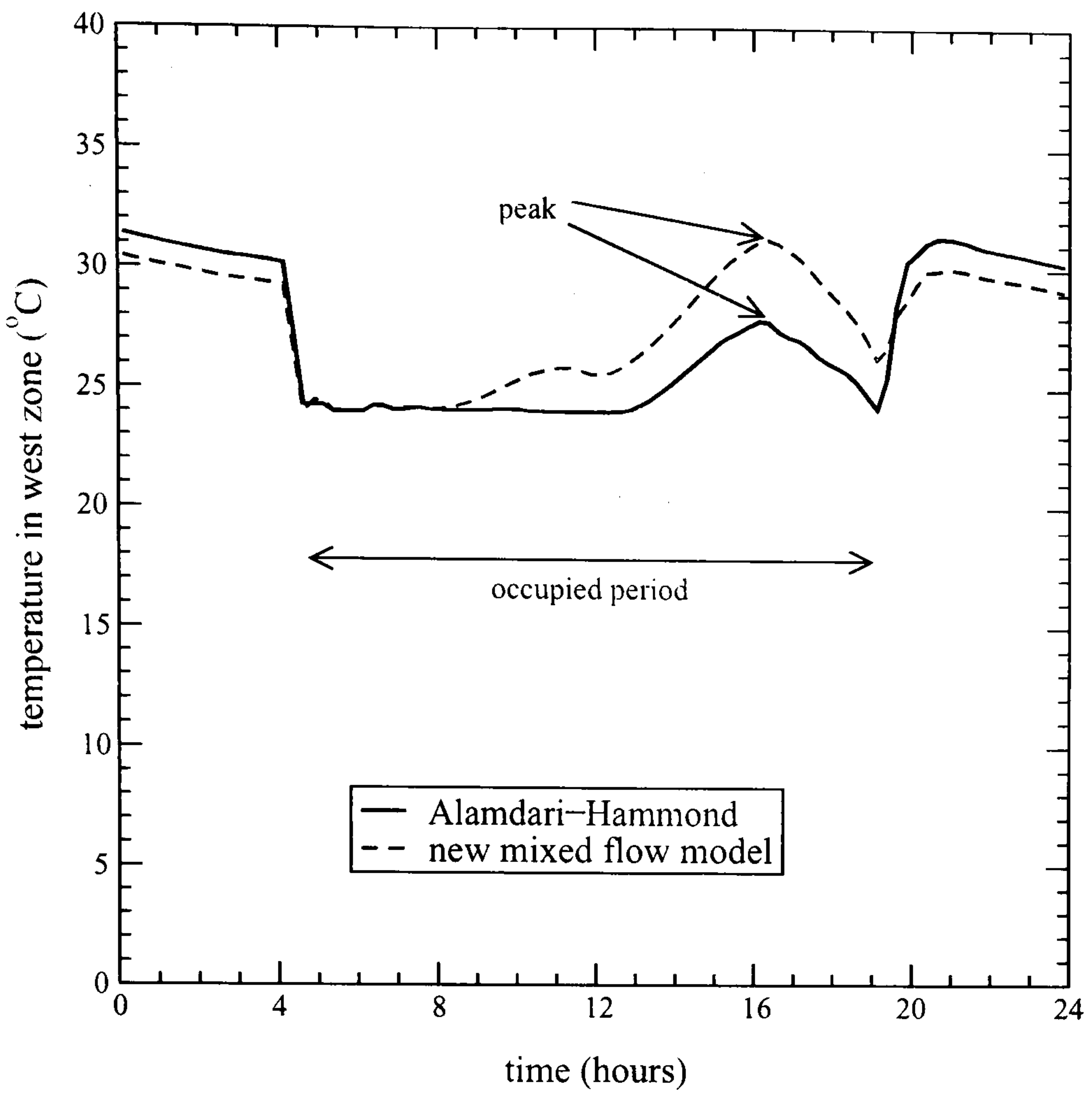

Figure 4.12: Air temperature in west zone on July 5

temperature of the zone drifts upwards, reaching a maximum just after 16h00 (see Figure 4.12). When the Alamdari-Hammond correlations are used, a peak zone temperature of 27.9°C is predicted: this might be acceptable to the designer. However, when the mixed flow model is employed, a peak zone temperature of 31.2°C is predicted; this would be deemed unacceptable, leading the designer to alter the architectural and/or mechanical features of the building.

Impact of h_c algorithm on assessment of design options

The designer might explore a number of options to address the overheating problem, including:

- Increasing the system's cooling capacity by 50% by increasing the air flow rate from 6 to 9 ac/h.
- Increasing the cooling capacity by approximately 25% by lowering the minimum supply air temperature from 13°C to 10°C.
- Changing to a VAV system with a constant supply temperature of 13°C, a minimum flow of 6 ac/h, and a maximum flow of 9 ac/h, effectively increasing cooling capacity by 50%.
- Reducing solar gains by adding window overhangs.
- Pre-cooling the building by night purging with 100% outdoor air at 6 ac/h.

Each of these design options was simulated twice: first with the Alamdari-Hammond correlations and then with the mixed flow model. All measures reduced the peak zone temperatures, with varying degrees of success, and all had an influence on cooling loads. Figure 4.13 plots the impact of the design changes on the cooling load for the month of July.

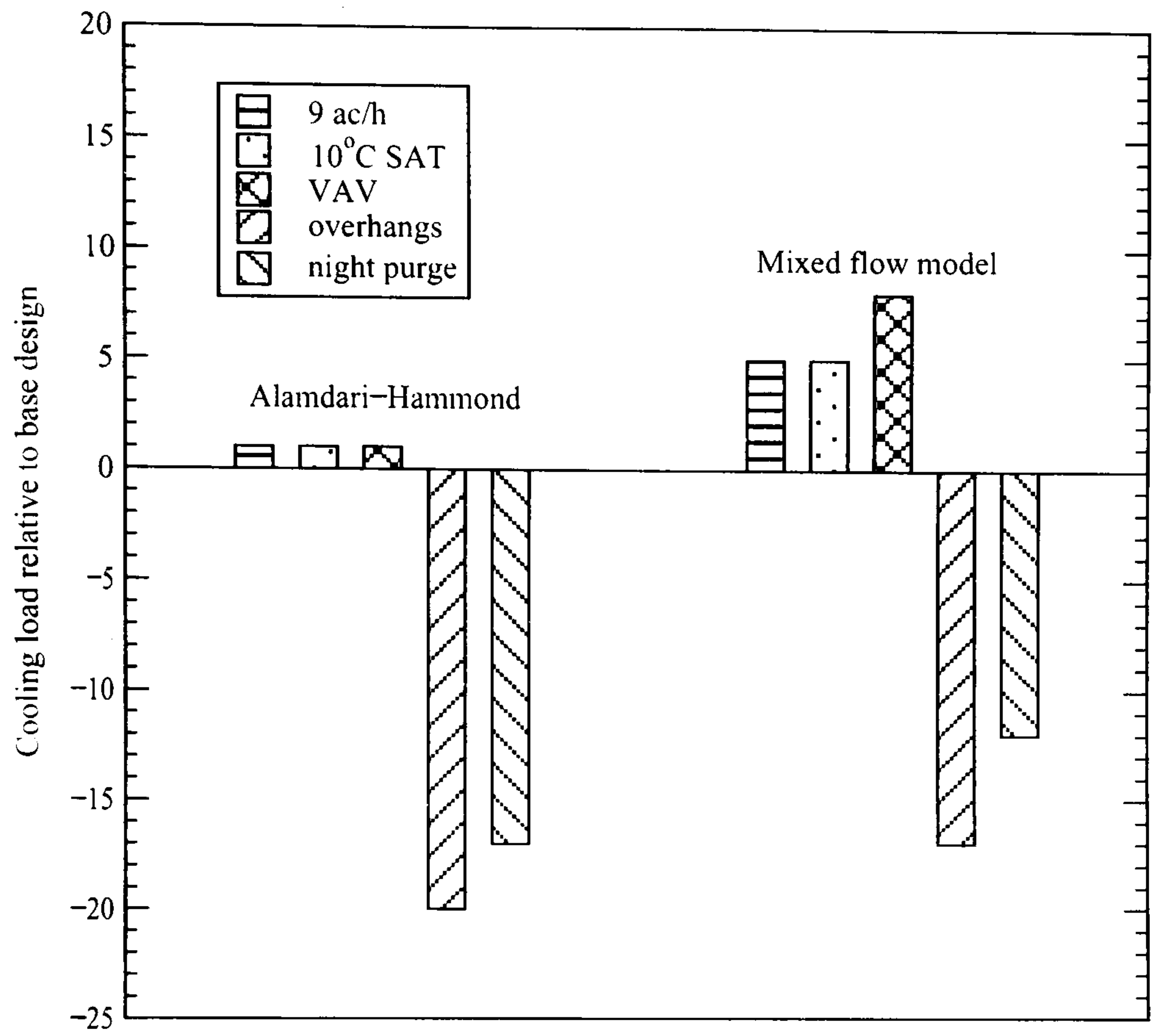

Figure 4.13: Impact of design options on cooling coil loads for July

The first three design options alter the convective regime: different air flow rates and supply air temperatures result. The mixed flow model is able to respond to these changes. It predicts higher cooling loads (5%, 4%, and 8%, respectively) for the first three design options, a result of the increased cooling capacity *and* increased surface convection. In contrast, the Alamdari-Hammond approach is not capable of responding to these changes in the flow regime. Consequently, cooling load predictions are only slightly higher (about 1%) and due entirely to the fact that the cooling system was able to extract more energy because of its higher capacity. In contrast, the Alamdari-Hammond correlations predicted greater savings with overhangs and night purging. These measures reduced cooling loads substantially with both convection methods, but the lower h_c produced in the Alamdari-Hammond runs overpredicted the savings.

4.6 Significance of Stratification

This section substantiates Chapter 1's claim that the well-stirred approach can preclude an accurate treatment of internal surface convection in certain cases. Consequently, it provides motivation for methods put forward in Chapter 5 for using the conflated modelling approach to resolve these cases where stratification[17] is significant.

As the previous section demonstrated, the selection of an h_c algorithm can have a significant impact on thermal simulation results. However, the appropriate selection of an h_c algorithm is not sufficient in itself to accurately characterize surface convection. The air temperature used to evaluate h_c and to establish the driving potential for the heat transfer are also of significance.

With the well-stirred model the room is treated as a well-mixed space of uniform temperature. The convection coefficients are calculated using this idealized temperature, essentially neglecting the influence of local air temperature variations on h_c. Further, this idealized temperature is used to establish the driving potential (ΔT) of the surface convection (see equation 2.14, page 18), again neglecting the influence of local air temperature variations. This treatment can lead to errors in estimating the surface convection if there is significant stratification within the room. For example, if for a given surface the well-mixed air temperature ($T_{room-air}$) underpredicts the air temperature driving the convection, both h_c and ΔT will be underestimated, resulting in an underprediction of heat transfer to the surface.

Refer again to the IEA empirical validation test room (see Section 4.5.2). When the radiator was on a plume of warm air would rise from the heater, resulting in some degree of stratification. Unfortunately, the temperature of the air was measured at only three (unspecified) locations in the room using a single vertical rake. Operation of the radiator was controlled using the rake's middle sensor while the simulation predictions were compared against the average of the three measurements. The measured data are time-filtered and available only at hourly intervals. Notwithstanding this integration (which tends to suppress extremes) and the paucity of measurement points, the data indicate significant stratification within the room, as illustrated in Figure 4.14 which plots the measurements from the three sensors over the heated period (data provided in Lomas et al 1994b).

---

[17] *Stratification* is used here to describe rooms with non-uniform air temperatures.

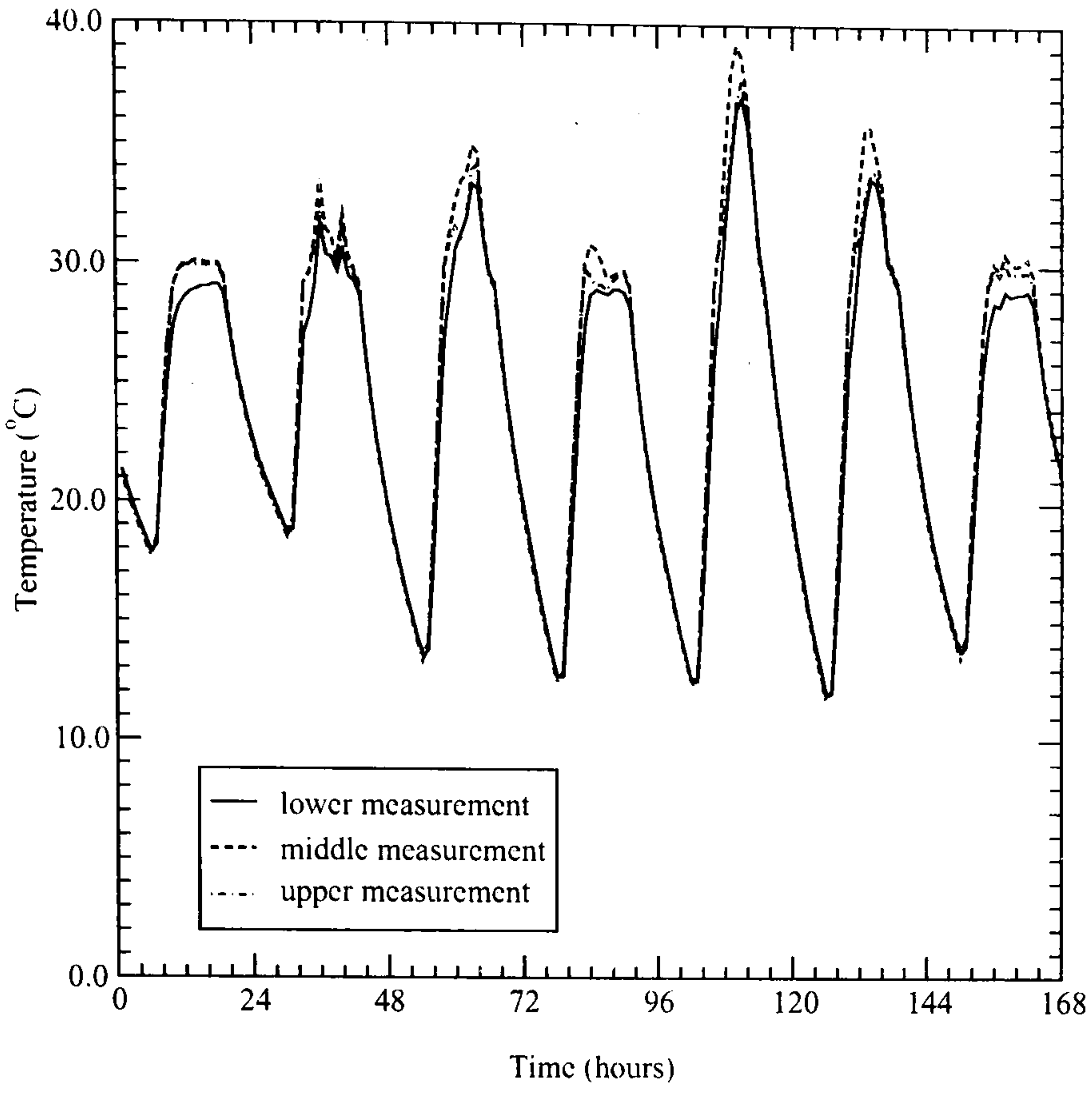

Figure 4.14: Air temperature measurements in test room

An analysis of these data during the hours of heater operation (6h00 to 18h00) indicates the following:

- The temperature is usually warmest at the middle location: the middle is hotter than both the top and bottom locations 73% of the time; the middle is never colder than both the top and bottom locations.
- Over the one-week period, the average temperatures are 27.1°C at the lower location, 28.5°C at the middle, and 28.1°C at the top (the average temperature at the middle location, the control point for the heater, is less than the set-point of 30°C due to the morning start-up period).
- The stratification between sensor locations is at least 1°C 73% of the hours; it is at least 2°C 26% of the hours.
- The greatest stratification between the locations for any one hour is 3.8°C.

A comparison of simulated and measured air temperatures over a single day period (October 23) provides further evidence of stratification (see Figure 4.15).

The heater turned on at 6h00 but it took until approximately 11h00 before the air within the vicinity of the sensors approached the setpoint temperature of 30°C. The performance of the heater was characterized in the IEA study, and it was found that 40% of its output was convective and 60% radiative[18]. As air has little thermal capacitance, the convective portion of the output would heat the

---

[18] In reality, the convective/radiative split would be dependent upon the temperatures of the radiator and surrounding fabric surfaces and upon the flow regime within the room. As this level of modelling resolution was not possible, an exploratory simulation was performed wherein the radiator was treated more explicitly. This indicated that the radiator would reach a quasi-steady-state rather quickly, so the fixed

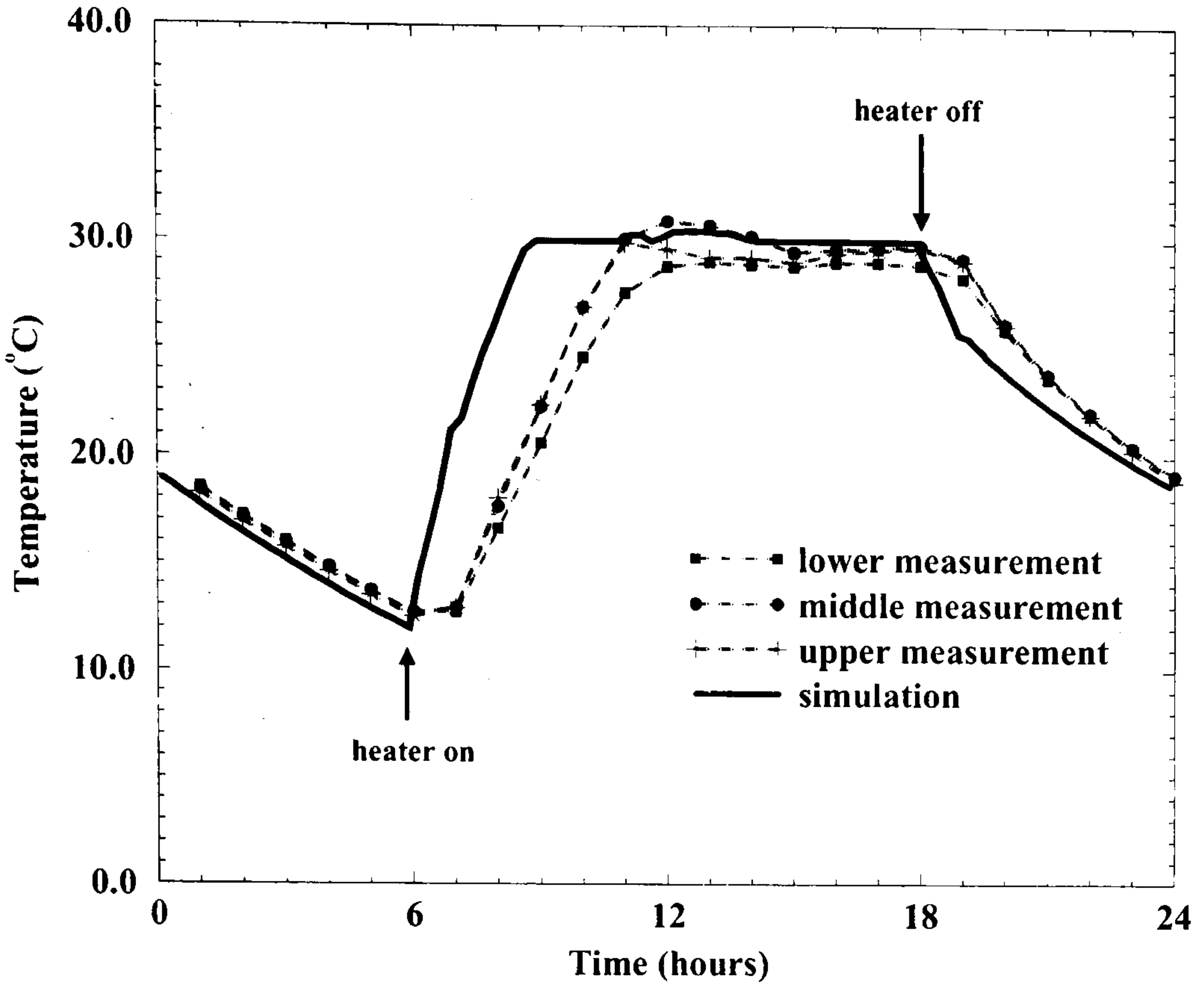

Figure 4.15: Air temperature on October 23: measurements versus simulation

air almost instantaneously; whereas, the radiative output would be absorbed by the internal surfaces before convecting to the air, resulting in a certain time lag in the response of the air temperature to heat injection.

These same phenomena were modelled, but considerably less time (before 9h00) was required before the air reached the setpoint temperature in the simulation. Figure 4.15 illustrates that in the simulation the air started warming immediately when the heater was switched on, whereas a delay is observed in the measured data (it is regrettable that the measurements are integrated over the hour). The gradient of the temperature ascent ($\partial T/\partial t$) is greater in the simulated than in the measured data. It should be noted that the thermal inertia of the oil-filled radiator was not considered in the simulation. Notwithstanding, its relatively short time constant (22 minutes) would not have a significant influence on the response of the air temperature.

One implication of the well-stirred model is that heat transferred to the air is distributed instantaneously and uniformly throughout the room volume. Consequently, in the model, the heat convected to the air surrounding the radiator would increase the temperature of all the air within the room at the same rate. The air volume would behave as though it had infinite conductivity.

The measured data speak to the validity of this assumption. The air within the vicinity of the sensors required considerable time to warm. This indicates that time was a factor in the diffusion and advection of heat within the air volume. The air adjacent to the heater would have warmed first, convective cells would have been established, and subsequently the heat distributed throughout the room.

---

convective/radiative split recommended in the IEA study is probably a reasonable assumption in this case.

It is unfortunate that the air temperature was measured at only three locations within the room and that there are no data to confirm this hypothesis, but a CFD analysis reported in the IEA study does corroborate it. The CFD analysis confirms the suspected flow pattern and indicates that air above the heater (and thus adjacent to the internal surface of the window) was about 3°C warmer than in the middle of the room.

Clearly, these data demonstrate that there is a good deal of stratification within the test room[19]. Despite this stratification, all the simulation models in the IEA study treated the test rooms as well-mixed spaces of uniform temperature. This raises some (interdependent) questions:

- What air temperature should be used to calculate h_c and ΔT? Should local or zone-averaged (well-stirred) air temperatures be used?
- Are the available h_c algorithms valid for stratified environments?
- Given that the operation of the radiator was controlled by the temperature sensed at a single point within the room, should the well-stirred temperature be used to control the operation of the radiator in the simulation?

Simple answers to these questions do not exist, but their implications may be significant. In order to gauge the importance of these issues, two additional variants of the IEA test hut were simulated during the October heated period. These were identical to the *internal surface convection* variant described in Table 4.7, except that the setpoint temperature was raised from 30°C to 31.5°C in the first run, and to 33°C in the second run. The well-stirred approach was still employed. Khalifa's correlations for radiators located under windows were used to calculate h_c for the walls, ceiling, and window, while Alamdari-Hammond was used for the floor and for all surfaces when the heater was off. Although this analysis does not examine the influence of local temperature variations, it does give some indication of the model's sensitivity to the air temperature, and there is clearly uncertainty in the correct value to use for $T_{room-air}$ in the simulation. These simulation results are presented in Figure 4.16.

Figure 4.16 clearly shows that the model is highly sensitive to $T_{room-air}$. Increasing the setpoint to 31.5°C had an even greater impact on the predicted energy consumption than switching the h_c algorithm. Therefore, the model is substantially more sensitive to $T_{room-air}$ than to the other modelling variants compared in Figure 4.9. For a setpoint of 33°C, the predicted energy consumption is within 3.1% of the measured value. Both the 31.5°C and the 33°C results are within the uncertainty bands of the measurement.

The choice of an appropriate value for $T_{room-air}$ is a non-trivial task when applying the well-stirred model to a stratified room. Given this and the model's high degree of sensitivity to $T_{room-air}$, the appropriateness of the well-stirred model for simulating the IEA test room (and other

---

[19] Interestingly, Khalifa (1989) measured a similar degree of stratification in his test cell when the room air temperature was elevated to 30°C.

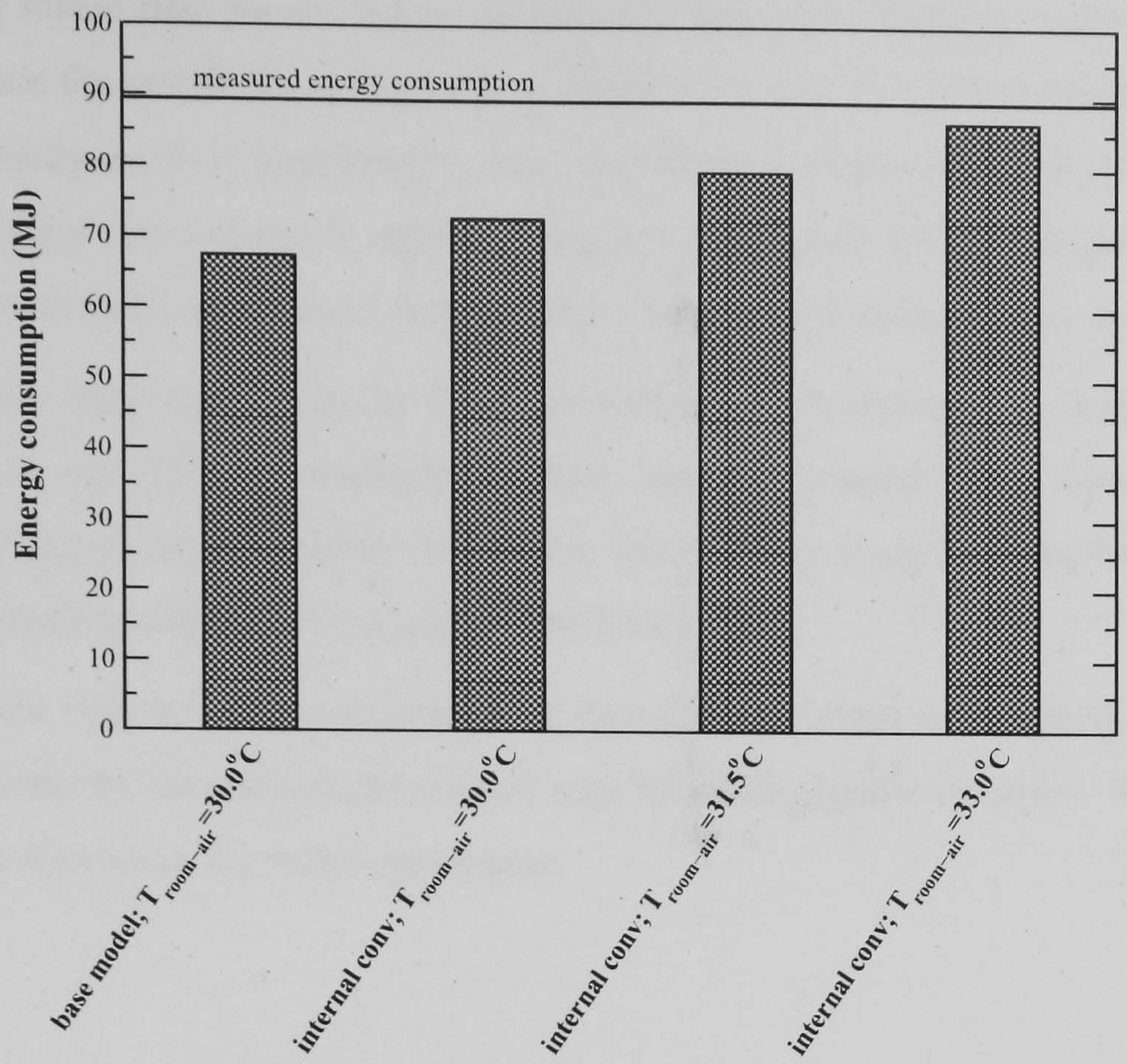

Figure 4.16: Sensitivity of IEA test hut to stratification

configurations like this) is dubious.

4.7 Closing Remarks

This chapter has demonstrated the significance of accurately modelling internal surface convection. While Chapter 2 showed how pervasive convection coefficients are in the zone matrix, this chapter has illustrated the extent to which erroneous convection coefficients distort the system of equations. The two cases studies presented here demonstrated how energy and thermal comfort predictions are affected by the choice of h_c algorithm, and more importantly, how this choice can alter the design decisions drawn from a simulation based analysis. Clearly, more resolved modelling techniques are required to treat this important heat transfer path within dynamic whole-building simulation.

The treatment of internal surface convection is equally significant in the high-resolution modelling of indoor air motion, because this is the pivot point between the CFD and thermal modelling domains (as discussed in previous chapters). Again, more resolved modelling techniques are required to move this conflated modelling approach forward.

Solutions to address this need have been put forward in this chapter. Firstly, a scheme was presented for broadly classifying indoor air flows for the purposes of calculating convection coefficients. Although the five regimes included in the scheme represent a coarse classification, this is a pragmatic and extensible approach for enabling building simulation to calculate convection coefficients in response to the forces that govern indoor air motion. Secondly, empirical methods were extracted from the literature for calculating convection coefficients for four of the five convective regimes. The basis of these methods, their applicability, and their implementation into ESP-r (including an algorithm for predicting the convective regime induced by forced-air HVAC systems) were described. Thirdly, a new method for characterizing convection coefficients for mixed flow was put forward.

Collectively these algorithms can calculate convection coefficients for most flows of practical interest. As such, they form the foundation for the following chapter which describes methods that allow the modelling of internal surface convection, and the pivot point between the CFD and thermal domains, to respond dynamically to changes in the flow regime.

Finally, this chapter has also demonstrated that when the room air is significantly stratified, the limitations imposed by the well-stirred method may introduce significant errors. Methods to address this are also put forward in the following chapter.

CHAPTER 5

Flow Responsive Convection Modelling and Conflation

5.1 Introduction

The previous chapter demonstrated the significance of accurately modelling internal surface convection. It showed how the choice of h_c algorithm can significantly affect simulation results and impact design decisions. It also put forward a scheme for classifying convective regimes and a suite of methods for calculating convection coefficients for these regimes. The current chapter builds upon this foundation with an algorithm (described in Section 5.2) that controls the calculation of surface convection in a dynamic fashion. Demanding only minimal data input from the simulationist, the *adaptive convection algorithm* appraises a configuration to assign an appropriate set of h_c equations to each internal surface. Then, as the simulation evolves, the algorithm toggles between the h_c equations in response to the prevailing convective regime.

Chapter 3 described the theoretical basis of the $k-\varepsilon$ turbulence model and its log-law wall functions, the methods currently employed in ESP-r's CFD code. Although this approach has successfully predicted many room air flows, it cannot accurately calculate surface convection in many circumstances. In response to this shortcoming, ESP-r's CFD model is populated with promising alternative turbulence and near-wall modelling approaches in Section 5.3.

In light of the information presented in Chapters 2 to 4, it is clear that the success of the conflated modelling approach is critically dependent upon the handshaking between the thermal and CFD modelling domains, and, more precisely, upon the treatment of the physics at their pivot point: the room's internal surfaces. Firstly, inaccurate CFD surface convection predictions can substantially distort the system of thermal equations. Secondly, the CFD air flow predictions are sensitive to the thermal boundary conditions prescribed. Therefore, building upon the advances of the adaptive convection algorithm, a series of alternate handshaking approaches and boundary condition treatments are put forward in Section 5.4. These enable either modelling domain (or both domains acting cooperatively) to resolve the surface convection.

These three elements described above are then brought together in the *adaptive conflation controller*, which is described in Section 5.5. This empowers the simulator to dynamically control how CFD interacts with the thermal domain. Drawing upon the adaptive convection algorithm, and the suite of optional turbulence, near-wall, handshaking, and boundary condition methods, the controller selects an appropriate combination of approaches each time-step, based upon an ongoing appraisal of the flow regime. In this manner, the adaptive conflation controller advances the modelling of indoor air motion by controlling CFD in a fashion appropriate for the prevailing conditions. It also advances the modelling of surface convection by using CFD to resolve the heat transfer when it is able, but also by providing safeguards to prevent erroneous CFD results from distorting the thermal domain.

Finally, closing remarks are made in Section 5.6.

5.2 The Adaptive Convection Algorithm

The purpose of the adaptive convection algorithm is twofold: to increase the resolution and accuracy of thermal simulation; and to support the adaptive conflation controller.

Chapter 4 described how ESP-r has been populated with 28 equations (each with limited applicability) for calculating convection coefficients. Since convection regimes vary throughout a simulation, this is not sufficient in itself to accurately characterize convection. It is also necessary to assign an appropriate h_c equation to each internal surface at each time-step of the simulation, and to adapt this selection to the prevailing flow conditions.

Therefore, an adaptive convection algorithm is devised that has the ability to interrogate the configuration and chose from amongst the suite of h_c correlations. It demands only minimal data input from the simulationist, and is broken into two primary steps (described in the following subsections):

1) The configuration is appraised prior to commencing the time-step simulation. Each internal surface is attributed with a set of h_c algorithms appropriate for the flow regimes anticipated over the duration of the simulation.
2) As the simulation progresses, a controller monitors critical simulation variables to assess the flow regime. Based upon this assessment, it dynamically assigns (for each surface) an appropriate h_c algorithm from amongst the set attributed in step 1.

5.2.1 Attributing surfaces with convection calculation control data

The adaptive convection algorithm appraises the building during the problem definition stage to determine which h_c methods are appropriate for the prevailing conditions in each room. This is accomplished through a series of user prompts and automated appraisals which are performed on a zone-by-zone basis. A pragmatic approach was devised to minimize data entry and detail specification.

Selecting h_c correlations for the room

Conditions in each zone are first matched to one of the five principle convective regimes listed in Table 4.1 (see page 75). Where sufficient h_c methods are available, a second level of questioning is used to sub-classify the flow regime (illustrated in Figure 5.1). For instance, h_c algorithms exist to discriminate between two B regimes: one generated by a heating device located under a window (called B1), and another generated by a heating device located elsewhere in the room (B2). The suite of 28 h_c correlations enabled a total of nine unique convective classifications.

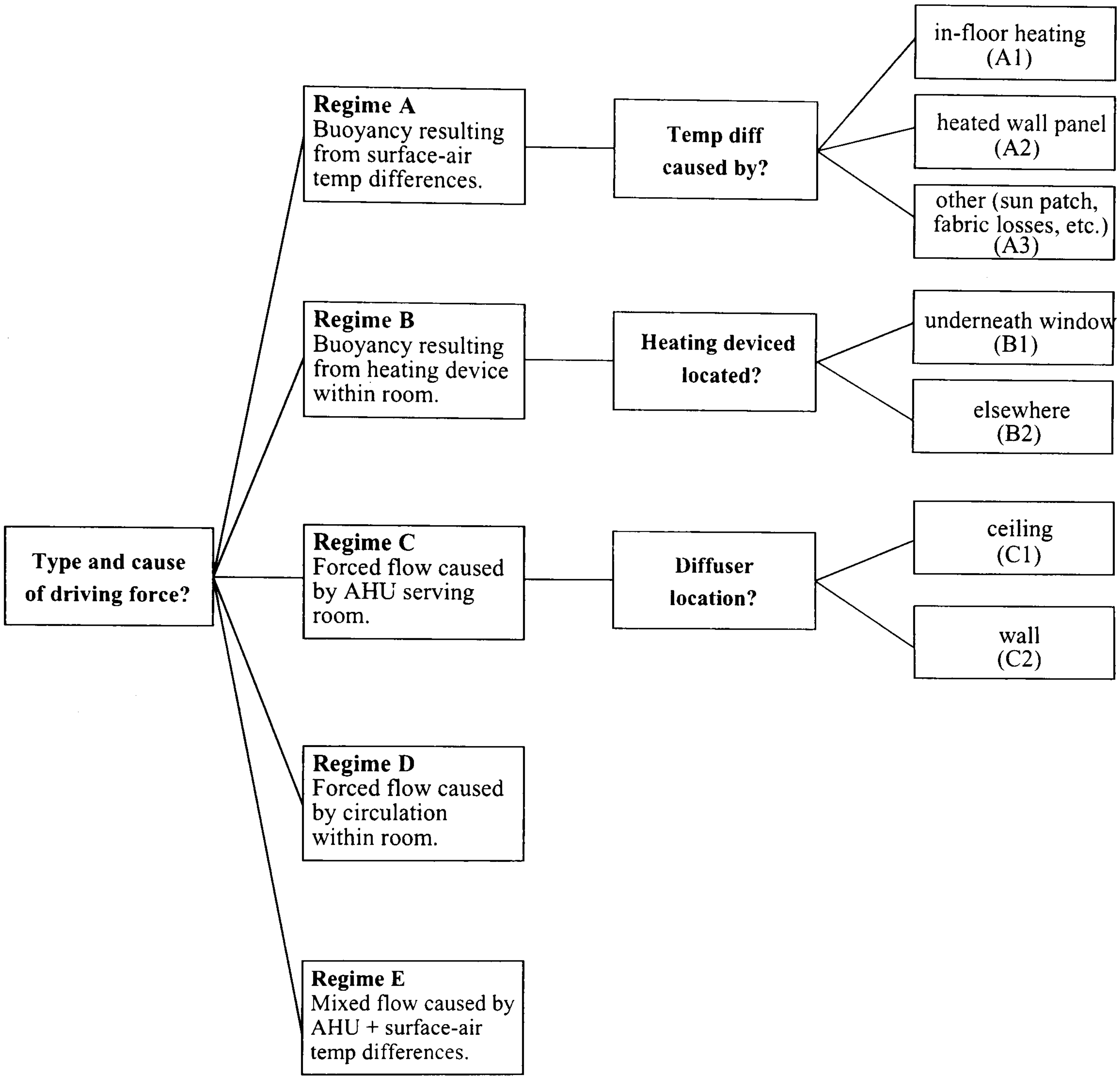

Figure 5.1 User prompts for appraising flow regime

Table 5.1 lists the h_c equations that were selected to characterize each of the nine convective classifications. The assignment of h_c methods was based on the applicability assessments presented in Section 4.3. This scheme builds upon the synergies between methods. The treatment of heated wall panels (regime A2) is a case in point. The Awbi-Hatton heated wall equation is suitable for the heated wall surface, but not for the other surfaces in the room. Khalifa's equation 6 is applicable for rooms with heated wall panels, but only for the wall and window surfaces which are not heated. Similarly,

convective regime		h_c methods applicable in room	surface and dynamic assignment
A	in-floor heating (**A1**)	• Khalifa eq 3 for walls and windows • Awbi-Hatton heated floor eq • Khalifa eq 4 for ceilings	Table E.1
	heated wall panel (**A2**)	• Awbi-Hatton heated wall eq for heated surface • Khalifa eq 6 for non-heated walls and for windows • Alamdari-Hammond stable horizontal eq for floors • Khalifa eq 7 for ceilings	Table E.2
	other (**A3**)	• Alamdari-Hammond vertical eq for walls and windows • Alamdari-Hammond stable horiz eq for floors & ceilings • Alamdari-Hammond buoyant horiz eq for floors & ceilings	Table E.3
B	heater under window (**B1**)	• Khalifa eq 6 for walls • Khalifa eq 6 or 9 for windows • Alamdari-Hammond stable horizontal eq for floors • Khalifa eq 7 for ceilings	Table E.4
	heater not under window (**B2**)	• Khalifa eq 5 for walls close to heater • Khalifa eq 3 for walls not close to heater • Khalifa eq 3 or 10 for windows • Alamdari-Hammond stable horizontal eq for floors • Khalifa eq 4 for ceilings	Table E.5
C	ceiling diffusers (**C1**)	• Fisher or Fisher-Pedersen ceiling-jet wall eq for walls and windows • Fisher or Fisher-Pedersen ceiling-jet floor eq • Fisher or Fisher-Pedersen ceiling-jet ceiling eq	Table E.6
	wall diffusers (**C2**)	• Fisher horizontal-jet wall eq • Fisher horizontal-jet floor eq • Fisher horizontal-jet ceiling eq	Table E.7
D		• Khalifa eq 8 for walls and windows blown on by fan • Khalifa eq 3 for other walls and windows • Alamdari-Hammond stable horizontal eq for floors • Khalifa eq 4 for ceilings	Table E.8
E		• mixed flow wall eq • mixed flow floor eq • mixed flow ceiling eq	Table E.9

- The Alamdari-Hammond correlations are given in Table 2.1 on page 19.
- The Khalifa correlations are given in Table 4.2 on page 80.
- The Awbi-Hatton correlations are given in Table 4.4 on page 83.
- The Fisher ceiling-jet correlations are the first set given in Table 4.5 on page 88.
- The Fisher-Pedersen ceiling-jet correlations are the second set given in Table 4.5 on page 88.
- The Fisher horizontal-jet correlations are given in Table 4.5 on page 88.
- The mixed flow correlations are given in Table 4.6 on page 95.

Table 5.1: Assigning h_c correlations to convection regimes

Khalifa's equation 7 can resolve the ceiling. As neither Khalifa nor Awbi-Hatton supply an equation for the floor in this case, Alamdari-Hammond's equation for stably stratified horizontal surfaces is used to complete the characterization of the room.

All 28 h_c methods presented in Chapter 4 are utilized by this scheme. Although most flows of practical interest can be modelled, there is much potential for refinement. When additional h_c calculation methods become available the convective regimes can be further sub-classified and the scope broadened without altering the structure.

Assigning h_c correlations to surfaces

Once a set of h_c methods has been selected for the room's convective regime, the algorithm then assigns appropriate equations to each internal surface. This is accomplished by examining surface orientation and type (wall, window, floor, ceiling). The algorithm operates on standard geometrical and attribution data which has already been defined, and as such requires minimal input from the user. Additional questions are posed only in cases where decisions cannot be resolved without further user intervention. This is necessary when the selection of h_c methods hinges upon details which are not required in the standard geometrical model, such as: whether the jet from a circulating fan strikes a wall; or whether the heating device is adjacent to a wall.

User input is required in two other circumstances. In the case of convective regime C1, when air is supplied to the room through ceiling diffusers, the user must choose between the two optional sets of correlations (refer to page 87 and Appendix C). As well, since it is suspected that Khalifa's window correlations overpredict h_c (refer to Section 4.3.2) the user is given the choice of whether to apply these or alternate equations for windows.

Primary and secondary convective regimes

The above logic assigns h_c methods to each surface for the room's primary convective regime. However, as most of the convective regimes (all but A3) are driven by the operation of HVAC equipment, it would be inappropriate to use these h_c methods at all time-steps of the simulation. For a mechanically ventilated room, for example, the mixed flow method is appropriate for calculating h_c values at the ceiling when the system is delivering air to the room. But when the system is shut off at night, convection to the ceiling is not governed by the fan, but rather by buoyancy caused by surface-air temperature differences. Therefore, an additional (in some cases two) equation is assigned to each surface, this to calculate the convection coefficient for the room's secondary convective regime (i.e. when the HVAC equipment is not operating).

For the purposes of demonstrating this approach, it is assumed that the secondary convective regime is classification A3, flow driven by surface-air temperature differences. It would be conceptually simple to extend the approach to consider more complex scenarios, including the possibility of tertiary flow regimes. For example, a mechanically ventilated room may use a baseboard heater to maintain the setback temperature when the air-handling system is shut off at night. In this case, the primary regime could be E (fan operating), the secondary regime B1 (fan off, but baseboard operating), and the tertiary regime A3 (fan and baseboard off).

The last column in Table 5.1 references additional tables (these are located in Appendix E) which detail the assignment of h_c equations to surfaces for each of the nine convection classifications. These tables list the h_c equations selected to characterize both the primary and secondary convective regimes.

Attributing surfaces with convection calculation control data

Once this information is collected (the process only requires a few seconds per zone), each internal surface is attributed with a set of h_c correlations to characterize the primary and secondary convective regimes. The h_c correlations are identified using the ICOR flags which were introduced in Chapter 4 (see page 81). A convection calculation control law is also assigned to each surface. This instructs the simulator on how to toggle between the h_c correlations during the time-step simulation, a concept that will be treated in the next subsection. These data are stored by the *Project Manager* for subsequent use by the simulator in the *convection calculation control file*. The format of this data file is defined in Appendix F.

Example of attributing convection calculation control data

The process is best illustrated with a simple example. Consider the model of the IEA test room shown in Figure 4.8 (page 100). The user must make only two menu selections to specify that the room is heated by a radiator located underneath the window. As Table 5.1 indicates, there are four h_c equations that can characterize the room's primary convective regime (Khalifa's equations 6, 7, and 9, and Alamdari-Hammond's stably stratified horizontal correlation) and three that can characterize the secondary convective regime (the three Alamdari-Hammond correlations).

The geometry is then scanned to make the final attribution of h_c methods to surfaces (see Figure 5.2). For example, three equations are assigned to the ceiling: Khalifa's equation 7 for when the heater is on, and the two Alamdari-Hammond horizontal equations. Both Alamdari-Hammond equations are required, as flow under the ceiling may be buoyant or stably stratified, depending upon the air and surface temperatures.

5.2.2 Dynamically controlling convection calculations

The previous subsection described how each surface is attributed with a set of ICOR flags and a control law prior to commencing the time-step simulation. Governed by the control law, the adaptive convection algorithm toggles between the set of ICOR flags during the simulation in response to the

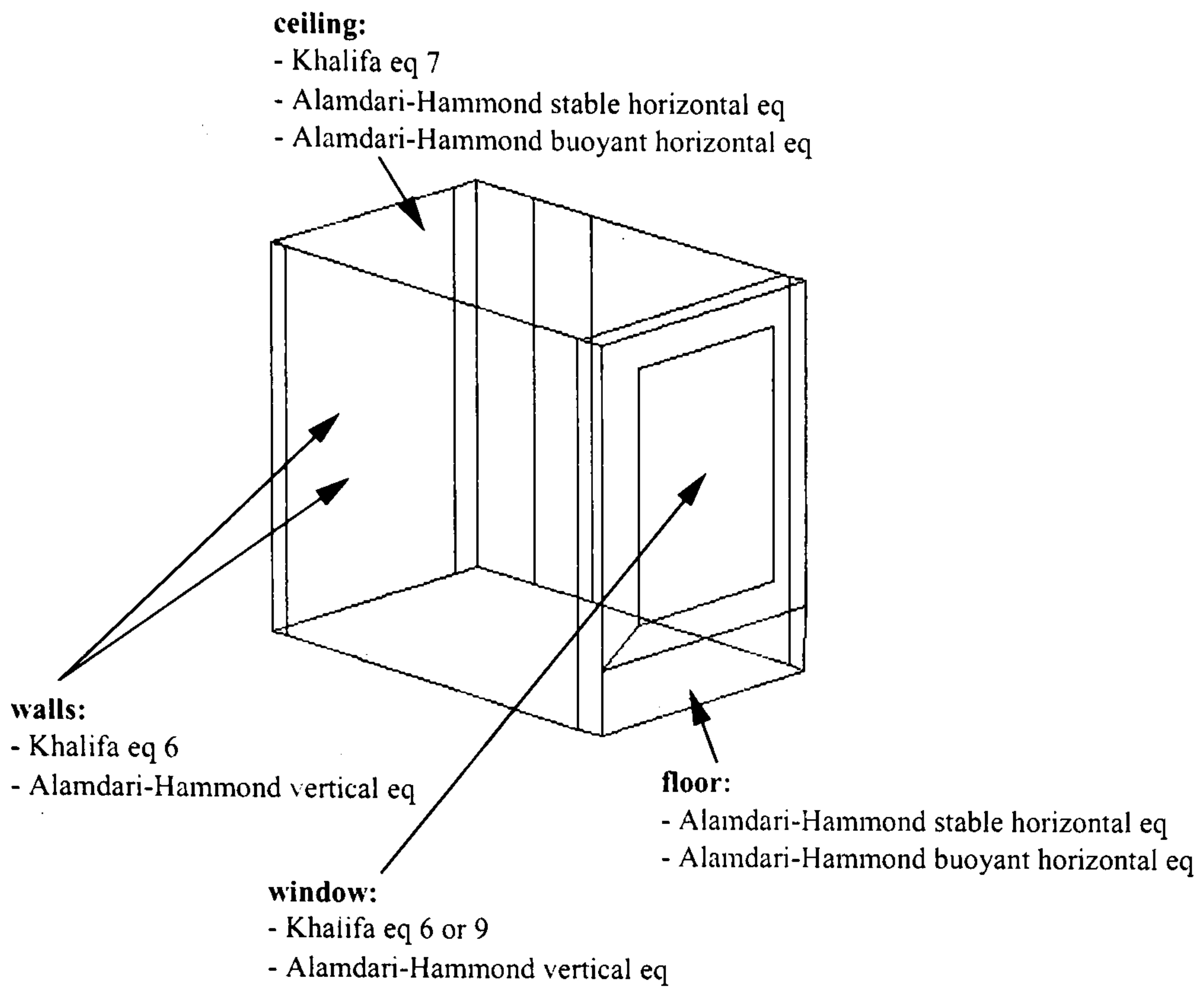

Figure 5.2 Attributing surfaces with h_c correlations

prevailing flow regime. This process is performed on a surface-by-surface basis each time-step of the simulation.

Convection calculation control laws

Two control laws were implemented to demonstrate this approach. Both adapt the convection calculations in response to the operational state of HVAC equipment. The first is applicable for terminal heating devices (this could be a heated wall panel, in-floor heating, a circulating fan heater, or a radiator) and the second for air-based heating and cooling systems.

Figure 5.3 illustrates the control logic applied for the first control law. The controller is called once per zone each time-step of the simulation. It first determines whether the terminal device is supplying heat to the room (based on the value of the q_{plant} variables in equation 2.22, page 23). If the device is heating the room, the ICOR flags are set to calculate the convection coefficients using the correlations for the primary convection regime. And if the terminal device is not heating the room, the ICOR flags are set to use the correlations for the secondary convection regime. When considering horizontal surfaces for the secondary convective regime, a test is performed (using the air-point and surface temperatures) prior to setting the ICOR flag. This determines whether the flow is stably stratified or buoyant. The controller is invoked prior to zone matrix formation, and therefore operates with previous time-step temperature and plant simulation results.

The control logic employed for air-based HVAC systems is illustrated in Figure 5.4. It is tightly integrated with the idealized HVAC model introduced in Chapter 4 and detailed in Appendix D. If the

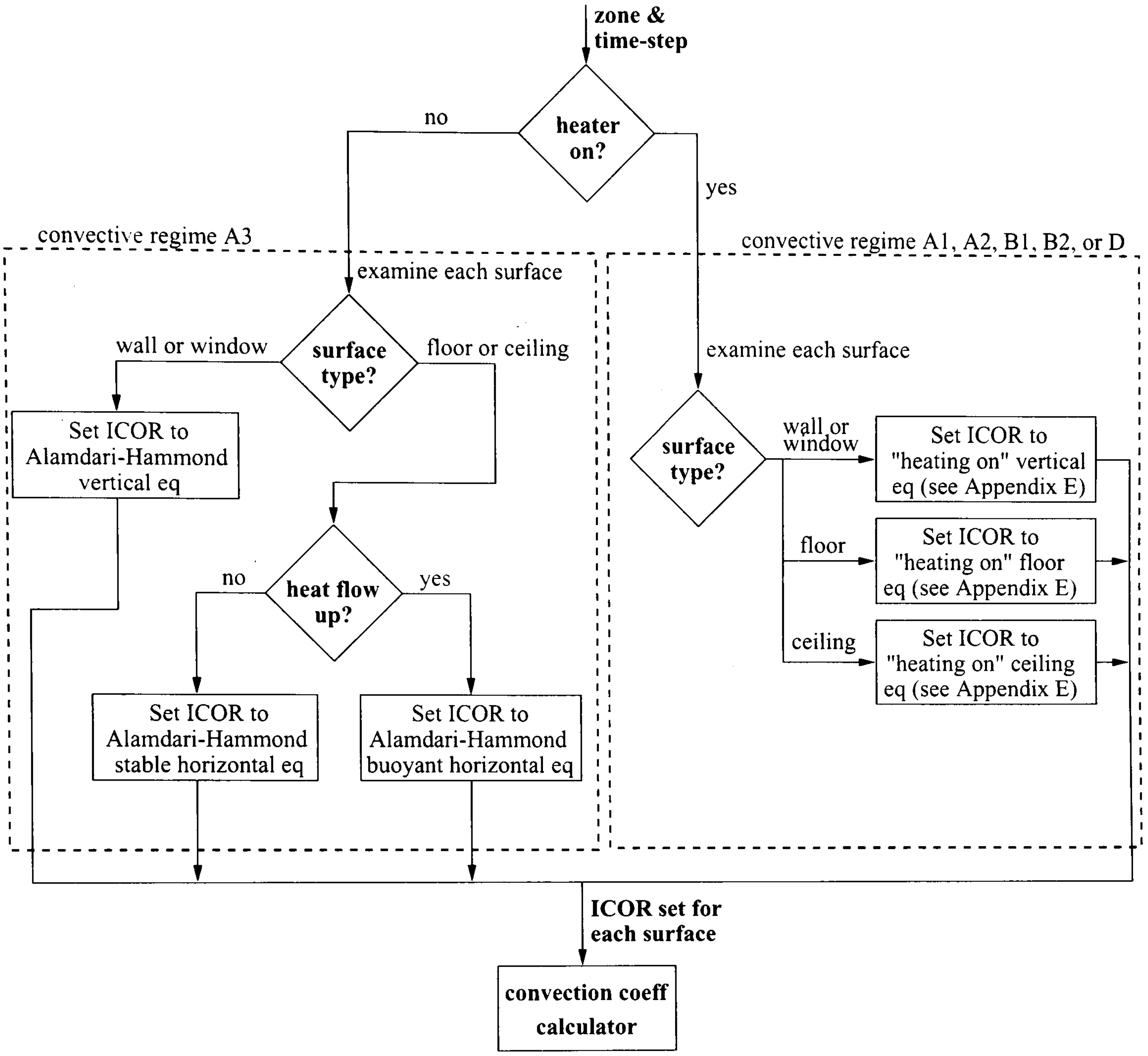

Figure 5.3 Adaptive convection control law for terminal heating devices

controller detects that the mechanical system's fan is operating, it calls upon the idealized HVAC model to render the flow regime in the room. It then assigns the ICOR flags to calculate convection coefficients using the correlations for the primary convective regime. The procedure is identical to the terminal heating device control law when the system is inoperative.

Example of dynamically adapting convection calculations

An application of the air-based HVAC system control law is demonstrated in Figure 5.5. The room is mechanically ventilated from 5h00 to 20h00 and is allowed to free float during unoccupied periods. The mixed flow model is employed. Up until 5h00, the dynamic controller senses that the system is off, and thus employs the Alamdari-Hammond correlations. When the system's fan switches on at 5h00 the dynamic controller sets the ICOR values to calculate h_c with the mixed flow model. The idealized HVAC model determines the flow rate and temperature of air supplied to the

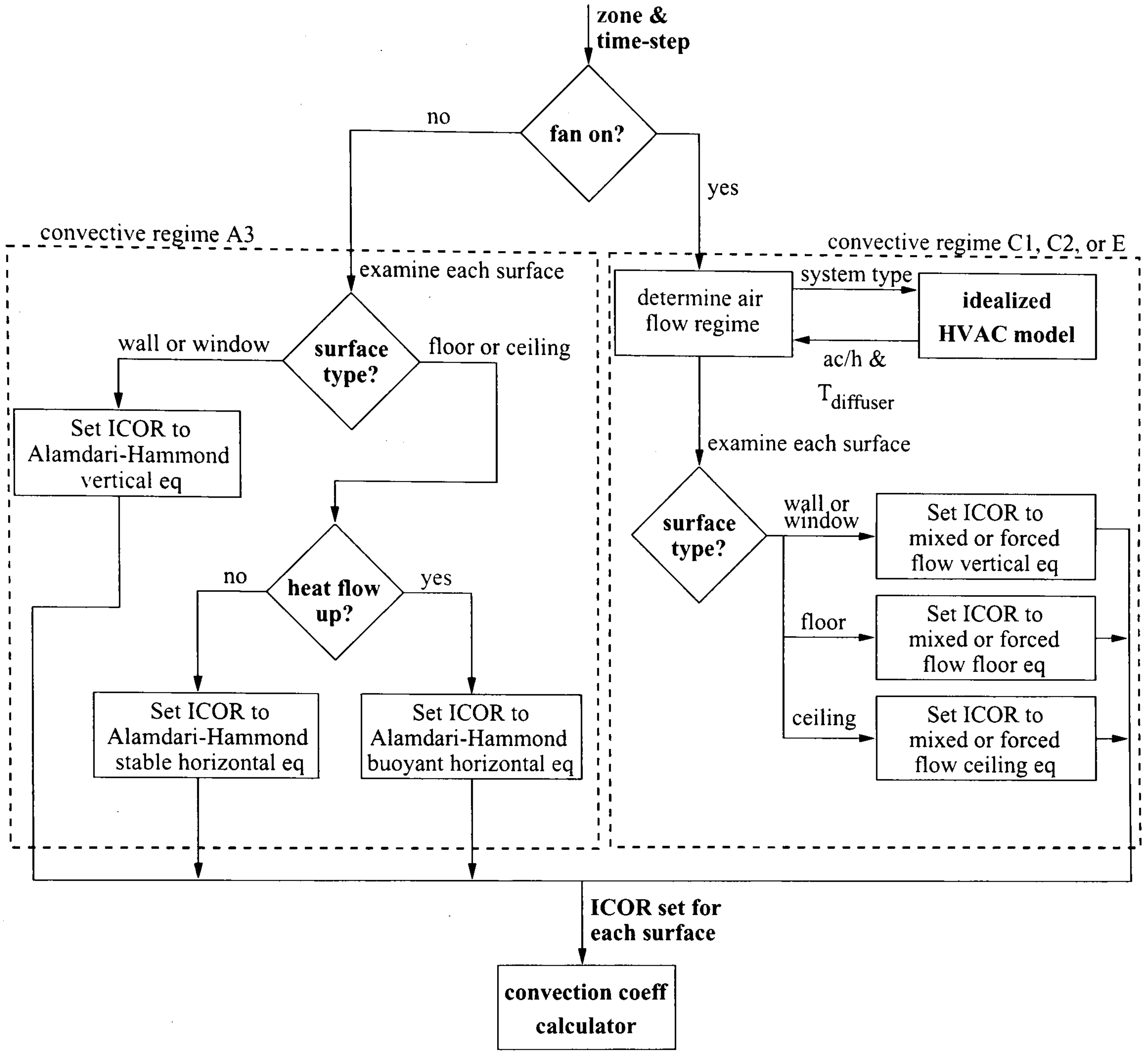

Figure 5.4 Adaptive convection control law for air-based HVAC systems

room, and the h_c calculator applies the mixed flow equations to establish the convection coefficients for the zone matrix. The graph shows how dramatically surface convection at the ceiling increases at 5h00. When the fan shuts off at 20h00, the dynamic controller switches to convective regime A3. At first it determines that flow under the ceiling is buoyant (the ceiling is colder than the room air so buoyant plumes form), but shortly thereafter stably stratified conditions develop.

Extensibility

The general principle of the dynamic controller is simple: a simulation variable that governs the convective regime is sensed; a decision on which convective regime prevails is made; the ICOR values of the surfaces in the room are set; and the h_c values are calculated. This approach has been demonstrated for terminal heating devices and for air-based HVAC systems, but the same logic could be applied in a host of other ways to extend the applicability of the adaptive convection algorithm.

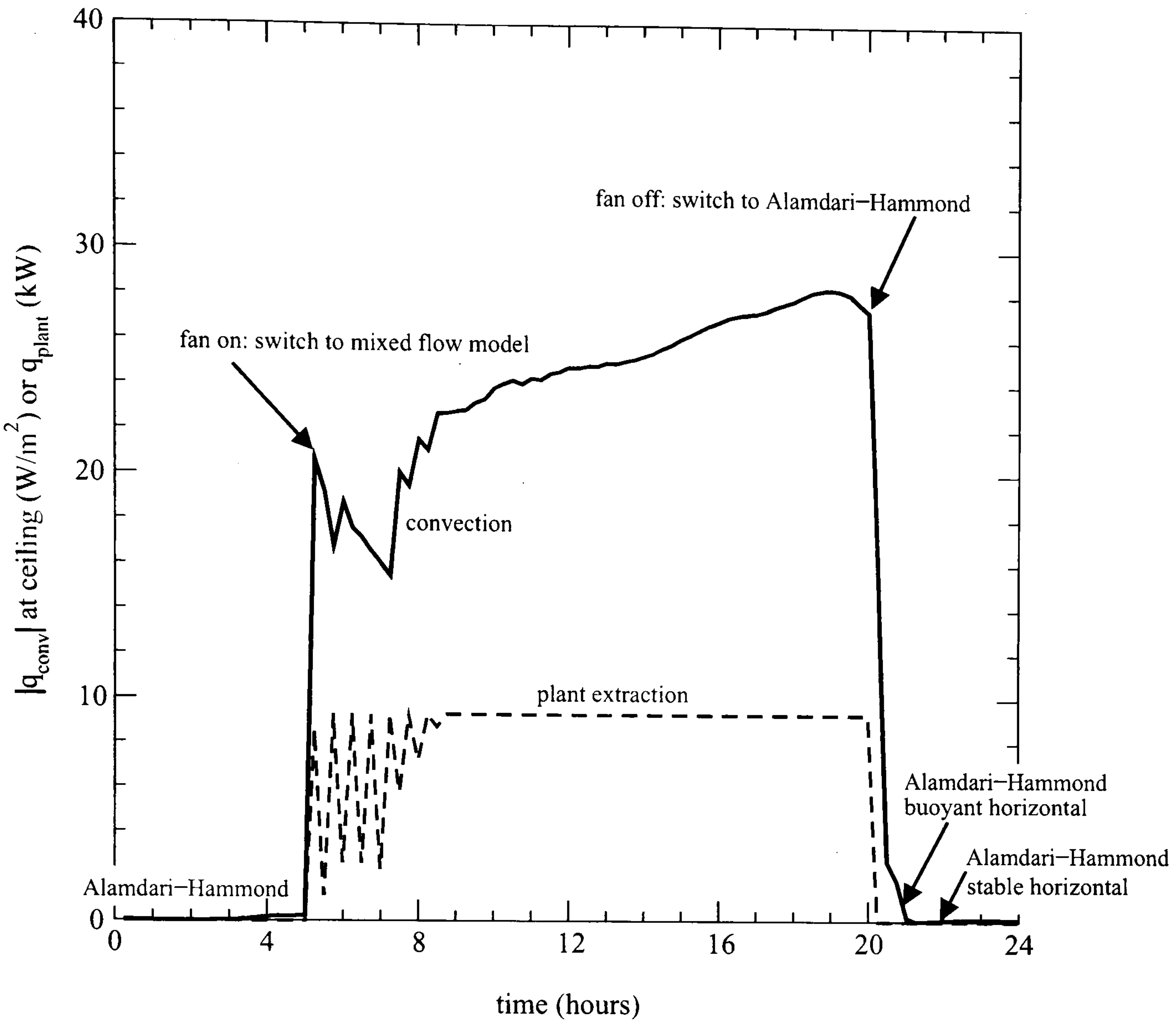

Figure 5.5 Example of dynamically adapting convection calculations

As an example, consider a building with a hybrid ventilation system. On days with moderate cooling loads, the cooling equipment and forced-air distribution system are shut off and the building is cooled naturally by ventilation through openable windows. A network air flow model could be established to simulate the opening and closing of windows, the natural ventilation, and the operation of the cooling equipment and forced-air system.

A control law could be created to allow the adaptive convection algorithm to sense the network air flow connections representing the windows. If the windows were open, the controller could set the ICOR flags to employ an h_c calculation approach for rooms ventilated through windows (one was mentioned in Section 4.2.2). And when it sensed the windows were closed and the cooling system was on, the controller could set the ICOR flags to use the mixed flow model.

5.3 Turbulence and Near-wall Modelling Options

Chapter 3 explained that the standard $k-\varepsilon$ turbulence model with log-law wall functions was formulated for fully developed turbulent flow, a flow regime rarely found in rooms. As a result of this incongruity, the method often gives poor surface convection predictions. This is because the log-law wall functions poorly characterize the boundary layer of many room air flows and because the $k-\varepsilon$ model poorly predicts the turbulent diffusion in weakly turbulent regions.

Given that the conflated modelling approach is critically dependent upon resolving the surface convection, alternate turbulence and near-wall approaches must be available to the adaptive conflation controller. A number of alternatives (some only emerging) were described in Chapter 3. Two of the most promising are assessed and implemented here.

5.3.1 Yuan wall functions

Wall functions, as Chapter 3 explained, bridge the gap between the wall and the next-to-wall grid point. They do this by assuming the form of the velocity and temperature profiles within the boundary layer. This is easily seen by examining the thermal log-law wall function (equation 3.48, page 60). It gives the local surface convection as a function of the temperature and turbulence kinetic energy of the next-to-wall grid point. Similarly, the momentum wall function (equation 3.47, same page) gives the local wall shear as a function of velocity and turbulence kinetic energy of the next-to-wall grid point.

If behaviour within the boundary layer deviates from the assumed temperature and velocity profiles, the wall functions will introduce errors into the CFD calculation domain. In the case of the thermal wall functions, errors will not be restricted to the surface convection predictions. Air flow calculations will also be impacted because the thermal wall function imposes the influence of the wall's temperature on the momentum equations. This is particularly important in natural convection situations, because it is the temperature gradients next to the wall that determine the buoyancy that drives the air flow.

Chapter 3 presented significant evidence from the literature to demonstrate that the log-law wall functions are deficient at calculating surface convection in room air flows in general, and in buoyancy-driven flows in particular. Surface convection predictions have been found to be highly sensitive to the placement of the next-to-wall grid points. This is problematic because an optimal grid cannot be selected until the details of the flow and heat transfer field have been calculated. If the next-to-wall grid points are placed too close to the wall the log-law wall functions tend to overpredict surface convection, and when placed too far they tend to underpredict.

To address these deficiencies, Yuan et al (1993) developed a new set of wall functions for the $k-\varepsilon$ model specifically for the case of natural convection along vertical surfaces. They postulated a functional form for the wall functions based on a dimensional analysis of the governing equations.

The constants in the functions were then established by fitting the equations to the experimental data of Tsuji and Nagano (1988). The resulting thermal wall function, whose validity was confirmed by comparison to other sets of experimental data, is given by,

$$T^* = \begin{cases} y^* & \text{if } y^* \leq 1 \\ 1 + 1.36(\ln y^*) - 0.135(\ln y^*)^2 & \text{if } 1 < y^* \leq 100 \\ 4.4 & \text{if } y^* > 100 \end{cases} \tag{5.1}$$

Where y^* is a dimensionless distance between the wall and the the next-to-wall grid point, and T^* is a dimensionless temperature. These are given by,

$$y^* = \left(\frac{\rho Pr \Delta x_P}{\mu} \right) \cdot u_q \tag{5.2}$$

$$T^* = \frac{T_{wall} - T_P}{T_q} \tag{5.3}$$

Δx_P, T_{wall}, and T_P are illustrated in Figure 3.7 (page 61). u_q is a velocity scale based on the heat flux $\{m/s\}$, while T_q is known as the heat flux temperature $\{K\}$. These are given by,

$$u_q = \left[\frac{g \beta \mu q''_{wall}}{\rho^2 c_p Pr} \right]^{1/4} \tag{5.4}$$

$$T_q = \left[\frac{(q''_{wall})^3 Pr}{g \beta \mu \rho^2 (c_p)^3} \right]^{1/4} \tag{5.5}$$

Examination of equations 5.2 through 5.5 reveals that the surface convection heat flux (q''_{wall}) appears on both the left and right sides of the thermal wall function (equation 5.1). Consequently, the Yuan thermal wall function requires an iterative solution approach. This iterative solution must be performed for each next-to-wall grid point, each time the energy equation is formed and solved within the sequential and iterative solution process (see Figure 3.6, page 51). This contrasts with the relative simplicity and computational efficiency of the log-law wall functions (compare equation 3.48, page 60, with equations 5.1 to 5.5).

To initiate the iteration for a given next-to-wall grid point, the surface convection is first guessed and y^* calculated with equations 5.4 and 5.2. T^* is then determined using equation 5.1. Next, T_q is solved with equation 5.3 and subsequently used in equation 5.5 to yield an updated estimate of q''_{wall}. This process is repeated until convergence is achieved. The converged surface convection heat flux is then absorbed into the algebraic relation for the next-to-wall grid point using the standard approach described in Section 3.2.3.

A similar process was used to establish the velocity wall function. Its form is more complex than the thermal wall function, as separate correlations were developed for the inner and outer sublayers of the natural convection boundary layer[20],

$$
\begin{aligned}
&u^{**} = \min\{f_i, f_o\} \\
&f_i = \begin{cases} 1.41y_i^{**} - 3.11(y_i^{**})^2 + 2.38(y_i^{**})^3 & \text{if } y_i^{**} \leq 0.53 \\ 0.228 & \text{if } y_i^{**} > 0.53 \end{cases} \\
&f_o = \begin{cases} 0.228 & \text{if } y_o^{**} \leq 0.005 \\ -0.458 - 0.258\ln y_o^{**} - 0.02425(\ln y_o^{**})^2 & \text{if } 0.005 < y_o^{**} \leq 0.09 \\ 0.024776e^{-y_o^{**}} & \text{if } y_o^{**} > 0.09 \end{cases}
\end{aligned}
\tag{5.6}
$$

Where u^{**} is a dimensionless velocity and y_i^{**} and y_o^{**} are dimensionless distances. The former distance is applicable if the next-to-wall grid point lies within the inner sublayer while the latter is applicable if it lies within the outer sublayer. These three dimensionless quantities are given by,

$$u^{**} = \frac{u_q^3 w_P}{u_\tau} \tag{5.7}$$

$$y_i^{**} = \frac{\Delta x_P u_q^3 \rho Pr}{u_\tau^2 \mu} \tag{5.8}$$

$$y_o^{**} = \frac{\Delta x_P u_q^7 \rho Pr}{u_\tau^6 \mu} \tag{5.9}$$

Where w_P is the vertical component of the velocity at the next-to-wall grid cell $\{m/s\}$. u_q is an outcome of the thermal wall function converged solution (equation 5.4) for the next-to-wall grid point under consideration. u_τ is the friction velocity $\{m/s\}$ and is given by,

$$u_\tau = \left(\frac{\tau_{wall}}{\rho}\right)^{1/2} \tag{5.10}$$

Again, an iterative solution is required. A wall shear (τ_{wall}) is guessed. y_i^{**} and y_o^{**} are calculated with the u_q results from the solution of the thermal wall function using equations 5.10, 5.8, and 5.9. u^{**} is then determined with equation 5.6 and an updated wall shear calculated with equations 5.7 and 5.10. This process is repeated until a converged state is achieved.

The Yuan wall functions were implemented into ESP-r's CFD model using an iterative solution approach as described above[21]. Rather than replacing the $k-\varepsilon$ model's log-law wall functions, the Yuan wall functions were added as a modelling option. The code was structured so that either set of wall functions could be applied to a given surface at a given time-step. In this way, the Yuan wall functions can be applied to some surfaces and the log-law wall functions to others, and this treatment

---

[20] Yuan et al (1993) and Yuan (1995) give different forms for f_o. The latter is shown here as use of the former lead to numerical instabilities.

[21] Modifications to the iterative solution approach proposed by Yuan (1995) were incorporated to enhance convergence and provide numerical stability.

can vary as the simulation progresses.

The implementation into ESP-r was tested on a simple buoyancy-driven case. Two opposing walls of a high-aspect-ratio rectangular cavity (0.5m by 0.5m by 2.5m high) were maintained at a temperature differential (one surface was at 33.2°C and the other at 11.5°C.), while all other surfaces were close to adiabatic. Three simulations were performed using the $k-\varepsilon$ model with the Yuan wall functions. The gridding in the direction perpendicular to the heated and cooled surfaces was varied from one simulation to the next to assess the impact of the next-to-wall grid spacing (Δx_P), while gridding in the other two directions was held constant. The three gridding scenarios examined were: 10x6x30, 20x6x30, and 30x6x30. Solver criteria were set to ensure a well converged solution. The set of simulations was then repeated with the log-law wall functions.

Figure 5.6 compares the flow field predicted with the two sets of wall functions. The general pattern of the recirculating flow is properly predicted in both cases: the flow rises along the hot surface and falls along the cold surface. However, much higher velocities (as much as 50%) are calculated when the Yuan wall functions are used. As well, the boundary layers are seen to penetrate further into the cavity.

The surface heat flux predictions for the three gridding scenarios are compared in Figure 5.7. As can be seen, the Yuan wall functions predict much higher surface convection than the log-law wall functions. Consistent with the evidence from the literature that was presented in Chapter 3, surface convection predictions are highly sensitive to the placement of the next-to-wall grid points when the log-law wall functions are used. In contrast, the Yuan wall functions are relatively insensitive to the gridding.

Not only are the surface convection predictions from the Yuan wall functions less sensitive to gridding, they are also more accurate. Figure 5.8 examines the CFD heat transfer predictions integrated over the heated wall. The graph also includes results from two empirical correlations for comparison purposes. Since the wall is heated, one of the empirical approaches selected for the comparison is the Awbi-Hatton heated wall correlation that was described in Chapter 4. The second empirical method is one recommended by Catton (1978),

$$\overline{Nu_L} = 0.22\left(\frac{Pr}{0.2+Pr}Ra_L\right)^{0.28}\left(\frac{H}{L}\right)^{-1/4} \tag{5.11}$$

This correlation, which gives convection as a function of the temperature difference between the heated and cooled surfaces, is specifically for natural convection within rectangular enclosures, and is applicable at this high aspect ratio and temperature difference.

Figure 5.8 illustrates again the relative grid-insensitivity of the Yuan wall functions: the coarse grid predicts 9% less heat transfer than the fine grid. The log-law wall functions, in contrast, predict less than half as much heat transfer with the coarse grid as with the fine grid. Compared to the empirical correlations, the Yuan wall functions predict about the same or slightly more than Awbi-Hatton

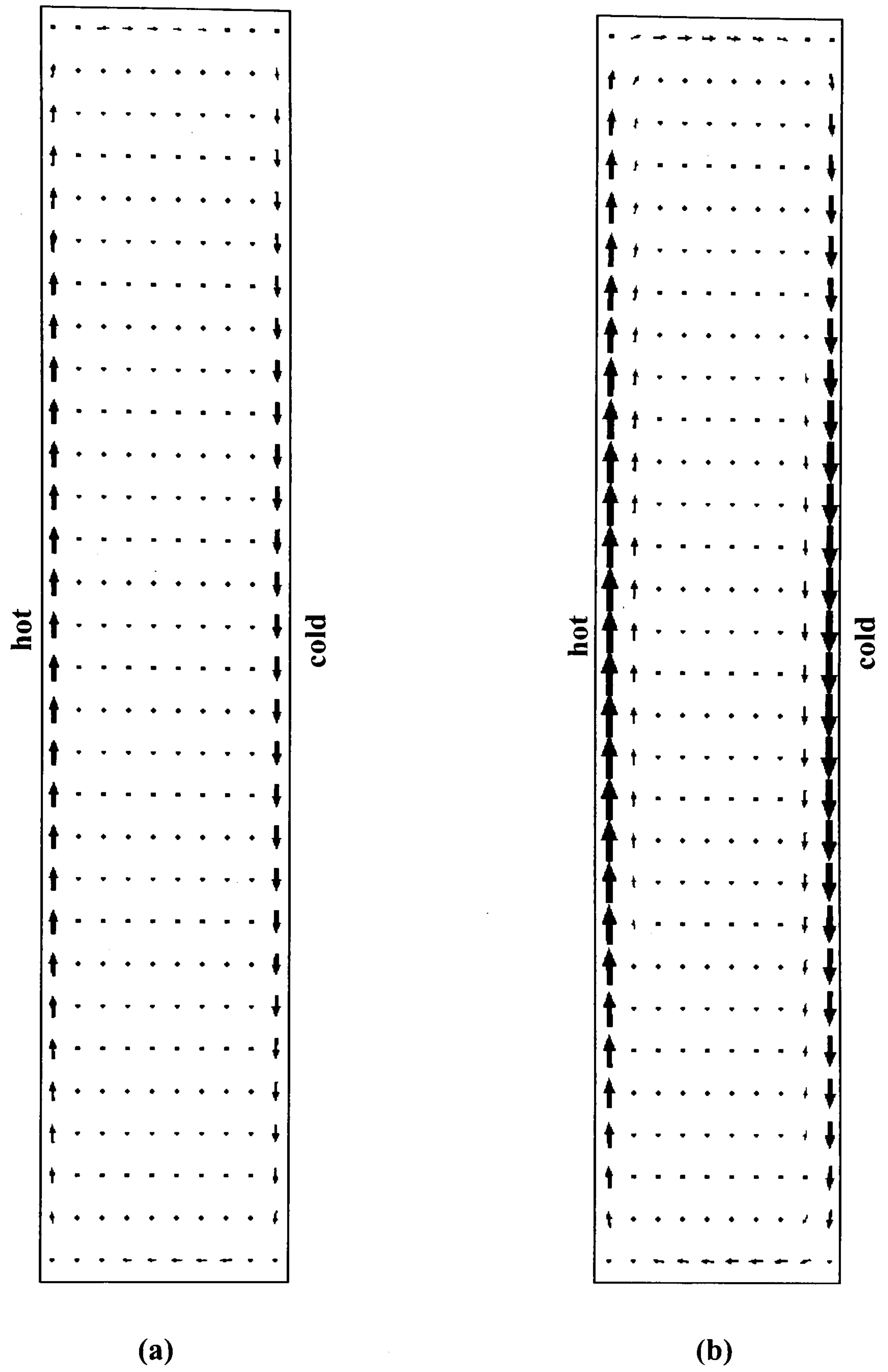

Figure 5.6 Buoyancy-driven cavity flow predicted with 10x6x30 grid: (a) log-law wall functions and (b) Yuan wall functions

and 15-30% higher than equation 5.11. As can be seen, with a (fortuitously) appropriate grid spacing, the log-law wall functions can give acceptable agreement with the empirical methods. However, they can just as easily underpredict heat transfer by more than 50-60%.

The inability of the log-law wall functions to reasonably predict the heat transfer explains the flow patterns observed in Figure 5.6. Flow in this case is driven exclusively by the surface convection.

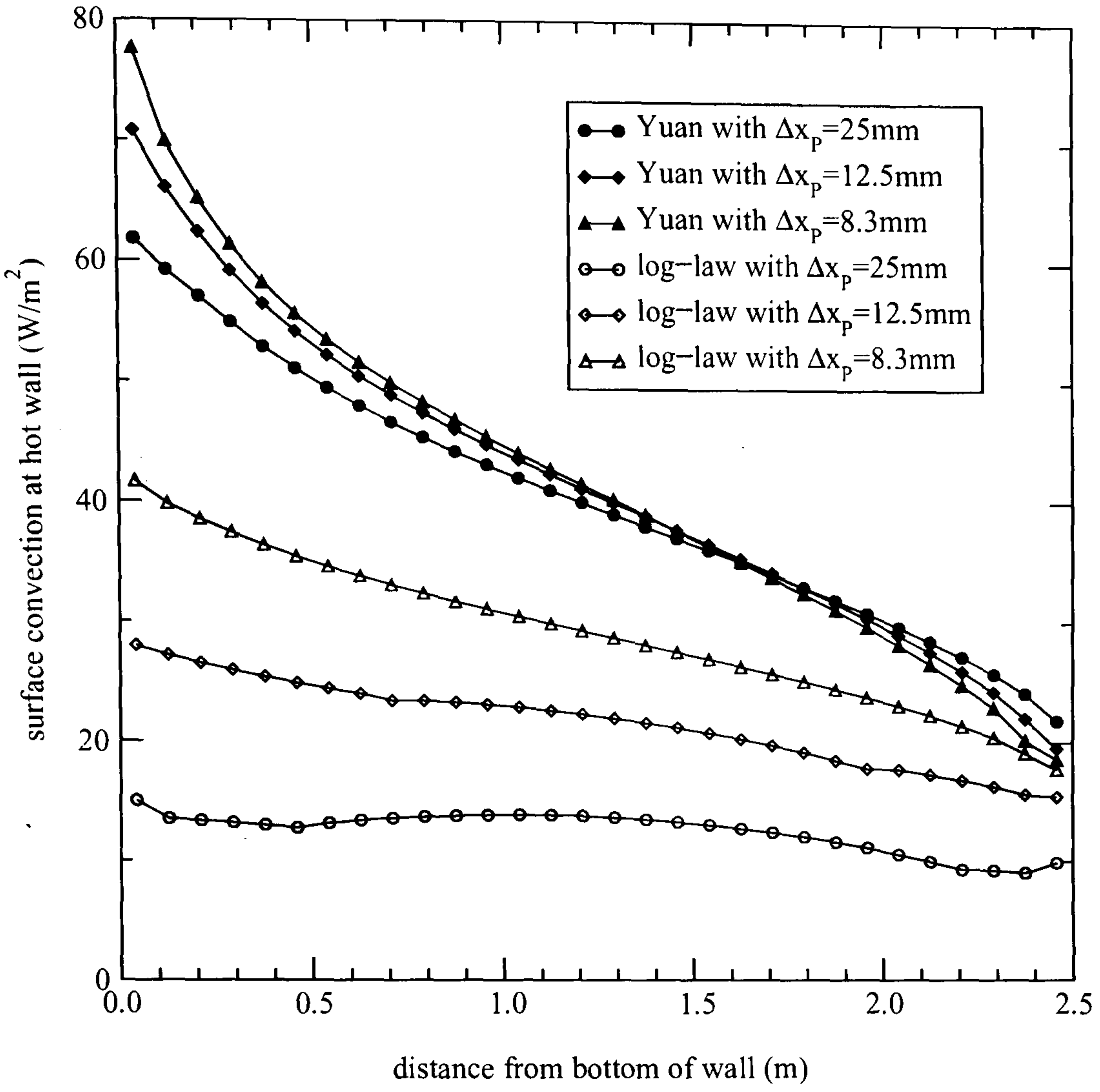

Figure 5.7 Local surface convection predictions for buoyancy-driven cavity flow

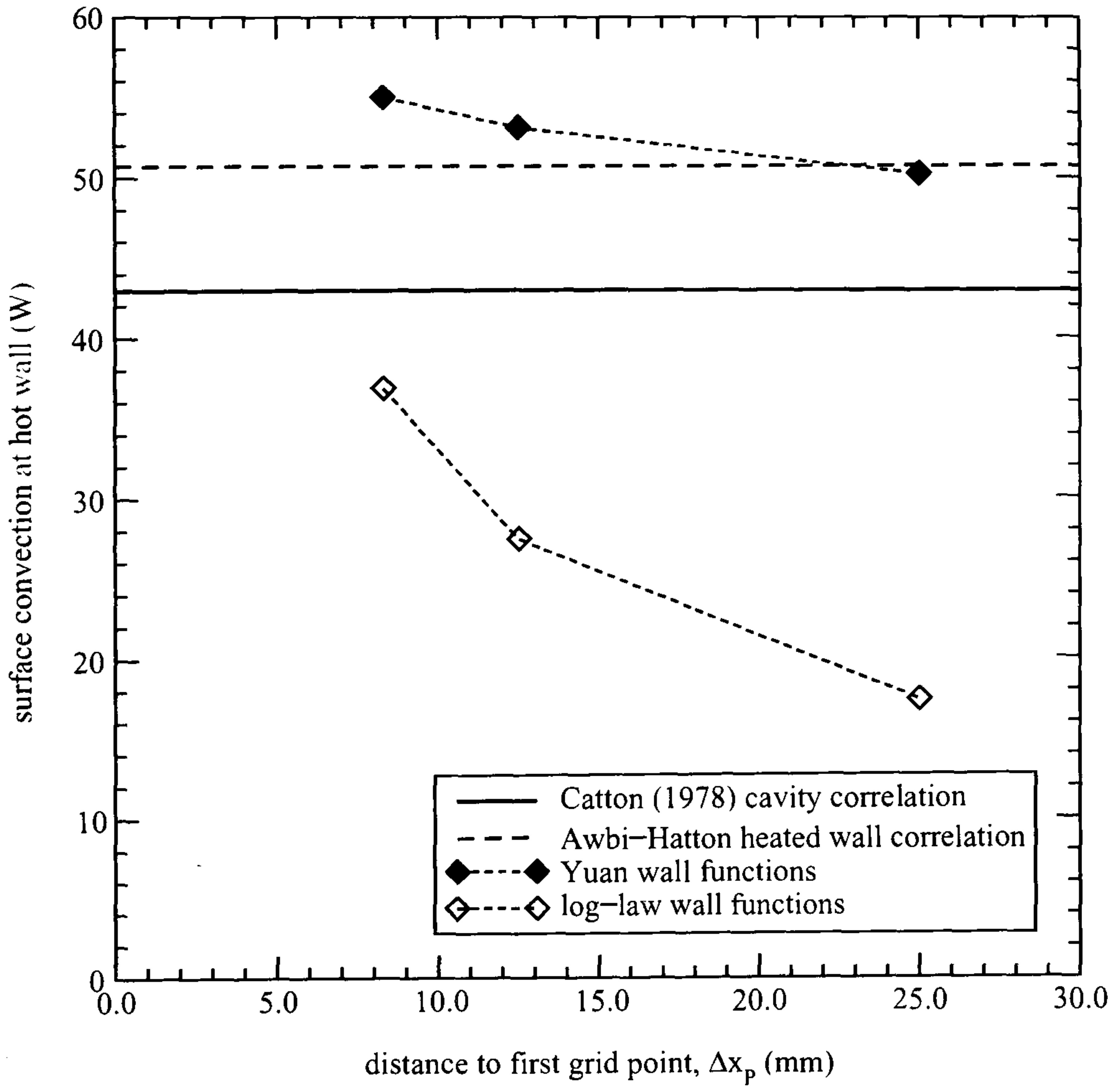

Figure 5.8 Total surface convection predictions for buoyancy-driven flow

Therefore, by underpredicting the heat transfer, the wall functions have underestimated the magnitude of the air velocities.

5.3.2 Chen and Xu zero-equation turbulence model

The Chen and Xu (1998) zero-equation turbulence model, which was put forward as an alternative to the $k - \varepsilon$ model for room air flow analysis, was introduced in Chapter 3. Like the $k - \varepsilon$ model, it characterizes the turbulent diffusion of heat and momentum with an eddy viscosity. However, it does not relate the eddy viscosity to the local values of k and ε (see equation 3.44, page 59) and thus does not require the solution of the k and ε transport equations. Rather, and this substantially reduces computational requirements, the eddy viscosity distribution is determined with a simple algebraic equation,

$$\mu_t = 0.03874 \rho \bar{V} l \tag{5.12}$$

where $\bar{V}$ is the local time-mean velocity and l is a length scale equal to the distance from the grid point to the nearest solid surface (Xu 1998).

The constant 0.03874, which is universally applicable for room air flows, has a semi-empirical basis: the value was established by examining the performance of the model for a number of indoor air flows. An inherent assumption behind equation 5.12 is that the eddy viscosity, and therefore the turbulent diffusion of momentum and energy, is greatest in regions of higher air velocity.

The zero-equation model does not rely upon wall functions. Rather, the wall shear is calculated using a no-slip formulation in which the eddy viscosity is substituted for the molecular viscosity (note the similarity with equation 3.16, page 47),

$$\tau_{wall} = \mu_t \cdot \left(\frac{\partial v}{\partial x}\right)_{wall} \approx \frac{\mu_t v_P}{\Delta x_P} \tag{5.13}$$

where v_P is the velocity parallel to the wall at the next-to-wall grid point.

The boundary condition for the energy equation is given as,

$$q''_{wall} = h_c \cdot (T_{wall} - T_P) \tag{5.14}$$

where the local convection coefficient is calculated from the eddy viscosity distribution,

$$h_c = \frac{c_P \mu_t}{\sigma_t \Delta x_P} \tag{5.15}$$

Equations 5.14 and 5.15 are derived from a Dirichlet type condition wherein the turbulent diffusivity of heat (see equation 3.36, page 57) replaces the conductivity (note the similarity with equation 3.18, page 47),

$$q''_{wall} = -c_P \Gamma \left.\frac{\partial T}{\partial x}\right|_{wall} \tag{5.16}$$

These boundary conditions are easily absorbed into the algebraic relations for the next-to-wall grid points using the technique elaborated on pages 46 to 48.

The zero-equation model has been validated against experimental data for a range of indoor air flow regimes (Chen and Xu 1998; Srebric et al 1999): displacement ventilation, natural convection with infiltration, and forced and mixed convection. Although reducing computational requirements was the prime motivating factor for the zero-equation model, it actually performed better than the $k-\varepsilon$ model in some cases. However, this validation work did not examine the accuracy of the model's surface convection predictions.

The Chen and Xu zero-equation turbulence model was implemented into ESP-r's CFD code. The $k-\varepsilon$ model was not replaced, but rather the code was structured so that either the $k-\varepsilon$ or the zero-equation turbulence model could be invoked at any given time-step. The implementation was tested with a simulation of the IEA Annex 20 two-dimensional test case (see Figure 3.8, page 63). A 20x20 grid was employed and the solution was driven to a fully converged state.

The flow pattern predicted with the zero-equation model is illustrated in Figure 5.9. For comparison purposes the flow pattern generated with the $k-\varepsilon$ model with log-law wall functions (using the same gridding) is also displayed. As can be seen, the two turbulence models predict similar flow fields with two notable differences. Relative to the $k-\varepsilon$ model and the measured data, the zero-equation model predicts slower flow along the ceiling and down the right wall. Unlike the $k-\varepsilon$ model, however, the zero-equation model is able to predict the small recirculation areas that Nielsen (1990) observed in the upper right and the lower left corners of the room (see enlarged areas of figure).

Recall from Section 3.7.2 that the $k-\varepsilon$ model poorly characterized the eddy viscosity distribution near the left wall, where flow rates are very low. Its predicted μ_t/μ ratios in this region were characteristic of fully turbulent flow. In contrast, the zero-equation model gives more realistic estimates. Its predictions for μ_t/μ range from 1 to 15, this indicating a laminar to weakly turbulent flow. This is in agreement with expectations. And along the flow path of the incoming air, the zero-equation model's estimates are consistent with those of the $k-\varepsilon$ model. Therefore, it can be concluded that the zero-equation model is a useful tool for assessing the nature of turbulence in rooms.

To assess the zero-equation model's ability to predict surface convection, a model was constructed of a sealed room heated by a wall-mounted hydronic panel. Two simulations were conducted, the first with a coarse mesh (10x11 grids in the plane of interest), and the second with a finer mesh (20x22). These simulations were performed in conflated mode, so that ESP-r's thermal model predicted the wall panel and surface temperatures in response to the prevailing conditions. Results were extracted for a time-step with a significant heating load when the wall panel's temperature was elevated (74°C) to supply heat to the room.

The flow pattern predicted with the finer mesh is illustrated in Figure 5.10. As expected, the heat output from the wall panel results in buoyant flow over the left wall at and above the location of

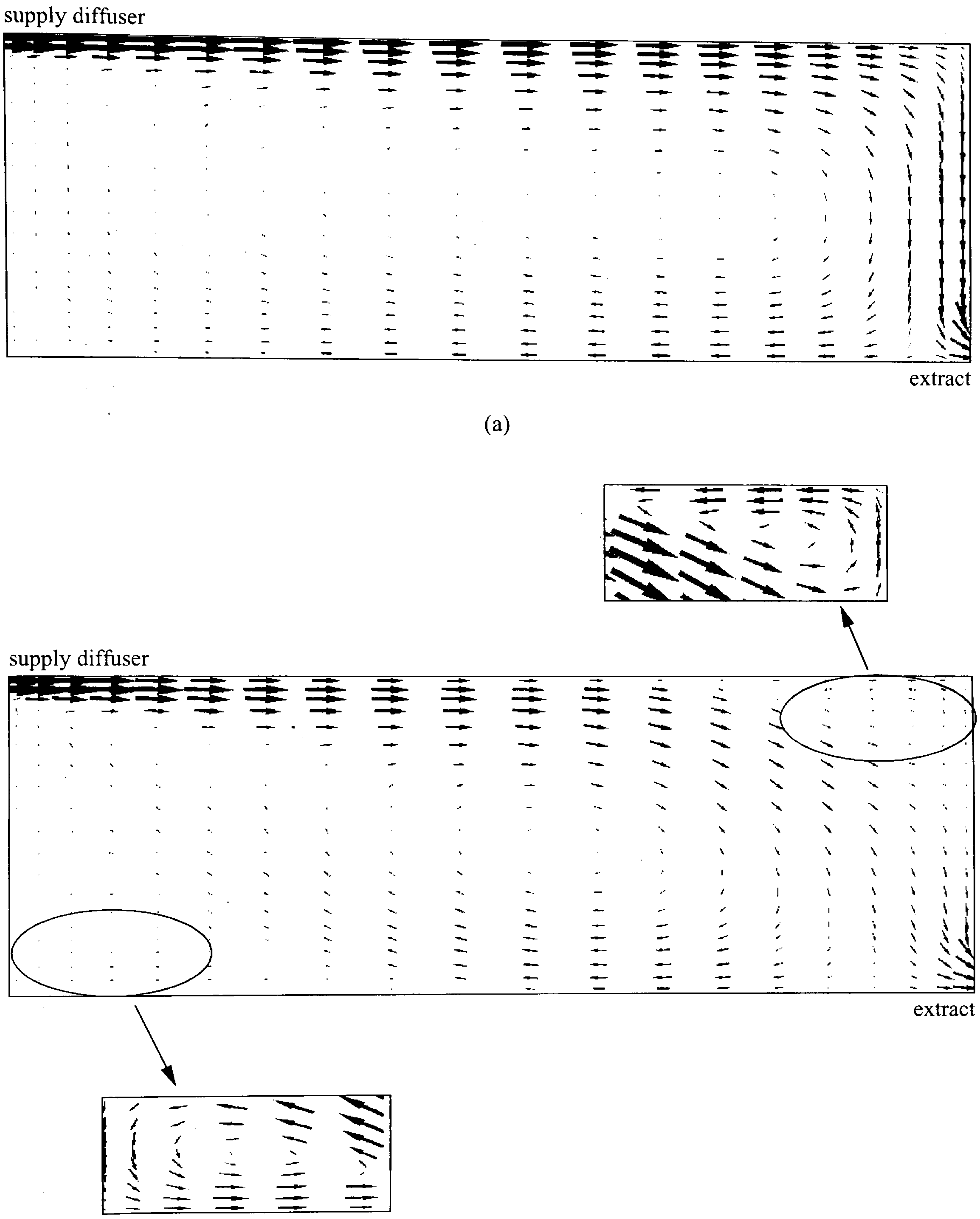

(a)

(b)

Figure 5.9 Air flow predictions for Annex 20 test room:

(a) $k - \varepsilon$ with log-law wall functions and (b) Chen and Xu zero-equation model

the panel. Flow continues along the ceiling initially, but then detaches due to the formation of cold buoyant plumes caused by heat transfer from the air to the cool surface. There is also some buoyant flow down the cool wall opposite the heater panel and some recirculation at the room's mid-height. The air remains relatively stagnant throughout the bottom half of the room.

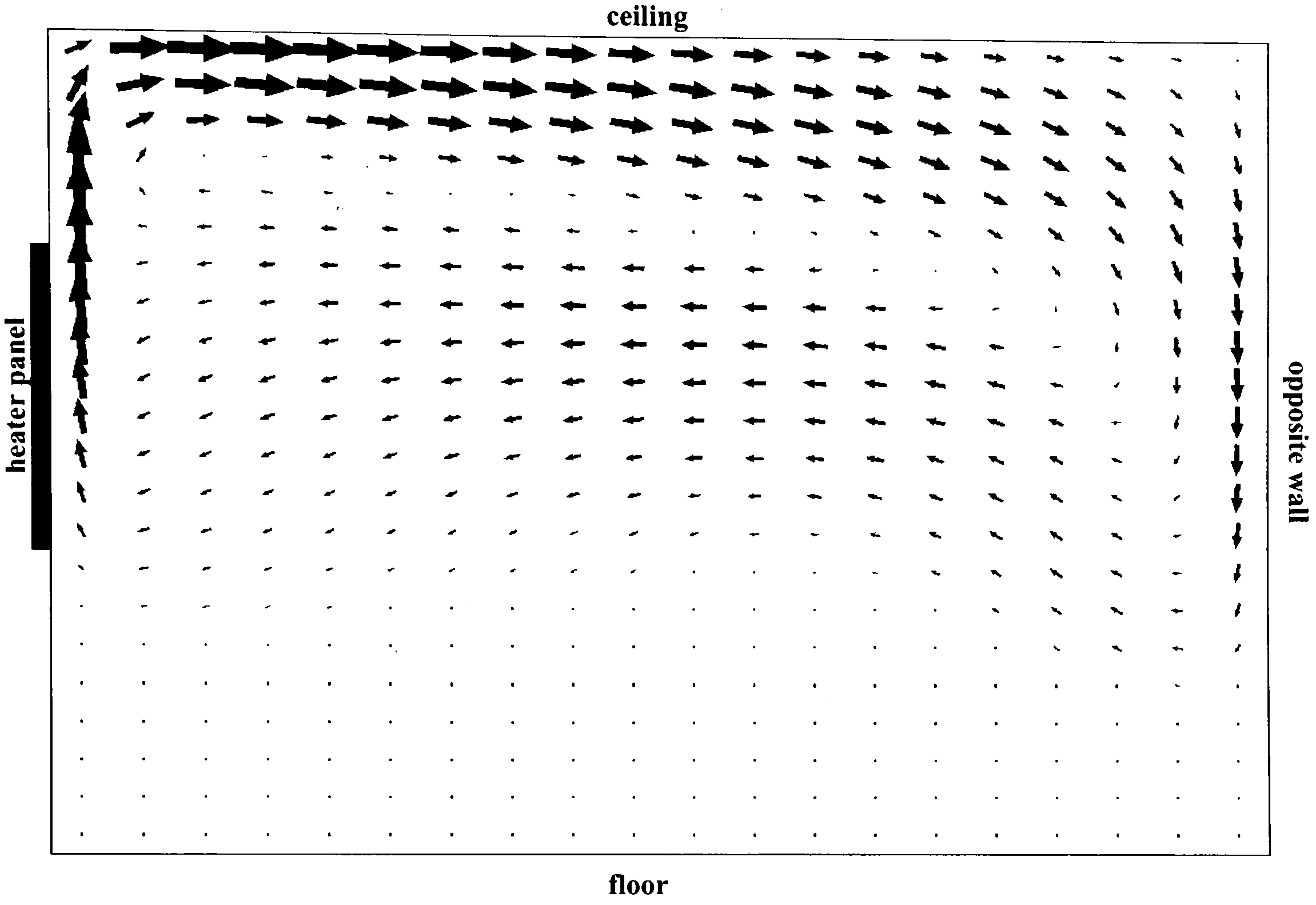

Figure 5.10 Flow field driven by wall panel as predicted with zero-equation model

The surface convection coefficients predicted by the zero-equation model for the two gridding scenarios are presented in Figure 5.11. The surface heat transfer has been normalized by surface area and by the temperature difference between the surface and the room air-point (as predicted by ESP-r's thermal model) so that the results from the various surfaces can be displayed in the same figure. This configuration is like convective regime A2 described in Section 5.2.1. Therefore, the h_c values predicted by the empirical correlations listed in Table 5.1 for convective regime A2 are also presented in the figure.

As can be seen, the zero-equation model's surface convection predictions are quite sensitive to gridding. At the surfaces with significant convection (the heater panel, ceiling, and opposing wall), the model predicts 45%-70% higher heat transfer with the finer grid. Relative to the empirical correlations, the zero-equation model predicts much higher heat transfer from the heater panel and to the ceiling, locations where the velocity is highest. It predicts somewhat less heat transfer to the opposite wall where velocities are modest, and virtually no heat transfer to the floor, above which the air is almost stagnant.

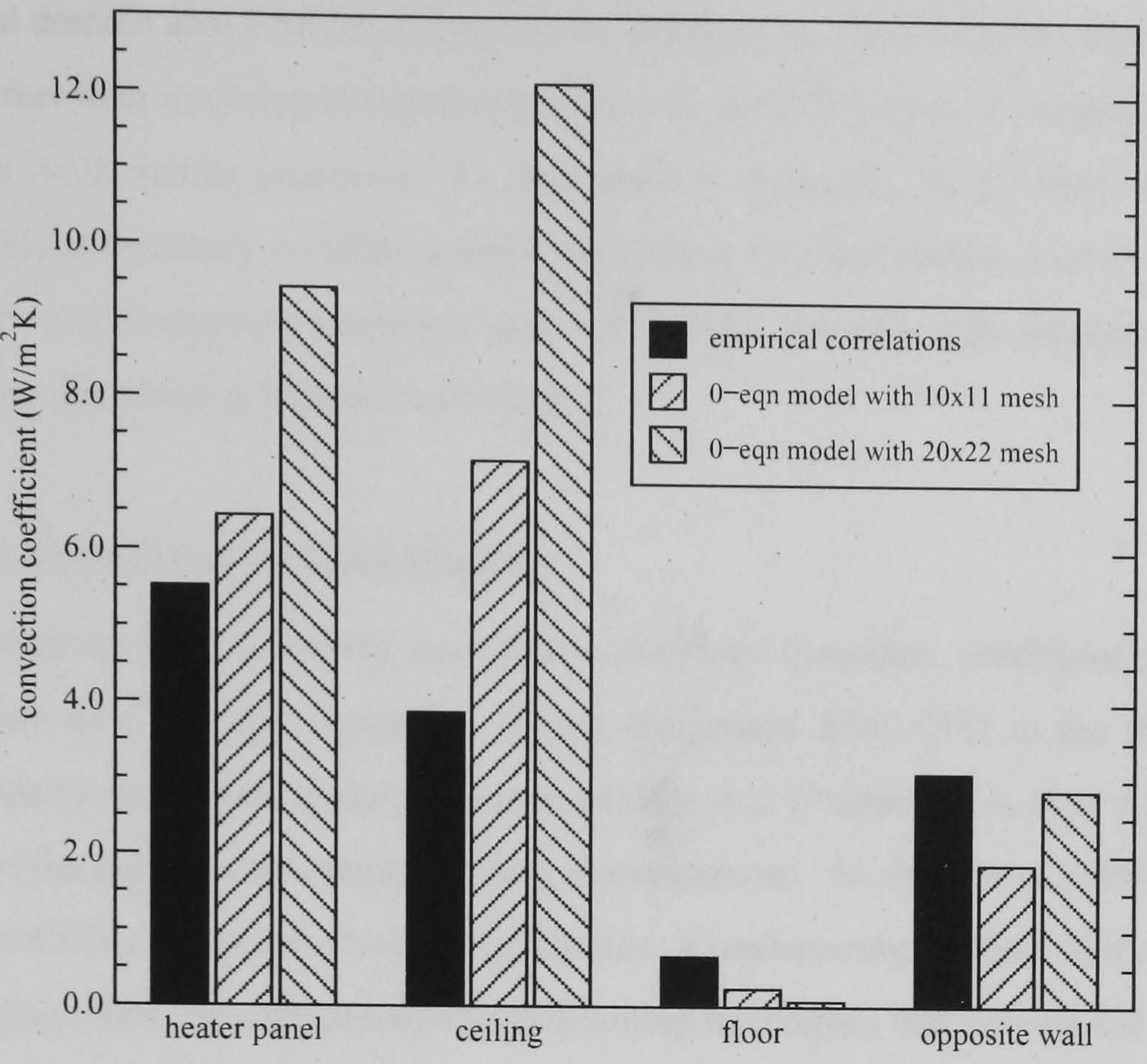

Figure 5.11 Comparison of surface heat transfer predictions for buoyancy-driven flow: Chen and Xu zero-equation model versus empirical correlations

These results can be explained by the zero-equation model's thermal boundary condition. Examination of equations 5.12 and 5.15 reveals that the convection coefficient is directly proportional to the predicted local time-mean velocity. Clearly, as these results show, this approach cannot adequately capture the behaviour in the thermal boundary layer, at least in the case of buoyancy-driven flow.

5.4 Optional Approaches for Handshaking and Resolving the Pivot Point

5.4.1 Handshaking between the thermal and CFD domains

Chapter 2 described the two basic approaches for handshaking between the CFD and thermal modelling domains. With one approach the thermal domain establishes boundary conditions for CFD, while the CFD model calculates convection coefficients for the thermal domain. The thermal domain uses these coefficients to establish the zone matrix of heat balance equations (Figure 2.10, page 27 shows which coefficients are affected by CFD) and then solves the building's thermal state. This approach can be described as *surface* conflation: the two solution domains operate independently but exchange information at the internal surfaces at the beginning of each simulation time-step. This is illustrated in Figure 5.12). The boxed coefficients in the matrix are those affected by the CFD-predicted convection coefficients.

The thermal domain also establishes boundary conditions for CFD with the second handshaking approach. But rather than returning convection coefficients, the CFD solver is encapsulated within the thermal domain's zone matrix processor. As described in Appendix B, the thermal domain's $\mathbf{R}''$ matrix passes updated boundary conditions and CFD returns updated surface convection predictions, as the two solvers march together towards a converged state. As such, this approach (illustrated in Figure 5.13) can be described as *integrated* conflation.

One-way and conditional two-way handshaking

Both handshaking schemes can be described as *two-way*: boundary conditions are passed from the thermal domain to CFD, and convection results are passed from CFD to the thermal domain. Based on the evidence presented in the preceding sections and chapters, it is clear that CFD cannot accurately resolve the surface convection in many circumstances. In such cases, two-way handshaking will propagate CFD's errors into the thermal domain. Consequently, success of the conflate simulator is critically dependent upon establishing handshaking techniques that prevent the propagation of erroneous results between the modelling domains.

This leads to two alternate handshaking concepts: *one-way* and *conditional two-way*. With one-way handshaking the thermal domain still establishes boundary conditions for CFD but the (direct) link from CFD to the thermal domain is broken. One-way handshaking is an attractive option when conditions are such that CFD can resolve the air flow but not the surface convection. This enables an accurate estimate of the flow regime without risking the distortion of the zone matrix of heat balance equations. Although this handshaking approach does not directly enhance the thermal simulation, Section 5.5 will point to some techniques that can be used to allow the thermal domain to respond to the CFD flow predictions.

Conditional two-way handshaking is identical to the two-way handshaking approach described above, with the addition of a decision-making step following the convergence of the CFD solution. The CFD results are appraised and a decision made on whether to propagate the CFD surface convection predictions into the thermal domain. This provides the thermal domain with a level of security to prevent the distortion of the heat balance matrix by unrealistic CFD results.

The advantages of surface conflation

Although integrated conflation enables tighter binding between the two solution domains, in practice it offers little advantage over surface conflation. When simulation time-steps are sufficiently small to resolve the building's evolving thermal state, there is inappreciable cost to the surface conflation approach of applying boundary conditions one time-step in arrears. Moreover, because the CFD and thermal solvers converge together with integrated conflation, it is impossible to exploit the one-

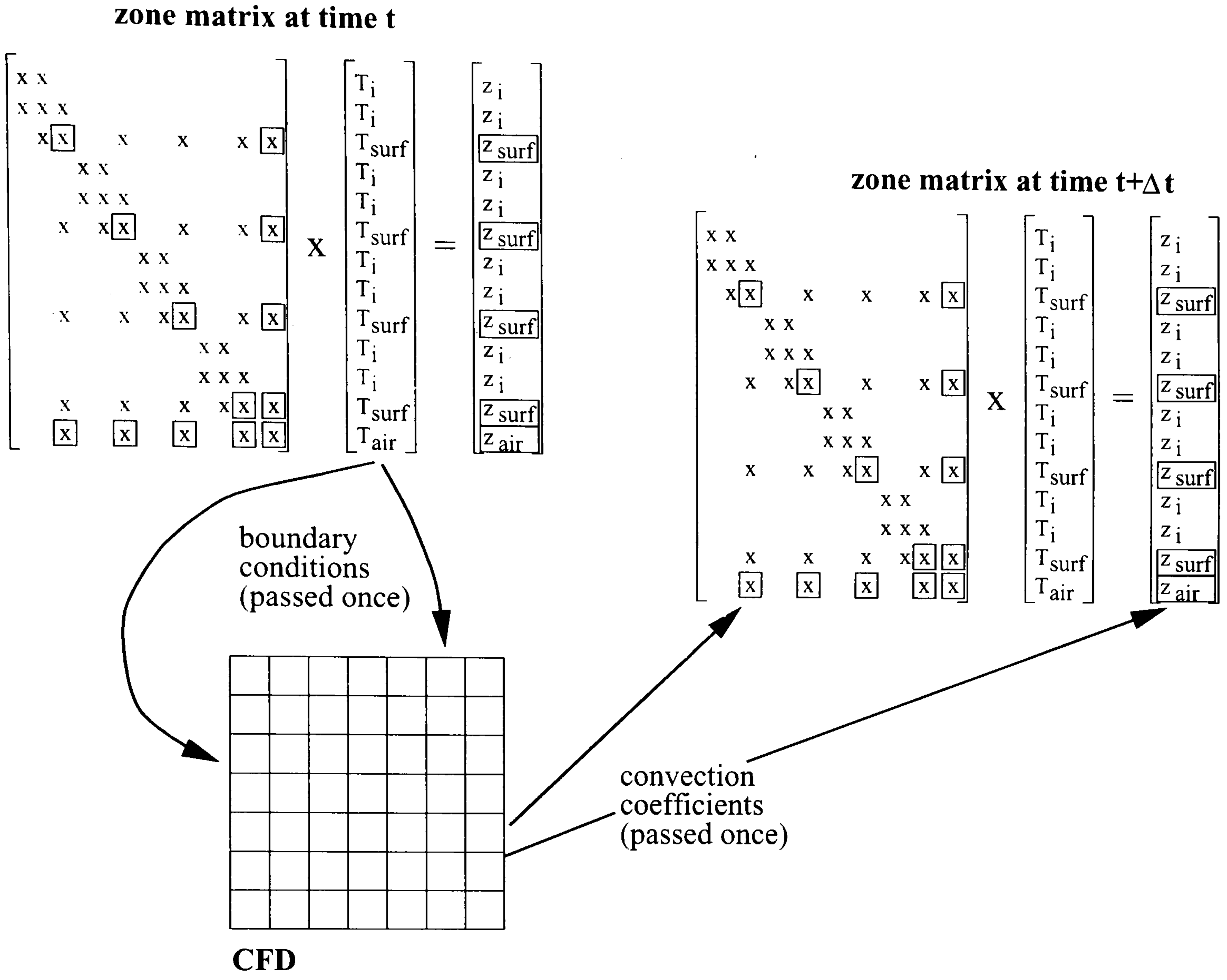

Figure 5.12 Surface conflation

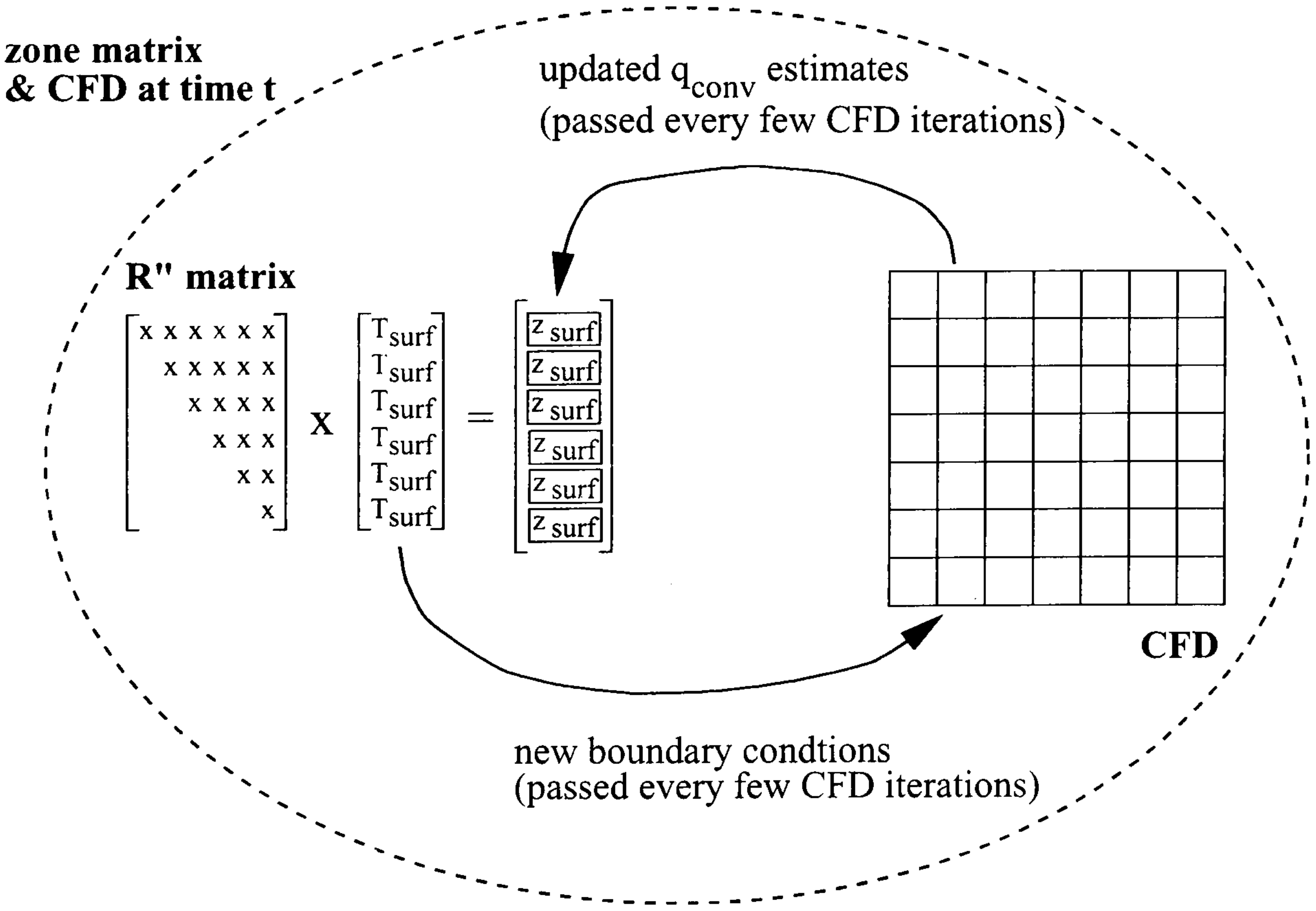

Figure 5.13 Integrated conflation

way and conditional two-way concepts with this approach.

In converse, surface conflation allows greater flexibility in handshaking and boundary condition treatments, and therefore is the approach used in this research. The advantages of surface conflation include the following:

- It allows one-way and conditional two-way handshaking.
- Boundary conditions can be devised to allow the thermal domain to resolve the surface convection when conditions are such that CFD cannot manage the task.
- Boundary conditions can be devised to allow the thermal and CFD domains to cooperatively resolve the surface convection.
- Each surface can be independently assigned appropriate handshaking and boundary condition treatments. As such, the conflation can adapt to local flow regimes.
- The surface convection can be resolved by CFD at some surfaces, while the thermal domain completely resolves surface convection at other surfaces.

5.4.2 Resolving the pivot point

A number of boundary condition treatments were devised to support the one-way and conditional two-way surface conflation approaches. These give the simulator three basic options for resolving the pivot point:

- CFD calculates the air-to-surface heat transfer using an appropriately selected turbulence and near-wall model;
- the thermal domain calculates the heat transfer using the adaptive convection algorithm;
- the CFD and thermal domains cooperatively calculate the heat transfer with support from the adaptive convection algorithm.

CFD calculates surface convection

A Dirichlet boundary condition is used to allow CFD to resolve the surface convection. With this, the thermal domain prescribes the temperature of the internal surface and CFD resolves the boundary layer using its calculated temperature, velocity, and turbulence fields in conjunction with a near-wall treatment. All three near-wall treatments described in Section 5.3 are supported: the $k - \varepsilon$ model with log-law wall functions; the $k - \varepsilon$ model with the Yuan wall functions; and the Chen and Xu zero-equation model with equation 5.14.

The Dirichlet boundary condition is absorbed into the next-to-wall grid points using an approach similar to that described in Section 3.2.3 (see page 47). Referring to the next-to-wall grid point (P) in Figure 5.14, this is accomplished by adjusting the neighbour, self-coupling and source coefficients of the discretized form of the energy balance (equation 3.14, page 44) as follows,

$$a_W = 0 \tag{5.17}$$

$$a_P = a_P + [dydz] \cdot \gamma$$

$$b = [dydz] \cdot \gamma \cdot T_{wall}$$

Where γ is derived from equation 3.48 (page 60), equation 5.1, or equation 5.14 depending upon the near-wall modelling approach in use.

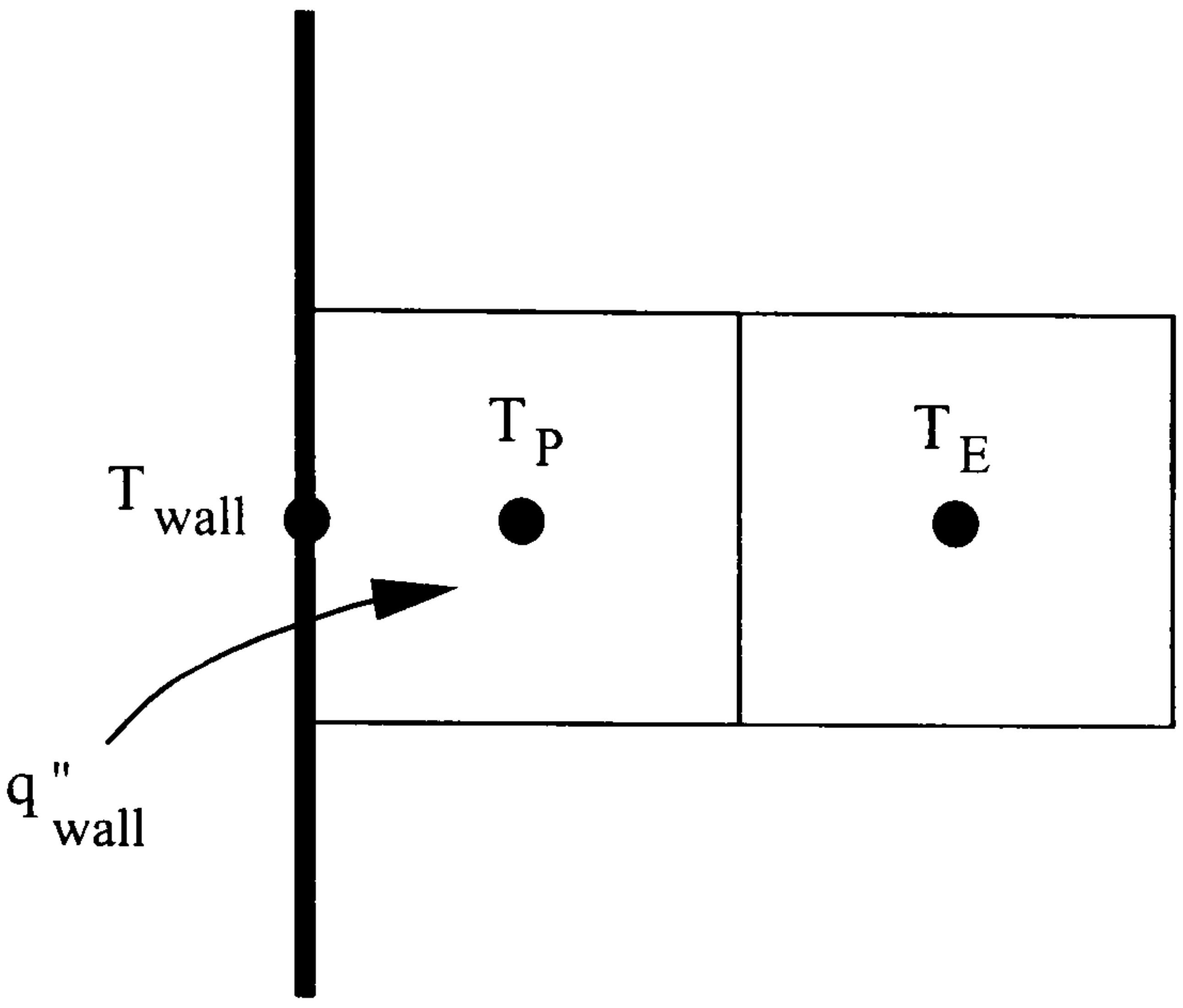

Figure 5.14 Thermal balance on next-to-wall grid point

The Dirichlet boundary condition can be used with either one-way or conditional two-way handshaking. It is known that the $k - \varepsilon$ model with log-law wall functions can give poor surface convection estimates but can give reasonable flow field predictions in many circumstances. Consequently, it is appropriate for use with one-way conflation. It can also be used with conditional two-way conflation as long as appropriate criteria are used to judge its heat transfer estimates.

The $k - \varepsilon$ model with the Yuan wall functions can give accurate surface convection estimates, but only for buoyancy-driven flow over vertical surfaces. Therefore, in these cases it is a good candidate for use with conditional two-way conflation. The Chen and Xu zero-equation model's ability to predict surface convection has not been examined in depth, but the results presented in Section 5.3.2 indicate that it is inappropriate for buoyancy-driven flows. As such, its use should be restricted to one-way conflation.

Thermal domain resolves surface convection

A Neumann boundary condition (this was introduced in Chapter 3) is used to enable the thermal domain to resolve the pivot point. This imposes a surface convection heat transfer on the CFD domain. As such, it does not require a thermal wall function to assume the temperature profile between the wall and the next-to-wall grid point. Rather, the heat transfer prescribed by the thermal domain directly enters the heat balance for the next-to-wall grid points in the CFD domain. Referring again to Figure 5.14 and equation 3.14, this is accomplished by adjusting the neighbour and source coefficients of the next-to-wall grid point as follows,

$$a_W = 0 \tag{5.18}$$

$$b = [dydz] \cdot q''_{wall}$$

Where convection (q''_{wall}) is treated as a surfaced-averaged quantity. It is calculated with the wall and room air-point temperatures solved by the thermal domain the previous time-step using a convection coefficient (the next section discusses how the adaptive convection algorithm is controlled to provide the coefficient),

$$q''_{wall} = \overline{h_c}(T_{wall} - T_{room-air}) \tag{5.19}$$

It is important to note that with a Neumann boundary condition, the wall's temperature is not absorbed into the next-to-wall grid point. Consequently, if all surfaces in a room are treated with the Neumann condition, a non-plausible temperature field can result. As surface convection is completely characterized by the thermal domain, this boundary condition is available only with one-way conflation. Its use is appropriate when the CFD's thermal results are so unreliable that they will substantially distort flow predictions.

Thermal and CFD domains cooperatively resolve surface convection

Two methods were devised to allow the thermal and CFD domains to cooperatively calculate the surface convection. The first uses a Neumann boundary condition. Like the above approach, the thermal domain establishes the surface temperature and the adaptive convection algorithm provides the convection coefficient. The surface convection is again calculated with equation 5.19. However, CFD rather than the thermal domain establishes the room-air temperature that drives the convection. The room-air temperature is calculated by mass-averaging the CFD-predicted temperature field over the cells of the computational domain,

$$T_{room-air} = \frac{1}{\int\limits_{room} \rho dV} \cdot \int\limits_{room} T_P \rho dV \tag{5.20}$$

Since the boundary condition is reapplied each solver iteration, equation 5.20 operates on the temperature results from the previous solver iteration. This boundary condition is absorbed into the next-to-wall grid points using equation 5.18.

The second cooperative method uses a Robin boundary condition,

$$q''_{wall} = h_c(T_{wall} - T_P) \tag{5.21}$$

In this case the convection coefficient is taken as a local value and the air temperature driving the convection is taken at the next-to-wall grid point (see Figure 5.14). This boundary condition is absorbed into the discretized form of the energy balance by adjusting the neighbour, self-coupling, and source terms as follows,

$$a_W = 0 \tag{5.22}$$

$$a_P = [dydz] \cdot h_c$$

$$b = [dydz] \cdot h_c \cdot T_{wall}$$

This cooperative boundary condition method allows the conflated simulator to consider the interdependencies between room air stratification and surface convection, while accurately resolving the wall heat transfer at the same time. This is accomplished even with one-way conflation, because surface convection becomes a function of the evolving temperature field.

There are two significant differences between the Neumann and Robin cooperative boundary conditions. The latter operates on local convection coefficients and local air temperatures. As such, the Robin condition can be used for one-way or conditional two-way conflation, whereas use of the Neumann condition is limited to one-way conflation.

Two inconsistencies of the Robin cooperative boundary condition must be recognized. The convection coefficient in equation 5.21 is treated as a local value. However, it is supplied by the adaptive convection algorithm which employs surface-averaged h_c correlations. It is felt that this introduces little inaccuracy, as neither Khalifa (1989) nor Awbi and Hatton (1999) found local h_c variations to be significant. The choice of the room air temperature in equation 5.21 is perhaps more problematic. The h_c correlations are based on average room conditions (except for the Awbi-Hatton correlations which are based on the temperature 100mm from the surface), but equation 5.21 uses the temperature of the next-to-wall grid point. Offsetting this inconsistency, however, is the fact that the Robin condition is able to predict the impact of stratification on surface convection. The significance of this phenomena was demonstrated in Section 4.6 where it was shown how accurately modelling of the IEA test room was critically dependent upon establishing the correct driving temperatures for the surface convection.

It is interesting to note that upon examining a number of thermal boundary condition treatments for modelling room air flows, Schild (1997) recommended a method like equation 5.21, although he left the choice of reference air temperature open to debate. A number of other researchers (such as Niu and van der Kooi 1992; Awbi 1998; Loomans 1998) have also recommended imposing convection coefficients and surface temperatures on the CFD domain, rather than employing a Dirichlet condition with wall functions.

5.5 The Adaptive Conflation Controller

The previous sections have laid the foundation for dynamically controlling the conflation between the thermal and CFD modelling domains. Supported by the adaptive convection algorithm, a suite of handshaking schemes, boundary condition treatments, and turbulence models have been implemented to provide optional approaches for resolving the pivot point between the two modelling domains.

Upon examining a number of alternatives, ten viable combinations of these approaches were selected for the adaptive conflation controller. These are summarised in Table 5.2. The $k-\varepsilon$ model with log-law wall functions is used in six of the schemes, although four of these do not employ the thermal wall function. Two schemes use the $k-\varepsilon$ model with the Yuan wall functions and two use the Chen and Xu zero-equation turbulence model. It is worth noting that the adaptive convection algorithm plays a central role in characterizing the pivot point in four of the ten schemes.

The last column of the table describes, in broad terms, the applicability and limitations of each scheme. As can be seen, a number of the schemes are useful for predicting the flow and temperature fields, while others can perform this function as well as calculate surface convection for the thermal domain. Some schemes are restricted to certain flow regimes (e.g. buoyancy-driven flow) while others are more generally applicable. Three of the schemes are particularly useful for dealing with stratified rooms.

Given the reality that thermal conditions outside the CFD domain are dynamic, the schemes laid out in Table 5.2 can not be fully exploited unless the simulator is supported by a controlling algorithm. This controller must monitor thermal and air flow conditions and dynamically select an appropriate scheme for the prevailing conditions.

A plethora of structural and logical options exist for devising the controller. It is outside the scope of this research to propose an optimal approach. However, two viable solutions were devised and implemented to demonstrate the concept. One is suitable when the objective of the analysis is to predict the flow and temperature field within the room, perhaps for the purposes of visualizing the flow, assessing thermal comfort, or studying pollutant dispersion. The other is suited to performing these tasks as well as enhancing the thermal simulation by providing surface convection estimates for the thermal domain. These two control approaches are described in the following subsections.

5.5.1 One-way adaptive conflation control

Figure 5.15 illustrates the logic employed in the one-way adaptive conflation controller. This controller is based on the surface conflation method and the link from CFD to the thermal domain is broken to protect the integrity of the thermal simulation. It makes use of a double-pass modelling

turbulence model	**handshaking mechanism**	**CFD thermal boundary condition**	**applicability**
$k-\varepsilon$ model & log-law wall functions (for momentum eqs)	one-way	• Dirichlet • CFD calculates q_{conv} with log-law wall function	• Predicting flow and temp field • Not suitable for buoyancy-driven flow • Not suitable for flows strong affec by q_{conv}
		• Neumann • thermal domain $\rightarrow T_{surf}$ • thermal domain $\rightarrow T_{room-air}$ • adapt conv algor $\rightarrow h_c$	• Predicting flow and temp field • Suitable for flows strongly affected by q_{conv}
		• coop Neumann • thermal domain $\rightarrow T_{surf}$ • CFD $\rightarrow T_{room-air}$ (avg) • adapt conv algor $\rightarrow h_c$	• Predicting flow and temp field • Suitable for flows strongly affected by q_{conv} • Useful when room stratified
		• coop Robin • thermal domain $\rightarrow T_{surf}$ • CFD $\rightarrow T_P$ (local) • adapt conv algor $\rightarrow h_c$	• Predicting flow and temp field • Suitable for flows strongly affected by q_{conv} • Useful when room stratified
	conditional two-way	• Dirichlet • CFD calculates q_{conv} with log-law wall function	• Predicting flow and temp field • Enhancing surf conv calcs • Not suitable for buoyancy-driven flow • Not suitable for flows strong affec by q_{conv} • Next-to-wall points must be properly placed
		• coop Robin • thermal domain $\rightarrow T_{surf}$ • CFD $\rightarrow T_P$ (local) • adapt conv algor $\rightarrow h_c$	• Predicting flow and temp field • Enhancing surf conv calcs • Suitable for flows strongly affected by q_{conv} • Useful when room stratified
$k-\varepsilon$ model & Yuan wall functions	one-way	• Dirichlet • CFD calculates q_{conv} with Yuan wall function	• Predicting flow and temp field • Only suitable for buoyancy-driven flow • Only suitable for vertical surfaces
	conditional two-way	• Dirichlet • CFD calculates q_{conv} with Yuan wall function	• Predicting flow and temp field • Enhancing surf conv calcs • Only suitable for buoyancy-driven flow • Only suitable for vertical surfaces
Chen & Xu 0-eqn model	one-way	• Dirichlet • CFD calculates q_{conv} with equation 5.14	• Predicting flow and temp field • Suitable for quick indication of flow • Less suitable for buoyancy-driven flow • Less suitable for flows strong affec by q_{conv}
	conditional two-way	• Dirichlet • CFD calculates q_{conv} with equation 5.14	• Predicting flow and temp field • Enhancing surf conv calcs • Less suitable for buoyancy-driven flow • Less suitable for flows strong affec by q_{conv} • Next-to-wall points must be properly placed

Table 5.2: Turbulence, handshaking, and boundary condition options for adaptive conflation controller

approach. An investigative CFD simulation is first performed to approximate the room's flow and temperature field. These results are appraised by the controller to determine the nature of the flow. Boundary condition treatments and other simulation parameters appropriate for the prevailing flow conditions are selected, and a second CFD simulation performed using the refined modelling approach. In other words, two CFD simulations are performed between the time-steps of the thermal domain (refer to Figure 5.12). In this implementation, the Chen and Xu zero-equation model is employed in the investigative analysis, and the $k - \varepsilon$ turbulence model is used in the refined CFD simulation.

Investigative CFD simulation

The purpose of the investigative simulation is not to accurately quantify the flow and temperature field, but rather to approximate the flow regime in order to establish appropriate modelling approaches. The zero-equation model is a good candidate for this task because of its stability and computational efficiency. Additionally, as Section 5.3.2 demonstrated, it is a useful tool for characterizing the nature of turbulence throughout the room because it gives realistic eddy viscosity predictions. For the investigative simulation, the zero-equation model is configured with a Dirichlet boundary condition, and it resolves the wall heat transfer with equation 5.14. The buoyancy term in the z-momentum equation is considered and the surface temperatures are mapped from the thermal domain's solution, as illustrated in Figure 5.12.

An approximate solution is adequate for the assessment. Therefore, the adaptive controller moderates the convergence criteria so that CFD may resolve the flow pattern with fewer solver iterations. Once the investigative simulation converges, the controller appraises the predicted flow and temperature field by calculating relevant dimensional groupings at each physical surface.

Each physical surface of the CFD domain is appraised independently. It is important to note that a physical surface may span numerous surfaces in the model. This is illustrated in Figure 5.16. To match the CFD domain to three independent zones in the thermal model, the wall on the left was divided into three surfaces. These three surfaces cannot be appraised independently, as boundary layer development is not affected by this modelling artifact. Therefore, the ability to recognize the relations between model surfaces was implemented into the controller. The temperature and flow field predictions from the investigative solution are discarded once the dimensionless groupings have been evaluated.

Dimensionless groupings

The Grashof and Reynolds numbers were selected as the relevant physical groupings. The Grashof number indicates the ratio of the buoyancy force to the viscous force acting on the fluid, and thus measures "how buoyant" the flow is adjacent to the surface. The Reynolds number serves a

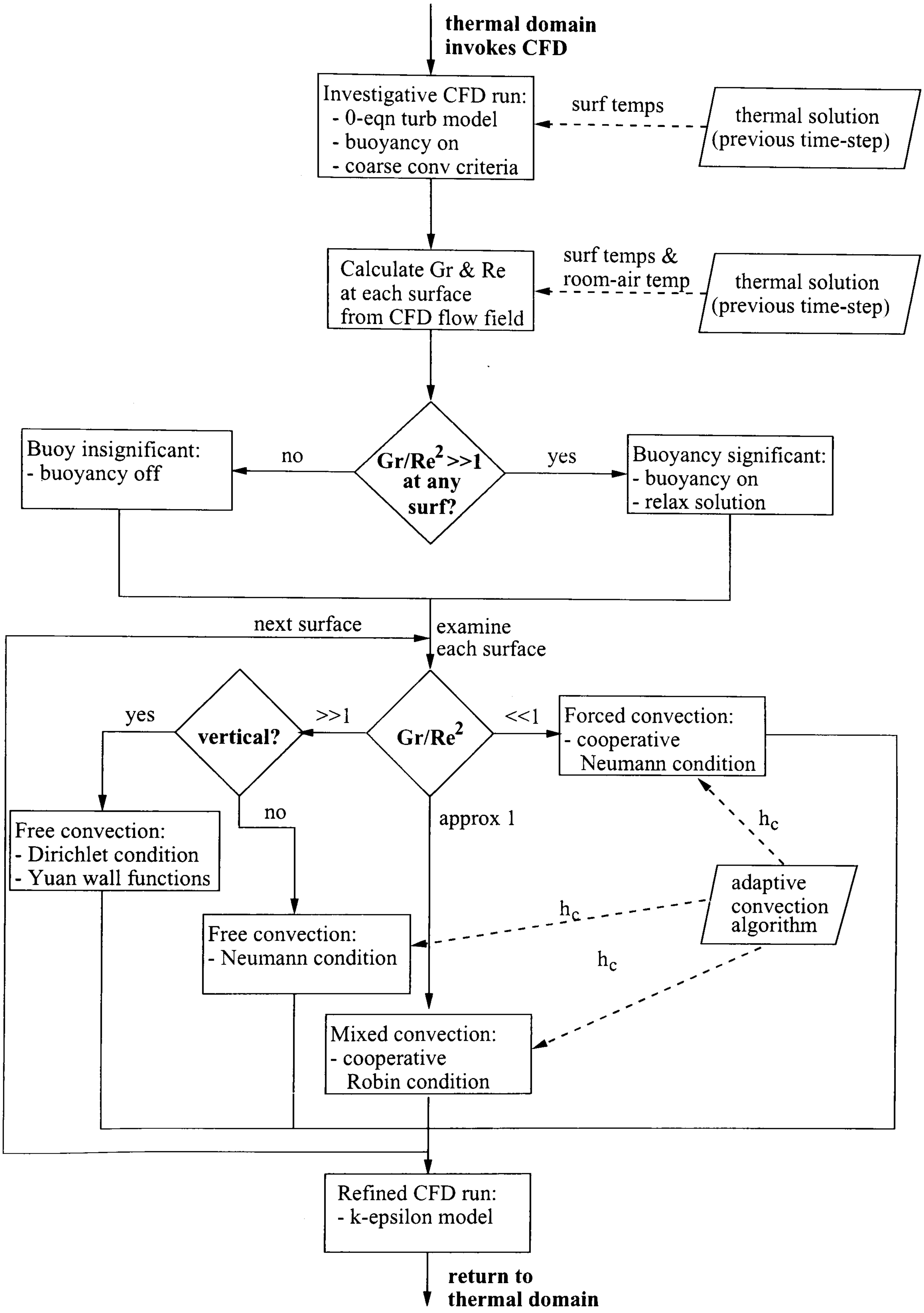

Figure 5.15 One-way adaptive conflation control

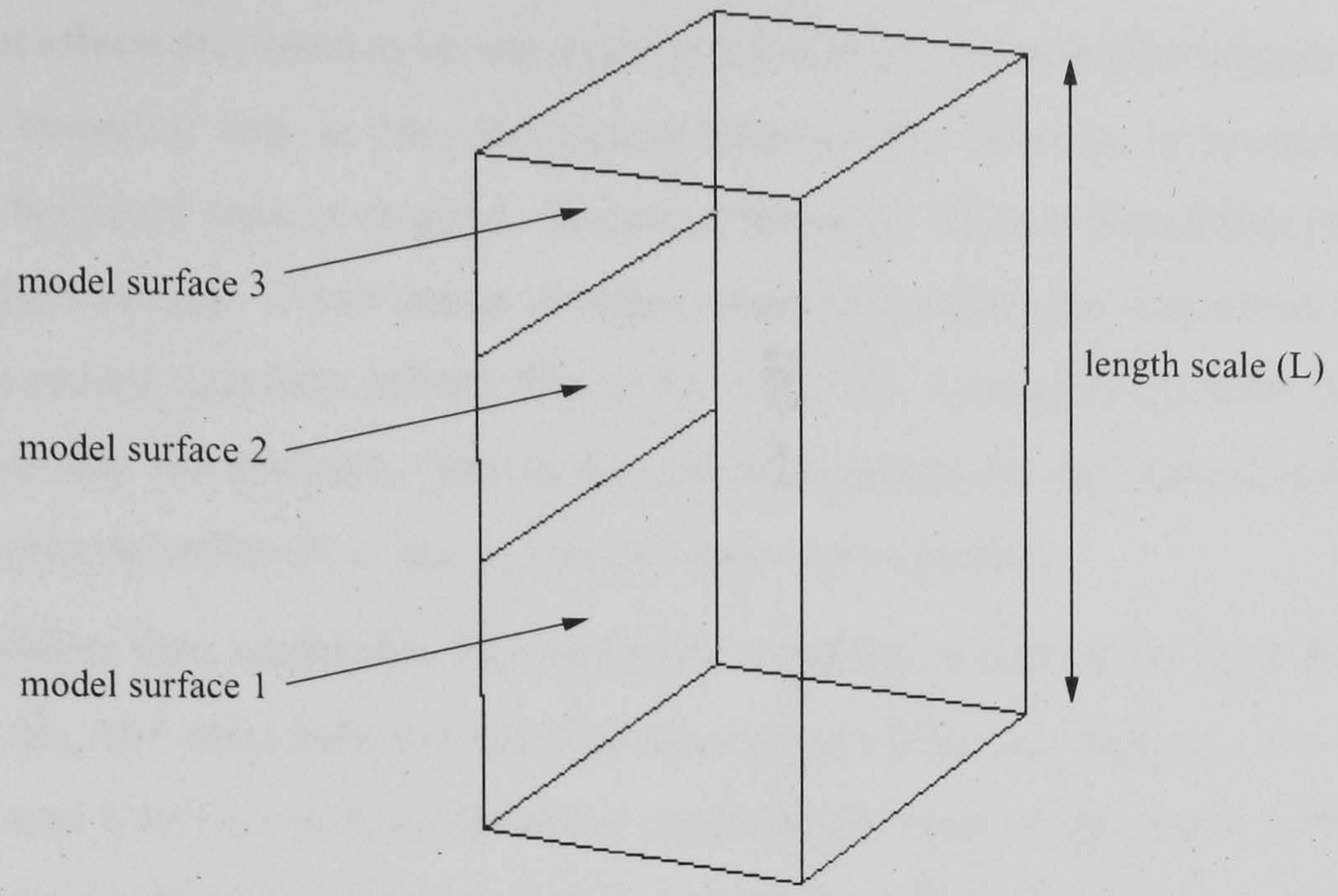

Figure 5.16 The relationship between model and physical surfaces

similar role in gauging "how forced" a flow is adjacent to a surface, as it indicates the ratio of the inertial to viscous forces. These dimensional groupings are given by,

$$Gr_L = \frac{g\beta\rho^2 |T_{wall} - T_{room-air}| L^3}{\mu^2} \tag{5.23}$$

$$Re_L = \frac{\rho V_{ref} L}{\mu} \tag{5.24}$$

The length scale (L) is automatically calculated by the adaptive conflation controller when the problem's geometry is read by the simulator, prior to the time-step simulation. It is equal to the height of vertical surfaces (see Figure 5.16) and the ratio of area to perimeter for horizontal surfaces.

The surface and room-air temperatures in equation 5.23 are taken from the thermal domain's solution (it would be a trivial extension to calculate $T_{room-air}$ from the investigative CFD predictions, but this would not affect the subsequent decisions taken by the controller). When numerous model surfaces span a physical surface, equation 5.23 is evaluated using the model surface temperature with the greatest deviation from the room-air temperature. The reference velocity (V_{ref}) in equation 5.24 is determined from the investigative CFD solution. It is equal to the greatest velocity predicted at any of the CFD grid points adjacent to the physical surface.

The nature of the flow in the vicinity of each surface is then determined by comparing the dimensionless groupings. When $Gr_L/Re_L^2 \ll 1$ it can be concluded that free convection is overwhelmed by forced convection effects (Incropera and Dewitt 1985). Similarly, when $Gr_L/Re_L^2 \gg 1$ free convection effects dominate. And when Gr_L and Re_L^2 are of the same order of magnitude, both forced and free effects are significant.

Setting boundary conditions and other simulation parameters

If buoyant effects are found to be important at any surface, the controller adjusts the CFD model to consider the buoyancy term in the z-momentum equation (the last term in equation 3.3, page 39); otherwise, this buoyancy term is dropped. Including buoyancy tends to destabilize the CFD iterative solution procedure because it provides a stronger coupling between the sequential solutions of the momentum and energy equations (refer to Figure 3.6, page 51). Consequently, when buoyancy is considered, the controller automatically reduces the relaxation factors for the velocity, pressure, temperature, and turbulence variables (k, ε, and μ_t) to encourage convergence.

The controller then establishes an appropriate boundary condition for each surface (independently). If the Gr_L/Re_L^2 ratio indicates that free convection effects are dominant at a vertical surface, then the Yuan wall functions with the Dirichlet condition are used. A Neumann condition is applied when free convection effects dominate at a horizontal surface. Since the choice of a reference air temperature can be difficult in this case, the thermal domain supplies the room air temperature and the adaptive convection algorithm is called upon to provide an appropriate convection coefficient for the surface.

If free convection effects are not important, then the cooperative Neumann condition is applied and the adaptive convection algorithm supplies a convection coefficient. When both free and forced effects are important, the cooperative Robin condition is employed, this to ensure local temperature effects are considered. Again, the adaptive convection algorithm supplies the convection coefficient.

This completes the preparation for the second CFD simulation. The CFD model is then invoked by the controller to refine the flow and temperature fields. The approximate flow and temperature field predicted by the investigative run is used to initialize the solution variables to accelerate convergence, and to provide greater numerical stability. The eddy viscosity distribution calculated by the zero-equation model (with equation 5.12) is used to initialize the k and ε fields using equation 3.44 (see page 59).

As the link from the CFD domain to the thermal matrix is broken with this one-way conflation approach, once the refined CFD solution converges the controller generates images of the flow, then returns control to the thermal domain. The thermal domain assembles and solves the zone heat balance matrices in the usual manner, then calls upon the adaptive conflation controller again at next time-step. The process elaborated above is then repeated.

5.5.2 Conditional two-way adaptive conflation control

Figure 5.17 illustrates the logic flow employed in the conditional two-way adaptive conflation controller. Its structure is very similar to the one-way controller, with one notable addition. There is an appraisal stage following the convergence of the refined CFD simulation, prior to convection coefficients being returned to the thermal domain. As well, some different thermal boundary conditions are employed.

Setting boundary conditions

The boundary conditions are set the same way as with the one-way controller when the Gr_L/Re_L^2 ratio indicates that free convection effects are dominant at a vertical surface (Yuan wall functions with the Dirichlet condition) or when both effects are significant (cooperative Robin condition). But in this case conditional two-way handshaking is used. Since no technique currently exists to satisfactorily resolve the heat transfer for free convection at horizontal surfaces, the one-way Neumann condition is applied, with the air temperature supplied by the thermal domain and the convection coefficient by the adaptive convection algorithm.

When forced effects dominate, the controller must consider additional criteria to select a boundary condition. Recall that the ratio of the eddy viscosity to the molecular viscosity (μ_t/μ) can be considered an indicator of "how turbulent" a flow is locally. As the zero-equation model gives a realistic μ_t distribution, the controller uses the investigative run's results to assess the nature of the turbulence. It examines the μ_t predictions at the grid points adjacent to the physical surface. If the average μ_t/μ ratio at these points is less than 30, it concludes that the flow is (locally) weakly turbulent. As Section 3.7.2 showed, in such conditions the $k-\varepsilon$ model cannot accurately predict the surface convection using the next-to-wall grid point temperatures, irregardless of the near-wall treatment. Therefore to protect the integrity of the thermal domain, the controller applies the cooperative one-way Neumann condition. And if the average μ_t/μ ratio of the grid points adjacent to the surface is greater than 30, the conditional two-way Dirichlet condition with log-law wall functions is used.

Assessing the CFD-predicted convection coefficients

With conditional two-way conflation, the CFD domain can return convection coefficients to the thermal domain (see Figure 5.12). The previous sections and chapters have shown how problematic the task of predicting surface convection is for CFD. Therefore, to avoid distorting the zone matrix of heat balance equations, the controller assesses (and where necessary rejects) the CFD-predicted convection coefficients prior to passing them to the thermal domain.

A two-stage screening process is employed (illustrated in Figure 5.18). Section 5.3.1 demonstrated that the $k-\varepsilon$ model with log-law wall functions can lead to realistic surface convection predictions when the next-to-wall grid points are appropriately placed. There is no consensus on how the gridding should be placed, but based on the recommendations of Niu and van der Kooi (1992), Chen (1995), Schild (1997), and Awbi (1998), the controller considers the gridding to be appropriate when the dimensionless spacing to the next-to-wall grid point (y^+) is in the range of 10 to 30. Therefore, following the convergence of the refined CFD simulation, the y^+ values of the next-to-wall grid points are calculated. If they lie outside this range, the CFD surface convection predictions at these surfaces

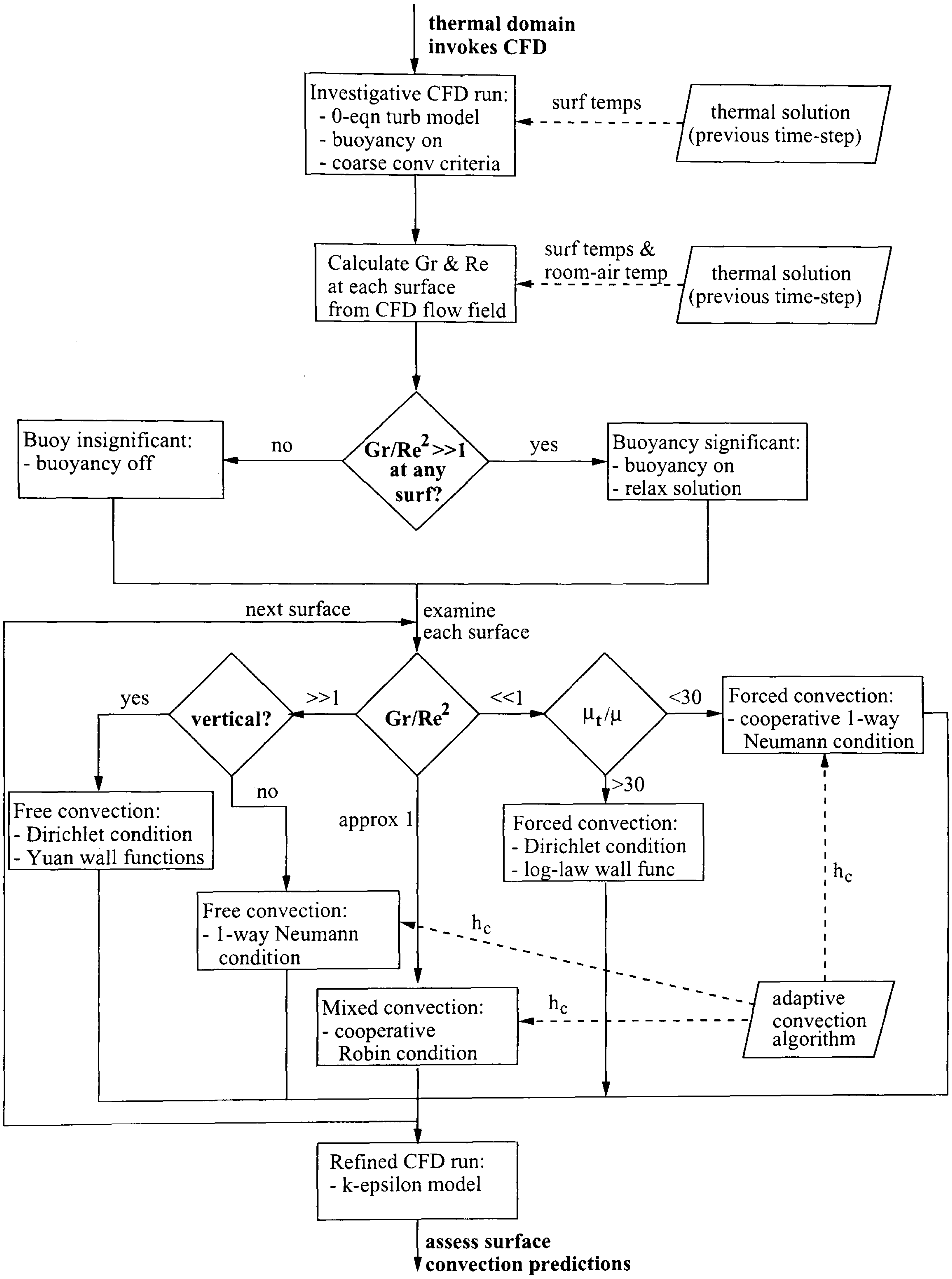

Figure 5.17 Conditional two-way adaptive conflation control

are rejected.

As a second level of screening, the CFD h_c predictions are compared to those from the adaptive convection algorithm. The CFD results are rejected if they are not within the same range as the empirical values: $0.2 \cdot h_{c,ACA} \leq h_{c,CFD} \leq 5 \cdot h_{c,ACA}$ where $h_{c,ACA}$ and $h_{c,CFD}$ are the convection coefficients predicted by the adaptive convection algorithm and CFD, respectively. Any CFD-predicted h_c values which pass this screening are sent to the thermal domain where they are used to establish the zone matrix. In this way, the convection coefficients predicted at some surfaces may be accepted for use by the thermal domain, while those at other surfaces are rejected.

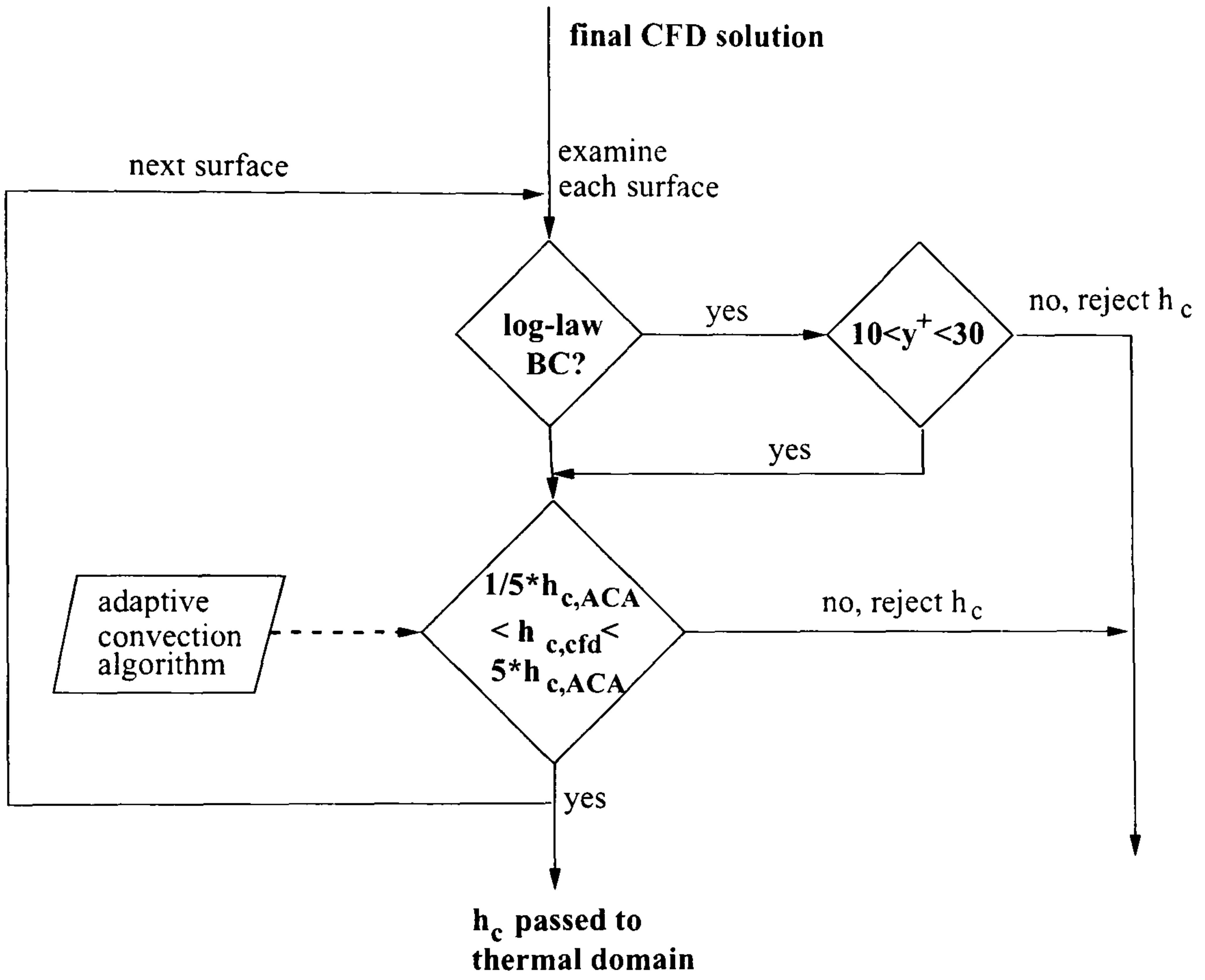

Figure 5.18 Assessing CFD-predicted h_c values

5.5.3 Other potential adaptive conflation control schemes

The previous subsections described two viable approaches for the adaptive conflation controller. Of course, many other control scenarios can be envisaged. The possibilities include:

- The degree of stratification could be measured from the investigative CFD simulation. The controller could opt for a boundary condition that is appropriate for stratified rooms if the range of temperatures throughout the room exceeded some threshold.
- The boundary conditions could be established based on the sensed condition of a plant component. For example, if a fan supplying air to the room was turned off, the Yuan wall functions could be employed.

- If the primary objective of the CFD simulation is to provide convection coefficients for the thermal domain, alternate convergence criteria could be set to accelerate the calculations. For example, rather than tracking the equation residuals (see equation 3.27, page 52) the controller could monitor the surface convection predictions and halt the CFD simulation when the relative change between two successive iterations was smaller than an acceptable tolerance.
- Operating on the flow field predictions of the investigative CFD run, a grid tuning algorithm (one is proposed by Schild 1997) could be used to modify the gridding for the refined CFD simulation in order to optimally locate the next-to-wall grid points for the purposes of predicting the heat transfer with the log-law wall functions.
- The investigative CFD simulation could be performed with a coarser grid to further reduce computational requirements.
- The CFD flow predictions could be used to communicate information back to the adaptive convection algorithm to help it decide which empirical correlation to use for calculating coefficients for the next time-step. For example, when velocities next to a surface reached a certain threshold, the adaptive convection algorithm could switch to an empirical h_c correlation appropriate for the velocity. This strategy could even be used when one-way conflation was active.
- The CFD flow predictions could be used to estimate the magnitude of the velocity adjacent to surfaces. These velocities could be used by the adaptive convection algorithm as inputs to a forced flow h_c correlation.
- Dimensionless groupings other than the Grashof and Reynolds number could be used to assess the nature of the flow. Additionally, a different length scale could be chosen for calculating the dimensionless groupings.

It is important to note that the adaptive conflation controller does not preclude the user from imposing one of the schemes outlined in Table 5.2. These (and others not listed in the table, including some integrated conflation schemes) can be manually assigned by the user and fixed in time.

5.6 Closing Remarks

This chapter has described the new adaptive convection algorithm and the new adaptive conflation controller. Collectively these realize the research objectives of advancing the modelling of indoor air motion and internal surface convection heat transfer.

The adaptive convection algorithm enhances ESP-r's thermal simulation method as well as playing a supportive role for the adaptive conflation controller. Working with a base of 28 convection coefficient correlations (the structure allows easy expansion when new methods become available), it assigns appropriate equations to each internal surface and adapts the selection in response to the room's evolving flow regime.

The adaptive conflation controller manages all interactions between the thermal and CFD modelling domains. It incorporates the latest turbulence modelling advancements applicable for room air flow simulation (again, new approaches can be easily incorporated within the structure when they become available) and possesses a suite of handshaking and thermal boundary condition treatments. The controller uses the CFD domain to perform an investigative flow assessment, then refines modelling approaches based upon these preliminary results. Where possible, the controller manages CFD to resolve the pivot point in order to predict surface convection coefficients for the thermal domain. However, safeguards are also provided to protect the integrity of the thermal domain's matrix of heat balance equations.

Techniques were incorporated to allow the thermal and CFD domains to cooperatively resolve the surface convection heat transfer. These allow the conflated simulator to consider the interdependencies between room air stratification and surface convection, while concurrently and accurately resolving the wall heat transfer. Consequently, the conflated simulator becomes a general and flexible method for characterizing stratified environments and internal air flow within rooms with time-varying boundary conditions. As such, it offers a more powerful and information rich alternative to the so-called zonal models (Inard et al 1996, 1997) and other more simplified techniques that have been put forward to deal with these important physical considerations.

CHAPTER 6

Validation and Application

6.1 Introduction

This chapter sets out to demonstrate how the new adaptive convection algorithm and the adaptive conflation controller enhance modelling resolution, and to examine the validity of these new approaches.

Validation is treated in Section 6.2. Firstly, the various approaches and constructs used to validate simulation programs are discussed. Results presented in previous chapters are described in the context of these validation constructs. Additional cases are then presented to further validate various aspects of the new developments.

Section 6.3 then presents some case studies to demonstrate how the new adaptive convection algorithm and the adaptive conflation controller can be applied to enhance the simulation of internal surface convection and indoor air motion.

The material presented in this chapter draws heavily upon a flow visualization facility that was developed to support the integrated modelling approach. This facility (described in Appendix G) allows the air flow at any cross-section in the room to be viewed, either instantaneously or over a period of time. While not central to the current research, its development—and the creation of a user-interface to integrate ESP-r's CFD domain into the *Project Manager*—are necessary steps to add robustness to the research and to make it accessible to the wider ESP-r user base. All flow images presented in this chapter (and those presented in Chapters 3 and 5) were generated with this flow visualization facility.

6.2 Validation

As discussed in Chapter 1, questions regarding the credibility of results remain one of the barriers impeding further adoption of simulation by the building design professions. Consequently, it is critical that any new development be adequately verified using state-of-the-art validation techniques.

The validation of simulation programs is a complex and challenging field in its own right. Numerous recent contributions (e.g. Judkoff and Neymark 1995; Lomas et al 1994; Jensen 1993; ASHRAE 1998) have moved the field forward, but much work remains. The currently accepted state-of-the-art validation methodology is followed here to examine the validity of the solutions put forward in Chapters 4 and 5. However, it must be acknowledged that it is beyond to scope of this work to comprehensively validate these methods.

6.2.1 Validation methodology

Judkoff et al (1983) classified simulation errors into seven categories:

External errors:

- Differences between the actual microclimate affecting the building and the weather input used by the program.
- Differences between the actual schedules, control strategies, and effects of occupant behavior and those assumed by the program user.
- User error in deriving building input files.
- Differences between the actual thermal and physical properties of the building and those input by the user.

Internal errors:

- Differences between the actual thermal transfer mechanisms taking place in the real building and the simplified model of those physical processes in the simulation.
- Errors or inaccuracies in the mathematical solution of the models.
- Coding errors.

The external errors principally relate to user factors that are outside the domain of the simulation program, although in practice the pragmatic design of user interfaces can mitigate many of these factors. For example, the adaptive convection algorithm described in the previous chapter minimizes the chances of user error in describing the convective regime. The internal sources of error are the focus of consideration in the context of the current research.

Due to the physical complexity of buildings and the nearly infinite possible data input combinations, the comprehensive validation of a detailed simulation program is an impossible task. Judkoff and Neymark (1995, based on Judkoff et al 1983) propose a pragmatic approach composed of three primary validation constructs to check for internal errors. These are:

- Analytical verification
- Empirical validation
- Comparative testing

With analytical verification, the program (or subroutine) output is compared to a well known analytical solution for a problem that isolates a single heat transfer mechanism. Typically this necessitates very simple boundary conditions. Although analytical verification is limited to simple cases for which analytic solutions are known, it provides an exact standard for comparison.

Program (or subroutine) outputs are compared to monitored data with empirical validation. The measurements can be made in real buildings, controlled test cells, or in a laboratory. The design and operation of experiments leading to high-quality data sets is complex and expensive, thus restricting this approach to a limited number of cases. The characterization of some of the more complex physical processes (such as heat transfer with the ground, infiltration, indoor air motion, and convection) is often excluded due to measurement difficulties and uncertainty.

A program is compared to itself or other programs with comparative testing. This includes both sensitivity testing and intermodal comparisons. This approach enables inexpensive comparisons at many levels of complexity. However, in practice the difficulties in equivalencing program inputs can lead to significant uncertainty in performing inter-model comparisons.

A general principle applies to all three validation constructs. The simpler and more controlled the test case, the easier it is to identify and diagnose sources of error. Realistic cases are suitable for testing the interactions between algorithms, but are less useful for identifying and diagnosing errors. Although the comparison of the actual long-term energy usage of a building with simulation results is perhaps the most convincing evidence of validity from the building designer's perspective, this is the least conclusive approach. This is because the simultaneous operation of all possible error sources combined with the possibility of offsetting errors means that good or bad agreement cannot be attributed to program validity.

The critical evaluation of theory and the checking of source code have been proposed as additions to the three basic validation constructs. Regarding the former, the previous chapters have presented significant material to explain the concepts and assumptions behind the selected approaches. Additionally, a series of publications have been prepared and presented on various aspects of the research to solicit peer review and critique (Clarke and Beausoleil-Morrison 1997; Beausoleil-Morrison and Clarke 1998; Beausoleil-Morrison and Strachan 1999; Beausoleil-Morrison 1999; Beausoleil-Morrison 2000).

A modular and structured programming approach was employed to implement the developments. Functionality was segregated into small program units to facilitate testing and maintenance. Unit testing was performed on each subroutine to ensure its outputs responded correctly to various input combinations. Coding was extensively examined and tested at each stage of the developments. A suite of benchmark cases was assembled to facilitate this task. When a new capability was added, a series of tests were performed with the benchmarks to ensure that existing capabilities were not compromised. These benchmarks were also used for sensitivity testing to examine and confirm the impact of a single algorithm change (e.g. comparing Dirichlet and Robin boundary condition treatments with one-way surface handshaking). Finally, all developments have been incorporated into the standard version of ESP-r, which exposes the coding to a sophisticated user base for critical review.

The remainder of this section focuses on the three principle validation constructs. The next subsection summarizes cases that were cited in previous chapters in terms of their contribution towards validation. It also discusses the contributions of others towards validating ESP-r's CFD model. Following this, additional analytical, empirical, and comparative cases are presented. More realistic cases are the topic of Section 6.3, these demonstrating the new capabilities and testing the interactions between the individual algorithms.

6.2.2 Summary of validation cases presented in previous chapters and by others

A number of comparative (sensitivity and inter-model) and empirical tests were described in the previous chapters. For example, the surface convection at the outer wall of an office predicted with the Fisher, Alamdari-Hammond, and the mixed flow models were compared in Figure 4.6 (page 94). This sensitivity analysis showed how the mixed flow model was able to capture the impact of both buoyant and forced effects.

The sensitivity of load and thermal comfort predictions to the use of these three convection methods was examined in a case study presented in Section 4.5.3. This showed that the choice of h_c algorithm had a significant impact on energy and thermal comfort predictions, and on the assessment of design options.

The case study presented in Section 4.5.2 examined the sensitivity of the IEA Annex 21/Task 12 empirical validation test room to a number of modelling assumptions and algorithms. This showed how modelling of the test room was highly sensitive to the choice of convection coefficient algorithm. It also illustrated the significant differences between two of the h_c algorithms implemented in the adaptive convection algorithm.

The sensitivity analysis described in Section 4.6 illustrated the significance of stratification. It showed how uncertainty over the air temperature could lead to significant errors in the predicted heating energy requirement of the IEA test room.

The validity of the Yuan wall functions was examined empirically and with a sensitivity analysis in Section 5.3.1. A series of comparative tests were performed to examine the grid sensitivity of the surface convection predictions for flow within a cavity. Comparisons were also made with empirical methods to demonstrate the validity of the surface convection predictions.

Section 5.3.2 presented a simulation of the IEA Annex 20 two-dimensional test case using the Chen and Xu zero-equation model. This represents an empirical validation, a sensitivity, and an inter-model comparison. Firstly, the ESP-r predicted flow pattern was found to be in general agreement with the measurements. A second ESP-r simulation performed with the $k-\varepsilon$ model showed that the two turbulence models predict similar flow fields with two notable differences (see Figure 5.9, page 133). Relative to the $k-\varepsilon$ model and the measured data, the zero-equation model predicts slower flow along the ceiling and down the right wall. Xu (1998) modelled the same case using the

PHOENICS CFD program (Spalding 1994) which included an implementation of the zero-equation turbulence model. The flow pattern and the greater jet decay found with the ESP-r simulation are consistent with Xu's PHOENICS results.

Negrão (1995) examined the validity of ESP-r's CFD model with analytical, empirical, and inter-model tests. He compared, for example, ESP-r's predictions to analytical solutions for two-dimensional laminar flow between flat plates. He also compared ESP-r and PHOENICS results for a series of two-dimensional and three-dimensional cases. Additionally, Loomans (1995) conducted an extensive assessment of ESP-r's CFD model using the IEA Annex 20 two-dimensional test case. He performed a detailed comparison of velocity and turbulence intensity predictions at various locations in the room against the empirical data. He also compared ESP-r's predictions with the published results of other CFD programs.

The following subsections present additional analytical, empirical, and comparative validation cases.

6.2.3 Analytical verification of h_c equation toggling

The adaptive convection algorithm dynamically adapts the calculation of convection coefficients in response to the flow regime. As such, the equations used to calculate h_c values can change from one simulation time-step to the next. Chapter 5 showed how the calculation of surface convection in a typical mechanically ventilated office could change dramatically over the course of a day when this approach is used. A test was devised to demonstrate the validity of this technique.

A simple one-zone model (called the "cooling cube") was created (see Figure 6.1). A single surface (labelled the "cooling surface") was selected as the focus of the test. By imposing the following assumptions, the model was configured so that surface convection from the room air to the cooling surface was the only significant heat transfer path affecting the room air temperature:

- Fictitious materials were created so that the fabric components had negligible mass and heat capacity relative to the room air.
- A highly conductive material was used to represent the cooling surface, thus eliminating indoor-outdoor temperature gradients across the surface.
- A very low conductivity material was used to represent all other fabric components. The internal convection coefficients for these surfaces were set to very low (constant) values, thus eliminating heat transfer through these components.
- Internal and external longwave radiation was virtually eliminated by setting the emissivity of all surfaces to 0.01.
- The absorptivity of all internal and external surfaces was set very low to virtually eliminate solar absorption.
- The external convection coefficient of the cooling surface was set to 100 W/m^2K, this to ensure that external surface approached the outdoor air temperature.

- Internal gains and infiltration were set to zero.

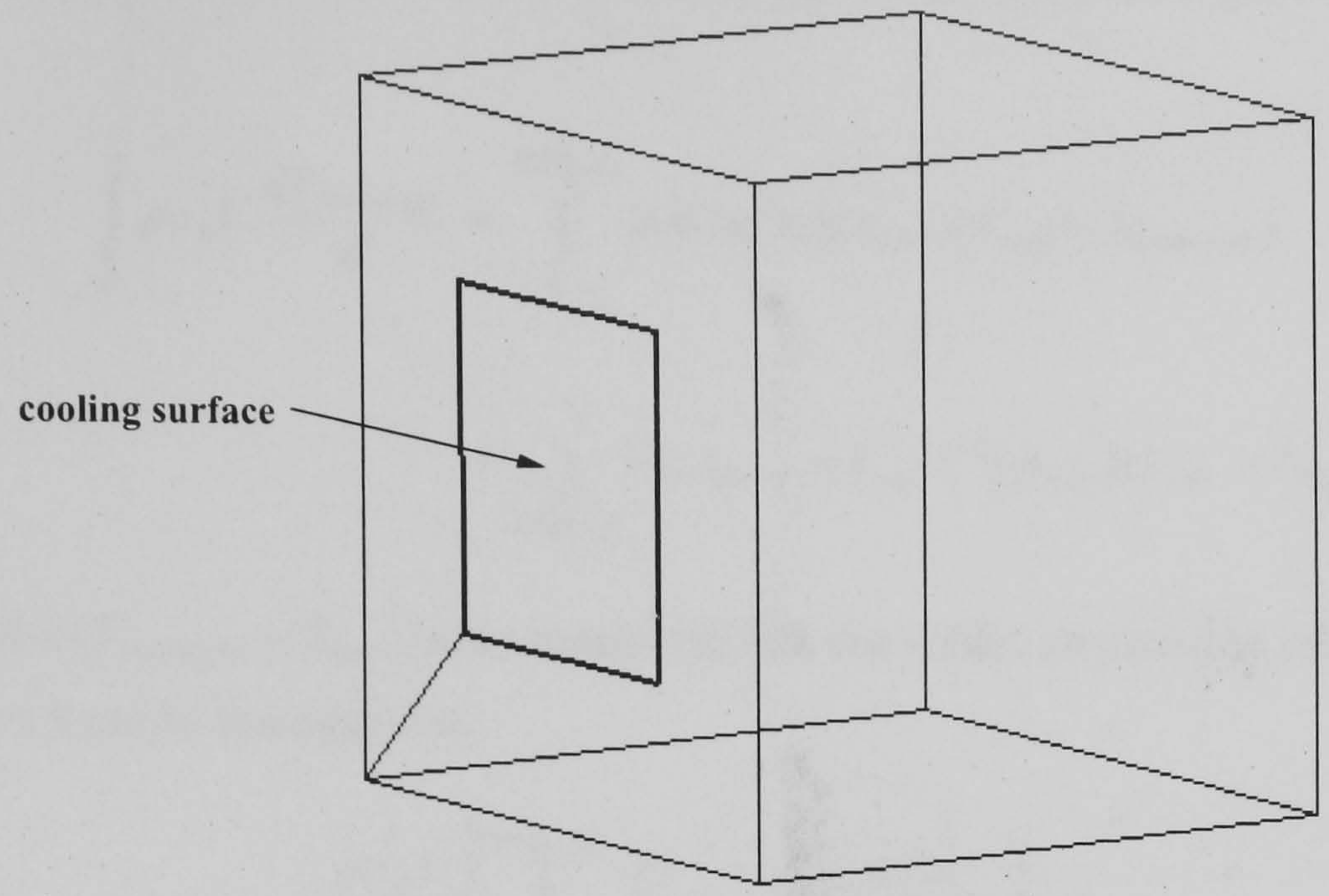

Figure 6.1 ESP-r model of cooling cube

With these assumptions, the room air can be treated as a lumped capacitance with only a single possible path (via the cooling surface) for exchanging heat with the outdoors. Further, due to the cooling surface's large external convection coefficient and high thermal conductivity, the internal surface convection coefficient offers the only significant resistance to heat flow between the room air and the outdoors.

Given this configuration, an analytical solution can be derived to relate the room air and external air temperatures. A disturbance from steady-state conditions caused by a sudden drop in the outdoor air temperature can be described with the well-known lumped capacitance model,

$$\rho c_p V \frac{dT_{room-air}}{dt} = h_c A_{surf}(T_{surf} - T_{room-air}) \tag{6.1}$$

Where V is the volume of air $\{m^3\}$ and T_{surf} is the internal temperature of the cooling surface.

The reaction of ESP-r's thermal matrix to the convection coefficient could be examined by holding h_c constant in equation 6.1. However, a more interesting test is to suddenly change the h_c calculation method during the cooling period, this mimicking the adaptive convection algorithm's ICOR toggling technique. In this test, h_c is held at a fixed value of 1 W/m^2K for the first hour of cooling. From this point on, h_c is calculated as a function of the temperature difference between the room air and the internal surface,

$$h_c = (T_{room-air} - T_{surf})^{1/2} \tag{6.2}$$

This simulates the control behavior of the adaptive convection algorithm, that is suddenly changing h_c calculation methods.

The room air temperature can be predicted analytically by integrating equation 6.1 over time. The integral is carried out in two parts to reflect the change in h_c calculation regime one hour into the cooling,

$$\int_0^t \rho c_p V \frac{dT_{room-air}}{dt} = \int_0^{3600\,sec} (1W/m^2K)(A_{surf})(T_{surf} - T_{room-air}) \tag{6.3}$$

$$+ \int_{3600\,sec}^{t} (T_{room-air} - T_{surf})^{1/2}(A_{surf})(T_{surf} - T_{room-air})$$

Letting $\theta = (T_{room-air} - T_{surf})$ and recognizing that the model assumptions result in a constant T_{surf}, equation 6.3 can be rearranged to,

$$-\frac{\rho c_p V}{A_{surf}}\left[\int_0^{3600\,sec} \frac{d\theta}{\theta} + \int_{3600\,sec}^{t} \frac{d\theta}{\theta^{3/2}}\right] = \int_0^t dt \tag{6.4}$$

The integration of equation 6.4 yields the following analytical solution for $T_{room-air}$,

$$T_{room-air} = \begin{cases} T_{surf} + \dfrac{T_{room-air}(t{=}0)}{e^{(tA_{surf}/\rho c_p V)}} & \text{for } t \le 3600\ sec \\ T_{surf} + \left[\dfrac{1}{\dfrac{1}{[T_{room-air}(t{=}3600) - T_{surf}]^{1/2}} + \dfrac{(t\text{-}3600)A_{surf}}{2\rho c_p V}}\right]^2 & \text{for } t > 3600\ sec \end{cases} \tag{6.5}$$

An ESP-r simulation of this scenario was performed. A climate file with a step-change in temperature from 20°C to 0°C was created for the simulation. This resulted in a gradual cooling of the room air due to heat transfer through the cooling surface. The analysis was conducted with a one-minute time-step in order to accurately track the room's response.

The analytical solution of equation 6.5 is compared with simulation results in Figure 6.2. The impact of the h_c algorithm change on the cooling of the room can be clearly seen. The simulation closely matches the analytical solution, both before and after the change in h_c algorithm. This demonstrates that ESP-r's thermal model responds correctly to the internal surface convection coefficient. It also demonstrates that the thermal model correctly responds to a sudden change in h_c calculation approaches, this providing confidence in the adaptive convection algorithm's approach of toggling h_c algorithms in response to changing flow regimes.

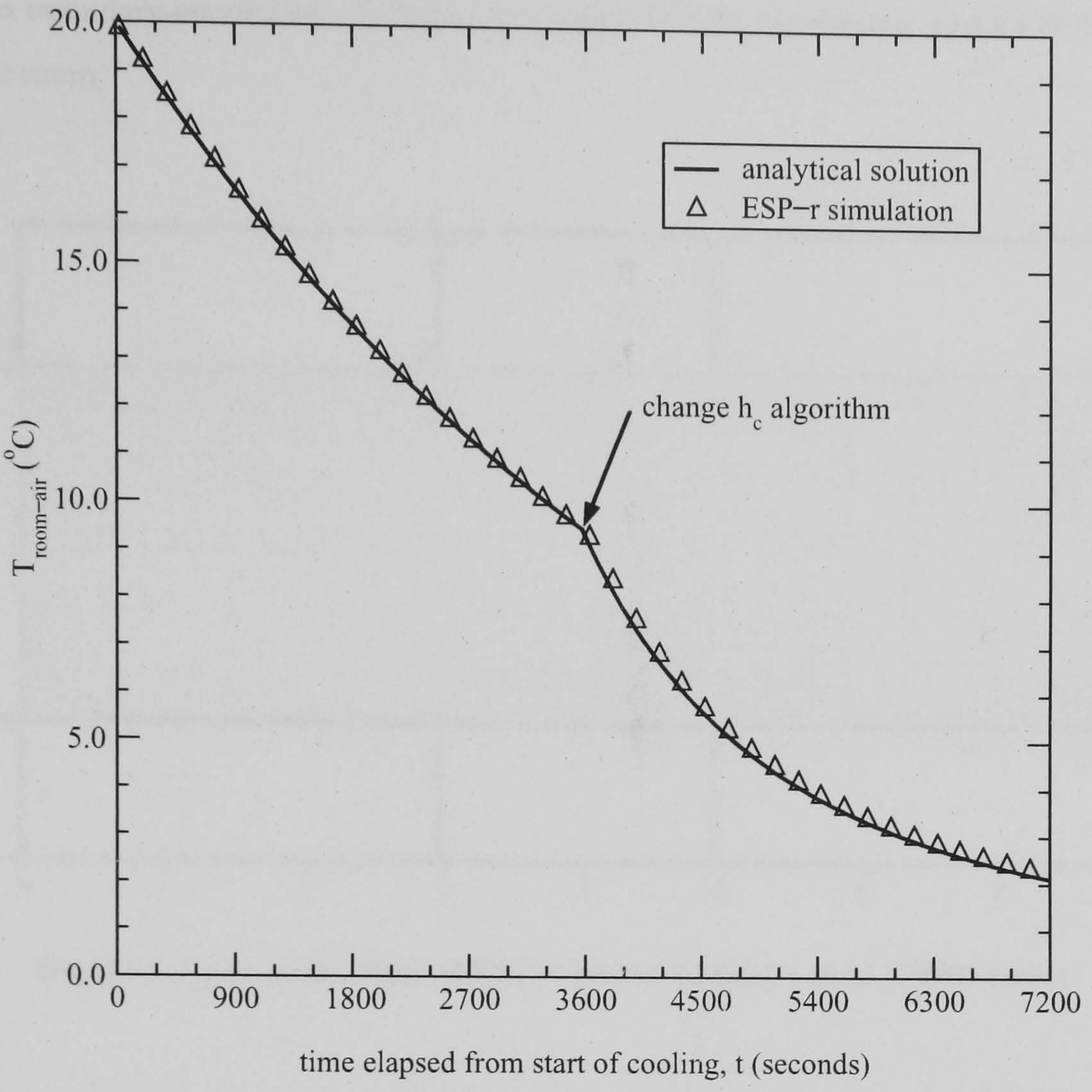

Figure 6.2 Comparison of simulation and analytical solutions for "cooling" cube

6.2.5 Comparative testing of CFD domain's air flow and convection predictions

Simulations of a high-aspect-ratio cavity were performed in Chapter 5 to demonstrate and assess the performance of the Yuan wall functions. This showed that ESP-r produces grid-insensitive solutions with these wall functions. As well, surface convection predictions were seen to be in reasonable agreement with two empirical correlations. This section further validates the implementation of these wall functions, as well as the implementation of the one-way handshaking approach, and two of the boundary condition treatments described in Chapter 5.

The test room of Olson et al (1990) was selected for this work. This room is 7.9m long, 3.9m wide, and 2.5m high. Most surfaces are adiabatic, while one wall is heated and its opposing wall cooled. As the room is sealed, flow is driven exclusively by the buoyancy forces resulting from the heated and cooled surfaces. Olson et al provide qualitative observations of the flow pattern and some measured data. Additionally, Yuan (1995) performed simulations of this configuration with a version of the PHOENICS CFD program (Spalding 1994) that included his wall functions. Therefore, this case provides an opportunity for both empirical and inter-program validation.

An ESP-r model of the test room was constructed (refer to Figure 6.3). The model was configured in conflated mode in order to test not only ESP-r's CFD model and the implementation of the

Yuan wall functions, but also to examine the one-way surface handshaking approach with the Dirichlet and Neumann boundary conditions. A zone was created in both the thermal and CFD domain to represent the test room.

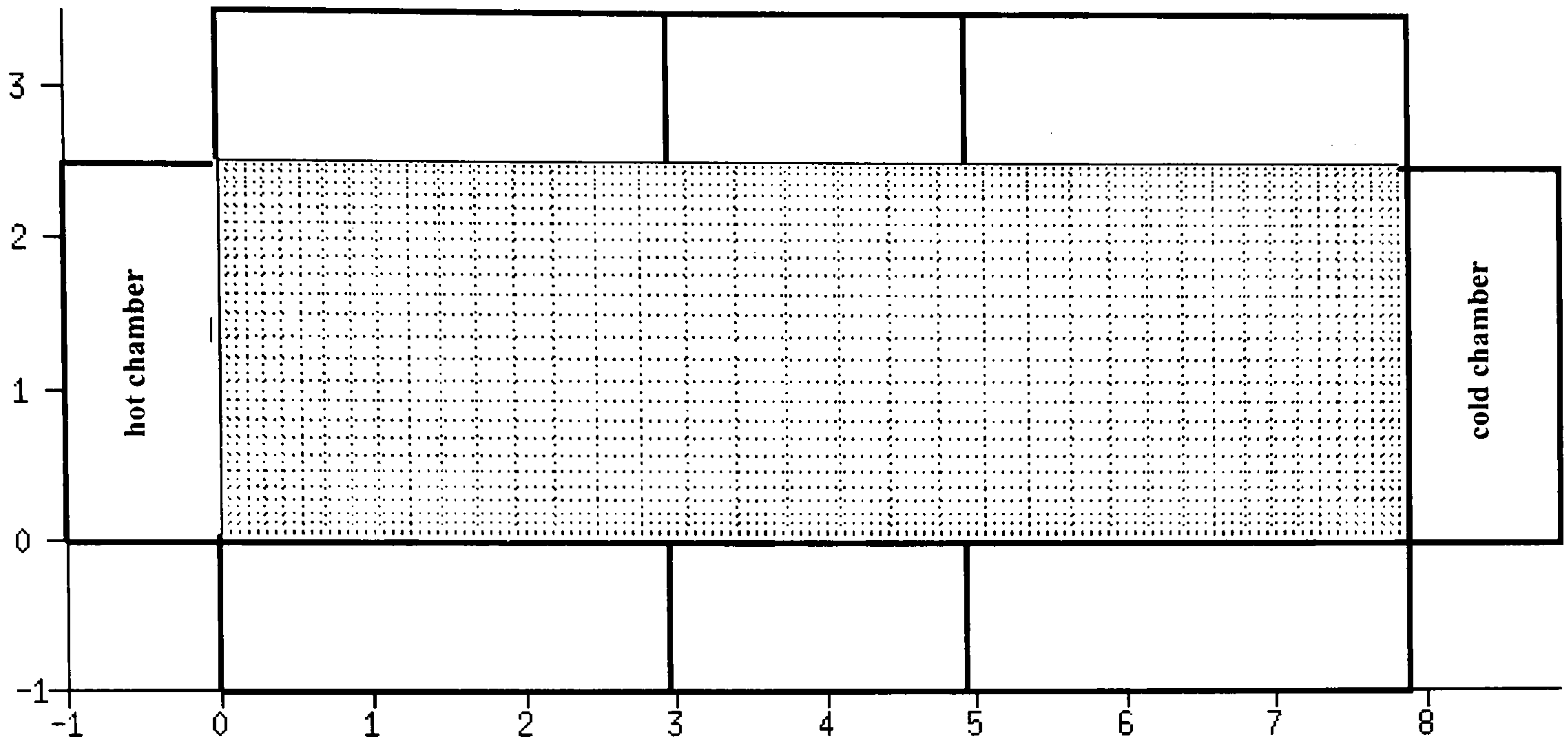

Figure 6.3 Elevation view of ESP-r model of Olson et al (1990) room

Olson et al defined the room's boundary conditions in terms of internal surface temperatures. Eight additional zones were created in the thermal domain to impose these boundary conditions upon the room. Each of these zones was configured with fabric components, convection coefficients, and control strategies to result in the appropriate temperature on the room's internal surface. Intermediate variables and results were examined to confirm that the one-way surface conflation was imposing the correct temperatures on the internal surfaces of the room.

Olson et al considered the floor and ceiling to be adiabatic. However, Yuan modelled these in PHOENICS with Dirichlet boundary conditions with the log-law wall functions. A sensitivity analysis was performed to compare these two treatments. In one case the ESP-r simulation was conducted with a Neumann boundary condition with a zero convection coefficient (to simulate an adiabatic surface). In the other a Dirichlet boundary condition with the log-law thermal wall function was employed. Insignificant differences in the resulting flow pattern and heat transfer at the cold and hot walls was found. Therefore, the remaining analysis was conducted with the Dirichlet boundary condition. A Dirichlet boundary condition with the Yuan wall functions was applied on the walls.

The CFD gridding density and the placement of the next-to-wall solution points were selected to correspond as closely as possible to one of the PHOENICS results presented by Yuan. A sensitivity analysis was performed to examine the impact of gridding on the surface convection predictions. Modest changes in the gridding in the horizontal and vertical directions was seen to have little impact on the surface convection predictions at the hot and cold walls.

The flow pattern predicted by ESP-r is shown in Figure 6.4. As expected, flow rises along the hot wall and falls along the cold wall. There is a large recirculation around the room, but the central core of the room is stagnant. These general trends are consistent with the observations of Olson et al and Yuan's PHOENICS simulation. The size of the stagnant region is also consistent with the measurements. However, the ESP-r simulation does not capture the small secondary flows observed along the horizontal surfaces.

In terms of quantitative comparisons, the ESP-r and PHOENICS simulations predicted similar vertical velocities for the next-to-wall grid point located at the mid-height of the hot wall: 0.21 m/s for ESP-r and 0.25 m/s for PHOENICS. The differences in the surface convection predictions at the hot and cold walls were more significant, however. PHOENICS predicted 72 W/m^2 at both walls, whereas ESP-r predicted 58 W/m^2 (19% less). The reasons for these differences are not known, although a sensitivity analysis confirmed that gridding was not a factor. Convection predictions were found to be quite sensitive to the state of convergence and the initial conditions assumed. As Yuan's convergence criteria were not specified, equivalencing these inputs was not possible.

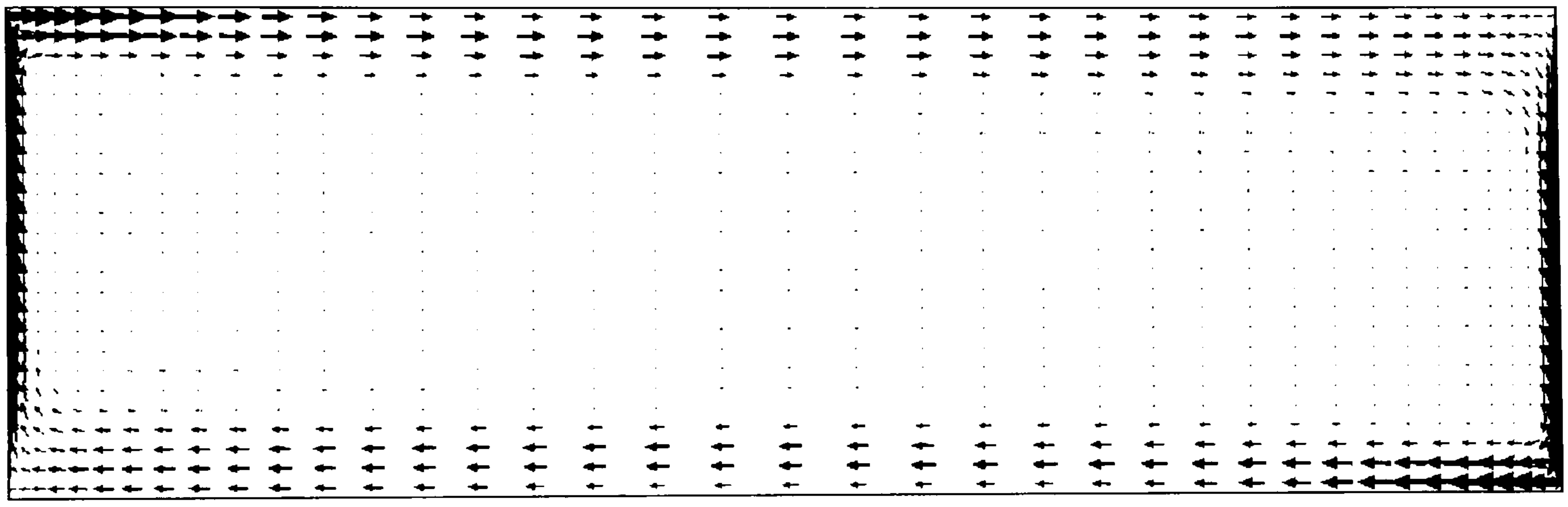

Figure 6.4 Flow pattern predicted for Olson et al (1990) room

6.2.4 Empirical validation of impact of HVAC operation and placement on h_c

The fundamental basis of the adaptive convection algorithm is to toggle between h_c correlations in response to the prevailing flow regime. Two control laws were implemented in Chapter 5 to demonstrate this approach. Both toggle the h_c equation in response to the operational state of HVAC equipment. Section 6.2.3 demonstrated that ESP-r's thermal model reacts properly to a sudden change in h_c algorithm. This section lends further credence to the adaptive convection algorithm by examining the validity of the toggling approach.

Few experimental data sets exist for validating the calculation of convection coefficients under dynamic operational conditions. A number of data sets were described in Chapter 4, but all were acquired from well-controlled laboratory experiments conducted under steady-state conditions. An interesting contribution to this body of knowledge was recently made by Wallentén (1998, 1999). He conducted experiments in a full-size test room located in Lund Sweden. The room was exposed to the outdoor environment through a south facing wall and window. Convection coefficients at these surfaces were experimentally determined in response to dynamic outdoor and operational conditions.

The room was instrumented to measure surface, air, and interstitial wall temperatures. Convection coefficients were derived from these data using a surface heat balance that considered convection, internal longwave radiation, and conduction through the wall. This is similar to the approach employed by Awbi-Hatton and Fisher (see equation 4.3, page 82), except that measurements were not taken under steady-state conditions. This introduced significant complexity (and uncertainty) in determining the conduction component of the heat balance. As the objective was to examine realistic operating conditions, no measures were taken to minimize internal longwave radiation. This added further uncertainty to the calculated h_c values. As a result, there is a great deal of scatter in Wallentén's h_c data (see Figure 6.5). Consequently, these data are not suitable for quantitative comparisons with the adaptive convection algorithm. However, the data do demonstrate some interesting trends, particularly in regards to the impact of the type and operational state of HVAC equipment.

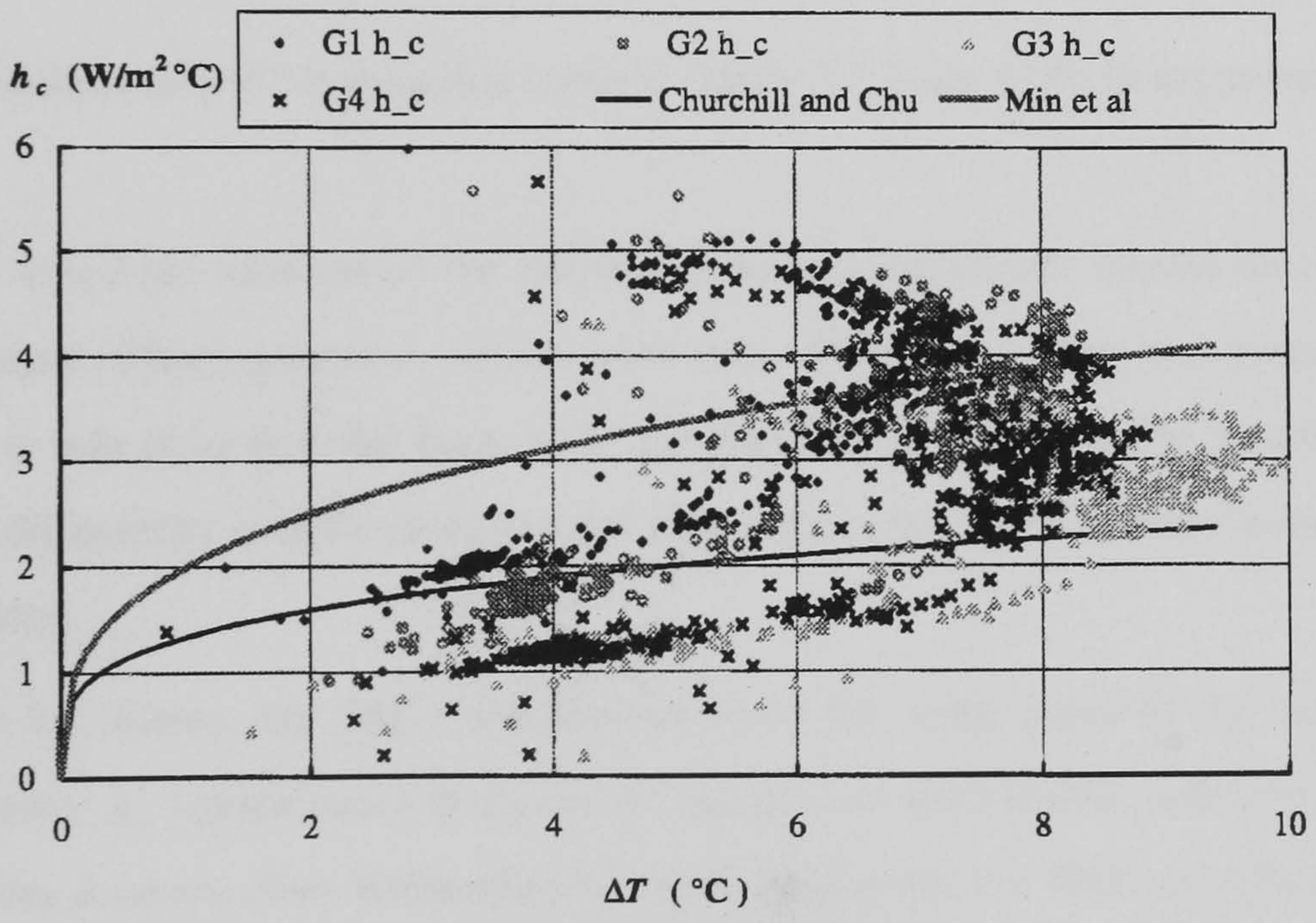

Figure 6.5 Wallentén empirical h_c data for a window (from Wallentén 1998)

Wallentén used various heating and ventilation strategies to condition the room throughout the experimental program. Two result sets for unventilated cases are considered here. In one case the room was heated by a radiator located under the window, while in the other case the radiator was moved to the back wall of the room. An ESP-r model of Wallentén's room was created (see Figure 6.6). The figure shows schematically the two radiator placements

Two detailed simulations using two-minute time-steps were performed for a 14-day period in January. A climate file typical of the region was employed as no Lund weather data were available for the period of the experments. The adaptive convection algorithm's primary convection regime was set

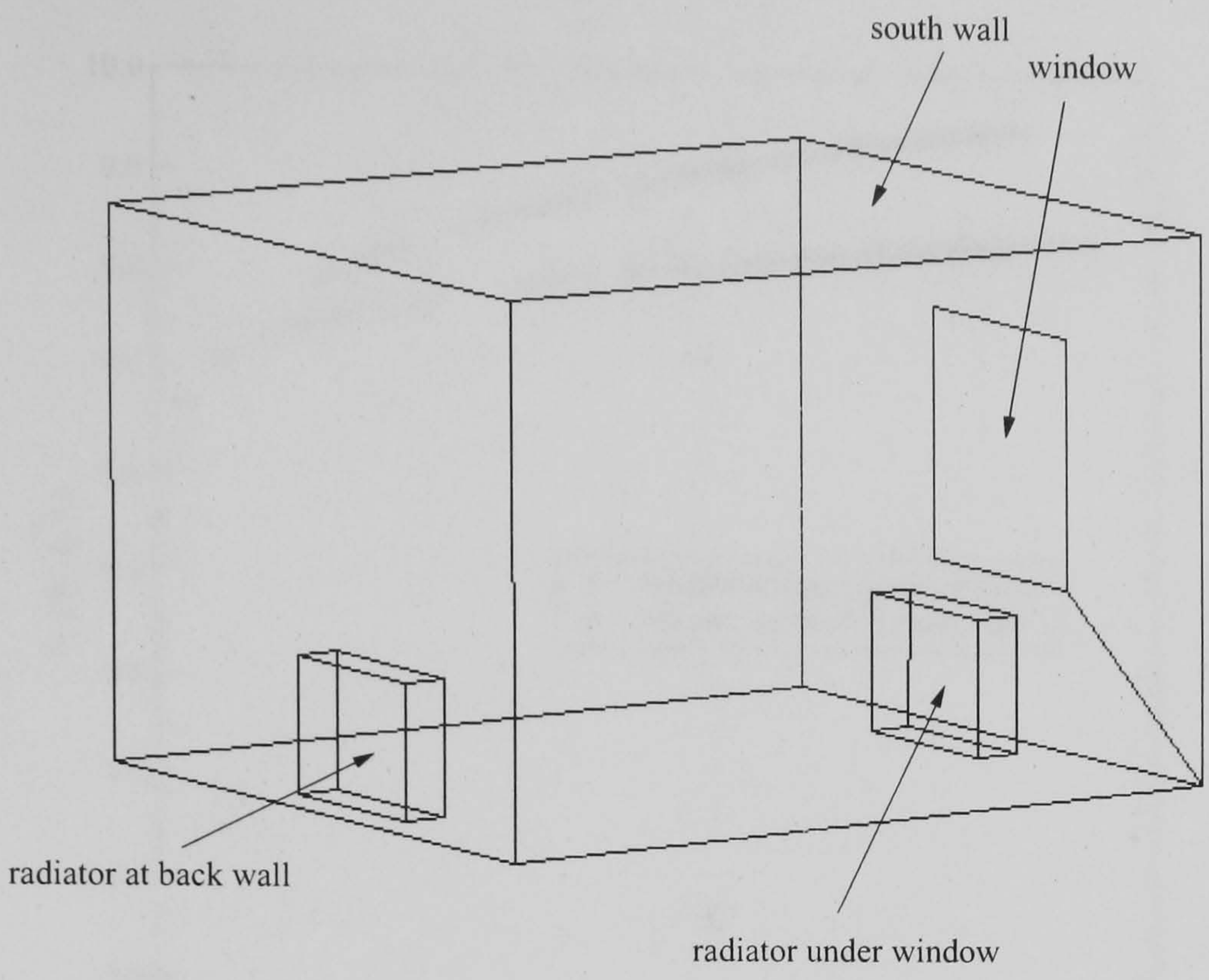

Figure 6.6 ESP-r model of Wallentén (1998) test room

to B1 in one simulation and B2 in the other (refer to Table 5.1, page 118), to represent the two radiator placements.

Wallentén found the location of the radiator to have a significant impact on convection coefficients at the window. Much greater h_c values were seen when the radiator was placed under the window than when it was placed at the back wall (for the time periods that the heater was operating). Quantifying the differences is difficult due to the data scatter, but Wallentén recommends a multiplier as high as 3.5 times.

As Figure 6.7 shows, the ESP-r simulations show the same trend in the window convection coefficients. Greater h_c values occur at almost all surface-air temperature differences. However, the differences are less dramatic than Wallentén observed. In general, the ESP-r predicted h_c values were greater than the measurements. This is further evidence to suggest that the Khalifa's window correlations tend to overestimate (refer to page 78).

Significantly, Wallentén noted a clustering of h_c data in a number of the experiments. By segregating the data according to the radiator's operational state, he has able to observe that the heat output from the radiator significantly affected the convective regime. Much higher h_c values were found when the radiator was operating.

Figure 6.8 illustrates ESP-r's predicted h_c values at the wall. The data are separated according to whether the radiator is operating. As Chapter 5 explained, the adaptive convection algorithm toggles the h_c correlations between the primary and secondary convective regimes in response to the radiator's operational state. As can be seen, ESP-r predicts substantially higher convection coefficients when the heater is operating. This phenomena is observed for both radiator placements, although the

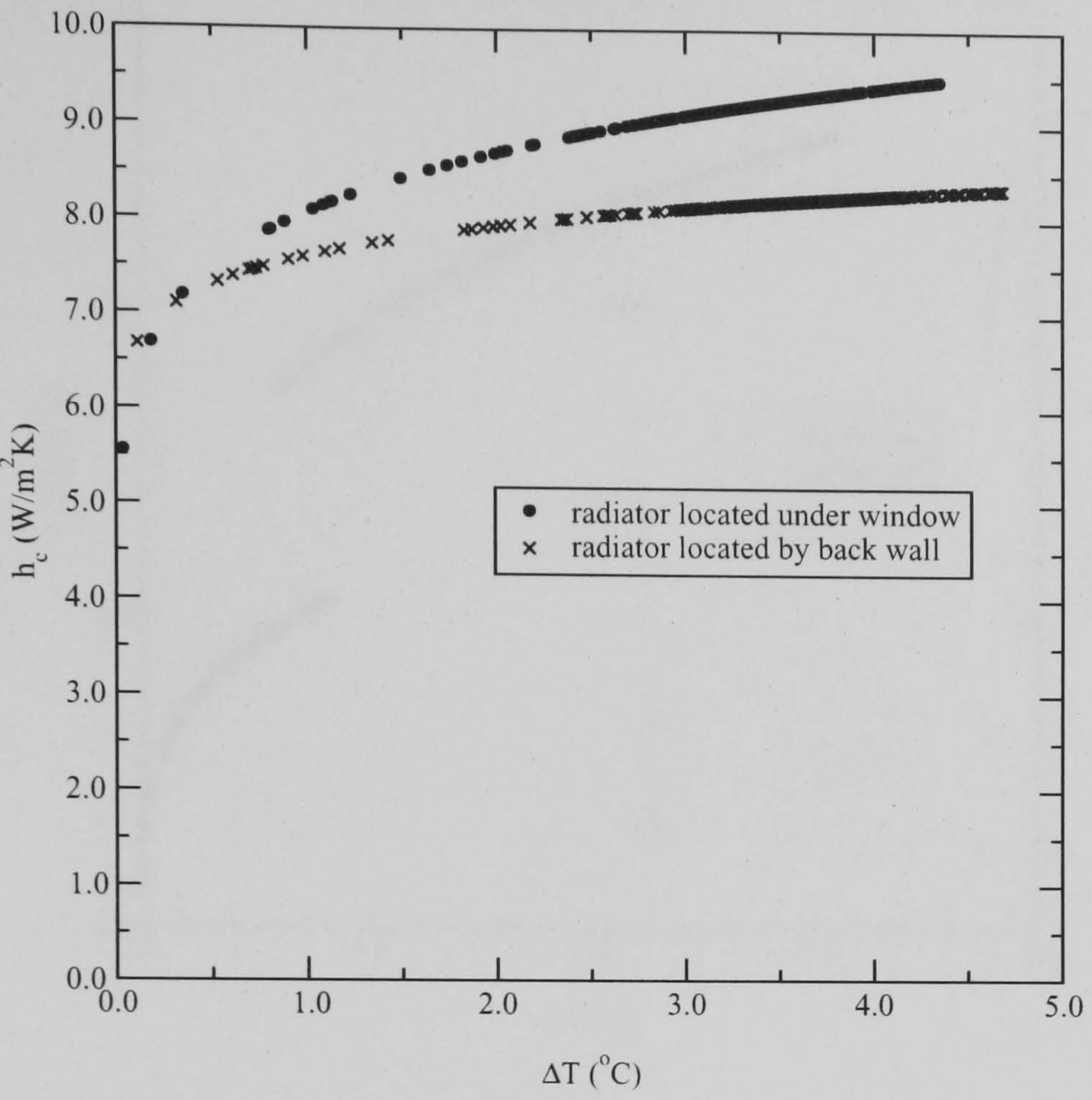

Figure 6.7 ESP-r h_c predictions for window for Wallentén room

differences are more significant when the radiator is placed under the window. These results are qualitatively consistent with Wallentén observations. Unfortunately there is simply too much spread in the measured data for quantitative comparisons, but the ESP-r results are of the correct order.

This comparison confirms the philosophy of the adaptive convection algorithm. That is, selecting a set of h_c correlations appropriate to the anticipated flow regimes, and toggling between these in response to changes in the flow.

6.3 Applications

This section presents three case studies to demonstrate how the new adaptive convection algorithm and the adaptive conflation controller can be applied to enhance the simulation of internal surface convection and indoor air motion.

6.3.1 Analyzing the impact of HVAC system selection on convective regimes

As Chapter 5 explained, the adaptive convection algorithm plays a supporting role to the adaptive conflation controller by supplying appropriately selected convection coefficients. However, it can also function independently to enhance thermal simulation, even when CFD is not active. This section illustrates how the algorithm and its supporting user interface can improve the integrity of thermal

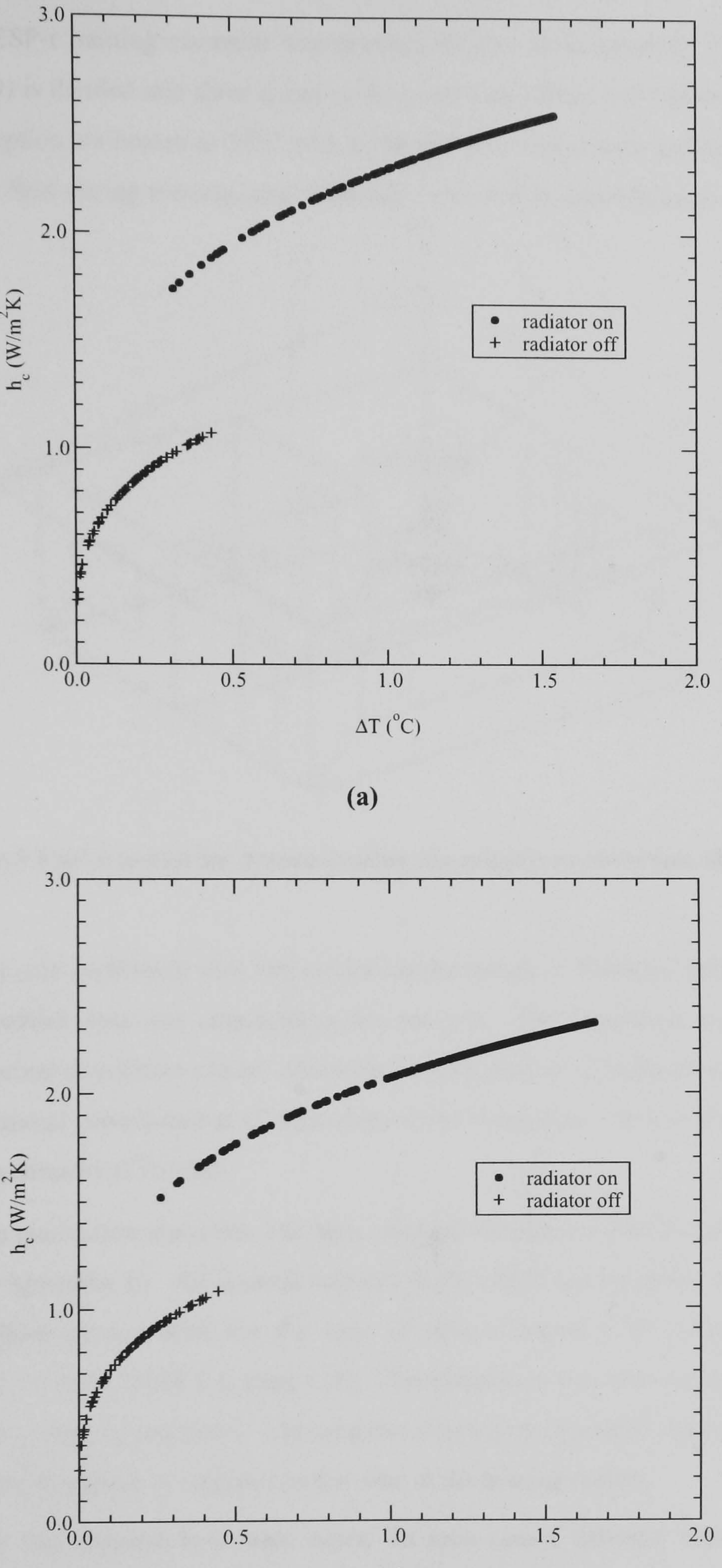

(a)

(b)

Figure 6.8 ESP-r h_c predictions for south wall for Wallentén room: radiator located (a) under window and (b) at back wall

simulations with little effort.

A standard ESP-r training exemplar was selected for this demonstration. The building (illustrated in Figure 6.9) is divided into three zones in the model: an office, a reception, and a roof space. The office and reception are heated to 20°C with a convection based system during occupied periods, and allowed to free float during evenings and weekends. The roof is unconditioned.

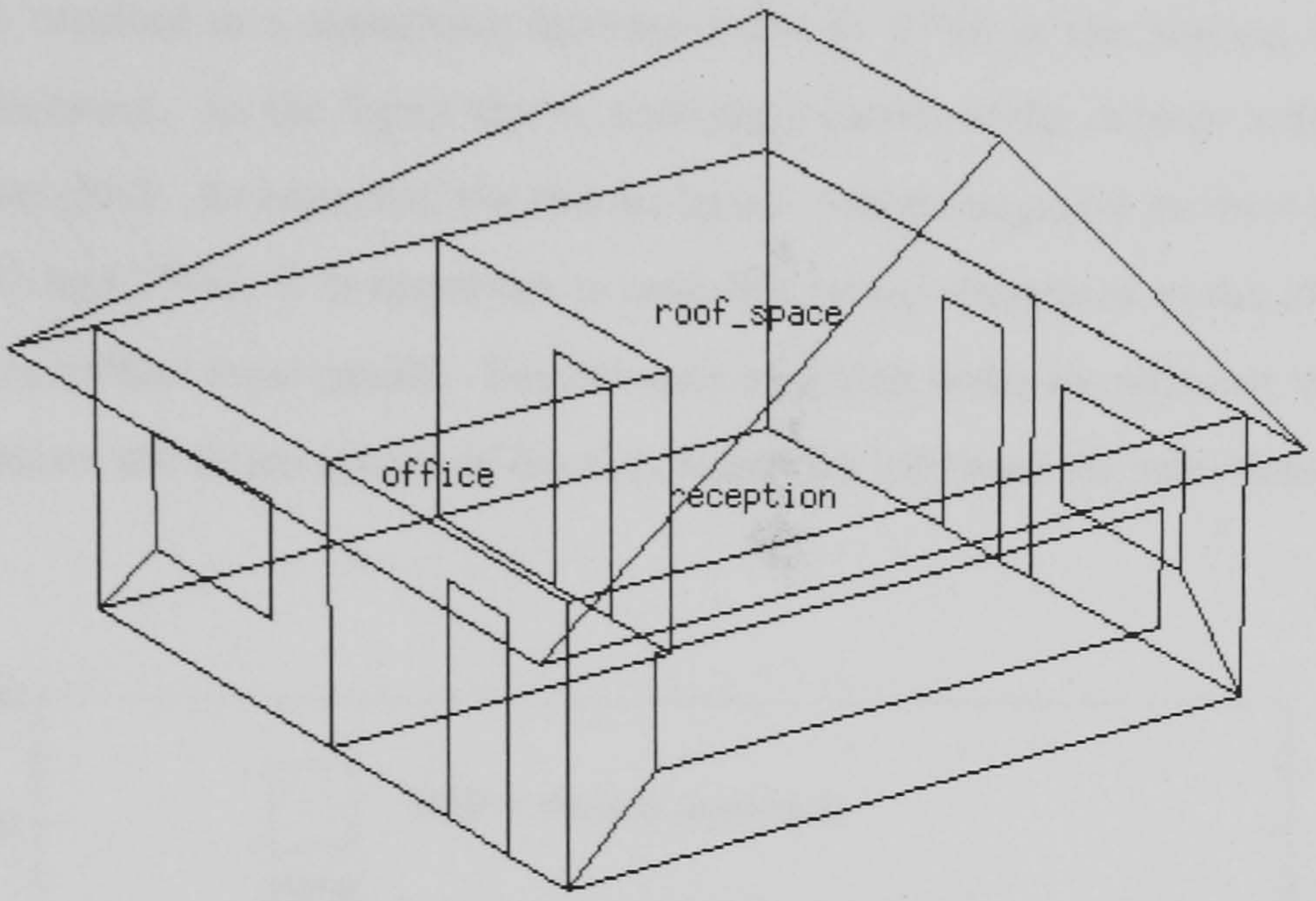

Figure 6.9 ESP-r model for demonstrating the adaptive convection algorithm

A simulation was performed with this model for the month of February using 30-minute time-steps. Glasgow weather data was employed in the analysis. The simulation was performed using ESP-r's default internal convection model: convection coefficients at all surfaces were calculated with the Alamdari-Hammond correlations at all time-steps of the simulation. This configuration resulted in a predicted heating demand of 590 MJ.

The adaptive convection algorithm was then invoked through the interface provided in the *Project Manager* (see Appendix F). All internal surfaces in the office and reception were attributed with convection calculation control data for the case of rooms heated with radiators located under windows[22] (regime B1 from Table 5.1, page 118). The simulation was then repeated using the same weather data and simulation parameters. The adaptive convection algorithm dynamically selected the h_c correlations for each surface in response to the state of the heating system.

This process was repeated four more times. In each case a different convective regime was assessed by the adaptive convection algorithm. The cases examined were: radiators located at internal walls; circulating fan heaters; a constant-volume variable-temperature system delivering heated air at 6 ac/h through ceiling diffusers; and hydronic wall panels.

---

[22] The windows were treated as walls for the purposes of the internal surface convection calculations. See the discussion regarding the tendency of Khalifa's window correlations to overpredict h_c on page 78.

No other changes were made to the model between variants. Typically when comparing different heating systems, alterations would be made to the zone control data to specify which nodes interact with the plant components (e.g. a node within the fabric would receive the plant injection in the case of in-floor heating). However, all runs presented here assumed the plant injected heat to the zone air-point, this to isolate the impact of the adaptive convection algorithm.

The results of these six simulations are presented in Figure 6.10. In each case, the adaptive convection algorithm resulted in a significant increase (12% to 27%) in the heating load compared to ESP-r's default treatment. As the figure shows, even the location of the radiator within the rooms has a significant impact (5%). As expected, the two air-based systems augment the heat losses by a significant margin (16% and 27%). It is important to note that minor alterations to the convection calculation control data can affect these results. Factors such as which walls are adjacent to the radiator, and which surfaces receive the direct stream of the circulating fan influence the selection of h_c correlations for each surface.

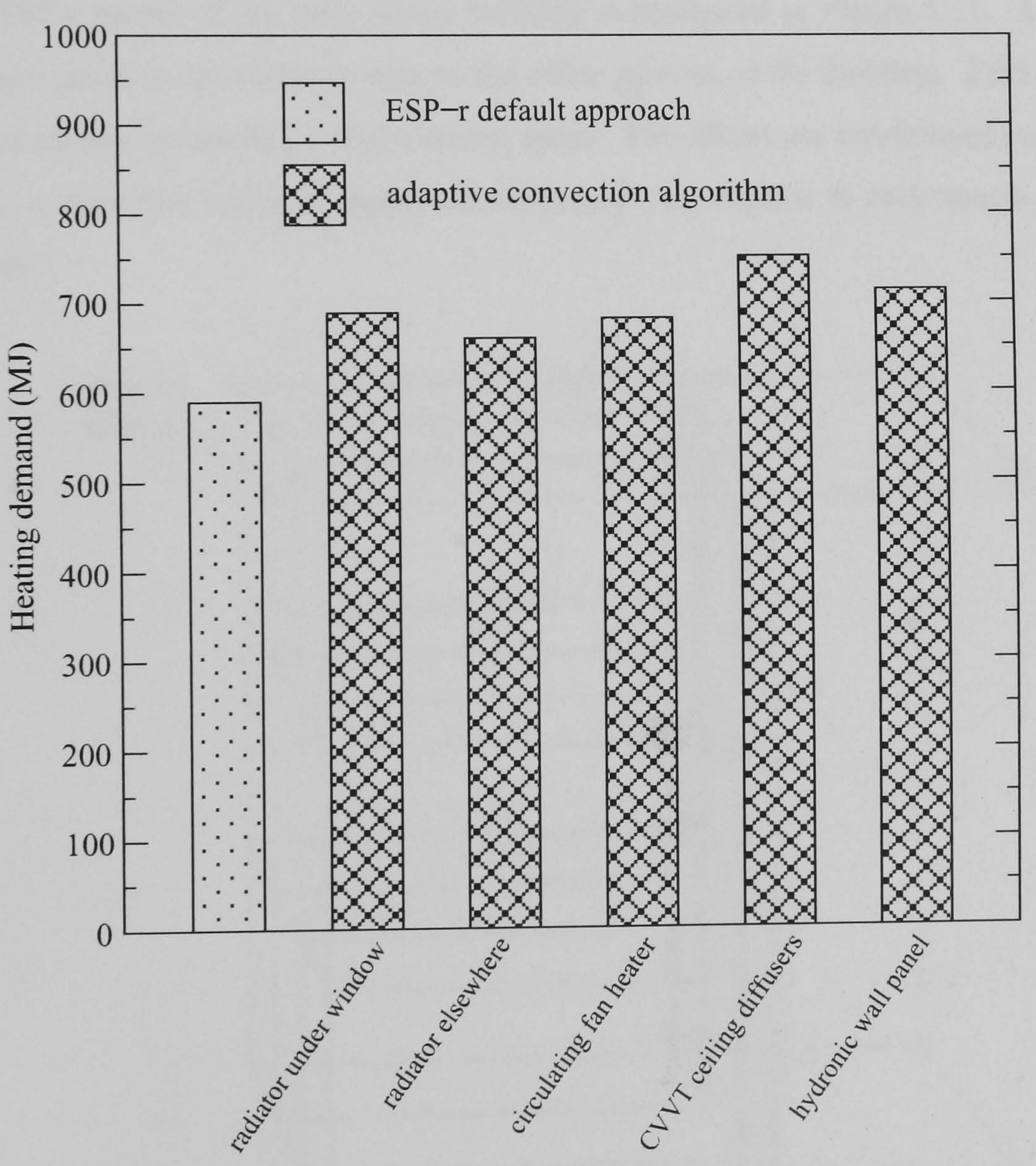

Figure 6.10 Impact of adaptive convection algorithm on heating load for February

This simple example illustrates how significant an impact the adaptive convection algorithm can have on thermal simulation results. It is important to note that the process of attributing surfaces with convection calculation control data requires only seconds per zone using the facility provided in the *Project Manager*. Given this and the results presented in Chapter 4, simulation users should give due consideration before accepting program defaults for internal surface convection coefficients.

6.3.2 Predicting air flow in a ventilated office under dynamic conditions

Description of test case

A model of a hypothetical office building was created to demonstrate and test the operation of the adaptive conflation controller. This example makes use of the one-way handshaking control logic as described in Figure 5.15 (page 145). This tests both the logic of the adaptive conflation controller and the combined performance and interactions between a number of developments and implementations put forward in earlier chapters. These include: the adaptive convection algorithm; the idealized HVAC model; the Yuan wall functions; the Chen and Xu zero-equation turbulence model; and the Dirichlet, cooperative Robin, and cooperative Neumann boundary condition treatments.

An ESP-r model of the three storey building is illustrated in Figure 6.11. A glazed unconditioned atrium provides an entrance area to the office portion of the building. Each office contains a large glazed surface connecting it to the atrium space. The offices are conditioned with a constant volume HVAC system that varies its supply air temperature in response to each zone's heating and cooling demands.

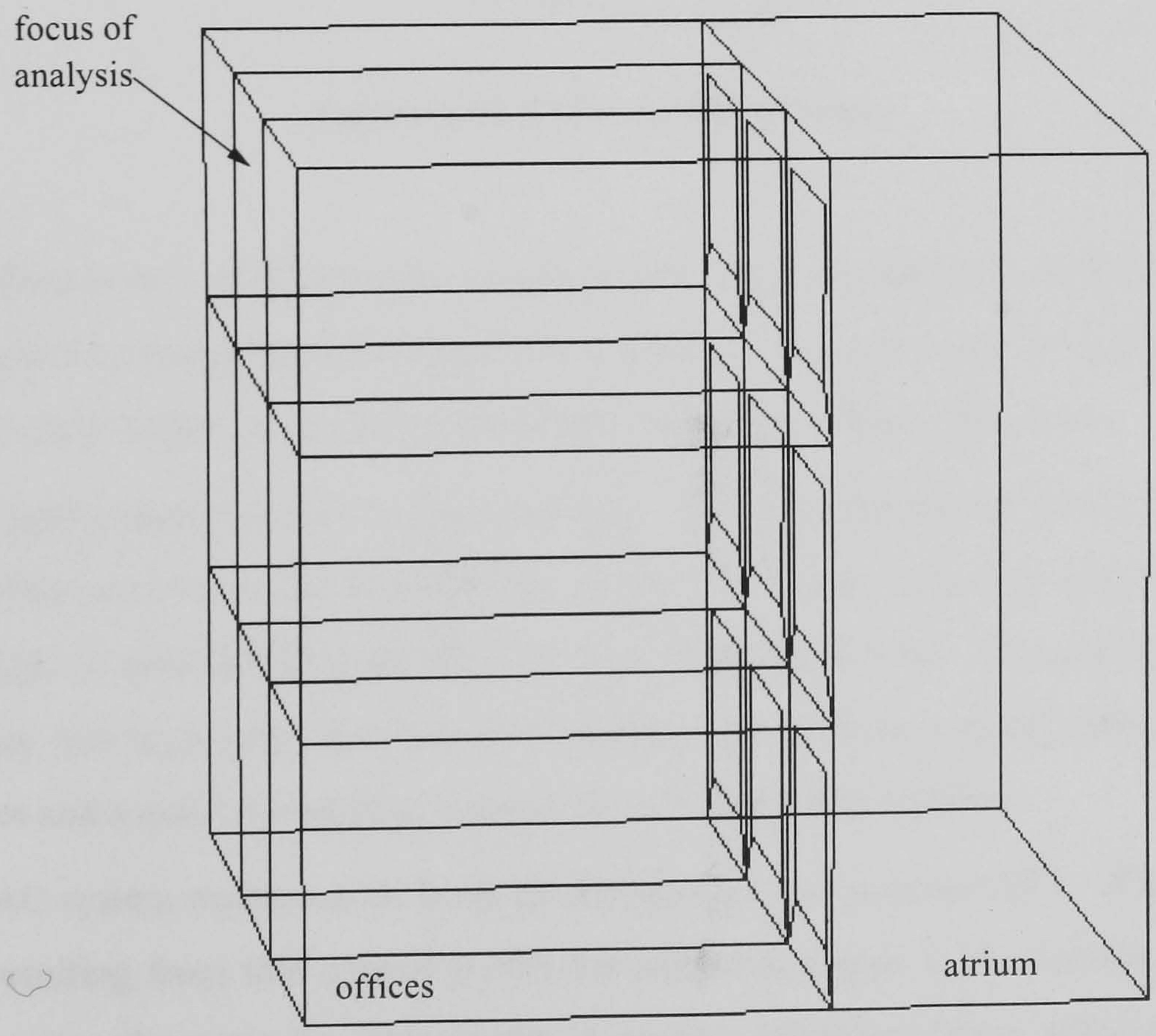

Figure 6.11 ESP-r model of office

Figure 6.12 focuses on a single office. The locations of the HVAC system's supply air diffuser and extract are shown in the figure. Heated or cooled air is supplied to the room as a horizontal jet, the diffuser being located high on the wall opposite the window. Return air is extracted at the same wall, but at a location near the floor. The goal of the system is to provide an even distribution of air and to extract pollutants from the room. The objective of this analysis is to examine the HVAC system's performance at ventilating the office. Air motion in the room is influenced not only by the HVAC system's flow rate, but also by buoyancy forces resulting from temperature differences between the supply air, internal surfaces, and the room air. Therefore, a conflated modelling approach is necessary to assess the system under realistic (dynamic) operating conditions.

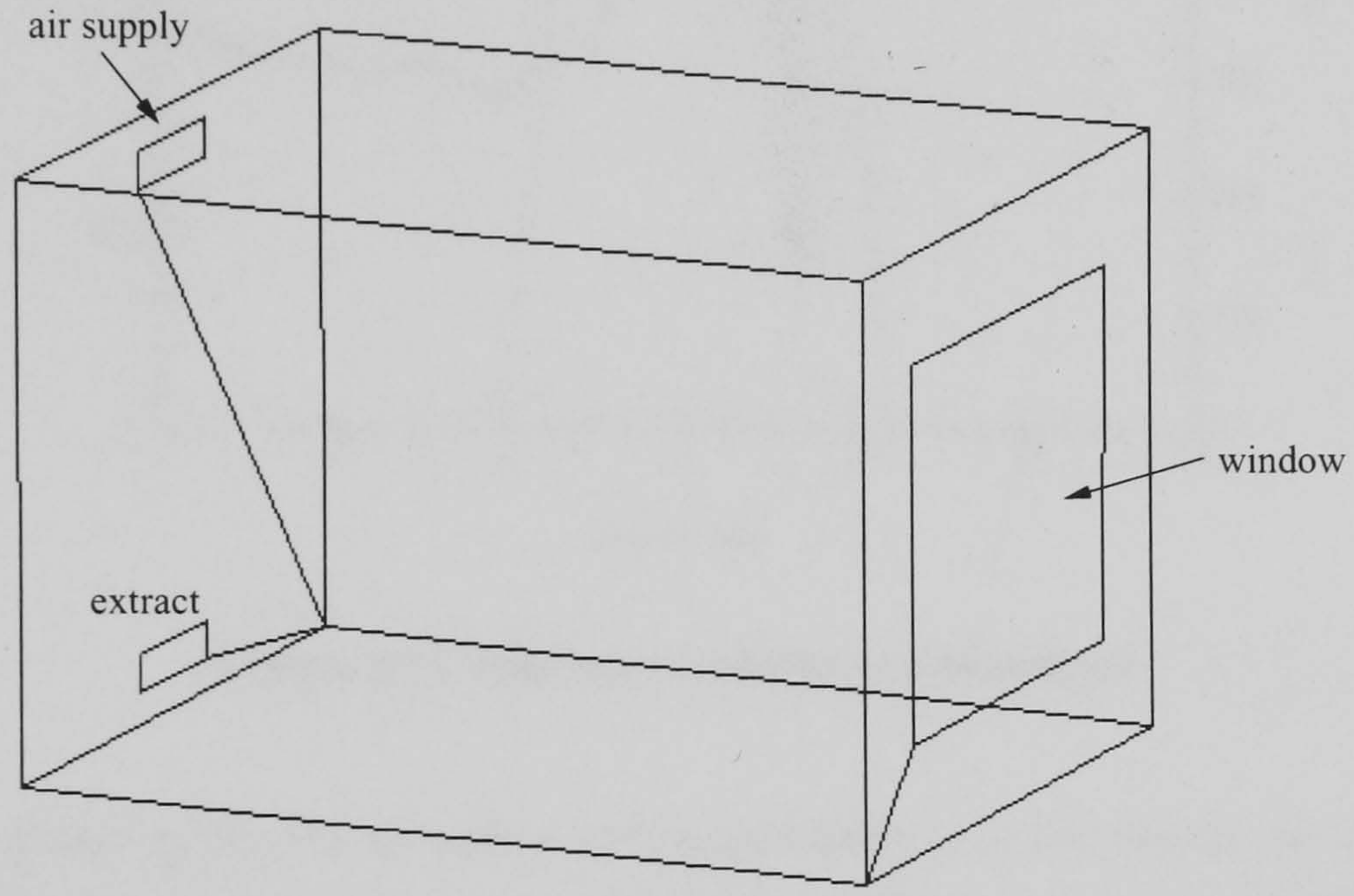

Figure 6.12 ESP-r model of office

A CFD domain was established for a single office. A coarse mesh of 12x10x12 grids was used, this being sufficient to characterize the general flow pattern. This gives next-to-wall grid spacings of a few centimetres, with volumes as large as 30x40x30 cm in the middle of the room.

Ottawa weather data was used in the simulation. The period from 10h00 to 13h00 on January 9 was chosen for the analysis as this provides the adaptive conflation controller with an interesting and challenging range of operational conditions over a short period of time. The relatively cold temperatures on this day and high solar radiation (see Figure 6.13) result in a rapid warming of the room's internal surfaces and a quickly changing load profile over the analysis period.

The HVAC system maintains the zone air temperature at a constant 20°C. The internal surface temperatures resulting from this control profile are shown in Figure 6.14. Initially, all internal surfaces are colder than the room air. This results in negative buoyancy forces adjacent to the surfaces. By about 11h00, however, the surfaces have warmed to above the room air temperature due to increasing solar insolation, this reversing the direction of the buoyancy forces adjacent to the surfaces.

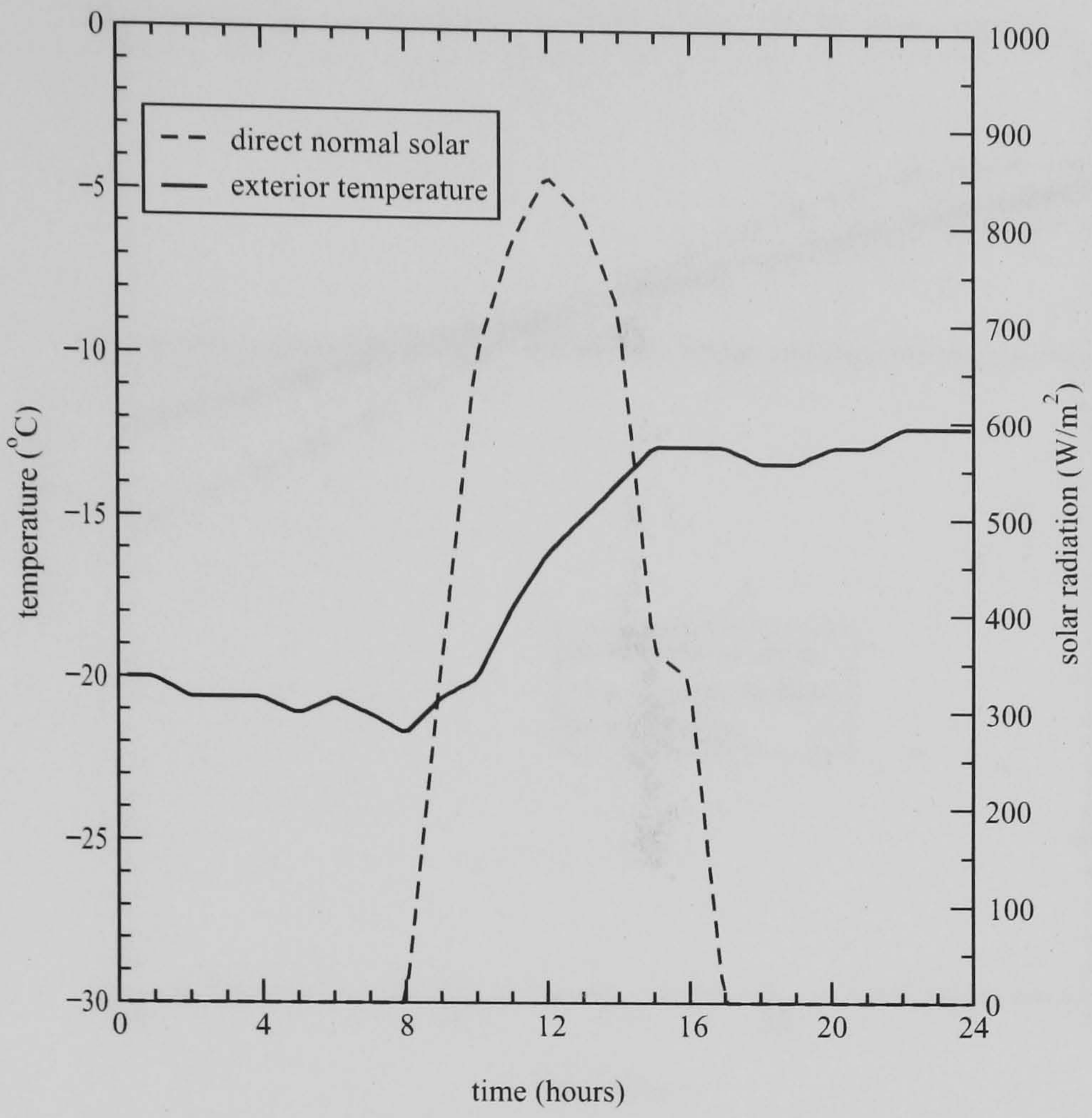

Figure 6.13 Weather conditions on January 9

The loads placed on the HVAC system vary considerably over this period. At 10h00, for example, the zone requires heating to maintain the setpoint temperature. As a result, the HVAC system supplies air at about 25°C (this is calculated by the idealized HVAC model described in Appendix D). The heating load diminishes with time. In fact, by 11h30 the internal and solar gains balance the heat losses so the system supplies air at the room temperature. And after this time, the HVAC system must supply cool air to the zone to extract excess heat. The temperature difference between the supply air and the room air produces a buoyancy force on the incoming jet. The jet will tend to rise when warm air is supplied, and will tend to detach from the ceiling and drop when it is cool. Therefore, the direction of the buoyancy force changes quite suddenly between 11h00 and 12h00, as illustrated in Figure 6.15.

Adapting modelling to the flow

The combined influence of these effects is simulated with the adaptive conflation controller. Simulations were performed using a 10-minute time-step in order to capture the impact of the rapidly varying conditions. Following a short start-up period to condition the model, the thermal domain invoked the adaptive conflation controller on January 9 at 10h00. The surface temperatures predicted by the thermal domain were passed to the CFD domain as boundary conditions. Likewise, the supply air temperature calculated by the idealized HVAC model was mapped to the CFD domain's air inlet

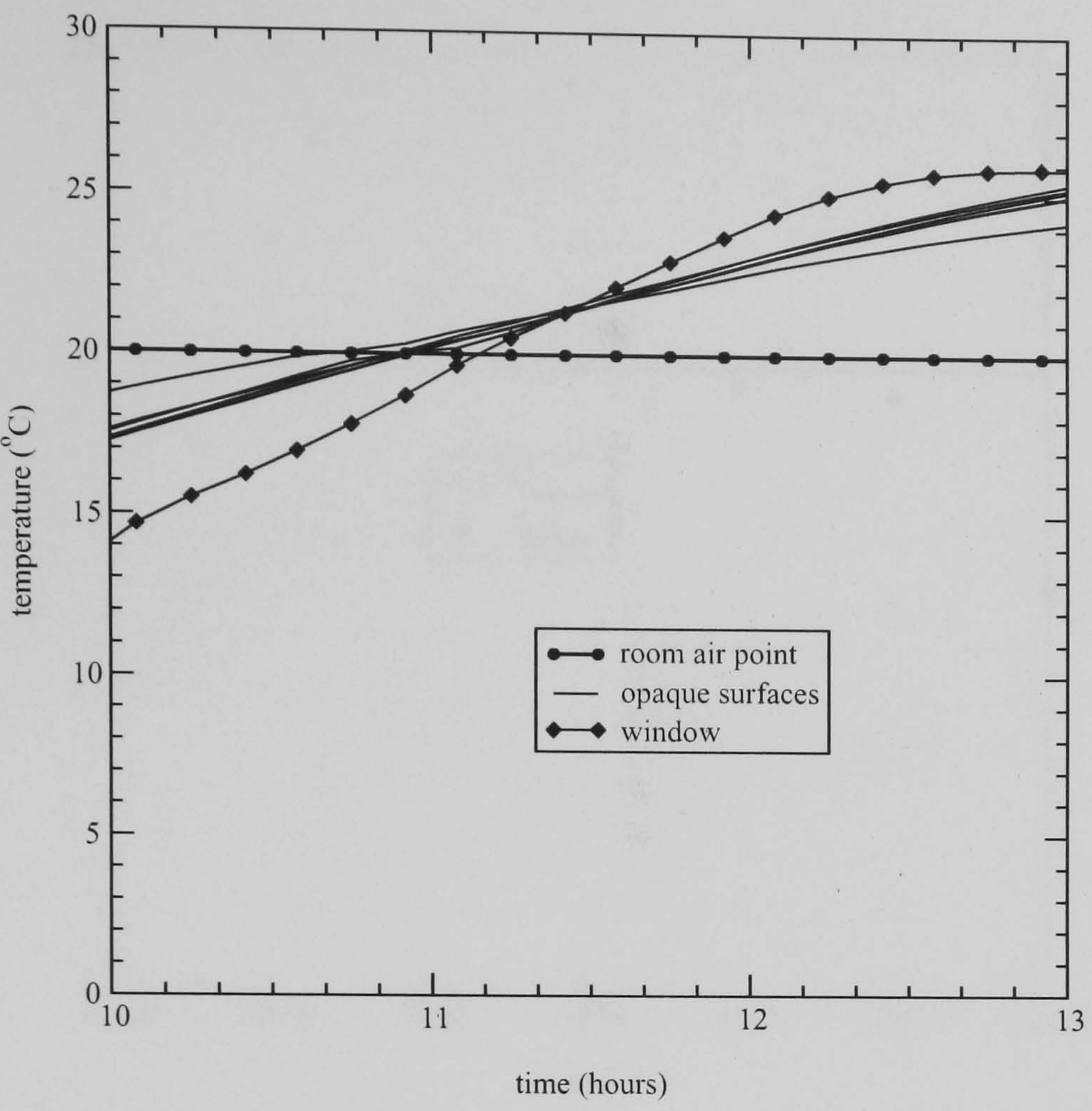

Figure 6.14 Zone air and internal surface temperatures on January 9

(in the case of VAV systems, the idealized HVAC model also maps the system's flow rate).

At this point, the adaptive conflation controller performs an investigative CFD run with the zero-equation model. Recall that the purpose of the investigative run is to approximate the flow field. As such, the convergence criteria are relaxed to accelerate the process. In this case, the iterative solution was halted when the sum of equation residuals (for mass and momentum) over the domain became less 2% of the value of the incoming air stream (refer to equation 3.27, page 52). This leads to a rapid estimate of the flow field (only a few hundred solver iterations are required).

The flow pattern predicted by the investigative run at this first time step is illustrated in Figure 6.16. Five views of the flow are displayed in the two-page figure. As can be seen in the first view in Figure 6.16(a) and the first view in Figure 6.16(b), there is a strong flow along the ceiling. The incoming jet spreads across the ceiling and reaches the opposite wall (the one with the window). The jet's warm temperature has helped it to adhere to the ceiling. The second and third views in Figure 6.16(a) indicate there is also strong flow down the side walls. The impact of the buoyant forces at the window can be seen in the third image in Figure 6.16(a). In this case the buoyant force assists the mechanically driven jet. The window surface is 13.5°C whereas the surrounding wall is 17.3°C. This results in a greater buoyancy force adjacent to the window, and thus greater velocity. Flow is quite diffuse and even across the floor, as seen in the second image in Figure 6.16(b).

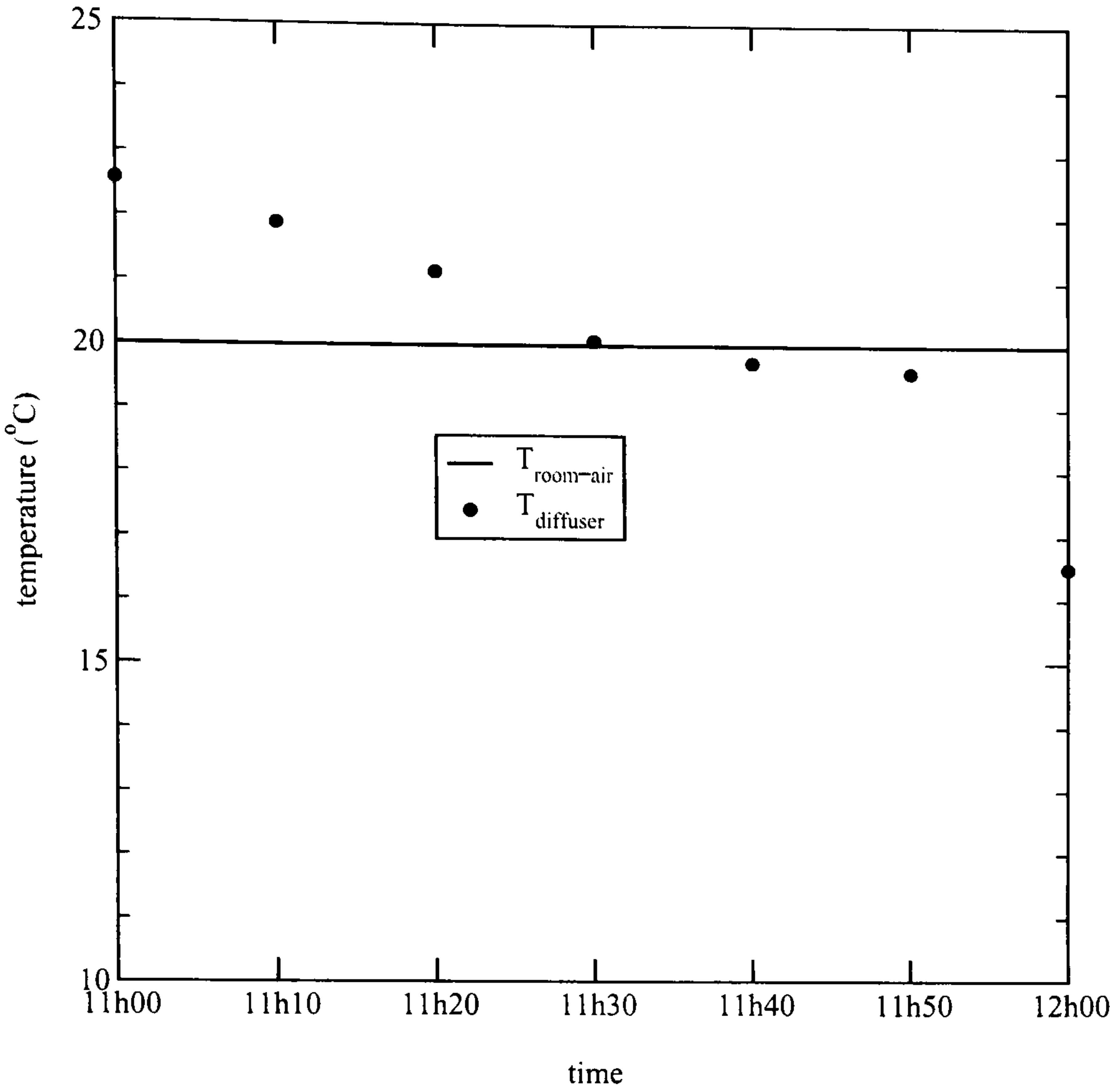

Figure 6.15 HVAC system supply air temperature

The adaptive conflation controller then assesses the flow and temperature field predicted by the investigative CFD run. It calculates the Grashof and Reynolds numbers for each surface (using equations 5.23 and 5.24, page 146) based on the temperatures and velocities solved at the next-to-surface grid points. By comparing these dimensionless groupings, the controller determines that flow at all vertical surfaces is primarily buoyant ($Gr_L/Re_L^2 \approx 10-20$). As a result, it selects the Dirichlet boundary condition with the Yuan wall functions for these surfaces. As Gr_L and Re_L^2 were approximately the same at the ceiling and floor, the controller concludes that flow at these surfaces is mixed. Therefore, the cooperative Robin boundary condition is employed at the horizontal surfaces. The adaptive convection algorithm supplies convection coefficients for the floor and ceiling, these calculated with the Fisher horizontal jet correlations (see Table 4.5, page 88).

Next, to resolve the flow in greater detail the controller adjusts the convergence criteria (to 0.1%), turns buoyancy on, reduces the relaxation factors, then invokes the CFD solver using the $k-\varepsilon$ model. The flow and temperature fields predicted by the investigative run are used as the initial conditions for the refined run. This was found to greatly enhance the stability of the calculations. Indeed, attempts to resolve this flow with the $k-\varepsilon$ model without these initial conditions invariably led to divergence. It is interesting to note that the refined CFD simulation for 10h00 required many more solver iterations (a sixfold increase) and much greater CPU time (by a factor of 10).

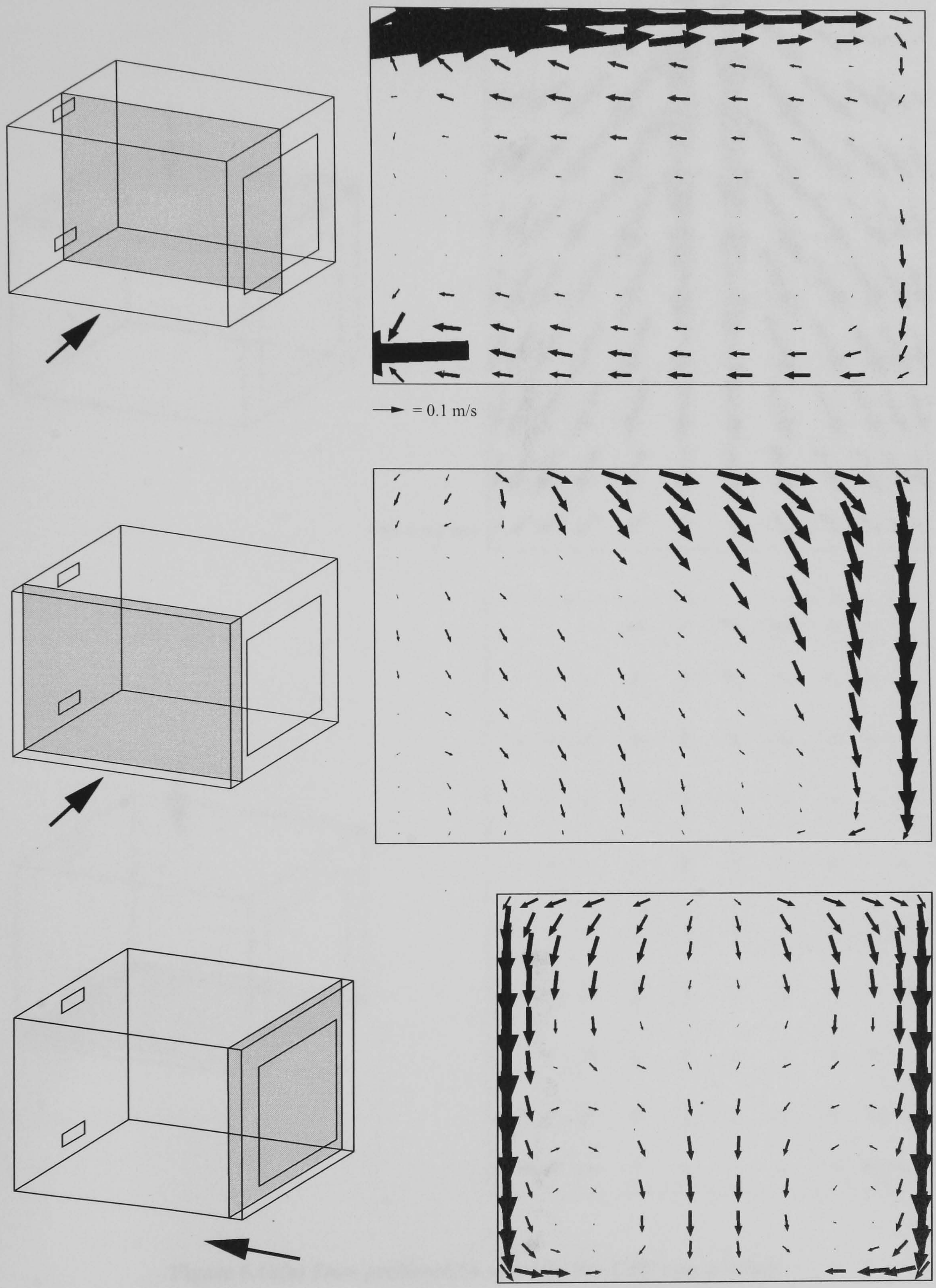

Figure 6.16(a) Flow predicted by investigative CFD run at 10h00

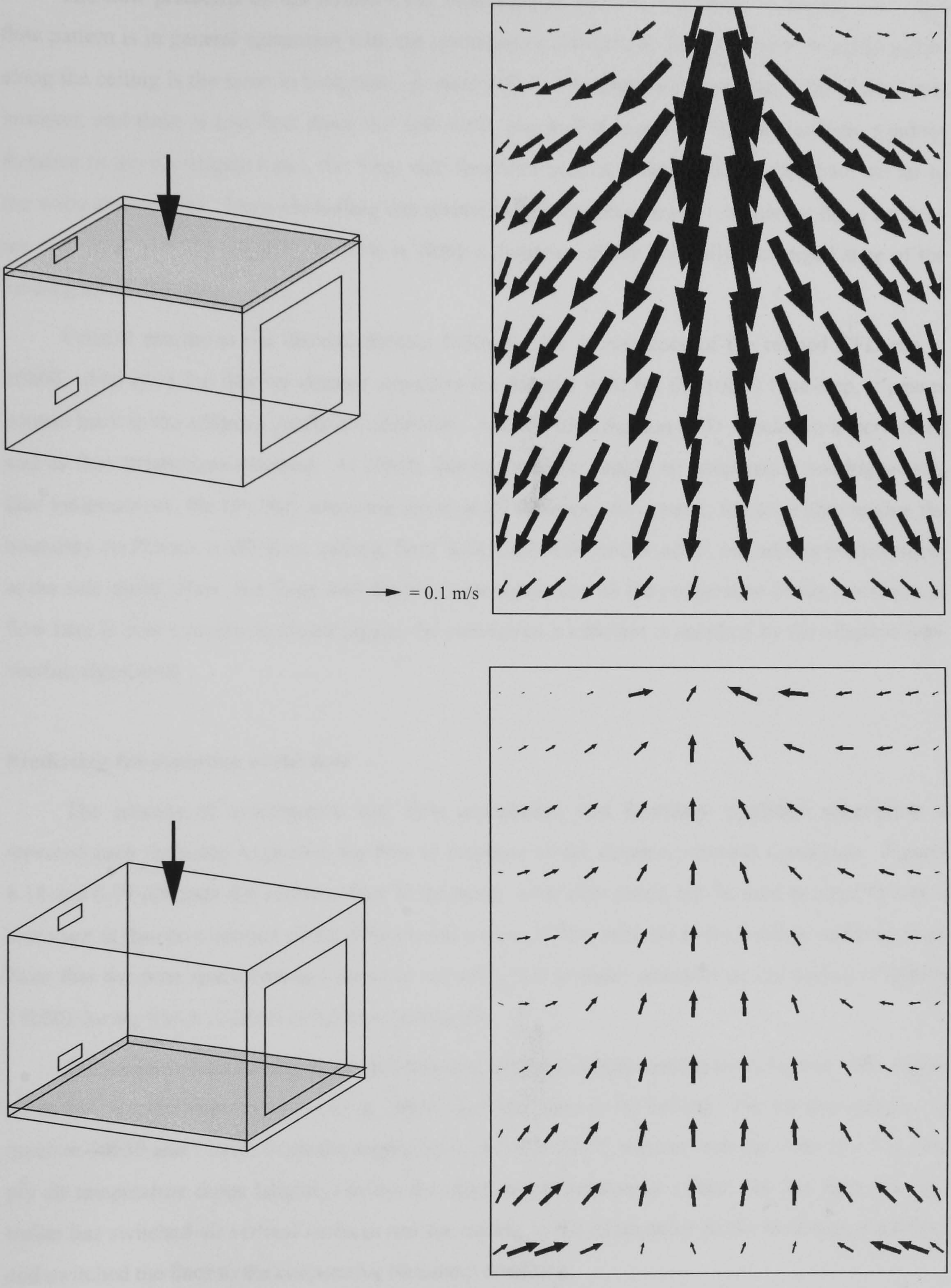

Figure 6.16(b) Flow predicted by investigative CFD run at 10h00

The flow predicted by the refined CFD simulation at 10h00 is illustrated in Figure 6.17. The flow pattern is in general agreement with the investigative simulation. The jet penetration and spread along the ceiling is the same in both runs. A more diffuse flow pattern is predicted in the refined run, however, and there is less flow down the side walls, the wall opposite the diffuser, and the window. Relative to the investigative run, the Yuan wall functions predict greater heat transfer from the air to the walls and window. Notwithstanding this greater buoyancy force, lower velocities at these surfaces are predicted with the refined run. This is likely a symptom of the non-fully converged state of the investigative CFD run.

Control returns to the thermal domain following the convergence of the refined CFD run at 10h00. And once the thermal domain simulates the thermal state for the 10h10 time-step, it passes control back to the adaptive conflation controller. Another investigation CFD simulation is performed and its flow predictions assessed. At 10h10, due to the lower supply air temperature and higher surface temperatures, the Gr_L/Re_L^2 ratios are lower at all surfaces. As a result, the controller retains the boundary conditions at the floor, ceiling, front wall, back wall, and window, but adjusts the treatment at the side walls. Here, the Yuan wall functions are replaced with the cooperative Robin condition as flow here is now considered mixed (again, the convection coefficient is supplied by the adaptive convection algorithm).

Predicting the evolution of the flow

The process of investigative run, flow assessment, and boundary condition adjustment is repeated each time-step to predict the flow in response to the changing thermal conditions. Figures 6.18 and 6.19 illustrate the evolving flow in the room. Two view points can be seen in these figures: a side view at the cross-section of the diffuser, and a view of flow adjacent to the window and back wall. Note that the time space between views is not even, this to focus attention on the period (11h00 to 12h00) during which changes occur most drastically.

The impact of the buoyancy of the incoming jet can be easily seen in these figures. The supply air is 5°C warmer than the room air at 10h00, and thus rises to the ceiling. The jet does not rise as much at 10h30 and 11h10, when the supply air is only 2 to 2.5°C warmer than the room air. The supply air temperature drops (slightly) below the room air temperature at 11h40. By this time, the controller has switched all vertical surfaces and the ceiling to the cooperative Robin boundary condition, and switched the floor to the cooperative Neumann condition.

The jet still penetrates to the back wall at 11h50, but is clearly detaching from the ceiling. Finally, at 12h00, the buoyancy of the supply air (now 3.5°C cooler than the room air) causes the jet to completely detach from the ceiling. Flow spills to the floor, where it separates, causing a recirculation region in the right half of the room. By 12h30 buoyancy forces dominate at the window and the front and back walls. As such, the controller switches to the Yuan wall functions on these surfaces.

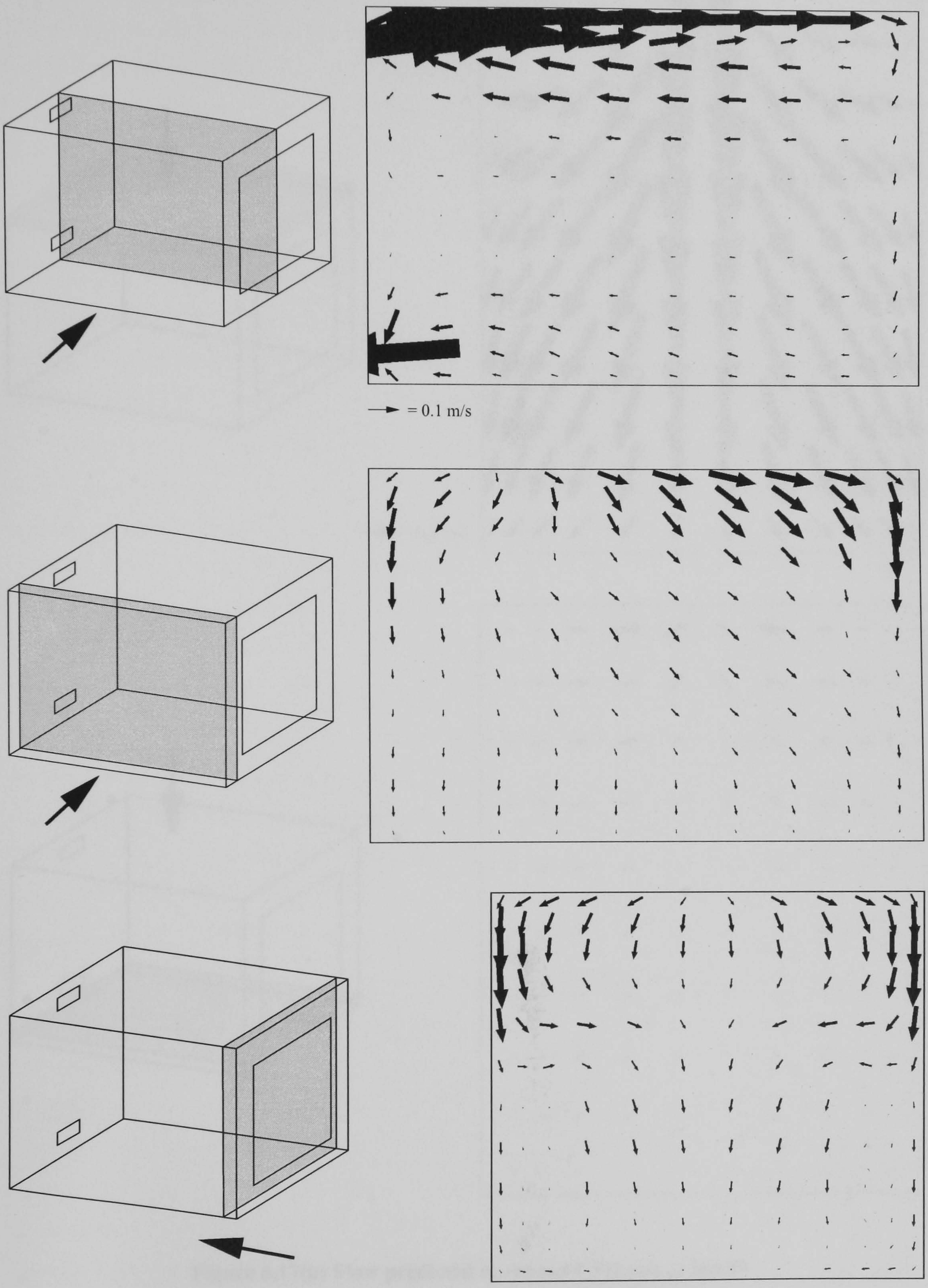

Figure 6.17(a) Flow predicted in refined CFD run at 10h00

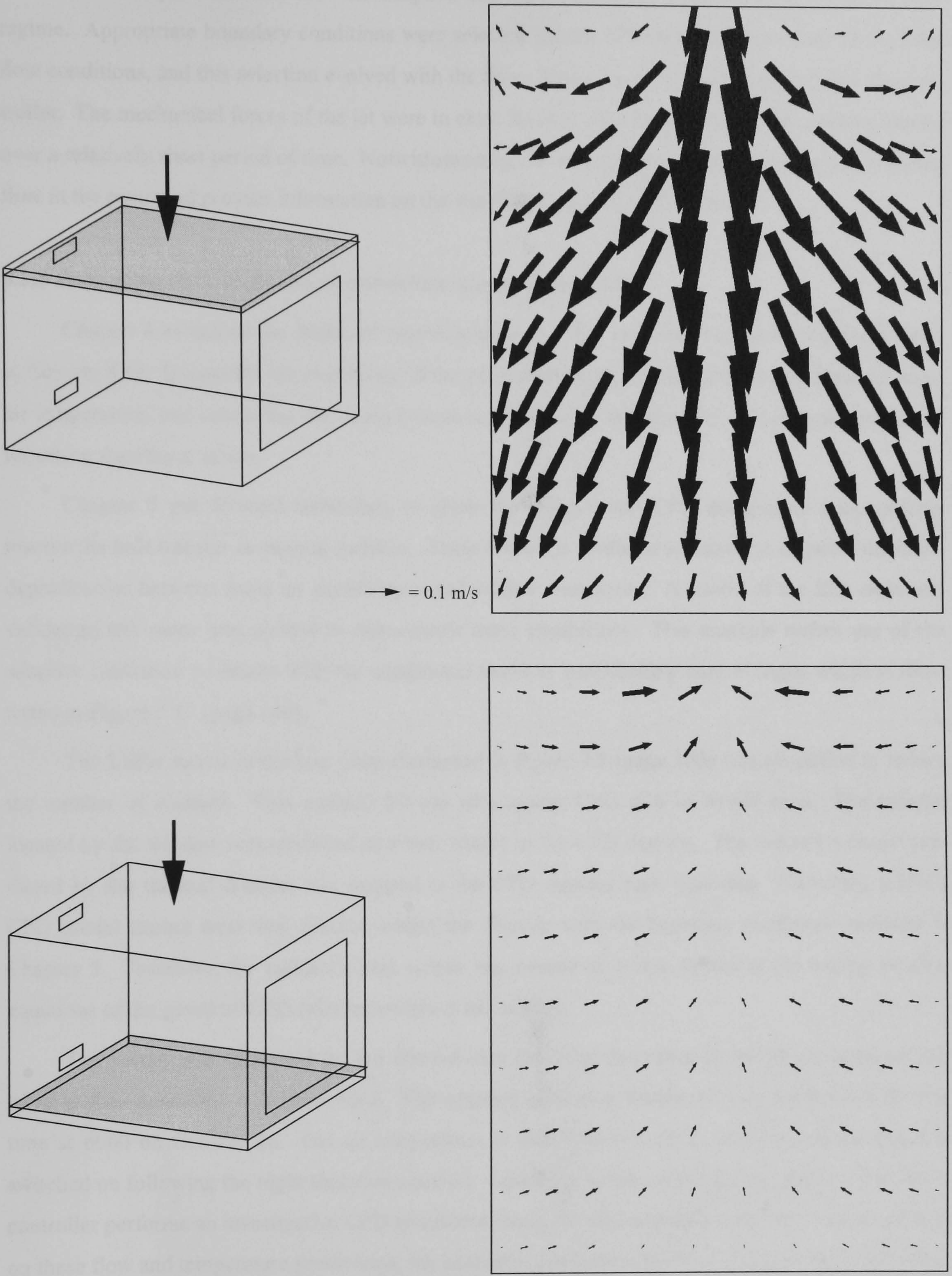

Figure 6.17(b) Flow predicted in refined CFD run at 10h00

This example illustrates how the adaptive conflation controller responds to the evolving flow regime. Appropriate boundary conditions were selected for the CFD domain in response to the local flow conditions, and this selection evolved with the flow. This case was a challenging test for the controller. The mechanical forces of the jet were in close balance with buoyancy, and this balance altered over a relatively short period of time. Notwithstanding, the controller was able to resolve the evolving flow in the room and provide information on the ventilation system's effectiveness.

6.3.3 Enhancing the calculation of convection in a stratified room

Chapter 4 examined the degree of stratification in the IEA empirical validation test room (refer to Section 4.6). It assessed the sensitivity of the predicted energy consumption to the assumed room air temperature, and concluded that when a room is significantly stratified the well-stirred method can introduce significant errors.

Chapter 5 put forward techniques to allow the thermal and CFD domains to cooperatively resolve the heat transfer at internal surfaces. These allow the conflated simulator to consider the interdependencies between room air stratification and surface convection. A model of the IEA empirical validation test room was created to demonstrate these capabilities. This example makes use of the adaptive conflation controller with the conditional two-way handshaking control logic, which is illustrated in Figure 5.17 (page 149).

The ESP-r model of the test room illustrated in Figure 4.8 (page 100) was simplified to reduce the number of surfaces. This enabled the use of a coarse CFD grid of 6x9x9 cells. The radiator located by the window was modelled as a heat source in the CFD domain. The radiator's output predicted by the thermal domain was mapped to the CFD domain each time-step. Currently, ESP-r's CFD model cannot treat heat sources within the domain with the boundary conditions outlined in Chapter 5. Therefore, the radiator's heat output was treated as a heat source in the energy balance equations of the group of CFD cells representing its location.

The model was simulated by the thermal domain using the same simulation parameters and weather data described in Section 4.5.2. The adaptive conflation controller was invoked for the first time at 6h00 on October 26. The air temperature at this time was 12°C, and the radiator was just switched on following the night shut-down period. Like the previous example, the adaptive conflation controller performs an investigative CFD simulation using the zero-equation turbulence model. Based on these flow and temperature predictions, the controller concludes that flow is mixed over all internal surfaces: the Gr_L/Re_L^2 ratios were in the range of 1 to 4. This indicates that the buoyant plume rising from the heater was of similar strength to the buoyant forces caused by surface-air temperature differences. As a result of this assessment, the controller treats all surfaces with the cooperative Robin boundary condition. Convection coefficients are supplied by the adaptive convection algorithm operating with the convective regime B1.

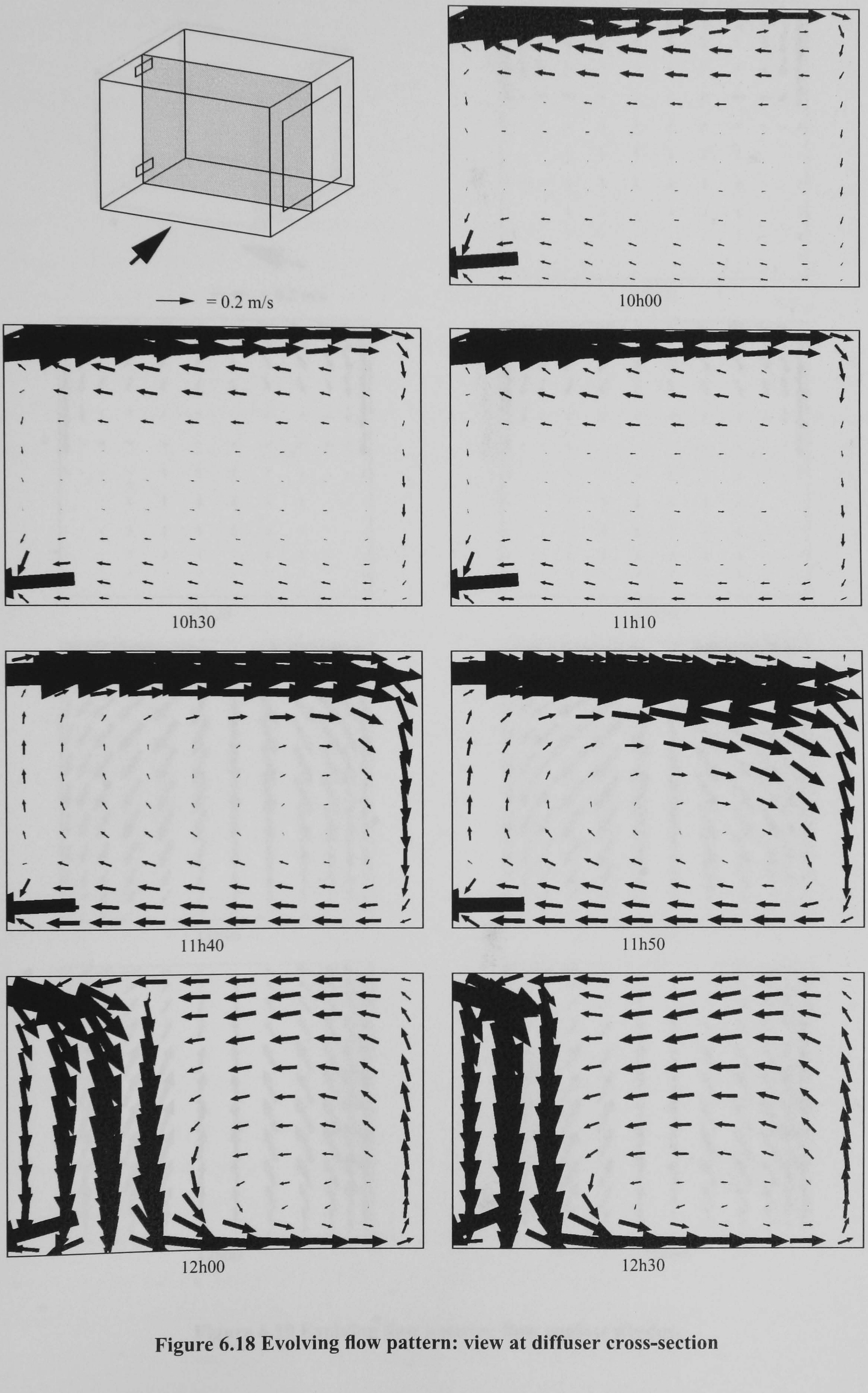

10h00

10h30

11h10

11h40

11h50

12h00

12h30

Figure 6.18 Evolving flow pattern: view at diffuser cross-section

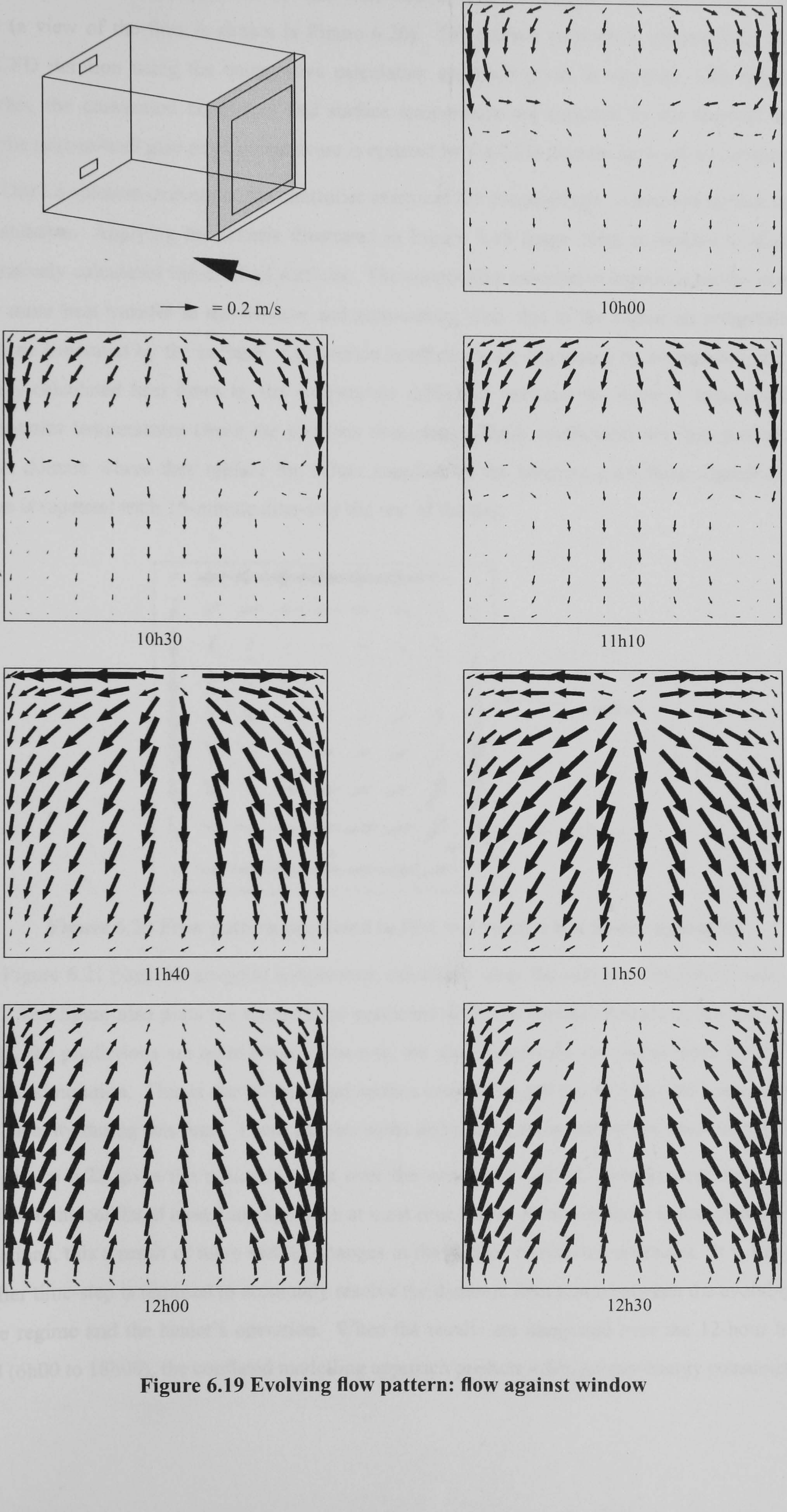

Figure 6.19 Evolving flow pattern: flow against window

The refined CFD simulation for this time-step is then performed using the $k-\varepsilon$ turbulence model (a view of the flow is shown in Figure 6.20). The surface convection estimates are updated each CFD iteration using the cooperative calculation approach given in equation 5.21 (page 141). With this, the convection coefficient and surface temperature are supplied by the thermal domain, while the next-to-wall grid point temperature is updated by the CFD domain each solver iteration.

Once a solution converges, the controller examines the cooperatively calculated surface convection estimates. Applying the criteria illustrated in Figure 5.18 (page 150), it decides to accept the cooperatively calculated values at all surfaces. The cooperative calculation approach results in significantly more heat transfer to the window and surrounding wall, due to the higher air temperatures in the plume generated by the radiator. Convection coefficients are calculated by normalizing the cooperatively calculated heat flows by the temperature difference between the thermal domain's surface and air-point temperatures (from the previous time-step). These coefficients are then passed to the thermal domain where they replace the values supplied by the adaptive convection algorithm. This process is repeated each 15-minute time-step the rest of the day.

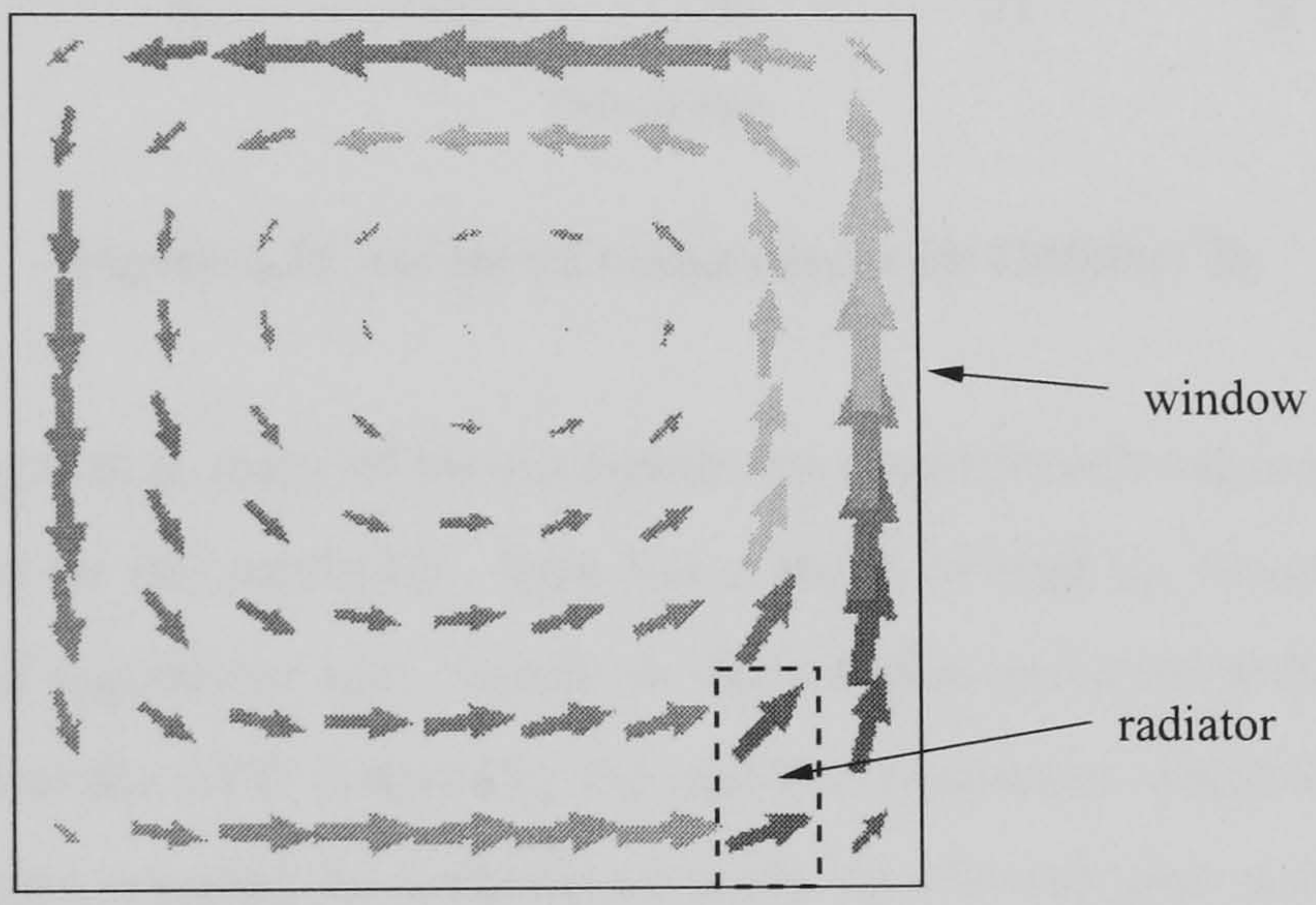

Figure 6.20 Flow pattern predicted in IEA test room when heater operating

Figure 6.21 plots the air-point temperature calculated when the adaptive conflation controller is active. The figure also plots the temperature predicted when the thermal domain acts alone. As can be seen, the predictions are quite close. However, the air-point warms somewhat more slowly in the conflated simulation. This is due to increased surface convection and the fact that the heater is operating at capacity during this time. There are also some differences at the start of the cool-down period.

Figure 6.22 gives the radiator output over the simulation period. Greater heat output is predicted with the conflated modelling approach at most time-steps. However, there is less stability in the calculations, this a result of more sudden changes in the surface convection estimates. It is likely that a smaller time-step is required to accurately resolve the dynamic interaction between the evolving convective regime and the heater's operation. When the results are integrated over the 12-hour heating period (6h00 to 18h00), the conflated modelling approach predicts 4.6% greater energy consumption.

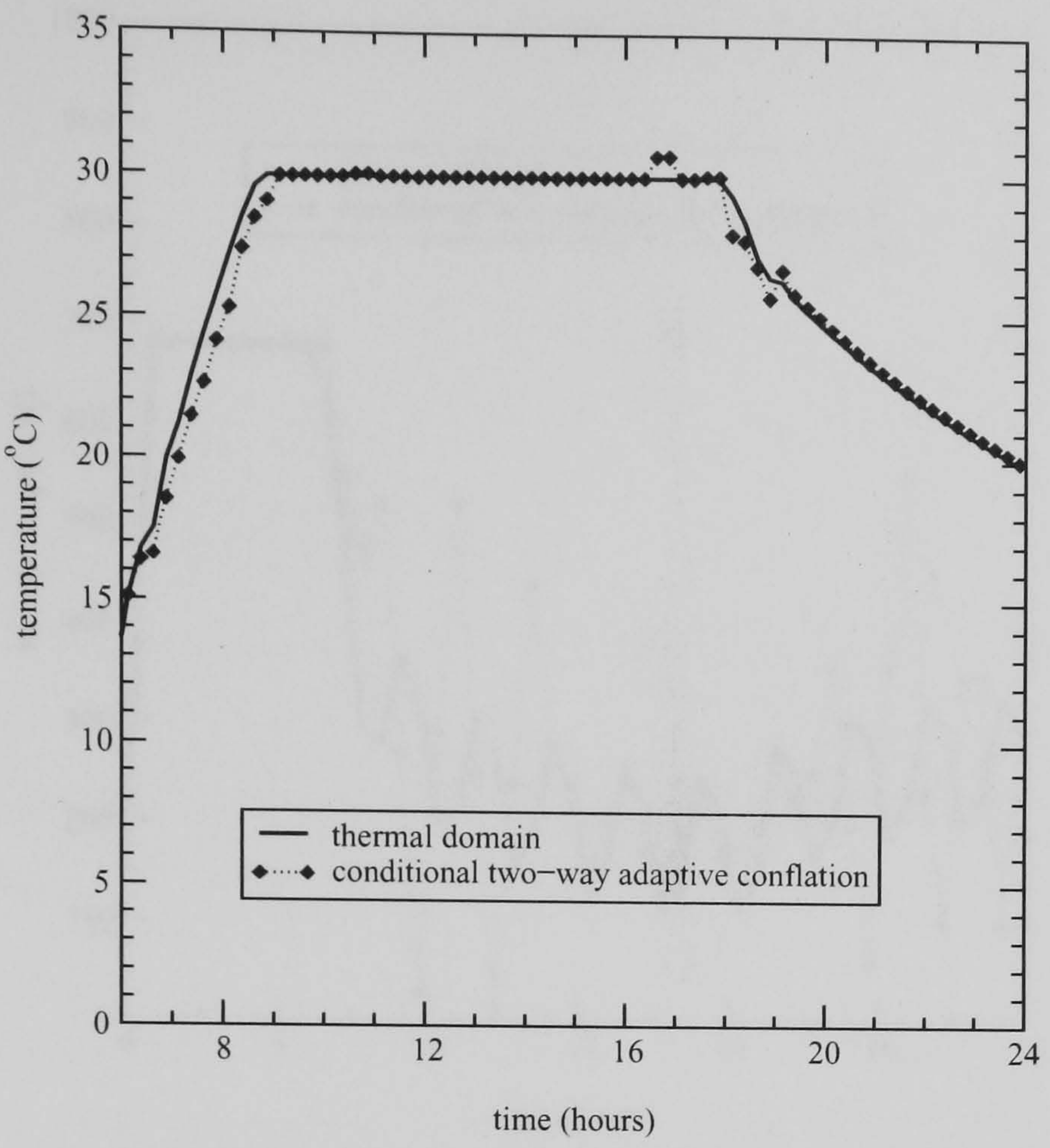

Figure 6.21 Air-point temperature on October 26

It is worth noting that at many of the time-steps the cooperatively calculated surface convection estimates were rejected by the controller. This was a result of high air temperatures in the thermal plume which generated significant heat transfer to the window and surrounding wall. Additionally, the h_c values supplied to the CFD domain by the adaptive convection algorithm are based on room-averaged air temperatures, whereas the temperature at the next-to-wall grid points was used in the simulation. This inconsistency was pointed out in Section 5.4.2, and unfortunately cannot be addressed until new h_c correlations appropriate for room air flow become available.

It is suspected that a finer CFD mesh would be required to accurately capture the details of the developing plume in order to more realistically predict this heat transfer. These improvements and other modelling refinements, such as a more explicit treatment of radiator's impact on the flow, more appropriate convergence criteria for the energy equation (convergence was judged on the residuals of the momentum and continuity equations), and performing the simulation over the entire week would be required in order to directly compare these results with those presented in Chapter 4. Notwithstanding, these results do indicate the adaptive conflation controller's capability to consider the impact of stratification on internal surface convection. It is interesting to note that the CPU time required by the investigative CFD simulations represents a small fraction of the total (less than 5%). Consequently, the investigative CFD run adds little computational burden while providing significant advantages in terms of refining the modelling approach.

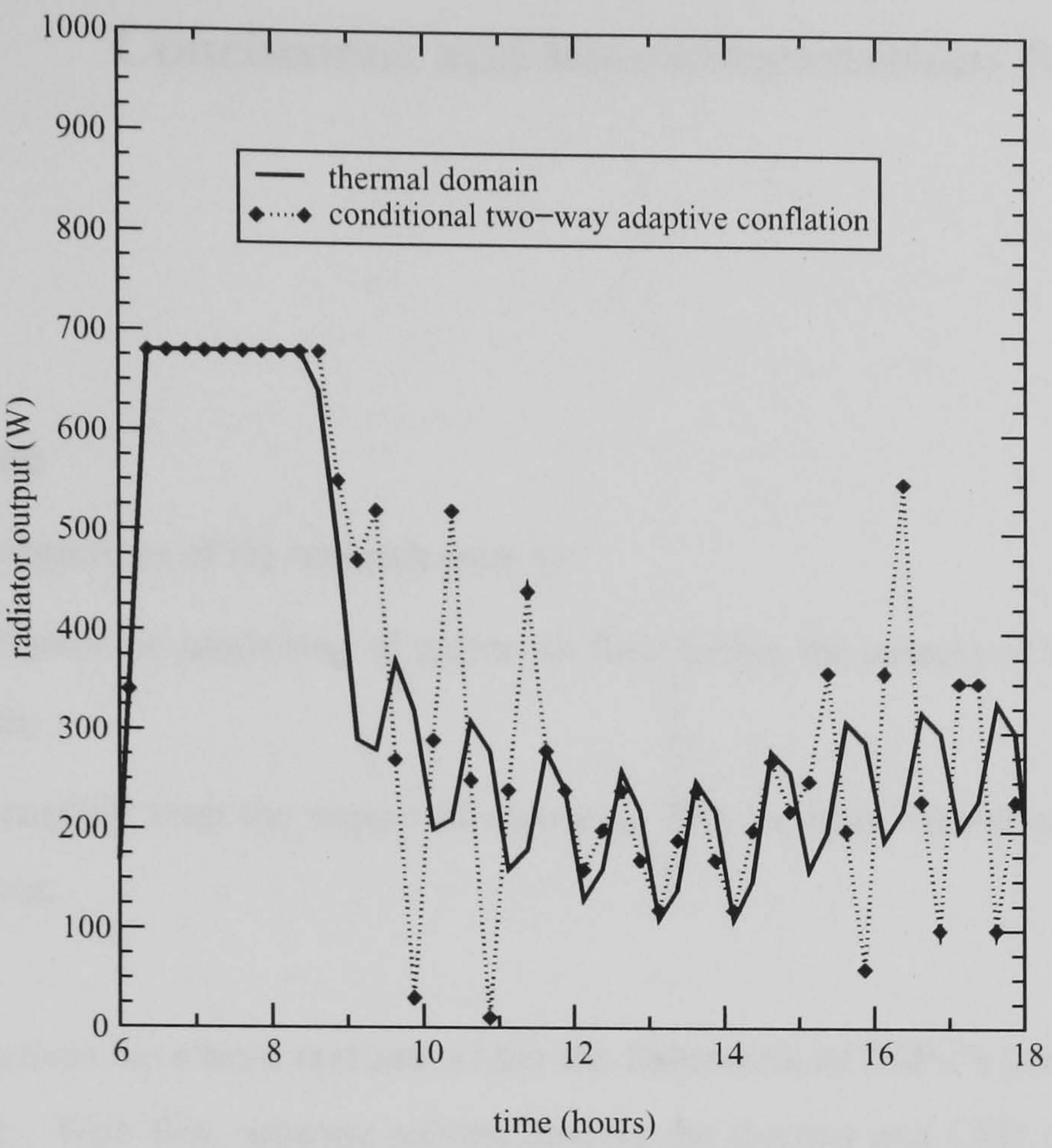

Figure 6.22 Radiator output on October 26

6.4 Closing Remarks

This chapter has demonstrated how the new adaptive convection algorithm and adaptive conflation controller have enhanced the modelling of internal surface convection and indoor air motion. Significant material was presented to verify the new approaches and implementations, although it must be acknowledged that the complexity of the physical processes precludes a comprehensive validation of these techniques.

CHAPTER 7

Conclusions and Recommendations for Future Work

7.1 Conclusions

The stated objectives of the research were to:

- advance the modelling of indoor air flow within the context of whole-building simulation;
- accurately treat the impact of indoor air flow on heat transfer at internal building surfaces.

These objectives have been realized within the framework of ESP-r's integrated and partitioned solution approach. With this, separate solvers process the thermal and CFD domains while interdependencies are handled by handshaking on a time-step basis. As a CFD solution is nothing more than the extrapolation of boundary conditions into the domain interior (i.e. the room), the first research objective was critically dependent upon this handshaking. Specifically, the physical process operating at the pivot point between the modelling domains—internal surface convection—was shown to be key.

This thesis has described the development of flow responsive modelling techniques to address the above mentioned issues. Two significant developments were put forward: the *adaptive convection algorithm* and the *adaptive conflation controller.* The former enhances ESP-r's thermal simulation domain as well as playing a supportive role for the adaptive conflation controller. Working with a base of 28 convection coefficient correlations (the structure allows easy expansion when new methods become available), the algorithm assigns appropriate equations to each internal surface and adapts the selection in response to the room's evolving flow regime.

The adaptive conflation controller manages all interactions between the thermal and CFD modelling domains. The controller incorporates the latest turbulence modelling advancements applicable for room air flow simulation (again, new approaches can be easily incorporated within the structure when they become available) and possesses a suite of handshaking and thermal boundary condition treatments. The controller uses the CFD domain to perform an investigative flow assessment, then refines modelling approaches based upon these preliminary results. Where possible, the controller manages CFD to resolve the pivot point in order to predict surface convection coefficients for the thermal domain. However, safeguards are also provided to protect the integrity of the thermal domain's matrix of heat balance equations.

The major steps leading to these developments are described as follows.

Characterizing surface convection in the thermal domain

Chapter 2 outlined how the well-stirred assumption is used to model internal surface convection within ESP-r's control-volume heat-balance methodology. This demonstrated how pervasive convection coefficients are in the resulting system of equations that characterize the zone's thermal state. Although ESP-r was already recalculating convection coefficients on a time-step basis at the commencement of the research, it did not have the ability to adapt the calculation approach to changes in the air flow regime. Additionally, it could not characterize some important flow regimes with its default and optional h_c algorithms.

Case studies presented in Chapters 4 and 6 illustrated how convection coefficients significantly affect the thermal domain's system of equations. These case studies demonstrated how energy and thermal comfort predictions are affected by the choice of h_c algorithm, and more importantly, how this choice can alter the design decisions drawn from a simulation based analysis.

Solutions to address these needs were put forward in Chapter 4. A pragmatic and extensible scheme was presented for broadly classifying the principle convective regimes encountered within buildings. Following an extensive survey, empirical methods were extracted from the literature and implemented into ESP-r for calculating coefficients for these regimes. A new method for modelling mixed flow was also put forward, as was an algorithm for predicting the convective regime induced by forced-air HVAC systems. Collectively these methods can calculate convection coefficients for most flows of practical interest.

Dynamically responding convection calculations to the flow

Since flow regimes can (or more typically, *do*) vary throughout a simulation, the inclusion of a suite of h_c equations is not sufficient in itself to accurately characterize convection. It is also necessary to assign an appropriate h_c equation to each internal surface at each time-step of the simulation, and to respond this selection to the prevailing flow conditions.

Chapter 5 described the two-step procedure that was devised to address this need. A series of automated appraisals and user prompts are applied during the problem definition stage to appraise conditions in each room. Each internal surface is attributed with a set of h_c equations appropriate for the flow conditions anticipated over the duration of the simulation. As the simulation progresses, a controller monitors critical simulation variables to assess the flow regime. Based upon this assessment, the controller dynamically assigns (for each surface) an appropriate h_c algorithm from amongst the set attributed at the problem definition stage.

This scheme builds upon the full suite of 28 h_c equations implemented into ESP-r and exploits the synergies between methods. In this way, it is able to resolve nine unique convection classifications (e.g. buoyancy caused by a heating device located under a window; mixed flow resulting from surface-air temperature differences and an air handling system delivering conditioned air through ceiling mounted diffusers). Two control laws were implemented to demonstrate this approach. Both adapt the convection calculations in response to the operational state of HVAC equipment. The first is applicable for terminal heating devices (this could be a heated wall panel, in-floor heating, a circulating fan heater, or a radiator) and the second for air-based heating and cooling systems.

The possibilities for extending the adaptive convection algorithm to consider additional convective regimes and control laws are limited only by the availability of appropriate h_c calculation equations.

Assessing CFD's applicability for modelling room air flow and heat transfer

CFD has been used to simulate indoor air flow for a quarter century. Most applications have employed the standard $k - \varepsilon$ turbulence model with log-law wall functions (the only techniques available within ESP-r at the commencement of the research). This approach was formulated for fully developed turbulent flows, which contrasts with the flow regimes commonly found in rooms. Although there have been many successful *air flow* predictions, the technology has proven deficient at predicting *convective heat transfer* at solid surfaces.

Chapter 3 summarised evidence from the literature to show that poor surface convection predictions are the result of the inability of the log-law wall functions to resolve the near-wall regions in room air flows. Results from a buoyancy-driven case presented in Chapter 5 added additional weight to this evidence. Additionally, the $k - \varepsilon$ model is unable to accurately characterize turbulent diffusion in weakly turbulent regions of a room. Numerical experiments presented in Chapter 3 showed that this has a negligible impact on air flow predictions, but significantly affects thermal calculations. This influence was seen to be local, however, indicating that the over-prediction of eddy viscosity in low-turbulence regions has a negligible influence on thermal predictions in high-turbulence regions of the flow.

Incorporating alternate turbulence models

A number of alternatives (some only emerging) to the $k - \varepsilon$ model with log-law wall functions were described in Chapter 3. In contrast to the universal nature of the log-law wall functions—which were meant to be applicable for a broad range of flow regimes and surface orientations—some of these alternative near-wall methods are only appropriate for specific cases (e.g. buoyancy-driven flow over vertical surfaces). Consequently, these techniques could only be exploited in the conflated modelling approach if the simulator was given the ability to (dynamically) select an appropriate method based on an appraisal of the flow regime.

Two of the most promising turbulence modelling alternatives were assessed and implemented in Chapter 5. A zero-equation model developed exclusively for room air flow modelling was found to give reasonable flow predictions, although its surface convection estimates were found to be grid sensitive and inaccurate (at least for buoyancy-driven flow). Thanks to its numerical stability and efficiency, this turbulence model is highly suited to producing rapid approximations of a flow regime.

A new set of wall functions for the $k-\varepsilon$ model were found to yield grid insensitive and reasonable surface convection predictions. However, their applicability is limited to buoyancy-driven flow over vertical surfaces.

Developing alternate handshaking and thermal boundary conditions

At the commencement of the research, the task of resolving the surface convection was the exclusive jurisdiction of the CFD domain. It employed the log-law wall functions for this task, and returned surface convection predictions to the thermal domain, where they were used in the formation of the zone matrix of heat balance equations. Alterations to this approach were required for two reasons. Firstly, inaccurate CFD surface convection predictions could substantially distort the system of thermal equations. Secondly, the CFD air flow predictions are sensitive to the thermal boundary conditions prescribed.

A series of alternate handshaking approaches and boundary condition treatments were put forward in Chapter 5. These enable either modelling domain (or both domains acting cooperatively) to resolve the surface convection. In some cases they are supported in this task by the adaptive convection algorithm, which is called upon to supply convection coefficients. The cooperative boundary conditions allow the conflated simulator to consider the interdependencies between room air stratification and surface convection.

The concepts of one-way and conditional two-way surface handshaking were introduced in Chapter 5. Their purpose is to prevent the propagation of erroneous results between the thermal and CFD modelling domains and to protect the integrity of the thermal calculations.

Dynamically controlling the conflation between the thermal and CFD domains

Ten viable combinations of handshaking scheme, boundary condition treatment, and turbulence model were recommended in Chapter 5 (although many more combinations are now available within ESP-r). Each combination has limited applicability. If, for example, the objective is to predict the air flow and temperature distribution in a room and it is known that the flow is strongly affected by surface convection, the $k-\varepsilon$ model with one-way handshaking and a Neumann boundary condition would be an appropriate approach. With this, the thermal domain calculates the surface convection

(h_c is supplied by the adaptive convection algorithm) and imposes this as a boundary condition on the CFD domain. But if the flow is driven by buoyancy caused by surface-air temperature differences and the objective is to use CFD to enhance the thermal domain, the $k-\varepsilon$ model with the alternate wall functions would be a more appropriate choice.

Given the reality that thermal conditions outside the CFD domain are dynamic, these combinations of modelling methods could only be fully exploited through the creation of a controlling algorithm. The job of this adaptive conflation controller is to monitor the evolving thermal and air flow conditions in the room and dynamically select an appropriate scheme for the prevailing conditions.

Two control schemes were implemented to demonstrate the concept. One is suitable when the objective of the analysis is to predict the flow and temperature field within the room, perhaps for the purposes of visualizing the flow, assessing thermal comfort, or studying pollutant dispersion. The other is suited to performing these tasks as well as enhancing the thermal simulation by providing surface convection estimates for the thermal domain.

Both schemes make use of a double-pass modelling approach. Each time-step that the thermal domain handshakes with CFD, the adaptive conflation controller performs an investigative simulation with the zero-equation turbulence model. This approximates the room's flow and temperature field. Using these estimates, the controller calculates dimensionless groupings to determine the nature of the flow (forced, buoyant, mixed, fully turbulent, weakly turbulent) adjacent to each internal surface. This information is used to select suitable boundary condition treatments for each surface (e.g. the alternate wall functions are used if flow is predominately buoyant and if the surface is vertical). In certain cases the controller calls upon the adaptive convection algorithm to supply an appropriately calculated convection coefficient. Key parameters that affect the numerical stability of the CFD solver are also adjusted in response to the flow appraisal (i.e. relaxation factors are reduced if buoyancy is significant). A second CFD simulation is then performed with the $k-\varepsilon$ model using the refined modelling approach to more accurately resolve the air flow, the temperature distribution, and to predict surface convection. In order to protect the thermal domain, a two-stage screening process is used to assess (and where necessary reject) the CFD-predicted surface convection estimates.

Transferring the technology to practice

Issues regarding accessibility of models and results were cited in Chapter 1 as barriers to the further adoption of simulation by the building design professions. To this end, all the developments described in this thesis have been made accessible within ESP-r's *Project Manager*. Menu-driven interfaces have been created to support the adaptive convection algorithm and to integrate the CFD domain within ESP-r's standard data model. Additionally, a flow visualization facility was developed to support the integrated modelling approach. This allows the air flow at any cross-section in the room to be viewed, either instantaneously or over a period of time.

Testing and demonstrating the developments

The validity of ESP-r's CFD model had been examined prior to commencement of this research with analytical, empirical, and comparative tests. Therefore, the tests presented in Chapter 6 (and earlier chapters) focused on aspects related to the new developments.

An analytic test was performed, for example, to verify that ESP-r's thermal domain responds correctly to a sudden change in h_c calculation method. The adaptive convection algorithm's approach was further verified with empirical data that qualitatively confirmed that convective regimes are affected by the placement and operation of HVAC equipment. The implementations of the zero-equation turbulence model and alternate wall functions were assessed with comparative tests (both inter-program and sensitivity) and against empirical data.

More realistic cases were used to test the interactions between the individual algorithms and to demonstrate how the new adaptive convection algorithm and the adaptive conflation controller can be applied to enhance the simulation of internal surface convection and indoor air motion.

7.2 Recommendations for Future Work

This research has identified a number of areas worthy of further study and has provided a platform for initiating future research. Although the work documented in this thesis represents a contribution towards the modelling of internal surface convection and indoor air motion, much work remains. Some recommendations are provided here.

The need for additional empirical h_c algorithms

This work has drawn heavily upon the experimental work of others who provide h_c correlations for various convective regimes. Approaches were found to characterize most of the principle convective regimes, however further research in this field is required.

Clearly the operation and placement of HVAC equipment has a profound impact on internal surface convection. Many systems have yet to be investigated. For example, no suitable method exists to characterize convection generated by forced-air heating systems that deliver air through floor-mounted diffusers located near windows (a common heating system in low-rise housing). Methods appropriate for displacement ventilation, induction units, and other air-based HVAC systems would also be welcomed.

Based upon the material presented in Chapters 4 and 6, it is clearly a challenge to design an experiment that can deliver highly accurate h_c data under realistic operating conditions. New experimental approaches or alternate techniques to derive h_c values from primary measurements may be required to advance this field.

Chapters 4 and 6 raised concerns over the validity of some of the h_c equations incorporated in this research, particularly in regards to the treatment of windows. The confirmation of these methods, or the development of alternate approaches would be a worthy topic of investigation. The method selected for this work for calculating h_c for mechanically ventilated rooms was based strictly on cooling experiments. Chapter 4 provided an argument to justify its use for room heating as well, but the validity of this should be examined in the future.

As a final remark regarding empirical h_c data, many of the experimental programmes have been conducted within rooms of fixed geometry. While the practical reasons for this approach are obvious and understandable, information on scale effects would be invaluable.

Validation and extension of the mixed flow model

A theoretical argument was provided in Chapter 4 to justify the need and the form of the mixed flow model. Although the model is based on the well-proven Churchill-Usagi blending approach, there are no empirical data to validate these assumptions. A sensitivity analysis was conducted to test the choice of blending coefficient and to examine the limit placed on the subtractive blending formula for opposing forces. But again, there are no data to validate these decisions. Given how common this flow regime is in mechanically ventilated buildings, the validation (and perhaps refinement and calibration) of this mixed flow model would be a worthy field of study.

It would also be interesting to extend the applicability of the mixed flow model by blending additional h_c correlations. For example, Chapter 4 discusses how a method for resolving mechanically ventilated rooms with reheating devices located underneath windows could be created by blending h_c equations that have already been implemented into ESP-r.

Extension of the adaptive convection algorithm

Two control laws were implemented to demonstrate the dynamic selection of convection correlations. Both adapt the convection calculations in response to the operational state of HVAC equipment. It would be interesting to extend this approach to control the calculations based on the sensed condition of other simulation variables, such as the state of a network air flow connection. Chapter 5 points to some possibilities.

The adaptive convection algorithm's supporting idealized HVAC model is used to resolve the room's convective regime, predicting the flow and temperature of air supplied to the room by the HVAC system. These techniques should be integrated with ESP-r's zone control method and network air flow model in the future to provide for greater modelling flexibility.

Handshaking and boundary condition improvements

Chapter 5 put forward the cooperative Robin boundary condition to allow the conflated simulator to consider the interdependencies between room air stratification and surface convection. The inconsistency of using an h_c correlation based on average room conditions for calculating convection with the next-to-wall grid point was acknowledged. The potential problems with this approach were pointed out in one of the examples presented in Chapter 6.

This warrants further investigation. One possible solution is to find or develop h_c correlations that can operate on next-to-wall grid points. Another possibility is to tune the CFD grid to appropriately locate the next-to-wall grid points when this boundary condition treatment is employed. It may also be possible and appropriate to calculate a reference temperature from a group of CFD cells near the surface, rather than operating exclusively on the next-to-wall grid point.

Although the structure has been put in place to enable concurrent handshaking between the thermal, network air flow, and CFD domains, this has not been extensively tested or assessed. Further work is also required to extend the one-way handshaking concept to the conflation between the network air flow and CFD domains. As well, it would be interesting to extend the adaptive conflation approach to dynamically control the coupling between the network air flow and CFD domains.

Additional turbulence and near-wall modelling options

Chapter 3 discussed a number of efforts that are underway to improve the modelling of turbulence, and in particular the near-wall regions. Many of these methods are being developed specifically for room air flow analysis. Once available, these methods should be assessed, and where applicable, implemented within the adaptive conflation controller. The code has been structured to allow the easy inclusion of additional turbulence and near-wall methods.

CFD domain enhancements

An automated gridding algorithm that optimizes the placement of grid points to enhance accuracy and stability, while also matching the CFD domain to ESP-r's standard geometrical model would greatly enhance the applicability of the conflated modelling approach.

As pointed out in Chapter 6, improvements to the treatment of heat sources and blockages within the room are required. The boundary condition and handshaking methods outlined in Chapter 5 should also be made applicable to objects within the room. The technique utilized in the example in Chapter 6 to allow the thermal domain to inject heat within the CFD domain should be generalized and extended. It would be interesting to integrate ESP-r's explicit plant model with CFD to allow, for example, the plant components to be controlled based on the temperature sensed at a CFD cell (or a group of CFD cells). This would also enable the explicit simulation of the convective heat transfer from a plant component in response to a room air flow pattern.

A number of developments could be undertaken to enhance the stability and efficiency of the CFD solution process:

- The loose coupling between the energy and z-momentum equations (through the buoyancy term) leads to divergence in many circumstances. This is of particular concern in modelling room air flow, as buoyancy is often a significant force driving air motion. Perhaps an alternate to the sequential solution process is required.
- Methods are required to control the solution process to encourage convergence. Techniques such as residual tracking, rewinding solutions following the initiation of divergence, and the dynamic adjustment of relaxation factors could be pursued.
- Despite rapidly increasing computer power, there is still a need for more efficient equation solvers. Techniques that adapt relaxation factors and solver sweeping schemes in response to the evolving solution could greatly reduce the number of iterations required to achieve convergence. It may be possible to develop algorithms that have the capacity to learn the relationships between to solver parameters, convergence potential, and convergence rate to assist in this (e.g. neural networks).

Optimizing the adaptive conflation controller

Two possible control schemes were proposed for the adaptive conflation controller in Chapter 5. As these schemes were based strictly on intuition and experience, there is much room for refinement and optimization. In particular, the criteria used to assess the CFD-predicted surface convection estimates when conditional two-way adaptive conflation control is active should be examined, critically reviewed, and optimized.

Although the investigative CFD simulation was found to add little computational burden, savings could be realized by using a coarser grid or by initiating the investigative run only when boundary conditions change significantly between time-steps.

New or different criteria could be used to establish boundary conditions for the refined CFD simulation. A number of suggestions were made in Chapter 5. These include: measuring the stratification in the investigative CFD simulation, sensing the operational state of plant components, and using different dimensionless groupings to assess the nature of the flow.

Adapting the convergence criteria to the objective of the analysis could realize significant computational savings. For example, halting the CFD simulation when the relative change in surface convection predictions between two successive iterations becomes smaller than an acceptable tolerance may be an appropriate (and efficient) criteria to apply when the objective of CFD is to predict the heat transfer.

It would be interesting to develop techniques to allow the CFD domain to handshake with the adaptive convection algorithm. CFD results could be used, for example, to help the algorithm select between optional h_c correlations. CFD flow predictions could also be used by the algorithm as inputs to forced flow correlations to improve h_c calculations.

Finally, two example applications of the adaptive conflation controller were given in Chapter 6. Further application is in order to test the robustness of the method and to refine the modelling approaches.

References

Aasem E.O.. (1993), *Practical Simulation of Buildings and Air-Conditioning Systems in the Transient Domain*, PhD Thesis, University of Strathclyde, Glasgow UK.

Alamdari F. and Hammond G.P. (1983), 'Improved Data Correlations for Buoyancy-Driven Convection in Rooms', *Building Services Engineering Research and Technology*, 4 (3) 106-112.

Alamdari F., Hammond G.P., and Melo C. (1984), 'Appropriate Calculation Methods for Convective Heat Transfer from Building Surfaces', Proc. 1st U.K. National Conf. on Heat Transfer, (2) 1201-1211.

Altmayer E.F., Gadgil A.J., Bauman F.S., and Kammerud R.C. (1983), 'Correlations for Convective Heat Transfer from Room Surfaces', *ASHRAE Transactions*, 89 (2A) 61-77.

Arnold P.D., Hammond G.P., Irving A.D., and Martin C.J. (1998), 'The Influence of Sun Patches on Buoyancy-Driven Air Movement and Heat Transfer within a Passive Solar Test Cell', *Proc. ASME Heat Transfer Division*, 361 (1) 47-57.

ASHRAE (1998), *Standard Method of Test for the Evaluation of Building Energy Analysis Computer Programs: ASHRAE Standard 140P*, Working Draft 98/2, American Society of Heating, Refrigerating, and Air-Conditioning Engineers, Atlanta USA.

Awbi H.B. (1991), *Ventilation of Buildings*, Chapman & Hall, London UK.

Awbi H.B., Croome D.J., and Gan G. (1992), 'Prediction of Airflow and Thermal Comfort in Offices', *Proc. Int Symp. on Room Air Convection and Ventilation Effectiveness*, Tokyo Japan.

Awbi H.B. (1998), 'Calculation of Convective Heat Transfer Coefficients of Room Surfaces for Natural Convection', *Energy and Buildings*, 28 219-227.

Awbi H.B. and Hatton A. (1999), 'Natural Convection from Heated Room Surfaces', *Energy and Buildings*, 30 233-244.

Ayres J.M. and Stamper E. (1995), 'Historical Development of Building Energy Calculations', *ASHRAE Journal*, February, 47-53.

Baker A.J., Williams P.T., and Kelso R.M. (1992), *A Computational Fluid Dynamics (CFD) Procedure for 3D Room Air Motion Prediction*, ASHRAE Research Project 464-RP Final Report.

Baker A.J., Williams P.T., and Kelso R.M. (1994a), 'Numerical Calculation of Room Air Motion—Part 1: Math, Physics, and CFD Modelling', *ASHRAE Transactions*, 100 (1) 514-530.

Baker A.J., Williams P.T., and Kelso R.M. (1994b), 'Development of a Robust Finite Element CFD Procedure for Predicting Indoor Room Air Motion', *Building and Environment*, 29 261-273.

Barp S. and Moser A. (1998), 'Heat Transfer Under Thermally Stratified Conditions at Horizontal Surfaces in Buildings', *Proc. ROOMVENT '98*, (2) 103-110, Stockholm Sweden.

Bauman F., Gadgil A., Kammerud R., Altmayer E., and Nansteel M. (1983), 'Convective Heat Transfer in Buildings: Recent Research Results', *ASHRAE Transactions*, 89 (1A) 215-232.

Bazjanac V. and Crawley D.B. (1997), 'The Implementation of Industry Foundation Classes in Simulation Tools for the Building Industry', *Proc. Building Simulation '97*, (1) 203-210. Int. Building Performance Simulation Association, Prague Czech Republic.

Beausoleil-Morrison I. and Clarke J.A. (1998), 'The Implications of Using the Standard $k - \varepsilon$ Turbulence Model to Simulate Room Air Flows which are not Fully Turbulent', *Proc. ROOMVENT '98*, (1) 93-100, Stockholm Sweden.

Beausoleil-Morrison I. and Strachan P. (1999), 'On the Significance of Modelling Internal Surface Convection in Dynamic Whole-Building Simulation Programs', *ASHRAE Transactions* 105 (2).

Beausoleil-Morrison I. (1999), 'Modelling Mixed Convection Heat Transfer at Internal Buildings Surfaces', *Proc. Building Simulation '99*, (1) 313-320, Int. Building Performance Simulation Association, Kyoto Japan.

Beausoleil-Morrison I. (2000), 'An Algorithm for Calculating Convection Coefficients for Internal Building Surfaces for the Case of Mixed Flow in Rooms', *to be published in Energy and Buildings*.

Bohn M.S., Kirkpatrick A.T., and Olson D.A. (1984), 'Experimental Study of Three-Dimensional Natural Convection High Rayleigh Number, *J. Heat Mass Transfer*, (106) 339-345.

Broyd T.W., Dean R.B., Oldfield S.G., and Moult A. (1983), 'The Use of a Computational Method to Assess the Safety and Quality of Ventilation in Industrial Buildings', *Proc. Conf on Heat and Fluid Flow in Nuclear and Process Plant Safety*, 65-74, London UK.

Buildings and Environment (1989), 'Numerical Solutions of Fluid Problems Related to Buildings, Structures and the Environment', 24(1) 3-110.

CEC (1999), *Energy Efficiency Standards for Residential and Nonresidential Buildings*, P400-98-001, California Energy Commission, Sacramento USA.

Catton I. (1978), 'Natural Convection in Enclosures' *Proc. 6th Int. Heat Transfer Conference*, (6) 13-31, Toronto Canada.

Chandra S. and Kerestecioglu A.A. (1984), 'Heat Transfer in Naturally Ventilated Rooms: Data from Full-Scale Measurements', *ASHRAE Transactions*, 90 (1B) 211-224.

Chen Q. and van der Kooi J. (1988), 'ACCURACY—A Computer Program for Combined Problems of Energy Analysis, Indoor Airflow, and Air Quality', *ASHRAE Transactions*, 94 (2) 196-214.

Chen Q., Moser A., and Huber A. (1990), 'Prediction of Buoyant, Turbulent Flow by a Low-Reynolds-Number $k-\varepsilon$ Model', *ASHRAE Transactions*, 96(1) 564-573.

Chen Q. and Jiang Z. (1992), 'Significant Questions in Predicting Room Air Motion', *ASHRAE Transactions*, 98 (1) 929-939.

Chen Q. (1995), 'Comparison of Different $k-\varepsilon$ Models for Indoor Air Flow Computations', *Numerical Heat Transfer*, B(28) 353-369.

Chen Q., Peng X., and van Paassen A.H.C. (1995), 'Prediction of Room Thermal Response by CFD Technique with Conjugate Heat Transfer and Radiation Models', *ASHRAE Transactions*, 3884 50-60.

Chen Q. (1996), 'Prediction of Room Air Motion by Reynolds-Stress Models', *Building and Environment*, 31 (3) 233-244.

Chen Q. and Xu W. (1998), 'A Zero-Equation Turbulence Model for Indoor Airflow Simulation', *Energy and Buildings*, 28 137-144.

Chen Q. and Srebric J. (1999), *Simplified Diffuser Boundary Conditions for Numerical Room Airflow Models*, ASHRAE Research Project 1009-TRP First Report.

Chikamoto T., Murakami S., and Kato S. (1992), 'Numerical Simulation of Velocity and Temperature Fields within Atrium based on a Modified $k-\varepsilon$ Model Incorporating Damping Effect due to Thermal Stratification', *Proc. Int. Symp. on Room Air Convection and Ventilation Effectiveness*, Tokyo Japan.

Churchill S.W. and Usagi R. (1972), 'A General Expression for the Correlation of Rates of Transfer and Other Phenomena', *AIChE Journal*, 18 (6) 1121-1128.

Churchill S.W. (1983), 'Combined Free and Forced Convection Around Immersed Bodies', in E.U. Schlunder, Ed-in-Chief, *Heat Exchanger Design Handbook*, Section 2.5.9, Hemisphere Publishing Corp, New York USA.

CIBSE (1988), *CIBSE Guide*, 5th edition, Chartered Institute of Building Services Engineers, U.K.

Clarke J.A. (1977), *Environmental Systems Performance*, PhD Thesis, University of Strathclyde, Glasgow UK.

Clarke J.A. (1982), 'Dynamic Energy Simulation: the Integration of Building and Plant', *Proc. Int. Conf. on System Simulation in Buildings*, 111-134, Commission of the European Communities, Liège, Belgium.

Clarke J.A. (1991), *Internal Convective Heat Transfer Coefficients: A Sensitivity Study*, Report to ETSU, University of Strathclyde, Glasgow U.K.

Clarke J.A. (1985), *Energy Simulation in Building Design*, Adam Hilger Ltd, Bristol and Boston.

Clarke J.A., Dempster W.M. and Negrão C. (1995a), 'The Implementation of a Computational Fluid Dynamics Algorithm within the ESP-r System', *Proc. Building Simulation '95*, 166-75, Int. Building Performance Simulation Association, Madison USA.

Clarke J.A., Hensen J.L.M. and Negrão C.O.R. (1995b), 'Predicting Indoor Air Flow by Combining Network Approach, CFD and Thermal Simulation', *Proc. 16th AIVC Conf.*, 145-53.

Clarke J.A., Hand, J.W., Strachan P.A., and Mac Randal D.F. (1995c), 'The Development of an Intelligent, Integrated Building Design System Within the European COMBINE Project', *Proc. Building Simulation '95*, 444-453, Int. Building Performance Simulation Association, Madison USA.

Clarke J.A. and Beausoleil-Morrison I. (1997), 'The Integration of Computational Fluid Dynamics into Building Simulation', *IBPSA News*, 9 (2).

Clarke J.A. (1999), 'Prospects for Truly Integrated Building Performance Simulation', *Proc. Building Simulation '99*, (3) 1147-1154, Int. Building Performance Simulation Association, Kyoto Japan.

Cockcroft J.P. (1979), *Heat Transfer and Air Flow in Buildings*, PhD Thesis, University of Glasgow, Glasgow U.K.

Dascalaki E., Santamouris M., Balaras C.A., and Asimakopoulos D.N. (1994), 'Natural Convection Heat Transfer Coefficients from Vertical and Horizontal Surfaces for Building Applications', *Energy and Buildings*, 20 243-249.

Emmerich S.J. (1997), *Use of Computational Fluid Dynamics to Analyze Indoor Air Quality Issues*, National Institute of Standards and Technology report NISTIR 5997, USA.

Emmerich S.J. and McGrattan K.B. (1998), 'Application of a Large Eddy Simulation Model to Study Room Airflow', *ASHRAE Transactions*, SF-98-10-2.

ESRU (1999), *The ESP-r System for Building Energy Simulations: User Guide Version 9 Series*, ESRU Manual U99/1, University of Strathclyde, Glasgow UK.

Feustel H.E. and Dieris J. (1992), 'A Survey of Airflow Models for Multizone Structures', *Energy and Buildings*, 18 79-100.

Fisher D.E. (1995), *An Experimental Investigation of Mixed Convection Heat Transfer in a Rectangular Enclosure*, PhD Thesis, University of Illinois, Urbana USA.

Fisher D.E. and Pedersen C.O. (1997), 'Convective Heat Transfer in Building Energy and Thermal Load Calculations', *ASHRAE Transactions*, 103 (2) 137-148.

Fischer V., Gritzki R., and Rösler M. (1998), 'Comparative Studies of Heating Systems by Building Simulation Including CFD', *Proc. ROOMVENT '98*, (2) 89-94, Stockholm Sweden.

GATC (1967), *Computer Program for Analysis of Energy Utilization in Postal Facilities: Volume 1 User's Manual*, General American Transportation Corporation, Niles USA.

Gosman A.D., Nielsen P.V., Restivo A., and Whitelaw J.H. (1980), 'The Flow Properties in Rooms with Small Ventilation Openings', *Trans. ASME J. Fluids Eng.*, 102 316-323.

Halcrow (1987), 'Heat Transfer at Internal Building Surfaces', *Report to the Energy Technology Support Unit, British Department of Energy*, Sir William Halcrow and Partners Ltd.

Hammond G.P. (1982), 'Profile Analysis of Heat/Mass Transfer Across the Plane Wall-Jet', *Proc. 7th Int. Heat Transfer Conference*, (3) 349-355, Munich Germany.

Hand J.W. (1998), *Removing Barriers to the Use of Simulation in the Building Design Professions*, PhD Thesis, University of Strathclyde, Glasgow UK.

Hand J.W., Irving S.J., Lomas K.J., McElroy L.B., Parand F., Robinson D., and Strachan P. (1998), *CIBSE Application Manual AM11 Building Energy and Environmental Modelling*, Chartered Institute of Building Services Engineers, London UK.

Hatton A. and Awbi H.B. (1995), 'Convective Heat Transfer Coefficients of Room Surfaces', *IMechE 4th National Heat Transfer Conference*, 201-206, Manchester UK.

Heiselberg P., Murakami S., and Roulet C.-A. (1998), *Ventilation of Large Spaces in Buildings: Analysis and Prediction Techniques*, IEA Energy Conservation in Buildings and Community Systems Programme Annex 26 Subtask 2 Final Report.

Hensen J.L.M. (1991), *On the Thermal Interaction of Building Structure and Heating and Ventilation System*, PhD Thesis, Eindhoven University of Technology, The Netherlands.

Holmes M.J., Lam J.K.-W., Ruddick K.G., and Whittle G.E. (1990), 'Computation of Conduction, Convection, and Radiation in the Perimeter Zone of an Office Space', *Proc. ROOMVENT '90*, Oslo Norway.

Inard C., Bouia H., and Dalicieux P. (1996), 'Prediction of Air Temperature Distribution in Buildings with a Zonal Model', *Energy and Buildings*, (24) 125-132.

Inard C., Depecker P., and Roux J.-J. (1997), 'Un Modèle Simplifé pour la Prédiction du Champ de Température dans les Bâtiments', Revue Génie Thermique, (36) 113-123.

Incropera F.P. and DeWitt D.P. (1985), *Fundamentals of Heat and Mass Transfer*, John-Wiley and Sons.

Irving S.J. (1982), 'Energy Program Validation: Conclusions of IEA Annex 1', *Computer Aided Design*, 14 (1) 33-38.

Jackman P.J. (1970), 'A Study of Natural Ventilation of Tall Office Buildings', *J. Inst. Heat. Vent. Eng.*, 38.

Jensen S.O., Ed. (1993), *Validation of Building Energy Simulation Programs*, Part I and II, Research Report PASSYS Subgroup Model Validation and Development, CEC, Brussels, EUR 15115 EN.

Jones P.J. and Waters R.A. (1990), 'Designing the Environment in and Around Buildings', *Construction*, 76 33-36.

Jones P.J. and Whittle G.E. (1992), 'Computational Fluid Dynamics for Building Air Flow Prediction —Current Status and Capabilities', *Building and Environment*, 27 (3) 321-38.

Judkoff R. and Neymark J. (1995), *International Energy Agency Building Energy Simulation Test (BESTEST) and Diagnostic Method*, IEA Energy Conservation in Buildings and Community Systems Programme Annex 21 Subtask C and IEA Solar Heating and Cooling Programme Task 12 Subtask B.

Kelly N.J. (1998), *Towards a Design Environment for Building-Integrated Energy Systems: The Integration of Electrical Power Flow Modelling with Building Simulation*, PhD Thesis, University of Strathclyde, Glasgow UK.

Khalifa A.J.N. (1989), *Heat Transfer Processes in Buildings*, PhD Thesis, University of Wales College of Cardiff, Cardiff UK.

Khalifa A.J.N. and Marshall R.H. (1990), 'Validation of Heat Transfer Coefficients on Interior Building Surfaces Using a Real-Sized Indoor Test Cell', *Int. J. Heat Mass Transfer*, 33 (10) 2219-2236.

Knappmiller K.D. and Kirkpatrick A.T. (1995), 'A Numerical Study Comparing ADPI and Ventilation Effectiveness for Conventional and Cold-Air Distribution Systems', *Proc. Indoor Air Quality '95*, ASHRAE.

Kusuda T. (1976), *NBSLD: The Computer Program for Heating and Cooling Loads in Buildings*, NBS Building Science Series No. 69, National Bureau of Standards, Washington USA.

Lam C.K.G. and Bremhorst K. (1981), 'A Modified Form of the $k-\varepsilon$ Model for Predicting Wall Turbulence', *Transactions of the ASME*, 103 456-460.

Launder B.E. and Spalding D.B. (1974), 'The Numerical Computation of Turbulent Flows', *Computer Methods in Applied Mechanics and Engineering*, 3 269-289.

Lebrun J., ed. (1982), *Proc. Int. Conf. on System Simulation in Buildings*, Commission of the European Communities, Liège, Belgium.

Lemaire A.D., Chen Q., Ewert M., Heikkinen J., Inard C., Moser A., Nielsen P.V., and Whittle G. (1993), *Room Air and Contaminant Flow, Evaluation of Computational Methods*, IEA Energy Conservation in Buildings and Community Systems Programme Annex 20 Subtask 1 Summary Report.

Liddament M. (1991), 'A Review of Building Air Flow Simulation', *AIVC Technical Note 33*, Air Infiltration and Ventilation Centre, U.K.

Lomas K.J., Eppel H., Martin C., and Bloomfield D. (1994a), *Empirical Validation of Thermal Building Simulation Programs Using Test Room Data, Volume 1: Final Report*, IEA Energy Conservation in Buildings and Community Systems Programme Annex 21 and IEA Solar Heating and Cooling Programme Task 12.

Lomas K.J., Martin C., Eppel H., Watson M., and Bloomfield D. (1994b), *Empirical Validation of Thermal Building Simulation Programs Using Test Room Data, Volume 2: Empirical Validation Package*, IEA Energy Conservation in Buildings and Community Systems Programme Annex 21 and IEA Solar Heating and Cooling Programme Task 12.

Lomas K.J., Ed. (1994c), *Empirical Validation of Thermal Building Simulation Programs Using Test Room Data, Volume 3: Working Reports*, IEA Energy Conservation in Buildings and Community Systems Programme Annex 21 and IEA Solar Heating and Cooling Programme Task 12.

Lomas K.J. (1996), 'The U.K. Applicability Study: An Evaluation of Thermal Simulation Programs for Passive Solar House Design', *Building and Environment*, 31 (3) 197-206.

Loomans M. (1995), 'Comments on and Simulations with the Domain Flow Solver', *FAGO Report 95.45.W*, Eindhoven University of Technology, The Netherlands.

Loomans M.G.L.C (1998), 'Measurements at and Simulations of the (Improved) Desk Displacement Ventilation Concept', *Proc. ROOMVENT '98*, (1) 241-248, Stockholm Sweden.

MacQueen J. (1997), *The Modelling and Simulation of Energy Management Control Systems*, PhD Thesis, University of Strathclyde, Glasgow UK.

Maver T.W. and Clarke J.A. (1984), *Major Extensions to the ESP System*, Final Report for Science and Engineering Research Council Grant GR/C/2283.7, University of Strathclyde, Glasgow UK.

McLean D.J. (1982), *The Simulation of Solar Energy Systems*, PhD Thesis, University of Strathclyde, Glasgow U.K.

Min T.C., Schutrum L.F., Parmelee G.V., and Vouris J.D. (1956), 'Natural Convection and Radiation in a Panel-Heated Room', *ASHAE Transactions*, 62 337-358.

Moser A., Schalin A., Off F., Yuan X. (1995), 'Numerical Modelling of Heat Transfer by Radiation and Convection in an Atrium with Thermal Inertia', *ASHRAE Transactions*, SD-95-14-4.

Murakami S., Kato S., and Suyama Y. (1989), 'Numerical Study on Diffusion Field as Affected by Arrangement of Supply and Exhaust Openings in Conventional Flow Type Clean Room', *ASHRAE Transactions*, 95 (2) 113-127.

Murakami S., Kato S., Zeng J. (1998), 'Numerical Simulation of Contaminant Distribution Around a Modeled Human Body: CFD Study on Computational Thermal Manikin—Part II', *ASHRAE Transactions*, 104 (2) 226-233.

Nakamura Y., Mizuno M., Sekimoto Y., Akagi K., Kunimatu Y., Otaka K., and Kohyama M. (1996), 'Study of Thermal Comfort and Energy Conservation of Task-Ambient Air Conditioning System', *Proc. ROOMVENT '96*, (1), Yokohama Japan.

Nakhi A.E. (1995), *Adaptive Construction Modelling within Whole Building Dynamic Simulation*, PhD Thesis, University of Strathclyde, Glasgow UK.

NRC (1997), *Model National Energy Code of Canada for Buildings*, National Research Council of Canda, Ottawa.

NRCan (1999), *Commercial Building Incentive Program for Energy-Efficient New Construction: Technical Guide for Office Buildings*, M92-157-4-1999E, Natural Resources Canada, Ottawa.

Neitzke K.-P. (1998), 'The Behaviour of the Flow in Rooms Near Walls—Measurements and Computations', *Proc. ROOMVENT '98*, (2) 293-298, Stockholm Sweden.

Negrão C.O.R. (1995), *Conflation of Computational Fluid Dynamics and Building Thermal Simulation*, PhD Thesis, University of Strathclyde, Glasgow UK.

Nielsen P.V. (1974), *Flow in Air Conditioned Rooms*, PhD Thesis, Technical University of Denmark, Copenhagen Denmark.

Nielsen P.V. (1989), 'Airflow Simulation Techniques —Progress and Trends', *Proc. 10th AIVC Conf.*, (1) 203-223.

Nielsen P.V. (1990), 'Specification of a Two-Dimensional Test Case', *IEA Annex 20 Research Item 1.45 Technical Report*, University of Aalborg, Aalborg Denmark.

Nielsen P.V. (1998), 'The Selection of Turbulence Models for Prediction of Room Airflow', *ASHRAE Transactions*, SF-98-10-1.

Nielsen J.R., Nielsen P.V., and Svidt K. (1998), 'The Influence of Furniture on Air Velocity in a Room—an Isothermal Case', *Proc. ROOMVENT '98*, (2) 281-286, Stockholm Sweden.

Nielsen P.V. and Tryggvason T. (1998), 'Computational Fluid Dynamics and Building Energy Performance Simulation', *Proc. ROOMVENT '98*, (1) 101-107, Stockholm Sweden.

Niu J. and van der Kooi J. (1992), 'Grid-Optimization for $k-\varepsilon$ Turbulence Model Simulation of Natural Convection in Rooms', *Proc. ROOMVENT '92*, (1) 207-223, Aalborg Denmark.

Olson D.A., Glicksman L.R., and Ferm H.M. (1990), 'Steady-State Natural Convection in Empty and Partitioned Enclosures at High Rayleigh Numbers', J. Heat Transfer, (112) 640-647.

Papamichael K. (1999), 'Application of Information Technologies in Building Design Decisions', *Building Research & Information*, 27 (1) 20-34.

Park C., Clark D.R., and Kelly G.E. (1985), 'An Overview of HVACSIM+, a Dynamic Building/HVAC Control Systems Simulation Program', *Proc. 1st Building Energy Simulation Conference*, Int. Building Performance Simulation Association, Seattle USA.

Patankar S.V. (1980), *Numerical Heat Transfer and Fluid Flow*, McGraw-Hill.

Raithby G.D. and Hollands K.G.T. (1985), Natural Convection, Chapter 6, in *Handbook of Heat Transfer Fundamentals*, Rohsenow W.M., Harntett J.P., and Ganić E.N., Editors, McGraw-Hill.

Rodi W. (1980), *Turbulence Models and their Applications in Hydraulics—A State of the Art Review*, International Association for Hydraulic Research, Delft The Netherlands.

Sander D.M. (1974), *FORTRAN IV Program to Calculate Air Infiltration in Buildings, DBR Computer Program No. 37*, National Research Council Canada, Ottawa.

Schild P. (1997), *Accurate Prediction of Indoor Climate in Glazed Enclosures*, PhD Thesis, Norwegian University of Science and Technology, Trondheim Norway.

Schlichting H. (1968), *Boundary Layer Theory*, 6th Edition, McGraw-Hill.

Spalding D.B. (1994), *PHOENICS Reference*, CHAM Limited, London UK.

Spitler J.D., Pedersen C.O., and Fisher D.E. (1991), 'Interior Convective Heat Transfer in Buildings with Large Ventilative Flow Rates', *ASHRAE Transactions*, 97 505-515.

Spitler J.D. (1996), *Annotated Guide to Load Calculation Models and Algorithms*, ASHRAE.

Srebric J., Chen Q., and Glicksman L.R. (1999), 'Validation of a Zero-Equation Turbulence Model for Complex Indoor Airflow Simulation', *ASHRAE Transactions*, 105 (2).

Sherman M.H. and Grimsrud D.T. (1980), 'Infiltration-Pressurization Correlation: Simplified Physical Model', *ASHRAE Transactions*, 86 (2) 778-807.

Stankov P., Denev J., and Stamov S. (1999), 'Velocity and Temperature Prediction in an Office Room with Furniture', *Proc. Indoor Air '99*, (1) 702-708, Edinburgh UK.

Stephenson D.G. and Mitalas G.P. (1967), 'Cooling Load Calculations by Thermal Response Factor Method', *ASHRAE Transactions* 73 (1) 508-515.

Takemasa Y., Kurabuchi T., and Kamata M. (1992), 'Numerical Simulations of Indoor Air Temperature and Wall Heat Flow Distribution of a Heated and Cooled Room', *Proc. Int Symp. on Room Air Convection and Ventilation Effectiveness*, 99-107, Tokyo Japan.

Tang D. (1985), *Modelling of Heating and Air-Conditioning Systems*, PhD Thesis, University of Strathclyde, Glasgow U.K.

Tennekes H. and Lumley J.L. (1972), *A First Course in Turbulence*, MIT Press, London UK.

Tsuji T. and Nagano Y. (1988), 'Characteristics of a Turbulent Natural Convection Boundary Layer Along a Vertical Flat Plate', *Int. J. Heat Mass Transfer*, (31) 1723-1734.

Versteeg H.K. and Malalasekera W. (1995), *An Introduction to Computational Fluid Dynamics: The Finite Volume Method*, Longman Group.

Wallentén P. (1998), *Heat Flows in a Full Scale Room Exposed to Natural Climate*, Report TABK-98/3051, Lund University, Lund Sweden.

Wallentén P. (1999), 'Heat Transfer Coefficients in a Full Scale Room with and without Furniture', *Proc. Building Simulation '99*, (1) 305-312, Int. Building Performance Simulation Association, Kyoto Japan.

Walton G.N. (1983), *Thermal Analysis Research Program Reference Manual*, NBSIR 83-2655, National Bureau of Standards, Washington USA.

Waters J.R. (1980), 'The Experimental Verification of a Computerised Thermal Model for Buildings', *Building Services Engineering Research & Technology*, (1) 76-82.

White F.M. (1979), *Fluid Mechanics*, McGraw-Hill, New York USA.

Whittle G.E. (1986), 'Computation of Air Movement and Convective Heat Transfer Within Buildings', *Int. J. Ambient Energy*, 7 (3) 151-164.

Xu W. and Chen Q. (1998). 'Numerical Simulation of Air flow in a Room with Differentially Heated Vertical Walls', *ASHRAE Transactions*, 104 (1) 168-175.

Xu W., Chen Q., and Nieuwstadt F.T.M. (1998), 'A New One-Equation Turbulence Model for Near-wall Natural Convection', *Int. J. Heat Mass Transfer*, 41 3161-3176.

Xu W. (1998), *New Turbulence Models for Indoor Airflow Simulation*, PhD Thesis, Massachusetts Institute of Technology, USA.

Yuan X., Moser A. and Suter P. (1993), 'Wall Functions for Numerical Simulation of Turbulent Natural Convection Along Vertical Plates', *Int. J. Heat Mass Transfer*, 36 (18) 4477-4485.

Yuan X., Moser A. and Suter P. (1994), 'Wall Functions for Numerical Simulation of Turbulent Natural Convection', *Proc. 10th International Heat Transfer Conf.*, Brighton UK, 191-196.

Yuan X. (1995), *Wall Functions for Numerical Simulation of Natural Convection along Vertical Surfaces*, PhD Thesis, Swiss Federal Institute of Technology, Zurich Switzerland.

APPENDIX A

Zone Matrix Solution Procedure

The technique ESP-r uses to solve the matrix of zone heat balance equations is described in this appendix. Formation of the equations was treated in Chapter 2 (see pages 12 to 28).

The technique for processing the zone matrices is demonstrated by focusing on the foyer of Figure 2.8 (see page 26). The matrix of heat balance equations for this zone was given in Figure 2.10 and is repeated here,

$$\begin{bmatrix}
a_{1.1} & a_{1.2} & & & & & & & & & & & & & & & & & & \\
a_{2.1} & a_{2.2} & a_{2.3} & & & & & & & & & & & & & & & & & a_{2.20} \\
 & a_{3.2} & a_{3.3} & & & a_{3.6} & & & a_{3.9} & & & a_{3.12} & & & a_{3.15} & & & a_{3.18} & a_{3.19} & \\
 & & & a_{4.4} & a_{4.5} & & & & & & & & & & & & & & & \\
 & & & a_{5.4} & a_{5.5} & a_{5.6} & & & & & & & & & & & & & & \\
 & & a_{6.3} & & a_{6.5} & a_{6.6} & & & a_{6.9} & & & a_{6.12} & & & a_{6.15} & & & a_{6.18} & a_{6.19} & \\
 & & & & & & a_{7.7} & a_{7.8} & & & & & & & & & & & & \\
 & & & & & & a_{8.7} & a_{8.8} & a_{8.9} & & & & & & & & & & & \\
 & & a_{9.3} & & & a_{9.6} & & a_{9.8} & a_{9.9} & & & a_{9.12} & & & a_{9.15} & & & a_{9.18} & a_{9.19} & \\
 & & & & & & & & & a_{10.10} & a_{10.11} & & & & & & & & & \\
 & & & & & & & & & a_{11.10} & a_{11.11} & a_{11.12} & & & & & & & & \\
 & & a_{12.3} & & & a_{12.6} & & & a_{12.6} & & a_{12.11} & a_{12.12} & & & a_{12.15} & & & a_{12.18} & a_{12.19} & \\
 & & & & & & & & & & & & a_{13.13} & a_{13.14} & & & & & & \\
 & & & & & & & & & & & & a_{14.13} & a_{14.14} & a_{14.15} & & & & & \\
 & & a_{15.3} & & & a_{15.6} & & & a_{15.9} & & & a_{15.12} & & a_{15.14} & a_{15.15} & & & a_{15.18} & a_{15.19} & \\
 & & & & & & & & & & & & & & & a_{16.16} & a_{16.17} & & & \\
 & & & & & & & & & & & & & & & a_{17.16} & a_{17.17} & a_{17.18} & & \\
 & & a_{18.3} & & & a_{18.6} & & & a_{18.9} & & & a_{18.12} & & & a_{18.15} & & a_{18.17} & a_{18.18} & a_{18.19} & \\
 & & a_{19.3} & & & a_{19.6} & & & a_{19.9} & & & a_{19.12} & & & a_{19.15} & & & a_{19.18} & a_{19.19} &
\end{bmatrix}
\times
\begin{bmatrix}
T_{A.1} \\ T_{A.2} \\ T_{A.s} \\ T_{B.1} \\ T_{B.2} \\ T_{B.s} \\ T_{C.1} \\ T_{C.2} \\ T_{C.s} \\ T_{D.1} \\ T_{D.2} \\ T_{D.s} \\ T_{E.1} \\ T_{E.2} \\ T_{E.s} \\ T_{F.1} \\ T_{F.2} \\ T_{F.s} \\ T_a \\ q_{plant}
\end{bmatrix}
=
\begin{bmatrix}
z_1 \\ z_2 \\ z_3 \\ z_4 \\ z_5 \\ z_6 \\ z_7 \\ z_8 \\ z_9 \\ z_{10} \\ z_{11} \\ z_{12} \\ z_{13} \\ z_{14} \\ z_{15} \\ z_{16} \\ z_{17} \\ z_{18} \\ z_{19}
\end{bmatrix}$$

Figure A.1: Zone matrix of heat balance equations

The first step in solving the zone matrix is sub-partitioning. A sub-matrix is formed for each construction by extracting (from the zone matrix) the heat balance for the construction's external-surface node and the heat balances for its intra-constructional nodes (the constructions in this example have only one intra-constructional node, but in general there are many). These construction sub-matrices are known as the $\mathbf{S}_i$ matrices, where i identifies the construction. The six $\mathbf{S}_i$ matrices in this example are shown in Figure A.2.

The remaining equations from the zone matrix—the heat balances for the internal-surface nodes and for the air-point node—are gathered into another sub-matrix, known as the **R** matrix (shown in Figure A.3).

The heat balances for the internal-surface nodes are contained in the **R** matrix, but the internal-surface nodal temperatures also appear in the $\mathbf{S}_i$ matrices. Similarly, the balances on the next-to-

$$\begin{bmatrix} a_{1,1} & a_{1,2} & & \\ a_{2,1} & a_{2,2} & a_{2,3} & a_{2,20} \end{bmatrix} \times \begin{bmatrix} T_{A,1} \\ T_{A,2} \\ T_{A,s} \\ q_{plant} \end{bmatrix} = \begin{bmatrix} z_1 \\ z_2 \end{bmatrix} \qquad \begin{bmatrix} a_{4,4} & a_{4,5} & \\ a_{5,4} & a_{5,5} & a_{5,6} \end{bmatrix} \times \begin{bmatrix} T_{B,1} \\ T_{B,2} \\ T_{B,s} \end{bmatrix} = \begin{bmatrix} z_4 \\ z_5 \end{bmatrix}$$

$$\begin{bmatrix} a_{7,7} & a_{7,8} & \\ a_{8,7} & a_{8,8} & a_{8,9} \end{bmatrix} \times \begin{bmatrix} T_{C,1} \\ T_{C,2} \\ T_{C,s} \end{bmatrix} = \begin{bmatrix} z_7 \\ z_8 \end{bmatrix} \qquad \begin{bmatrix} a_{10,10} & a_{10,11} & \\ a_{11,10} & a_{11,11} & a_{11,12} \end{bmatrix} \times \begin{bmatrix} T_{D,1} \\ T_{D,2} \\ T_{D,s} \end{bmatrix} = \begin{bmatrix} z_{10} \\ z_{11} \end{bmatrix}$$

$$\begin{bmatrix} a_{13,13} & a_{13,14} & \\ a_{14,13} & a_{14,14} & a_{14,15} \end{bmatrix} \times \begin{bmatrix} T_{E,1} \\ T_{E,2} \\ T_{E,s} \end{bmatrix} = \begin{bmatrix} z_{13} \\ z_{14} \end{bmatrix} \qquad \begin{bmatrix} a_{16,16} & a_{16,17} & \\ a_{17,16} & a_{17,17} & a_{17,18} \end{bmatrix} \times \begin{bmatrix} T_{F,1} \\ T_{F,2} \\ T_{F,s} \end{bmatrix} = \begin{bmatrix} z_{16} \\ z_{17} \end{bmatrix}$$

Figure A.2: S_A, S_B, S_C, S_D, S_E, and S_F matrices

$$\begin{bmatrix} a_{3,2} & a_{3,3} & & a_{3,6} & & a_{3,9} & & a_{3,12} & & a_{3,15} & & a_{3,18} & a_{3,19} \\ & a_{6,3} & a_{6,5} & a_{6,6} & & a_{6,9} & & a_{6,12} & & a_{6,15} & & a_{6,18} & a_{6,19} \\ & a_{9,3} & & a_{9,6} & a_{9,8} & a_{9,9} & & a_{9,12} & & a_{9,15} & & a_{9,18} & a_{9,19} \\ & a_{12,3} & & a_{12,6} & & a_{12,6} & a_{12,11} & a_{12,12} & & a_{12,15} & & a_{12,18} & a_{12,19} \\ & a_{15,3} & & a_{15,6} & & a_{15,9} & & a_{15,12} & a_{15,14} & a_{15,15} & & a_{15,18} & a_{15,19} \\ & a_{18,3} & & a_{18,6} & & a_{18,9} & & a_{18,12} & & a_{18,15} & a_{18,17} & a_{18,18} & a_{18,19} \\ & a_{19,3} & & a_{19,6} & & a_{19,9} & & a_{19,12} & & a_{19,15} & & a_{19,18} & a_{19,19} \end{bmatrix} \times \begin{bmatrix} T_{A,2} \\ T_{A,s} \\ T_{B,2} \\ T_{B,s} \\ T_{C,2} \\ T_{C,s} \\ T_{D,2} \\ T_{D,s} \\ T_{E,2} \\ T_{E,s} \\ T_{F,2} \\ T_{F,s} \\ T_a \end{bmatrix} = \begin{bmatrix} z_3 \\ z_6 \\ z_9 \\ z_{12} \\ z_{15} \\ z_{18} \\ z_{19} \end{bmatrix}$$

Figure A.3: R matrix

surface nodes are contained in the $\mathbf{S}_i$ matrices, and the next-to-surface nodal temperatures appear again in **R**. This duality binds the **R** and $\mathbf{S}_i$ matrices. The linkages are maintained through the $a_{2,3}$, $a_{5,6}$, $a_{8,9}$, $a_{11,12}$, $a_{14,15}$, and $a_{17,18}$ coefficients in the $\mathbf{S}_i$ matrices which operate on the internal-surface temperatures; and through the $a_{3,2}$, $a_{6,5}$, $a_{9,8}$, $a_{12,11}$, $a_{15,14}$, and $a_{18,17}$ coefficients in **R** which operate on the next-to-surface nodal temperatures.

A six stage process is used to solve the partitioned matrices. First, a forward-reduction process employing Gausian elimination is applied to each construction sub-matrix. Each row of each sub-matrix is processed in turn to eliminate the coefficients below the main diagonal[23]. The resulting reduced construction sub-matrices, known as $\mathbf{S}'_i$ are shown in Figure A.4. Coefficients which are modified by the reduction process are shown with prime symbols[24].

$$\begin{bmatrix} a_{1,1} & a_{1,2} & & \\ & a'_{2,2} & a_{2,3} & a_{2,20} \end{bmatrix} \times \begin{bmatrix} T_{A,1} \\ T_{A,2} \\ T_{A,s} \\ q_{plant} \end{bmatrix} = \begin{bmatrix} z_1 \\ z'_2 \end{bmatrix} \qquad \begin{bmatrix} a_{4,4} & a_{4,5} & \\ & a'_{5,5} & a_{5,6} \end{bmatrix} \times \begin{bmatrix} T_{B,1} \\ T_{B,2} \\ T_{B,s} \end{bmatrix} = \begin{bmatrix} z_4 \\ z'_5 \end{bmatrix}$$

$$\begin{bmatrix} a_{7,7} & a_{7,8} & \\ & a'_{8,8} & a_{8,9} \end{bmatrix} \times \begin{bmatrix} T_{C,1} \\ T_{C,2} \\ T_{C,s} \end{bmatrix} = \begin{bmatrix} z_7 \\ z'_8 \end{bmatrix} \qquad \begin{bmatrix} a_{10,10} & a_{10,11} & \\ & a'_{11,11} & a_{11,12} \end{bmatrix} \times \begin{bmatrix} T_{D,1} \\ T_{D,2} \\ T_{D,s} \end{bmatrix} = \begin{bmatrix} z_{10} \\ z'_{11} \end{bmatrix}$$

$$\begin{bmatrix} a_{13,13} & a_{13,14} & \\ & a'_{14,14} & a_{14,15} \end{bmatrix} \times \begin{bmatrix} T_{E,1} \\ T_{E,2} \\ T_{E,s} \end{bmatrix} = \begin{bmatrix} z_{13} \\ z'_{14} \end{bmatrix} \qquad \begin{bmatrix} a_{16,16} & a_{16,17} & \\ & a'_{17,17} & a_{17,18} \end{bmatrix} \times \begin{bmatrix} T_{F,1} \\ T_{F,2} \\ T_{F,s} \end{bmatrix} = \begin{bmatrix} z_{16} \\ z'_{17} \end{bmatrix}$$

Figure A.4: $\mathbf{S}'_\mathbf{A}$, $\mathbf{S}'_\mathbf{B}$, $\mathbf{S}'_\mathbf{C}$, $\mathbf{S}'_\mathbf{D}$, $\mathbf{S}'_\mathbf{E}$, and $\mathbf{S}'_\mathbf{F}$ matrices

For each construction that does not contain plant interaction, the reduction process results in an equation (known as the characteristic equation, or *CE*) that operates only on the internal-surface node and the next-to-surface node (e.g. $a'_{5,5}T_{B,2} + a_{5,6}T_{B,s} = z'_5$ in $\mathbf{S}'_\mathbf{B}$). The CE in $\mathbf{S}'_\mathbf{A}$ also includes the plant interaction term.

In the second step, the $\mathbf{S}'_i$ CEs are used to eliminate the next-to-surface nodal temperatures from the **R** matrix. This is accomplished by adding each CE (multiplied by an appropriate constant) to the **R** matrix row equation that operates on the same construction. For example, $T_{B,2}$ is eliminated from **R** by multiplying the $\mathbf{S}'_\mathbf{B}$ CE by $\frac{-a_{6,5}}{a'_{5,5}}$ and adding this to the second row of **R**. This results in $\mathbf{R}'$ (shown in Figure A.5), a matrix with the same number of equations as **R**, but fewer unknowns. The plant interaction term is introduced into $\mathbf{R}'$ by inclusion of the $\mathbf{S}'_\mathbf{A}$ CE. $a^*_{2,20}$ operates on the plant interaction term at node $A, 2$ and has the value $\frac{-a_{3,2}}{a'_{2,2}}\, a_{2,20}$.

$\mathbf{R}'$ is then forward-reduced using Gausian elimination[25] in the third step. This results in the $\mathbf{R}''$ matrix, shown in Figure A.6. Coefficients from the original zone matrix that have been modified once by reduction are shown with prime symbols, while those that have been modified twice are shown with double primes.

---

[23] The reduction scheme used by ESP-r is a function of the control strategy employed, specifically depending on the locations of the sensed condition and the plant interaction. Other solution schemes are described by Clarke (1985).

[24] For example, $a'_{5,5} = a_{5,5} - \frac{a_{5,4}}{a_{4,4}} a_{4,5}$.

[25] The reduction process shown here is specific to the control strategy used in this example. ESP-r selects the reduction process based on the locations of the control and plant interaction nodes. Clarke (1985) describes the other possibilities.

$$\begin{bmatrix} a_{3,3} & a_{3,6} & a_{3,9} & a_{3,12} & a_{3,15} & a_{3,18} & a_{3,19} & \overset{*}{a}_{2,20} \\ a_{6,3} & a'_{6,6} & a_{6,9} & a_{6,12} & a_{6,15} & a_{6,18} & a_{6,19} & \\ a_{9,3} & a_{9,6} & a'_{9,9} & a_{9,12} & a_{9,15} & a_{9,18} & a_{9,19} & \\ a_{12,3} & a_{12,6} & a_{12,9} & a'_{12,12} & a_{12,15} & a_{12,18} & a_{12,19} & \\ a_{15,3} & a_{15,6} & a_{15,9} & a_{15,12} & a'_{15,15} & a_{15,18} & a_{15,19} & \\ a_{18,3} & a_{18,6} & a_{18,9} & a_{18,12} & a_{18,15} & a'_{18,18} & a_{18,19} & \\ a_{19,3} & a_{19,6} & a_{19,9} & a_{19,12} & a_{19,15} & a_{19,18} & a_{19,19} & \end{bmatrix} \times \begin{bmatrix} T_{A,s} \\ T_{B,s} \\ T_{C,s} \\ T_{D,s} \\ T_{E,s} \\ T_{F,s} \\ T_a \\ q_{plant} \end{bmatrix} = \begin{bmatrix} z_3 \\ z'_6 \\ z'_9 \\ z'_{12} \\ z'_{15} \\ z'_{18} \\ z_{19} \end{bmatrix}$$

Figure A.5: R′ matrix

$$\begin{bmatrix} & & & & & & a'_{3,19} & \overset{*}{a}_{2,20} \\ a_{6,3} & a'_{6,6} & a_{6,9} & a_{6,12} & a_{6,15} & a_{6,18} & a_{6,19} & \\ & a'_{9,6} & a''_{9,9} & a'_{9,12} & a'_{9,15} & a'_{9,18} & a'_{9,19} & \\ & & a'_{12,9} & a''_{12,12} & a'_{12,15} & a'_{12,18} & a'_{12,19} & \\ & & & a'_{15,12} & a''_{15,15} & a'_{15,18} & a'_{15,19} & \\ & & & & a'_{18,15} & a''_{18,18} & a'_{18,19} & \\ & & & & & a'_{19,18} & a'_{19,19} & \end{bmatrix} \times \begin{bmatrix} T_{A,s} \\ T_{B,s} \\ T_{C,s} \\ T_{D,s} \\ T_{E,s} \\ T_{F,s} \\ T_a \\ q_{plant} \end{bmatrix} = \begin{bmatrix} z'_3 \\ z'_6 \\ z''_9 \\ z''_{12} \\ z''_{15} \\ z''_{18} \\ z'_{19} \end{bmatrix}$$

Figure A.6: R″ matrix

A CE that relates the plant injection required to maintain the air-point at the setpoint temperature emerges from the reduction process: $a'_{3,19} \cdot T_a + \overset{*}{a}_{2,20} \cdot q_{plant} = z'_3$. As the control strategy constrains T_a to the setpoint temperature, the fourth step is to solve this equation to yield q_{plant}, the required heat injection to the underfloor heating system[26].

The fifth step is a straightforward back-substitution process on $\mathbf{R}''$. The last row is solved for $T_{F,s}$ using the newly established T_a. Back-substitution continues until all remaining internal-surface temperatures are solved. In the sixth and final step, the newly calculated internal-surface temperatures are substituted into the $\mathbf{S}'_i$ matrices and another back substitution process performed to yield the intra-constructional and external-surface temperatures. This completes the thermal simulation for the current time-step.

---

[26] If there should be insufficient plant capacity to maintain the setpoint temperature, q_{plant} is constrained and the resulting T_a calculated using the CE.

Zone Matrix Solution Procedure for Integrated Conflation

This appendix describes the technique ESP-r uses to solve the matrix of zone heat balance equations when CFD is integrated into the thermal domain's solver (see *method 2* handshaking on page 33 and Figure 5.13, page 136). As described in Section 2.4, in this approach CFD interacts directly with the thermal matrix solution procedure in order to drop (to a degree) the well-stirred assumption.

Formation of the zone matrix was treated in Chapter 2 (see pages 33 to 34). The matrix of equations to be solved is given in Figure 2.13 and is repeated here,

$$\begin{bmatrix}
a_{1.1}&a_{1.2}\\
a_{2.1}&a_{2.2}&a_{2.3}&&&&&&&&&&&&&&&&&a_{2.20}\\
&a_{3.2}&a_{3.3}&&&a_{3.6}&&&a_{3.9}&&&a_{3.12}&&&a_{3.15}&&&a_{3.18}\\
&&&a_{4.4}&a_{4.5}\\
&&&a_{5.4}&a_{5.5}&a_{5.6}\\
&&a_{6.3}&&a_{6.5}&a_{6.6}&&&a_{6.9}&&&a_{6.12}&&&a_{6.15}&&&a_{6.18}\\
&&&&&&a_{7.7}&a_{7.8}\\
&&&&&&a_{8.7}&a_{8.8}&a_{8.9}\\
&&a_{9.3}&&&a_{9.6}&&a_{9.8}&a_{9.9}&&&a_{9.12}&&&a_{9.15}&&&a_{9.18}\\
&&&&&&&&&a_{10.10}&a_{10.11}\\
&&&&&&&&&a_{11.10}&a_{11.11}&a_{11.12}\\
&&a_{12.3}&&&a_{12.6}&&&a_{12.6}&&a_{12.11}&a_{12.12}&&&a_{12.15}&&&a_{12.18}\\
&&&&&&&&&&&&a_{13.13}&a_{13.14}\\
&&&&&&&&&&&&a_{14.13}&a_{14.14}&a_{14.15}\\
&&a_{15.3}&&&a_{15.6}&&&a_{15.9}&&&a_{15.12}&&a_{15.14}&a_{15.15}&&&a_{15.18}\\
&&&&&&&&&&&&&&&a_{16.16}&a_{16.17}\\
&&&&&&&&&&&&&&&a_{17.16}&a_{17.17}&a_{17.18}\\
&&a_{18.3}&&&a_{18.6}&&&a_{18.9}&&&a_{18.12}&&&a_{18.15}&&a_{18.17}&a_{18.18}\\
&&&&&&&&&&&&&&&&&&a_{19.19}
\end{bmatrix}
\times
\begin{bmatrix}
T_{A.1}\\ T_{A.2}\\ T_{A.s}\\ T_{B.1}\\ T_{B.2}\\ T_{B.s}\\ T_{C.1}\\ T_{C.2}\\ T_{C.s}\\ T_{D.1}\\ T_{D.2}\\ T_{D.s}\\ T_{E.1}\\ T_{E.2}\\ T_{E.s}\\ T_{F.1}\\ T_{F.2}\\ T_{F.s}\\ T_a\\ q_{plant}
\end{bmatrix}
=
\begin{bmatrix}
z_1\\ z_2\\ z_3\\ z_4\\ z_5\\ z_6\\ z_7\\ z_8\\ z_9\\ z_{10}\\ z_{11}\\ z_{12}\\ z_{13}\\ z_{14}\\ z_{15}\\ z_{16}\\ z_{17}\\ z_{18}\\ z_{19}
\end{bmatrix}$$

Figure B.1: Revised zone matrix of heat balance equations

The zone matrix is processed as described in Appendix A, up to the point of solving the $\mathbf{R}''$ matrix: the zone matrix is partitioned into $\mathbf{S}_i$ and $\mathbf{R}$; the $\mathbf{S}_i$ matrices are reduced to $\mathbf{S}_i'$; $\mathbf{R}'$ is created by absorbing the $\mathbf{S}_i'$ CE's; and $\mathbf{R}'$ reduced to $\mathbf{R}''$.

The CE from $\mathbf{R}''$ is solved as before to get q_{plant}. This leaves the following set of equations,

$$\begin{bmatrix} a_{3,3} & a_{3,6} & a_{3,9} & a_{3,12} & a_{3,15} & a_{3,18} \\ & a''_{6,6} & a'_{6,9} & a'_{6,12} & a'_{6,15} & a'_{6,18} \\ & & a''_{9,9} & a'_{9,12} & a'_{9,15} & a'_{9,18} \\ & & & a''_{12,12} & a'_{12,15} & a'_{12,18} \\ & & & & a''_{15,15} & a'_{15,18} \\ & & & & & a''_{18,18} \end{bmatrix} \times \begin{bmatrix} T_{A,s} \\ T_{B,s} \\ T_{C,s} \\ T_{D,s} \\ T_{E,s} \\ T_{F,s} \end{bmatrix} = \begin{bmatrix} z'_3 \\ z'_6 \\ z''_9 \\ z''_{12} \\ z''_{15} \\ z''_{18} \end{bmatrix}$$

Figure B.2: R″ matrix when CFD integrated with thermal domain

At this point the CFD model is invoked. Boundary conditions are established by the thermal domain using surface temperatures calculated from Figure B.2 using $q_{air \to surface}^{CFD-wall\ functions}$ and $\sum q_{S \to air}^{CFD-wall\ functions}$ calculated the previous time-step. As the CFD iterative solver converges towards a solution, Figure B.2 is periodically solved using the current values of $q_{air \to surface}^{CFD-wall\ functions}$ and $\sum q_{S \to air}^{CFD-wall\ functions}$ to update the right side coefficients (z'_3, z'_6, z''_9, z''_{12}, z''_{15}, z''_{18}). In this manner, the thermal domain's calculation of the internal surface temperatures evolves as the CFD solver converges. The updated internal surface temperatures are subsequently passed to the CFD model to reset its boundary conditions.

Once the converged state is reached, the CFD-predicted temperature field is averaged to determine T_a[27]. This is returned to the thermal domain and a final solution of Figure B.2 performed to yield the internal surface temperatures. At this point, the thermal solution is completed as before (see Appendix A): the internal-surface temperatures are substituted into the $\mathbf{S}'_i$ matrices and a back substitution process performed to yield the intra-constructional and external-surface temperatures.

---

[27] Since T_a does not appear in Figure B.2 there is no connection between the solution of q_{plant} and T_a, and the internal surface temperatures. Therefore, the case of an undersized plant cannot be treated with this handshaking method.

APPENDIX C

Comparison of Convection Correlations for Ceiling Jets

This appendix compares the Fisher (1995) and Fisher and Pedersen (1997) correlations for ceiling jets in isothermal rooms. Both correlations, which were regressed from the same experimental data set, are presented in Table 4.5 (page 88). The correlations are similar in structure, but Fisher and Pedersen chose the functional form of theirs to prevent non-sensible h_c values in the event they were applied outside their range of validity (i.e. for $ac/h < 3$).

As Chapter 4 explained, Fisher presented his correlations in non-dimensional form (see equation 4.5, page 86). For the purposes of implementation into ESP-r, these were converted to the dimensional form presented in Table 4.5 by evaluating the thermophysical data at typical room temperatures and by fixing V_{room}. Fisher and Pedersen's equations were implemented into ESP-r unaltered.

Both correlations were implemented into ESP-r as they produce substantially different h_c values in some cases. The correlations are compared in the following three figures. To highlight the differences, the figures span the air flow rates typically found in mechanically ventilated buildings ($3 \le ac/h \le 12$) rather than the correlations's full range of validity ($3 \le ac/h \le 100$). Over this range of air flows, the Fisher and Pedersen correlation gives greater h_c for walls and ceilings, but lower values for floors. The h_c differences are in the order of 17% to 77% for walls, 5% to 28% for floors, and 6% to 18% for ceilings.

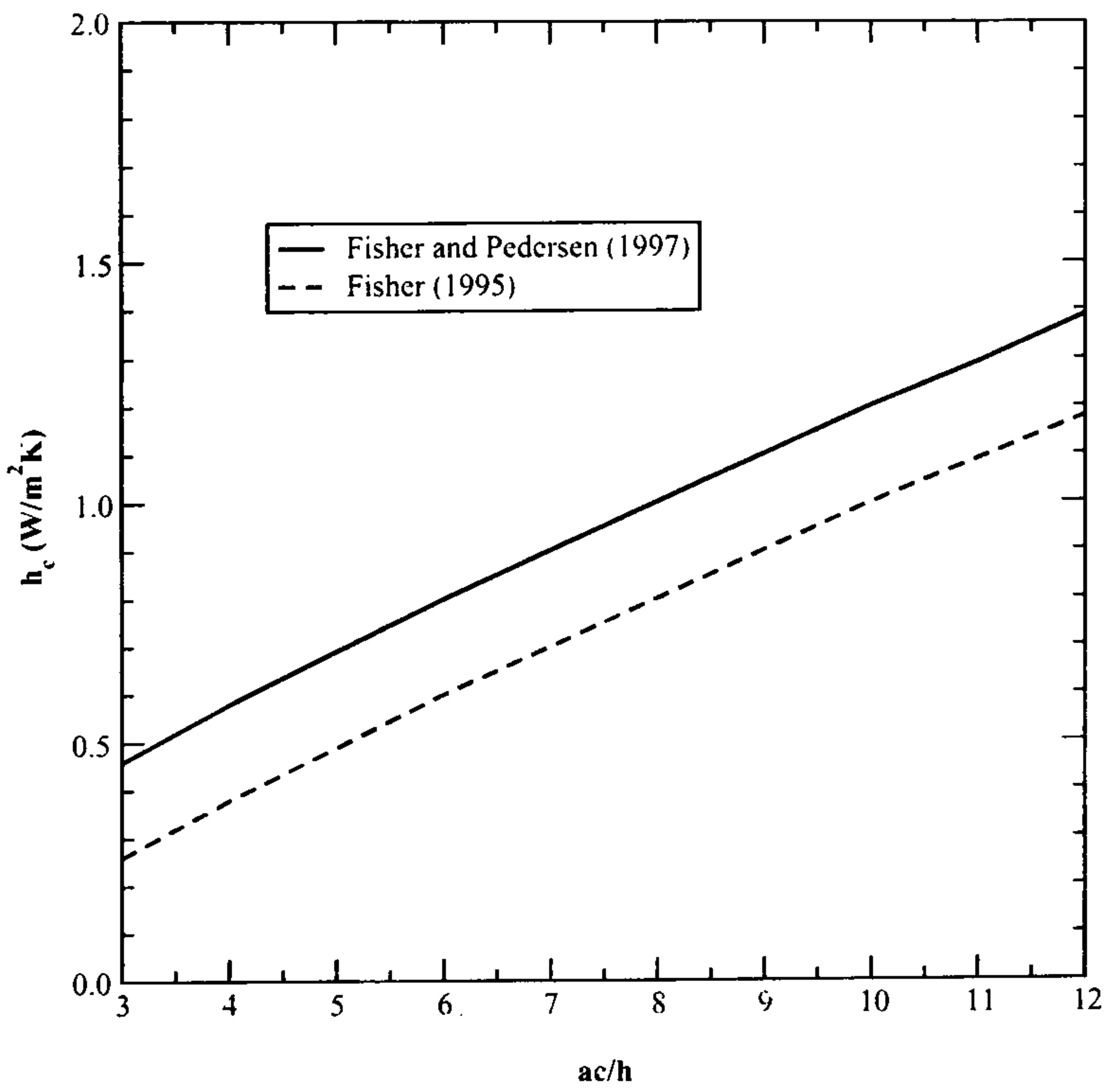

Figure C.1: Comparison of wall correlations

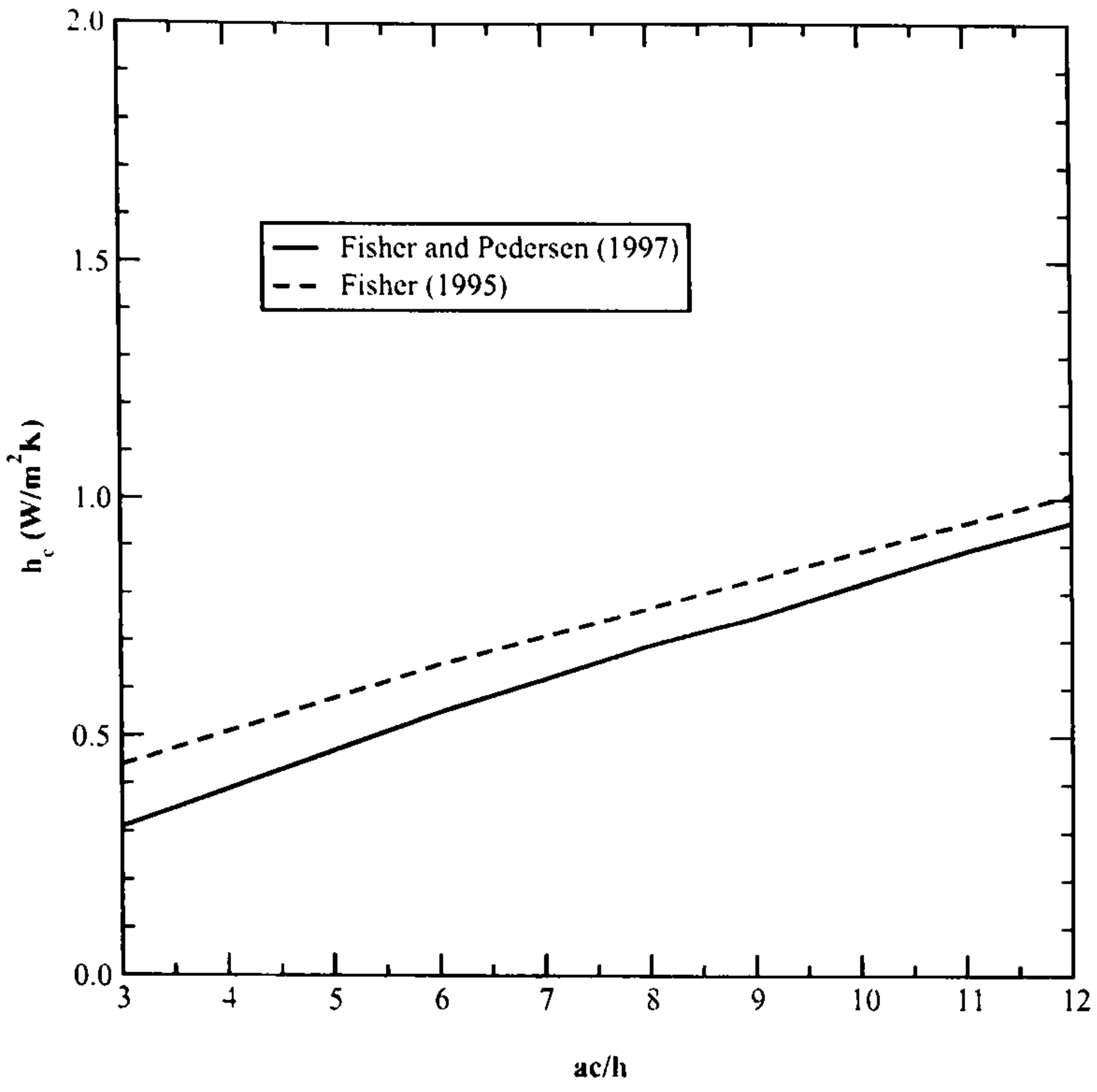

Figure C.2: Comparison of floor correlations

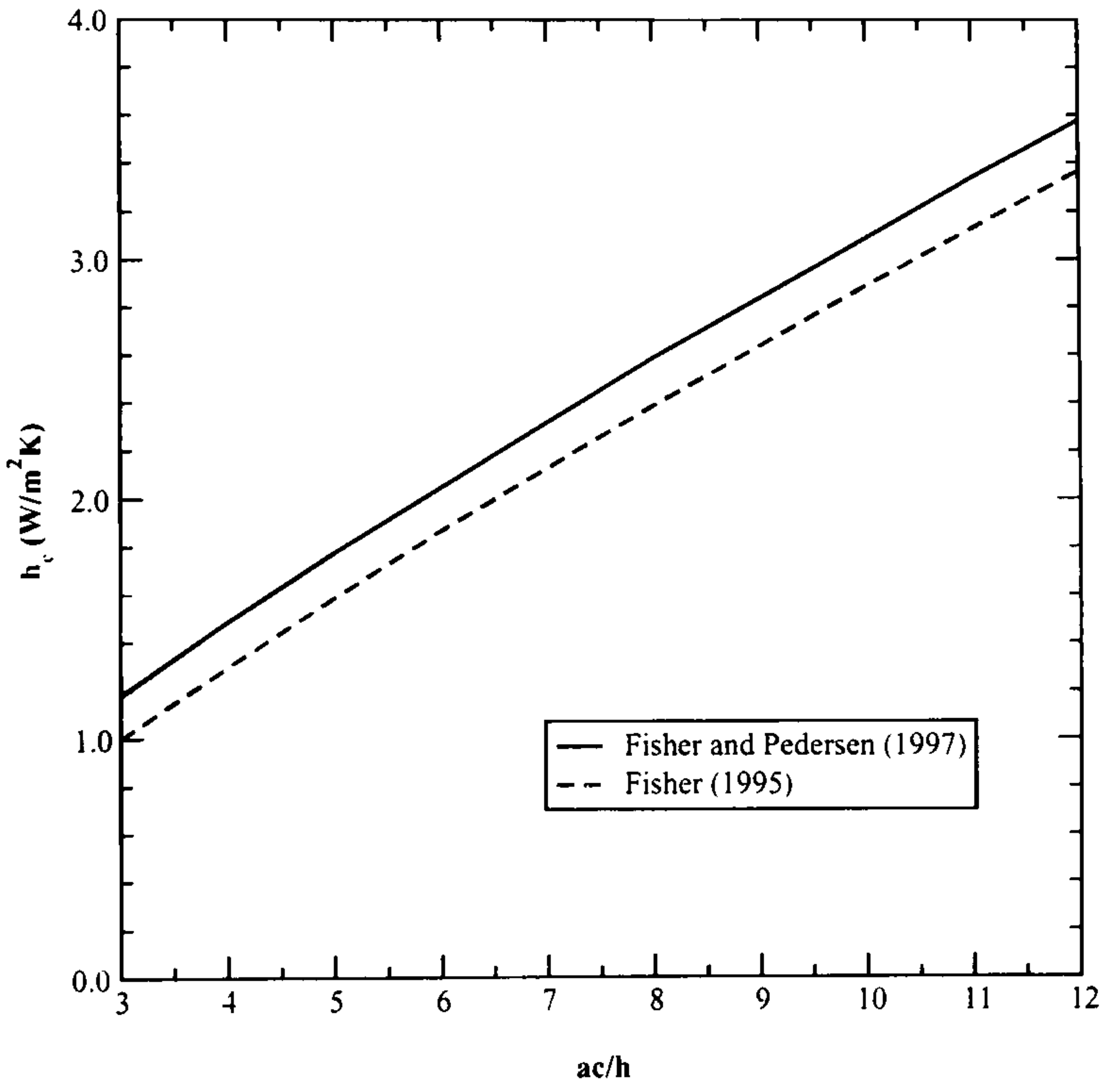

Figure C.3: Comparison of ceiling correlations

APPENDIX D

Modelling Convection Regimes Induced by HVAC Systems

D.1 Introduction

This appendix describes the model developed to simulate the convective regime induced in rooms by HVAC air handling systems. It was developed to support the implementation of the forced flow and mixed flow convection coefficient calculation methods described in sections 4.3.4 and 4.4.

This model treats the HVAC system conceptually in terms of its effect on the room's convection regime. To avoid onerous data input by the user, it does not simulate the detailed performance of, and interactions between, the HVAC system's constituent components (ducts, coils, fans, dampers, sensors, etc.). This approach is complimentary to ESP-r's zone controls wherein the thermal performance of the plant is modelled conceptually in terms of its ability to respond to the demands for energy.

The model predicts (on a time-step basis) the flow rate (ac/h) and temperature ($T_{diffuser}$) supplied by the HVAC system to the room. The calculations are based on the user's description of the HVAC system and the dynamic interaction between the building and the system. ac/h and $T_{diffuser}$ reflect the operational state of the HVAC system and are sufficient for characterizing the forced convection regime within the room. The use of these data for calculating the convection coefficients is detailed in sections 4.3.4 and 4.4.

Models for the two most common forced-air HVAC systems were developed: variable-volume (VAV) and constant-volume variable-temperature (CVVT) systems. There are two variants of the VAV system: one supplies a fixed flow of air in heating mode, while the other varies the flow in heating mode. The operational characteristics of these systems are described in the following sections.

D.2 Variable Air Volume System Model

VAV systems utilize adjustable dampers to alter air flow rates in order to meet varying zone loads. An idealized model of this system was created to model the common operating strategies, as described below.

When the zone requires cooling, the supply air is chilled to a constant temperature while the system adjusts the air flow to meet the cooling load. The minimum and maximum allowable flow rates to the zone are user specified. The constant temperature for the supply air is also user specified. Two alternate control strategies are supported for heating.

Constant-Volume Heating

Many VAV systems operate as constant-volume systems when the zone requires heating. The air flow is at a fixed rate, equal to the minimum damper position of the VAV box and equal to the minimum flowrate for cooling. Reheat coils warm the air upstream of the diffuser, the heat output being proportional to the zone's heating load. The reheat coils have finite capacity, expressed by the user in terms of the maximum allowable air temperature at the diffuser. If the reheat coil cannot satisfy the zone load due to its finite capacity, it is assumed the remaining heat is supplied from another source (e.g. baseboard heaters) which does not affect the flow regime. Figure D.1 illustrates the control of the VAV system with constant-volume heating.

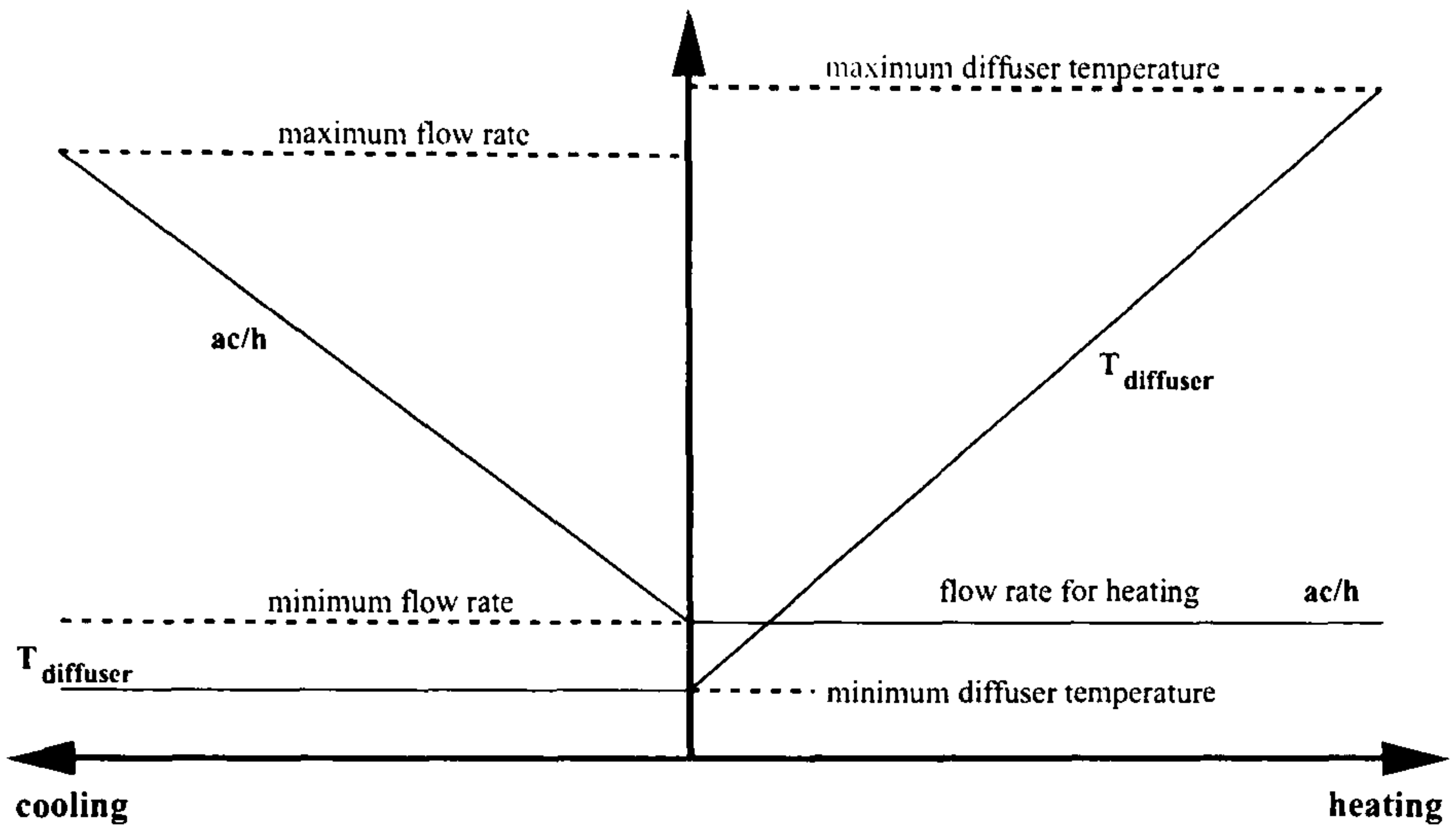

Figure D.1: VAV system with constant-volume heating

Variable-Volume Heating

The dampers and reheat coils work in conjunction to satisfy the zone's heating load. At low heating loads the system delivers air at the minimum flowrate (same minimum as for cooling) and the reheat coil heats the air to meet the load. When the heating load is sufficiently high that the reheat coil cannot meet the load (i.e. the maximum allowable air temperature at the diffuser is reached) the damper opens to increase the flowrate. The maximum allowable flowrate for heating is the same as for cooling. If the heating load cannot be met at full flowrate and at maximum reheat capacity, the remaining heat is supplied from another source (e.g. baseboard heaters) which does not affect the flow regime. Figure D.2 illustrates the control of the VAV system with variable-volume heating.

D.3 Constant-Volume Variable-Temperature System Model

The constant-volume variable-temperature (CVVT) system delivers a constant flow of air, varying the temperature of the supply air in response to zone loads. The supply-air temperature is usually controlled with a heating coil and a cooling coil, although in some cases reheat coils are also employed. The temperature of the air supplied to the zone must lie within limits set by the user.

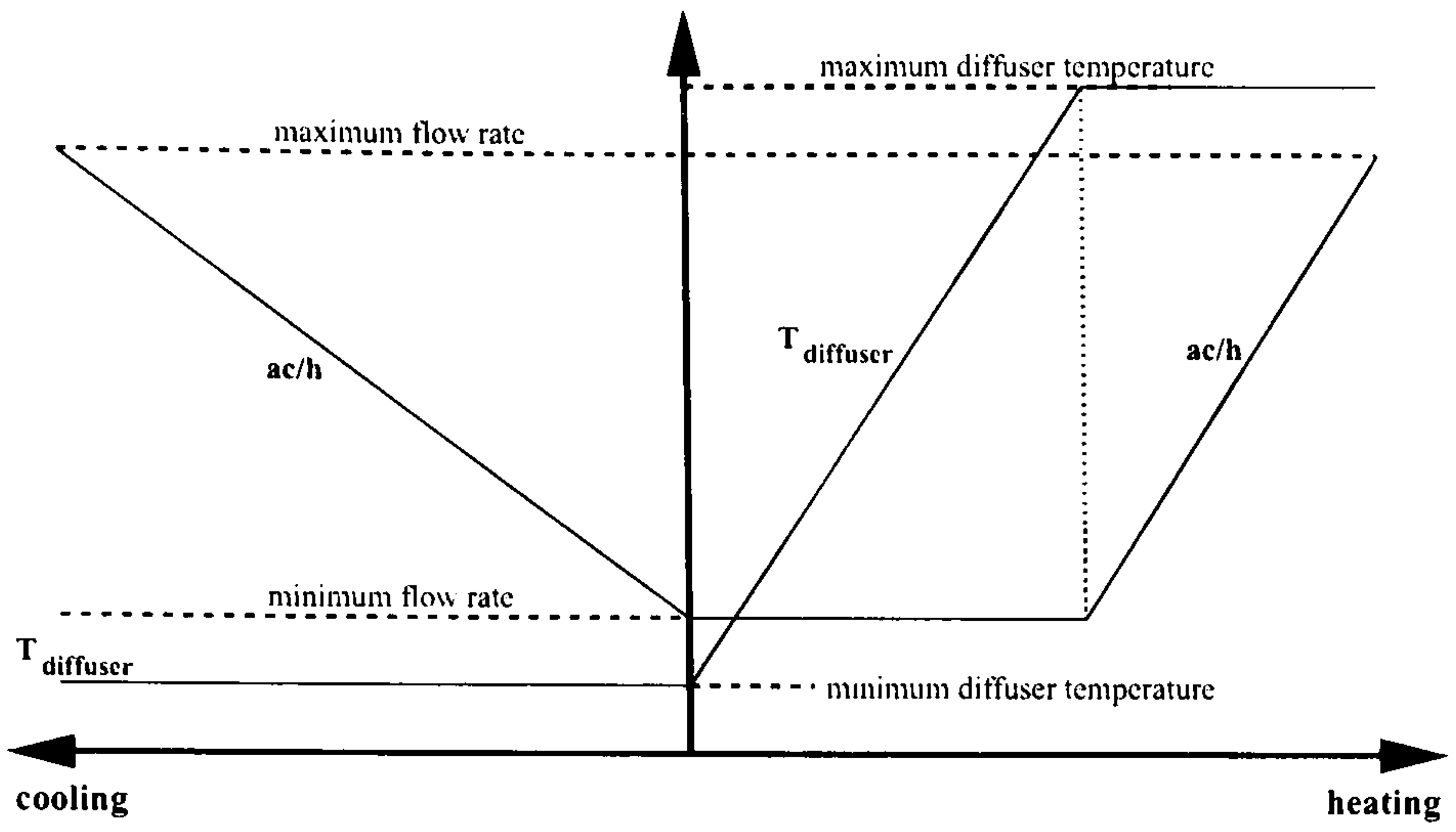

Figure D.2: VAV system with variable-volume heating

D.4 Calculating $T_{diffuser}$ and ac/h

The logic of the VAV and CVVT control strategies were implemented in a set of new subroutines. For each simulation time-step the algorithm first establishes either $T_{diffuser}$ or ac/h, depending on the system's control strategy (e.g. $T_{diffuser}$ is set for VAV systems which are cooling). The load met by the air-handling system (the *zone load*, q_{zone}) is then determined by,

$$q_{zone} = q_{plant} - q_{outdoor-air} \tag{D.1}$$

where q_{plant} is the total heat supplied or extracted (calculated by ESP-r in the usual fashion) and $q_{outdoor-air}$ is the energy required to heat or cool the outdoor air.

Equation D.1 is necessary because typically the outdoor air is conditioned within the air-handling system, so only the zone loads influence ac/h and $T_{diffuser}$. The user can treat the outdoor air supply as either infiltration or as ventilation from another zone (perhaps a zone created to model the air-handling system).

Once q_{zone} is determined the other required variable (ac/h or $T_{diffuser}$) is calculated with a heat balance on the zone,

$$q_{zone} = \dot{V}_{diffuser}\rho C_p(T_{diffuser} - T_{room-air}) \tag{D.2}$$

where ρ is the density $\{kg/m^3\}$ and C_p the heat capacity $\{J/kgK\}$ of air. $\dot{V}_{diffuser}$ is the flow rate of the air supplied to the room $\{m^3/s\}$: $ac/h = 3\ 600 \cdot \dot{V}_{diffuser}/V_{room}$.

The limiting constraints are then applied (minimum and maximum allowable ac/h and $T_{diffuser}$) and the results passed to the convection coefficient calculation subroutine.

D.5 Data Requirements

The data describing the idealized HVAC model is stored in the *convection calculation control file*, which is defined in Appendix F. ESP-r's *Project Manager* captures the necessary data through a series of menus and user prompts, and automatically creates this file. This process is also described in Appendix F.

Figure D.3 provides two examples of convection calculation control files. The first is for a CVVT system that ventilates the zone at 6 *ac/h* and has a supply temperature range of 13°C to 43°C. The outdoor air for this case is treated as ventilation from another zone (a zone representing the air handling unit) and the mixed flow method is used to calculate the convection coefficients. The second example is a VAV system with constant-volume heating. Its air flow rate ranges from 3 *ac/h* to 9 *ac/h*. The air is delivered at 13°C for cooling, and can rise to 43°C for heating. In this case the outdoor air is treated as infiltration in the model and Fisher's (1995) ceiling jet correlations are used to establish h_c.

```
[.htc for CVVT system]
  1 # number control intervals
  7 # number of constructions
 0.00    24.00 # start and end time of interval
  3 # calculation control type
  4. 6.0  43.  13.   2.   99.   4.  -1. # Mixed flow model, OA from AHU
  4. 6.0  43.  13.   2.   99.   4.  -1. # Mixed flow model, OA from AHU
  4. 6.0  43.  13.   2.   99.   4.  -1. # Mixed flow model, OA from AHU
  4. 6.0  43.  13.   2.   99.   4.  -1. # Mixed flow model, OA from AHU
  4. 6.0  43.  13.   2.   99.   4.  -1. # Mixed flow model, OA from AHU
  4. 6.0  43.  13.   2.   99.   4.  -1. # Mixed flow model, OA from AHU
  4. 6.0  43.  13.   2.   99.   4.  -1. # Mixed flow model, OA from AHU

[.htc for VAV system]
  1 # number control intervals
  7 # number of constructions
 0.00    24.00 # start and end time of interval
  3 # calculation control type
  2.  13.   3.  9.   1.  43.   2.  -1. # Fisher ceiling jet, OA infiltrated
  2.  13.   3.  9.   1.  43.   2.  -1. # Fisher ceiling jet, OA infiltrated
  2.  13.   3.  9.   1.  43.   2.  -1. # Fisher ceiling jet, OA infiltrated
  2.  13.   3.  9.   1.  43.   2.  -1. # Fisher ceiling jet, OA infiltrated
  2.  13.   3.  9.   1.  43.   2.  -1. # Fisher ceiling jet, OA infiltrated
  2.  13.   3.  9.   1.  43.   2.  -1. # Fisher ceiling jet, OA infiltrated
  2.  13.   3.  9.   1.  43.   2.  -1. # Fisher ceiling jet, OA infiltrated
```

Figure D.3: Sample descriptions of CVVT and VAV systems

APPENDIX E

Surface and Dynamic Assignment of Convection Correlations

This appendix documents the details of the adaptive convection algorithm's assignment of h_c correlations to surfaces. Nine tables are given, each one treating a convection regime classification. Table 5.1 (see page 118) indicates the correspondence between the convection regimes and the tables in this appendix. The second column of the tables indicates which correlations are assigned to each surface to calculate convection coefficients for the room's primary and secondary convection regimes. The remaining columns indicate how the adaptive convection algorithm toggles between the assigned correlations during the time-step simulation.

surface	applicable h_c correlations	dynamic assignment of h_c correlations		
wall	• Khalifa eq 3 • Alamdari-Hammond vert eq	heating on		Khalifa eq 3
		heating off		Alamdari-Hammond vert eq
window	• Khalifa eq 3 • Alamdari-Hammond vert eq	heating on		Khalifa eq 3
		heating off		Alamdari-Hammond vert eq
floor	• Awbi-Hatton heated floor eq • Alamdari-Hammond buoy horiz eq • Alamdari-Hammond stable horiz eq	heating on		Awbi-Hatton heated floor eq
		heating off	buoyant	Alamdari-Hammond buoy horiz eq
			stable	Alamdari-Hammond stable horiz eq
ceiling	• Khalifa eq 4 • Alamdari-Hammond buoy horiz eq • Alamdari-Hammond stable horiz eq	heating on		Khalifa eq 4
		heating off	buoyant	Alamdari-Hammond buoy horiz eq
			stable	Alamdari-Hammond stable horiz eq

Table E.1: Buoyancy caused by in-floor heating (regime A1)

surface	applicable h_c correlations	dynamic assignment of h_c correlations		
heated wall	• Awbi-Hatton heated wall eq	heating on		Awbi-Hatton heated wall eq
	• Alamdari-Hammond vert eq	heating off		Alamdari-Hammond vert eq
non-heated wall	• Khalifa eq 6	heating on		Khalifa eq 6
	• Alamdari-Hammond vert eq	heating off		Alamdari-Hammond vert eq
window	• Khalifa eq 6	heating on		Khalifa eq 6
	• Alamdari-Hammond vert eq	heating off		Alamdari-Hammond vert eq
floor	• Alamdari-Hammond buoy horiz eq • Alamdari-Hammond stable horiz eq	heating on		Alamdari-Hammond stable horiz eq
		heating off	buoyant	Alamdari-Hammond buoy horiz eq
			stable	Alamdari-Hammond stable horiz eq
ceiling	• Khalifa eq 7 • Alamdari-Hammond buoy horiz eq • Alamdari-Hammond stable horiz eq	heating on		Khalifa eq 7
		heating off	buoyant	Alamdari-Hammond buoy horiz eq
			stable	Alamdari-Hammond stable horiz eq

Table E.2: Buoyancy caused by heated wall panel (regime A2)

surface	applicable h_c correlations	dynamic assignment of h_c correlations	
wall	• Alamdari-Hammond vert eq		Alamdari-Hammond vert eq
window	• Alamdari-Hammond vert eq		Alamdari-Hammond vert eq
floor	• Alamdari-Hammond buoy horiz eq	buoyant	Alamdari-Hammond buoy horiz eq
	• Alamdari-Hammond stable horiz eq	stable	Alamdari-Hammond stable horiz eq
ceiling	• Alamdari-Hammond buoy horiz eq	buoyant	Alamdari-Hammond buoy horiz eq
	• Alamdari-Hammond stable horiz eq	stable	Alamdari-Hammond stable horiz eq

Table E.3: Buoyancy caused by other surface-air temperature differences (regime A3)

surface	**applicable h_c correlations**	**dynamic assignment of h_c correlations**		
wall	• Khalifa eq 6	heating on	Khalifa eq 6	
	• Alamdari-Hammond vert eq	heating off	Alamdari-Hammond vert eq	
window	• Khalifa eq 6 or 9 (user choice)	heating on	Khalifa eq 6 or 9	
	• Alamdari-Hammond vert eq	heating off	Alamdari-Hammond vert eq	
floor	• Alamdari-Hammond buoy horiz eq • Alamdari-Hammond stable horiz eq	heating on	Alamdari-Hammond stable horiz eq	
		heating off	buoyant	Alamdari-Hammond buoy horiz eq
			stable	Alamdari-Hammond stable horiz eq
ceiling	• Khalifa eq 7 • Alamdari-Hammond buoy horiz eq • Alamdari-Hammond stable horiz eq	heating on	Khalifa eq 7	
		heating off	buoyant	Alamdari-Hammond buoy horiz eq
			stable	Alamdari-Hammond stable horiz eq

Table E.4: Buoyancy caused by heater located underneath window (regime B1)

surface	applicable h_c correlations	dynamic assignment of h_c correlations		
wall close to heater	• Khalifa eq 5 • Alamdari-Hammond vert eq	heating on	Khalifa eq 5	
		heating off	Alamdari-Hammond vert eq	
wall not close to heater	• Khalifa eq 3 • Alamdari-Hammond vert eq	heating on	Khalifa eq 3	
		heating off	Alamdari-Hammond vert eq	
window	• Khalifa eq 3 or 10 (user choice) • Alamdari-Hammond vert eq	heating on	Khalifa eq 3 or 10	
		heating off	Alamdari-Hammond vert eq	
floor	• Alamdari-Hammond buoy horiz eq • Alamdari-Hammond stable horiz eq	heating on	Alamdari-Hammond stable horiz eq	
		heating off	buoyant	Alamdari-Hammond buoy horiz eq
			stable	Alamdari-Hammond stable horiz eq
ceiling	• Khalifa eq 4 • Alamdari-Hammond buoy horiz eq • Alamdari-Hammond stable horiz eq	heating on	Khalifa eq 4	
		heating off	buoyant	Alamdari-Hammond buoy horiz eq
			stable	Alamdari-Hammond stable horiz eq

Table E.5: Buoyancy caused by heater not located underneath window (regime B2)

surface	**applicable h_c correlations**	**dynamic assignment of h_c correlations**		
wall	• Fisher or Fisher-Pedersen ceiling-jet wall eq (user choice) • Alamdari-Hammond vert eq	fan on	ceiling-jet wall eq	
		fan off	Alamdari-Hammond vert eq	
window	• Fisher or Fisher-Pedersen ceiling-jet wall eq (user choice) • Alamdari-Hammond vert eq	fan on	ceiling-jet wall eq	
		fan off	Alamdari-Hammond vert eq	
floor	• Fisher or Fisher-Pedersen ceiling-jet floor eq (user choice) • Alamdari-Hammond buoy horiz eq • Alamdari-Hammond stable horiz eq	fan on	ceiling-jet floor eq	
		fan off	buoyant	Alamdari-Hammond buoy horiz eq
			stable	Alamdari-Hammond stable horiz eq
ceiling	• Fisher or Fisher-Pedersen ceiling-jet ceiling eq (user choice) • Alamdari-Hammond buoy horiz eq • Alamdari-Hammond stable horiz eq	fan on	ceiling-jet ceiling eq	
		fan off	buoyant	Alamdari-Hammond buoy horiz eq
			stable	Alamdari-Hammond stable horiz eq

Table E.6: Forced flow caused by air handling system with ceiling diffusers (regime C1)

surface	applicable h_c correlations	dynamic assignment of h_c correlations		
wall	• Fisher horizontal-jet wall eq	fan on	horizontal-jet wall eq	
	• Alamdari-Hammond vert eq	fan off	Alamdari-Hammond vert eq	
window	• Fisher horizontal-jet wall eq	fan on	horizontal-jet wall eq	
	• Alamdari-Hammond vert eq	fan off	Alamdari-Hammond vert eq	
floor	• Fisher horizontal-jet floor eq	fan on	horizontal-jet floor eq	
	• Alamdari-Hammond buoy horiz eq	fan off	buoyant	Alamdari-Hammond buoy horiz eq
	• Alamdari-Hammond stable horiz eq		stable	Alamdari-Hammond stable horiz eq
ceiling	• Fisher horizontal-jet ceiling eq	fan on	horizontal-jet ceiling eq	
	• Alamdari-Hammond buoy horiz eq	fan off	buoyant	Alamdari-Hammond buoy horiz eq
	• Alamdari-Hammond stable horiz eq		stable	Alamdari-Hammond stable horiz eq

Table E.7: Forced flow caused by air handling system with wall diffusers (regime C2)

surface	**applicable h_c correlations**	**dynamic assignment of h_c correlations**		
wall, fan blowing on	• Khalifa eq 8 • Alamdari-Hammond vert eq	heating on	Khalifa eq 8	
		heating off	Alamdari-Hammond vert eq	
wall, fan not blowing on	• Khalifa eq 3 • Alamdari-Hammond vert eq	heating on	Khalifa eq 3	
		heating off	Alamdari-Hammond vert eq	
window, fan blowing on	• Khalifa eq 8 • Alamdari-Hammond vert eq	heating on	Khalifa eq 8	
		heating off	Alamdari-Hammond vert eq	
window, fan not blowing on	• Khalifa eq 3 • Alamdari-Hammond vert eq	heating on	Khalifa eq 3	
		heating off	Alamdari-Hammond vert eq	
floor	• Alamdari-Hammond buoy horiz eq • Alamdari-Hammond stable horiz eq	heating on	Alamdari-Hammond stable horiz eq	
		heating off	buoyant	Alamdari-Hammond buoy horiz eq
			stable	Alamdari-Hammond stable horiz eq
ceiling	• Khalifa eq 4 • Alamdari-Hammond buoy horiz eq • Alamdari-Hammond stable horiz eq	heating on	Khalifa eq 4	
		heating off	buoyant	Alamdari-Hammond buoy horiz eq
			stable	Alamdari-Hammond stable horiz eq

Table E.8: Forced flow caused by circulating fan within room (regime D)

surface	**applicable h_c correlations**	**dynamic assignment of h_c correlations**		
wall	• Mixed flow wall eq	fan on	Mixed flow wall eq	
	• Alamdari-Hammond vert eq	fan off	Alamdari-Hammond vert eq	
window	• Mixed flow wall eq	fan on	Mixed flow wall eq	
	• Alamdari-Hammond vert eq	fan off	Alamdari-Hammond vert eq	
floor	• Mixed flow floor eq	fan on	Mixed flow floor eq	
	• Alamdari-Hammond buoy horiz eq	fan off	buoyant	Alamdari-Hammond buoy horiz eq
	• Alamdari-Hammond stable horiz eq		stable	Alamdari-Hammond stable horiz eq
ceiling	• Mixed flow ceiling eq	fan on	Mixed flow ceiling eq	
	• Alamdari-Hammond buoy horiz eq	fan off	buoyant	Alamdari-Hammond buoy horiz eq
	• Alamdari-Hammond stable horiz eq		stable	Alamdari-Hammond stable horiz eq

Table E.9: Mixed flow caused by air handling system with ceiling diffusers and surface-air temperature differences (regime E)

Convection Calculation Control Data

This appendix details the *convection calculation control file*. This file (usually named with a *.htc* suffix) is created by ESP-r's *Project Manager* and is used by the simulator to control the convection calculations. It stores the data required by the adaptive convection algorithm and by the supporting idealized HVAC model which simulates the convective regime induced in rooms by air handling systems (this model is described in Appendix D). Figure F.1 illustrates how the data are acquired from the user's perspective. The *convection calculation control file* is automatically generated by the *Project Manager* and requires no manipulation by the user.

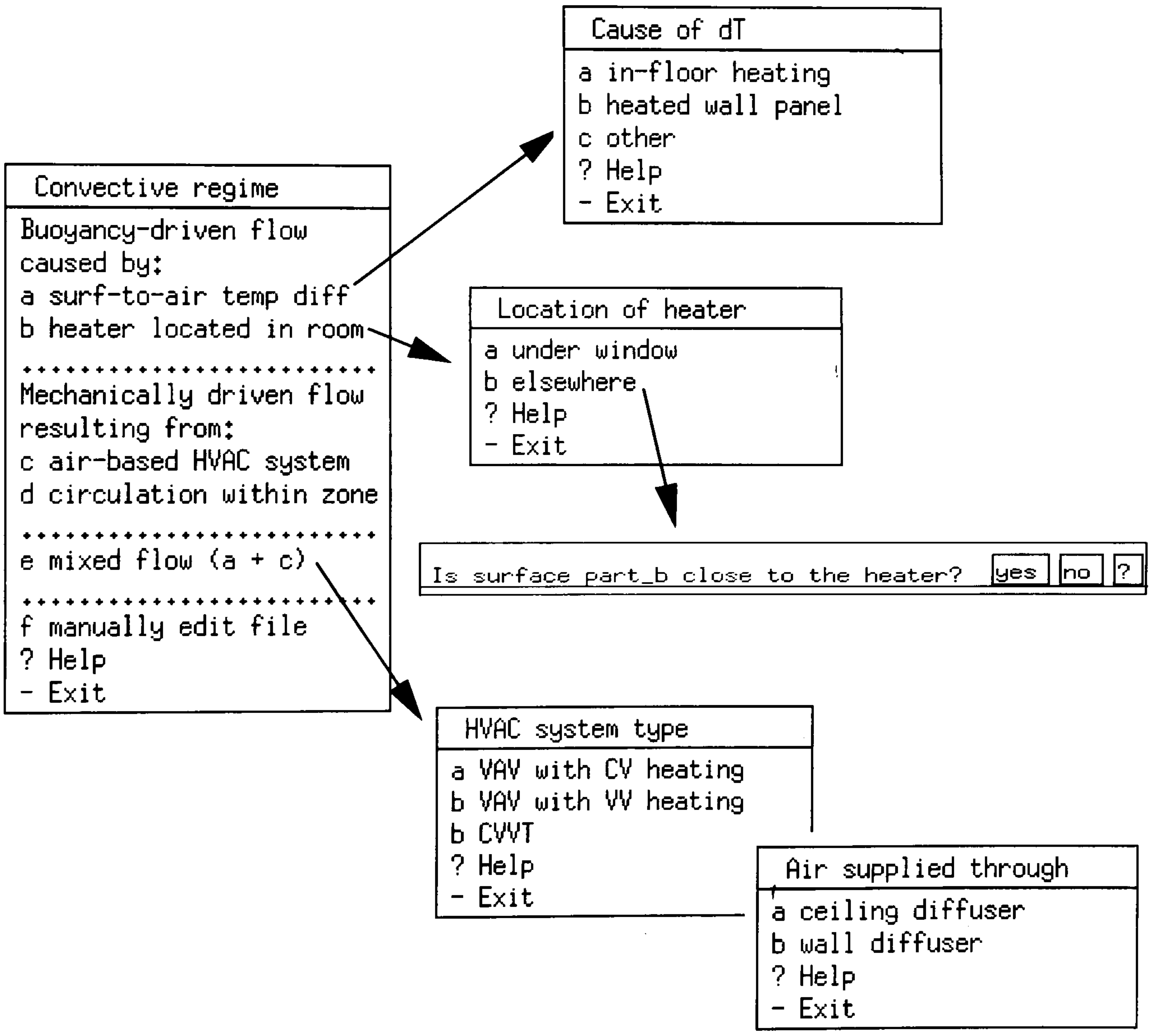

Figure F.1 User interface for appraising flow regime

A separate *convection calculation control file* is created for each zone. Each file contains header information (applicability times, number of surfaces, etc.) and a row for data for each surface in the zone. The surface-specific data fields are defined in Table F.1.

Data fields for each surface: a b c d e f g h
a indicates the type of HVAC system: • 1 for in-room heating device (e.g. radiator, in-floor heating, wall panel); • 2 for VAV with constant-volume heating; • 3 for VAV with variable-volume heating; • 4 for CVVT.
b indicates: • ICOR to use when system is on for in-room heating devices; • ac/h for CVVT systems; • the $T_{diffuser}$ cooling setpoint for VAV systems.
c indicates: • ICOR to use when system is off for in-room heating devices (-1 for simulation toggle); • the maximum allowable $T_{diffuser}$ for CVVT systems; • the minimum ac/h for VAV systems.
d indicates: • not used for in-room heating devices; • the minimum allowable $T_{diffuser}$ for CVVT systems; • the maximum ac/h for VAV systems.
e indicates the method for treating outdoor air ventilation (n/a for in-room heating devices): • 0 outdoor air is conditioned by the ventilation air (i.e. $q_{zone} = q_{plant}$ in equation D.1); • 1 outdoor air is treated as infiltration in the model; • 2 outdoor air is treated as ventilation from another zone in the model.
f indicates: • not used for in-room heating devices; • not used for CVVT systems; • the maximum allowable $T_{diffuser}$ for VAV systems.
g specifies which h_c correlation to use when the fan is operative (n/a for in-room heating devices): • 1 for Fisher and Pedersen's (1997) ceiling jet correlation (second set of ceiling jet equations in Table 4.5); • 2 for Fisher's (1995) ceiling jet correlation (first set of ceiling jet equations in Table 4.5); • 3 for Fisher's (1995) horizontal jet correlations (Table 4.5); • 4 for the mixed flow model.
h specifies which h_c correlation to use when the fan is inoperative (n/a for in-room heating devices): • > 0 indicates an ICOR flag; • -1 for the simulation toggle (Alamdari-Hammond by default).

Table F.1: Surface related data fields in convection calculation control file

APPENDIX G

Flow Visualization Facility

This appendix describes the flow visualization facility developed to support the integrated simulator. This facility allows the air flow at any cross-section in the room to be viewed, either instantaneously or over a period of time. Flow visualization is managed by the adaptive conflation controller according to the instructions provided by the user through the visualization parameters file. Any number of views can be generated, either each time CFD is invoked, or only periodically. All flow images presented in Chapters 3, 5, and 6 were generated with this facility.

The flow visualization facility is based on the same *point containment* approach utilized by ESP-r's solar shading and insolation algorithm. In fact, much of the coding was borrowed and adapted from this algorithm. Each flow vector in the plane of view is represented as a polygon (refer to Figure G.1). The length, thickness, and arrow head dimensions are all controlled by the user through the visualization parameters file. A mesh is superimposed on the viewing plane. Each mesh point represents a pixel in the resulting image (the resolution is also controlled by the user). Point containment tests are then performed to determine which pixels are covered by flow vectors in the viewing plane. Pixels are accordingly coloured and an X-bitmap image generated. The logic employed by the flow visualization facility is illustrated in Figure G.2.

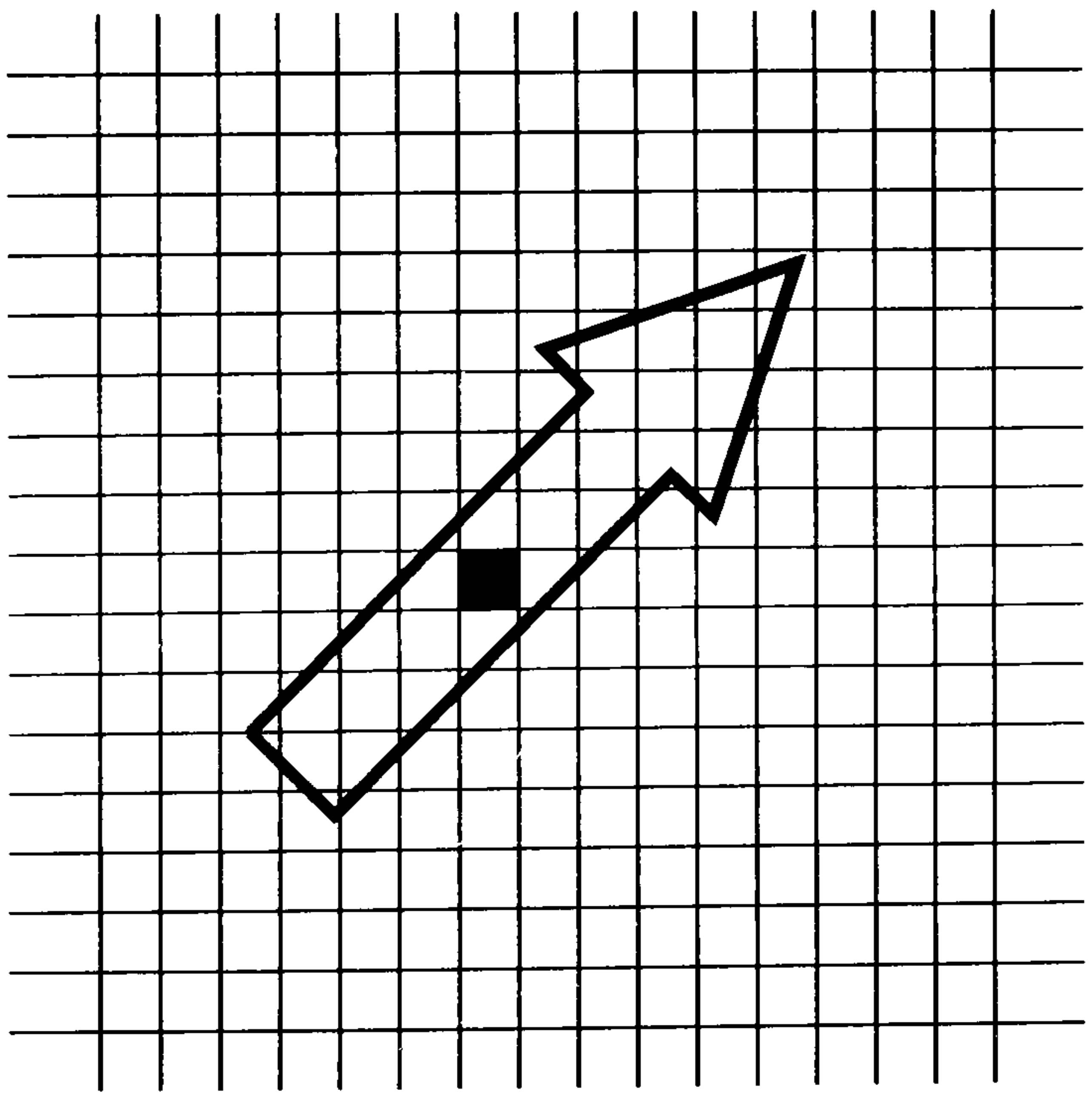

Figure G.1 Point containment test

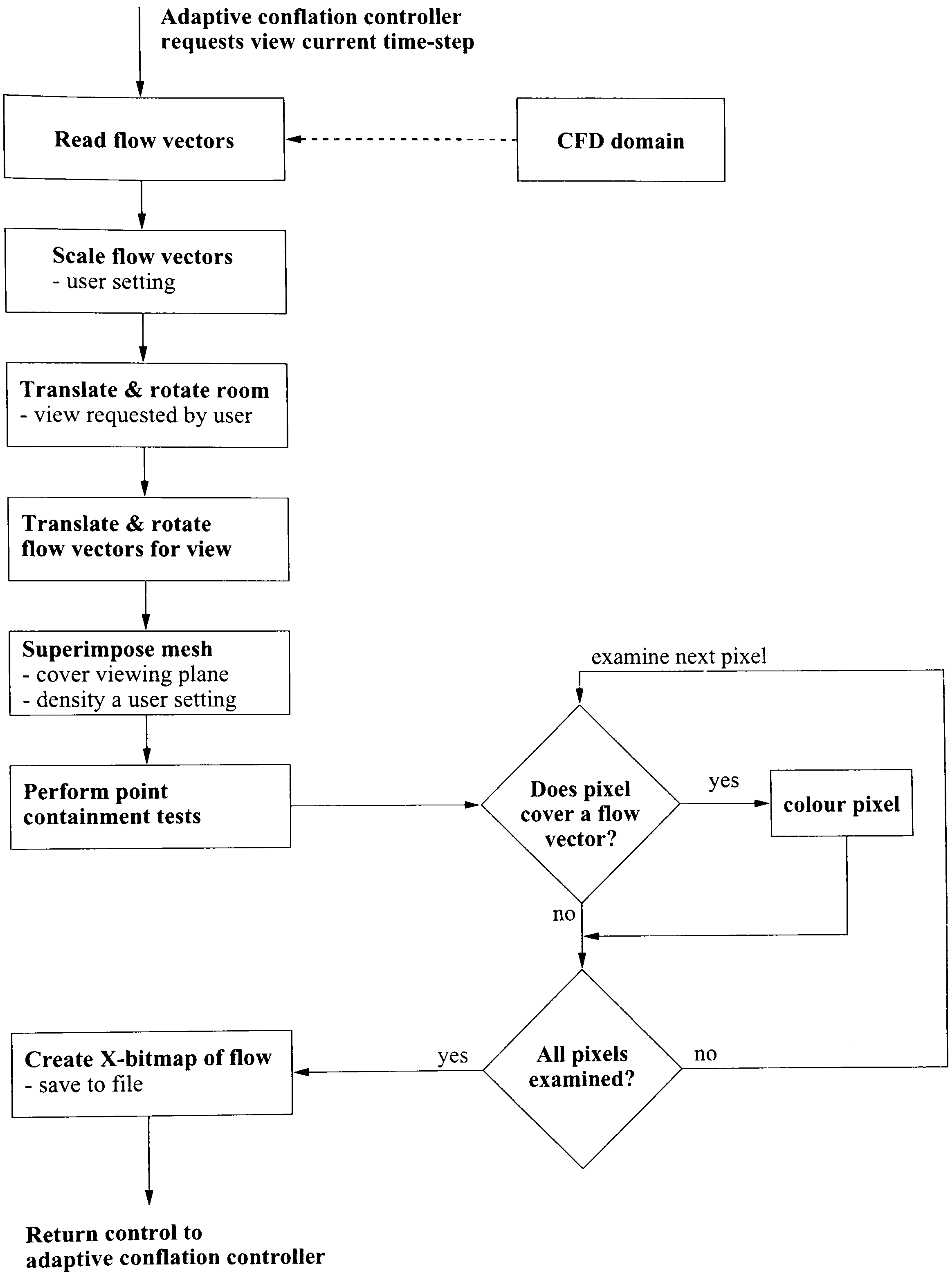

Figure G.2 Generating images of the flow pattern